

AD-A256 450



2

# NAVAL POSTGRADUATE SCHOOL Monterey, California

**S** DTIC  
ELECTE  
OCT 28 1992  
**A** **D**



## DISSERTATION

MODELING AND CONTROL OF A TRAILING  
WIRE ANTENNA TOWED BY AN  
ORBITING AIRCRAFT

by

James M. Clifton

September 1992

Dissertation Advisor: Louis V. Schmidt

Approved for public release; distribution is unlimited.

92-28336



00 10 02 134

UNCLASSIFIED

SECURITY CLASSIFICATION OF THIS PAGE

REPORT DOCUMENTATION PAGE				
1a REPORT SECURITY CLASSIFICATION <b>UNCLASSIFIED</b>		1b RESTRICTIVE MARKINGS		
2a SECURITY CLASSIFICATION AUTHORITY		3 DISTRIBUTION/AVAILABILITY OF REPORT Approved for public release; distribution is unlimited.		
2b DECLASSIFICATION/DOWNGRADING SCHEDULE				
4 PERFORMING ORGANIZATION REPORT NUMBER(S)		5 MONITORING ORGANIZATION REPORT NUMBER(S)		
6a NAME OF PERFORMING ORGANIZATION Naval Postgraduate School	6b OFFICE SYMBOL (If applicable) 55	7a NAME OF MONITORING ORGANIZATION Naval Postgraduate School		
6c ADDRESS (City, State, and ZIP Code) Monterey, CA 93943 5000		7b ADDRESS (City, State, and ZIP Code) Monterey, CA 93943 5000		
8a NAME OF FUNDING/SPONSORING ORGANIZATION	8b OFFICE SYMBOL (If applicable)	9 PROCUREMENT INSTRUMENT IDENTIFICATION NUMBER		
8c ADDRESS (City, State, and ZIP Code)		10 SOURCE OF FUNDING NUMBERS		
		Program Element No	Project No	Task No
				Work Unit Accession Number
11 TITLE (Include Security Classification)  MODELING AND CONTROL OF A TRAILING WIRE ANTENNA TOWED BY AN ORBITING AIRCRAFT				
12 PERSONAL AUTHOR(S) James M. Clifton				
13a TYPE OF REPORT Ph.D. Dissertation	13b TIME COVERED From To	14 DATE OF REPORT (year, month, day) September 1992	15 PAGE COUNT 244	
16 SUPPLEMENTARY NOTATION The views expressed in this thesis are those of the author and do not reflect the official policy or position of the Department of Defense or the U.S. Government.				
17 COSATI CODES		18 SUBJECT TERMS (continue on reverse if necessary and identify by block number)		
FIELD	GROUP	SUBGROUP		
		Towed Cable, Towed Wire, Dangling Chain, Vibrating String, Cantilevered Beam, TACAMO		
19 ABSTRACT (continue on reverse if necessary and identify by block number)  A model of the dynamics of a long trailing-wire antenna towed behind an orbiting aircraft was developed and then an investigation was made of several candidate schemes to control the wire's steady-state shape and oscillations due to wind gradients. A computer simulation was developed using the classic vibrating chain with free/fixed boundary conditions superimposed upon the wire's steady-state shape and tension distribution. Several forms of restorative and dissipative forces were considered in the analysis. The validity of the superposition approach was demonstrated for a wide operating range. A control law was developed which modulated the towplane orbit radius and demonstrated a potential for a 50 percent or better reduction in all oscillations. A second scheme using a controllable drogue at the trailing end of the wire was investigated. The controllable drogue had a limited success in oscillation reduction, but was found useful in tailoring the steady state shape of the wire.				
20 DISTRIBUTION/AVAILABILITY OF ABSTRACT <input checked="" type="checkbox"/> UNCLASSIFIED/DISTRIBUTED <input type="checkbox"/> SAME AS REPORT <input type="checkbox"/> DTIC USERS		21 ABSTRACT SECURITY CLASSIFICATION <b>UNCLASSIFIED</b>		
22a NAME OF RESPONSIBLE INDIVIDUAL Louis V. Schmidt		22b TELEPHONE (Include Area code) (408) 646-2972		22c OFFICE SYMBOL AA/Sc

DD FORM 1473, 84 MAR

83 APR edition may be used until exhausted  
All other editions are obsolete

SECURITY CLASSIFICATION OF THIS PAGE

UNCLASSIFIED

Approved for public release; distribution is unlimited.

Modeling and Control of a Trailing Wire Antenna  
Towed by and Orbiting Aircraft

by  
James M. Clifton  
Lieutenant Commander, United States Navy  
B.S. United States Naval Academy, 1982  
M.S. University of Tennessee, 1989  
M.S. Naval Postgraduate School, 1991

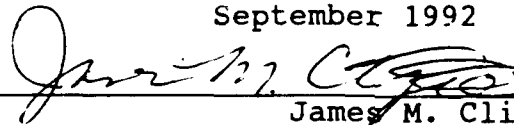
Submitted in partial fulfillment of the  
requirements for the degree of

DOCTOR OF PHILOSOPHY IN AERONAUTICAL ENGINEERING

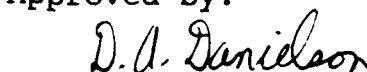
from the


NAVAL POSTGRADUATE SCHOOL  
September 1992

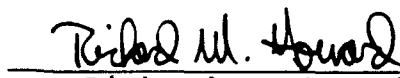
Author:

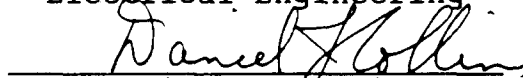
  
James M. Clifton

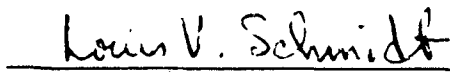
Approved by:

  
Donald Danielson  
Professor of Mathematics

  
Harold A. Titus  
Professor of  
Electrical Engineering

  
Richard M. Howard  
Professor of Aeronautics

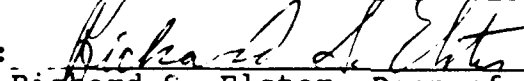
  
Daniel J. Collins  
Professor of Aeronautics

  
Louis V. Schmidt  
Professor of Aeronautics  
Dissertation Supervisor

Approved by:

  
Daniel J. Collins, Chairman, Department of  
Aeronautics and Astronautics

Approved by:

  
Richard S. Elster, Dean of Instruction

# ABSTRACT

A model of the dynamics of a long trailing-wire antenna towed behind an orbiting aircraft was developed and then an investigation was made of several candidate schemes to control the wire's steady-state shape and oscillations due to wind gradients. A computer simulation was developed using the classic vibrating chain with free/fixed boundary conditions superimposed upon the wire's steady-state shape and tension distribution. Several forms of restorative and dissipative forces were considered in the analysis. The validity of the superposition approach was demonstrated for a wide operating range. A control law was developed which modulated the towplane orbit radius and demonstrated a potential for a 50 percent or better reduction in all oscillations. A second scheme using a controllable drogue at the trailing end of the wire was investigated. The controllable drogue had a limited success in oscillation reduction, but was found useful in tailoring the steady-state shape of the wire.

DTIC QUALITY INSPECTED 2

Accession For	
NTIS	CRA21
DTIC	TAB
Unannounced	
Justification	
By	
Distribution/	
Availability Codes	
Dist	Avail and/or Special
A-1	

## TABLE OF CONTENTS

I.	INTRODUCTION.....	1
II.	BACKGROUND.....	4
III.	STEADY STATE MODEL.....	10
	A. FORMULATION OF THE WIRE EQUATIONS.....	10
	B. FORMULATION OF THE DROGUE EQUATIONS.....	32
	C. THE SHOOTING PROBLEM.....	39
	D. VALIDATION, VERIFICATION AND ANALYSIS.....	42
	E. SIDEFORCE MODEL.....	66
IV.	DYNAMIC MODEL.....	72
	A. FORMULATION OF THE DYNAMIC MODEL EQUATIONS...	72
	B. FORCING FUNCTION DEVELOPMENT.....	81
	C. SUPERPOSITION.....	84
	D. PSEUDO-DAMPING.....	85
	E. TENSION OSCILLATION.....	90
	F. VALIDATION, VERIFICATION AND ANALYSIS.....	96
V.	CONTROL OF WIRE OSCILLATIONS.....	115
	A. ANTI-YOYO.....	115
	B. FLYING DROGUE.....	139
VI.	CONCLUSIONS AND RECOMMENDATIONS.....	156
	APPENDIX A: STATIC MODEL CODE.....	158
	APPENDIX B: DANGLING CHAIN MODEL DEVELOPMENT.....	171
	APPENDIX C: FORCING FUNCTION DEVELOPMENT.....	188
	APPENDIX D: SUPERPOSITION EQUATIONS DEVELOPMENT.....	194

APPENDIX E: DYNAMIC MODEL CODE.....	198
APPENDIX F: EFFECTS OF ANTI-YOYO MANEUVER INDUCED TOWPLANE RADIUS AND ORBIT RATE VARIATIONS.....	222
APPENDIX G: FLYING DROGUE DESIGN.....	227
LIST OF REFERENCES.....	234
INITIAL DISTRIBUTION LIST.....	236

## ACKNOWLEDGEMENTS

This paper would not have been possible without the insight and support of Prof. Lou Schmidt. The most basic premise of the paper, involving superposition of classic dynamic solutions onto the steady state solution for the wire was first proposed by him. I would particularly like to thank him for the many long hours spent counseling, guidance and moral support. He is a true "shipmate".

I would also like to recognize Prof. Scandrett for his willing contributions to the project despite not being a member of the committee. He was always available to answer the hard questions and he did it on his own time.

## I. INTRODUCTION

There are a number of current and proposed uses for long cables or wires towed behind ships and aircraft. As examples, antisubmarine warfare ships tow long cables with acoustic equipment attached along the cable length for the purposes of isolating the equipment from the ship's noise sources, for penetrating temperature and salinity layers beneath the ocean surface and for providing a long baseline for passive acoustic ranging. A precise knowledge of the real time cable shape is required to determine the time dependent location of the sensors attached to the cable. Payne discusses the need for a knowledge of the cable shape during ship maneuvers and provides a bibliography of work done to model the dynamics of towed arrays. [Ref. 1] Several classes of aircraft trail long communications antennas required for low frequency/long distance communications. One interesting proposed application is to use a long cable towed from an orbiting cargo airplane to provide pinpoint airborne delivery of cargo. It will be seen later that this is possible due to the shape that the wire/cargo combination obtains when the towplane is in a steady-state orbit. [Ref. 2:p. 856] All of these applications share the same basic physics which are adapted and modified to study the individual case. Wire



oscillations and subsequent wire failures are problems common to many towed wire applications. It is the intent of this paper to focus upon the case of a cable and drogue system towed behind an airplane flying a circular orbit.

Irvine and Caughey [Ref. 3] provide an in-depth analysis of the vibrations of a cable which is fixed at both ends. This work is good background for the development of the governing equations of the towed wire. Anderson [Ref. 4] extends this work and analyzes the effects of the fluid and wire structure upon the vibrations. Skop and Choo [Ref. 2] provide an in-depth study of the equilibrium configuration of a cable towed behind a towplane flying a circular orbit as well as a discussion of the multi-valued nature of the governing equations. Anderson's student, Russell, continued this work in his dissertation [Ref. 5]. Matteis [Ref. 6] analyzed the dynamics of a sailplane while attached to the towplane. Matteis' discussion provides insight into the development of a model of the drogue on the end of the wire. The work mentioned above emphasizes the analytical solutions. The first thorough numerical model of the steady-state solution of the towed wire problem was provided by Huang [Ref. 7]. This report does an excellent job of outlining the algebraic and partial differential equations required to develop a computer simulation of the wire in a steady-state orbit but lacks a complete description of the numerical schemes employed. There is no documentation for

the software. Huang's paper was the basis upon which the static computer simulation in this dissertation was based. Crist [Ref. 8] developed the first computer simulation of the dynamics of the towed wire. The formulation of the problem and the numerical scheme limits the model of the wire to very long, lumped mass grid segments. The application of Crist's program has typically been limited to the analysis of wire dynamics during the reeling-in and reeling-out process. Fidelity has been a problem when applying the program to the analysis of the dynamics of the extended wire, for this reason, this dissertation emphasizes the orbiting phase of flight following reel-out. Finally, Lawton [Ref. 9] outlined a series of experiments performed onboard an EC-130 TACAMO airplane. Additionally, he made the suggestion of using the towplane as a trailing wire control device and documented deficiencies in the tension measurement equipment. This paper was the starting point for much of the wire control work done in this dissertation.

The most current and pressing application of the study of towed cables and drogues is the TACAMO. For this reason, the TACAMO configuration and physical parameters were chosen for use in this dissertation. Where possible, the modeling was kept as general as possible to allow application of the developed techniques to other problems.

## II. BACKGROUND

The problem of understanding the dynamics of a very long cable towed behind an aircraft has plagued the United States Navy for decades. A very long wire, on the order of 15,000 to 25,000 feet, is towed in a circular orbit behind the TACAMO strategic communications aircraft for use as a Very Low Frequency (VLF) antenna. A hollow, cone shaped drogue, with a weighted nose, is attached to the end of the wire for the advertised purpose of providing aerodynamic stabilization during the reel-out and reel-in process. The first TACAMO platforms were modified C-130 aircraft designated the EC-130. In 1971 the wire was changed from a 0.21 inch to a 0.16 inch diameter wire in order to reduce wire weight, drag and tension at the towplane. The change caused wild oscillations in tension and wire shape resulting in another switch to a stronger cable. In 1987 the EC-130 was replaced by the E-6A, a Boeing 707 variant. The oscillations experienced by the E-6A were more severe and several different wires and drogues were flight tested in an attempt to reduce the oscillations to an acceptable level. The success of this trial and error effort has been limited.

Oscillations in the trailing wire antenna result in three critical problems. First, the oscillations can cause contact between the wire and the towplane's horizontal tail.

The wire exits the towplane at a point in the lower fuselage approximately 45 feet forward of the tip of the towplane tail. During the oscillations the wire transcribes the approximate shape of a cone and as it rotates it often rubs the horizontal tail and flight control surfaces. There are three hazards associated with wire/aircraft contact. Most seriously, there is a possibility of fouling flight control surfaces. Next, abrasion of the aircraft structure leads to reliability and maintenance concerns. Lastly, abrasion of the wire leads to wire failure with the associated financial costs and the incumbent surface hazards from 20,000 feet of falling wire.

The second problem is that the oscillations in wire tension often result in exceeding the failure strength of the wire. This too causes the wire to part and fall to the surface. There are currently two types of wire in use. The older wire consists of 15 smaller steel wires wrapped in a single copper band in candy stripe fashion. This wire is commonly known as 1X15 due to its structure. The newer wire consists of 3 sets of wires wrapped in a 0.1582 inch diameter braid at approximately a 1.87 inch pitch. Each set consists of 6 wires symmetrically set around a seventh wire, all in a copper matrix. This wire is known as 3X7 wire. The old wire fails at approximately 2500 pounds of tension and the new wire at approximately 3000 pounds. The new wire

would be preferred due to its higher strength, however, the observed oscillations while using it are more severe.

The third problem caused by the oscillations is the significant degradation in the TACAMO's ability to perform its mission caused by the oscillations. Verticality is defined as the altitude of the towplane less the altitude of the drogue divided by the length of the wire. Thus a 100 percent verticality requires the wire to be perfectly vertical below the towplane. Since the wire is an antenna, transmission efficiency is a function of the trailing wire's shape. Verticality is a direct measure of the wire's ability to act as an antenna. As the verticality decreases below 60 percent or 70 percent, the transmitted power is drastically reduced. Oscillations that result in low verticality during portions of the cycle are evidenced by large oscillations in the voltage at the power amplifier and the signal received at test ground stations. The TACAMO is flown in a circular orbit with a bank angle on the order of 20 degrees to 40 degrees. In this orbit, the wire assumes the approximate shape of a helix with a smaller radius at the drogue than at the towplane. The wire typically makes  $\frac{1}{2}$  to a full turn in the helix shape from top to bottom. Flight test data shows that the oscillations occur at a frequency equal to the orbit rate of the towplane. The period is thus on the order of 100 to 200 seconds. Furthermore, the system requires from 2 to 30 minutes to

transmit a message and approximately 20 minutes to set up an orbit and trail the wire. It is thus crucial that the verticality be controlled over long periods of time. A short burst while the wire is at high verticality is not possible. Given that the average observed verticality is already in the range where transmission efficiency drops off, any oscillation in the verticality results in unacceptable variations in transmission efficiency.

To date, modifications to the wire and drogue configurations have been developed using flight-test based experiment. This has proven to be costly and subsequently has limited the number of options that have been explored. A cost effective means to better understand the dynamics and to explore various alternatives has long been required.

A good model of the time dependent motion of the wire was crucial to the understanding of the dynamics of a long wire trailed behind a towplane. The complexity of the system dictated the use of a digital simulation since the system could not be described in closed form. To be of use, the model had to allow for arbitrary forcing function inputs to be applied to the wire and it had to have provisions for tracking the locations and force histories for chosen points along the wire and allow other quantities to be easily added and tracked within the same program. Finally, the model's numerical program had to be both efficient and simple in order to allow candidate wire/drogue/towplane modifications

to be rapidly coded, added to the simulation and tested. It was the task of this dissertation to develop an adequate model of the dynamics of a very long wire towed in a circular orbit behind a towplane. As was mentioned earlier, the model was then used to explore several likely candidate ideas for control of the wire's oscillations. The models were written using the architecture and parameters specific to the TACAMO system. This was done because this is the most current and pressing application of the simulation. Most model analysis was performed using textbook derived aerodynamic coefficients for the current TACAMO 3X7 wire and drogue. Other physical parameters such as dimensions, weight, center of gravity of the drogue, etc. were measured using flight-worthy hardware. Note that the requirement that the numerical models be rapidly reconfigurable implies that they will be of use on other long towed wire problems. Where possible, the models were left in the most general form to facilitate changes.

The modeling of the wire dynamics was attacked in two steps. First, a program was developed which completely described the geometry and forces of the wire during steady-state, unforced conditions. Next, the oscillation mechanisms were modeled individually and superimposed upon the initial, steady-state solution. With the model of the wire dynamics in hand, the possibility of controlling the oscillations using the towplane to provide the control

inputs at the top of the wire was explored with good results. The next logical step was to attempt to control the oscillations using force feedback provided by a maneuvering drogue at the bottom of the wire. This technique had limited success for control of the oscillations, but proved useful in maximizing the mean verticality.



### III. STEADY-STATE MODEL

#### A. FORMULATION OF THE WIRE EQUATIONS

The steady-state model was fundamental to the trailing wire simulation. The steady-state solution provided the wire geometry and tension necessary as the initial condition of the dynamic model, as well as the solution upon which the dynamic small displacement analysis was superimposed. The static model developed here was based upon the 1969 Naval Air Development Center (NADC) static model governing equations [Ref. 7:pp.6-10]. An understanding of the static model was crucial to grasping the dynamic model, and so much of the NADC development of the equations was repeated and elaborated upon here. The numerical implementation used in this version of the static model relied upon second order accurate central differencing techniques. The derivation of the static solution began by first assuming that the wire was broken into a number of segments of uniform length equal to  $\Delta S$ . Second, it was assumed that shear forces were negligible and that only the tension forces were significant in the steady-state condition. Third, it was assumed that the wire was flying in a still, steady airmass with no winds. Lastly, as was mentioned above, the wire was in a steady-state condition with a constant circular orbit. Armed with these assumptions, a model manageable in both

analytical and numerical complexity was developed. Figure 3.1 is a graphical representation of the cylindrical coordinate system that was used for the static model. The system was modified slightly for the dynamic model.

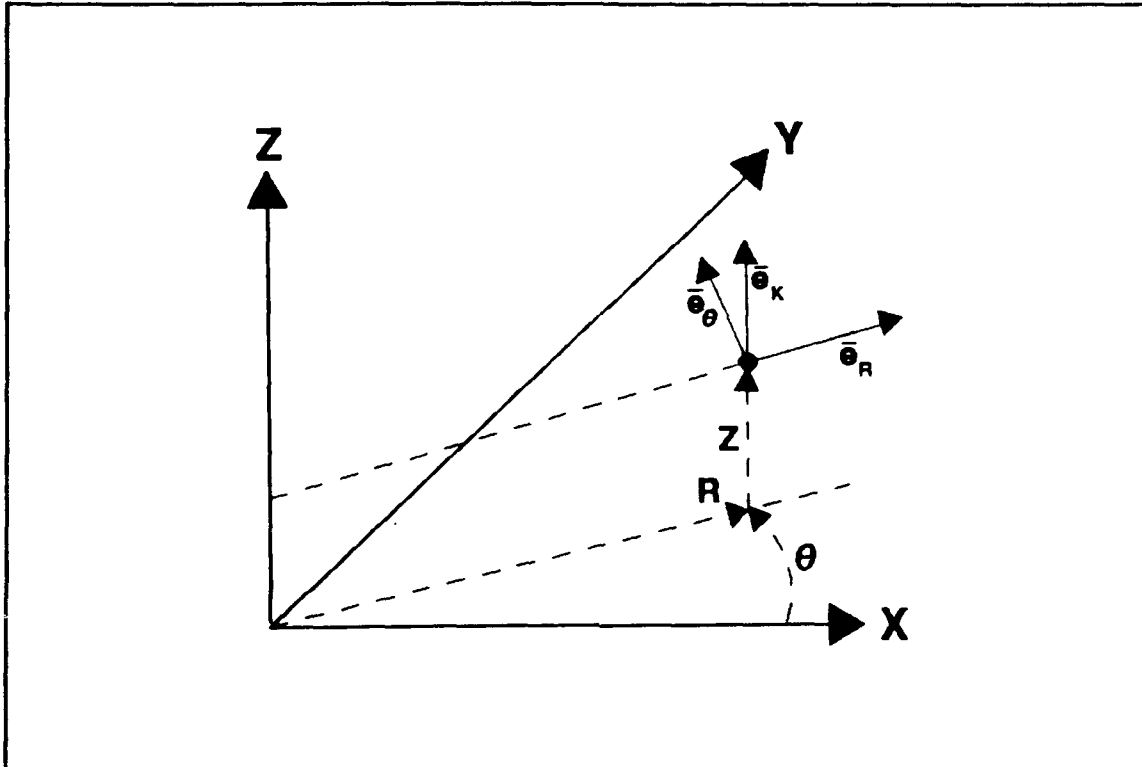


**Figure 3.1:** Cylindrical Coordinate System for Static Model

Figure 3.2 depicts the balance of forces upon a segment of the wire. Applying Newton's second law, the ordinary differential equation describing the balance of forces on an incremental section of the wire was written. This ordinary differential equation is provided as equation (3.1). Note that each term in equation (3.1) contains  $\Delta S$ .  $\Delta S$  was thus canceled from the entire expression.

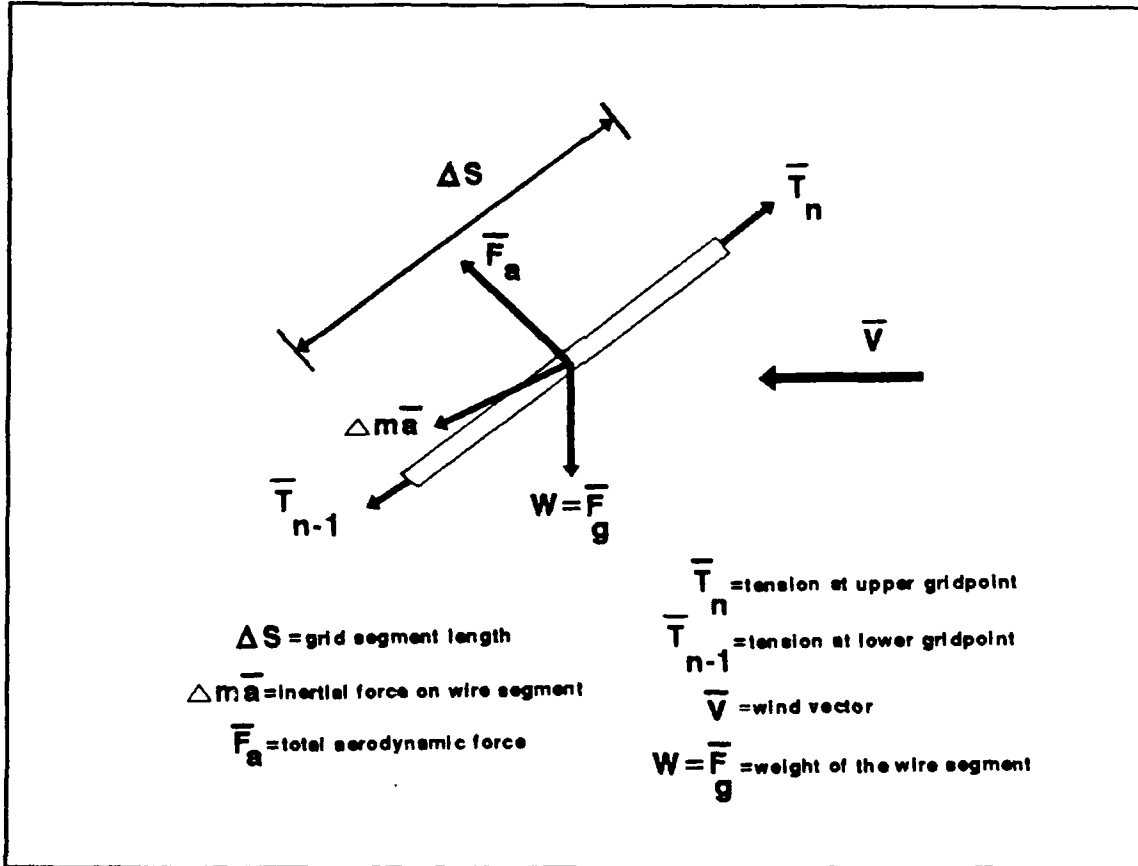


Figure 3.2: Summation of Forces Upon the Wire

$$\frac{d\bar{T}}{dS} \Delta S + \frac{\bar{F}_a}{\Delta S} \Delta S + \frac{\bar{F}_g}{\Delta S} \Delta S = \frac{m}{\Delta S} \Delta S \frac{d}{dt} \bar{V} = \frac{m}{\Delta S} \Delta S \bar{a} \quad (3.1)$$

Next, each term of equation (3.1) was considered individually, starting with the change in tension over the length of the segment as shown in equation (3.2). In equation (3.3),  $\bar{e}_{sn}$  was defined as the unit vector tangent to the wire at each gridpoint. Next, define  $|\bar{T}_n| = T_n$  and  $()'$  as the derivative with respect to  $S$ . Substituting equation (3.3) into equation (3.2) resulted in expression (3.4). Applying the product rule to equation (3.4) resulted in equation (3.5).

$$\left(\frac{d\bar{T}}{dS}\right)_n = \frac{d|\bar{T}_n|\bar{e}_{sn}}{dS} \quad (3.2)$$

$$\bar{e}_{sn} = \frac{dR}{dS}\bar{e}_R + R\frac{d\theta}{dS}\bar{e}_\theta + \frac{dZ}{dS}\bar{e}_K \quad (3.3)$$

$$\left(\frac{d\bar{T}}{dS}\right)_n = \frac{d}{dS}[T_n R'\bar{e}_R + T_n R\theta'\bar{e}_\theta + T_n Z'\bar{e}_K] \quad (3.4)$$

$$\begin{aligned} \left(\frac{d\bar{T}}{dS}\right)_n = & (T_n R')'\bar{e}_R + T_n R' \frac{d}{dS}\bar{e}_R \\ & + (T_n R\theta')'\bar{e}_\theta + (T_n R\theta') \frac{d}{dS}\bar{e}_\theta \\ & + (T_n Z')'\bar{e}_K + (T_n Z') \frac{d}{dS}\bar{e}_K \end{aligned} \quad (3.5)$$

Figure 3.3 is a sketch that illustrated the effects of  $\Delta\theta$  and its influence upon the unit tangent vectors  $\bar{e}_K$ ,  $\bar{e}_R$  and  $\bar{e}_\theta$ . Examining Figure 3.3, equation (3.6) was written. Equation (3.6) was substituted into the equation for  $(d\bar{T}/dS)_n$ , (3.5), resulting in (3.7). Equation (3.7) was then simplified to obtain equation (3.8).

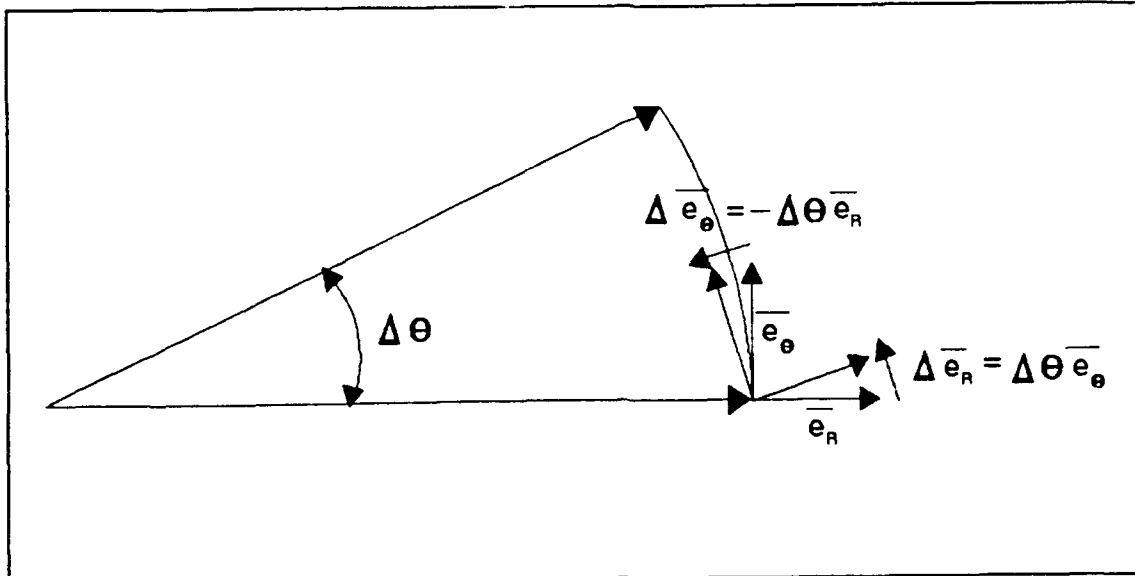


Figure 3.3: Effects of  $\Delta\theta$  in Cylindrical Coordinates

$$\begin{aligned}\frac{d}{dS}\bar{e}_K &= 0 \quad \text{always} \\ \frac{d}{dS}\bar{e}_\theta &= -\theta'\bar{e}_R \\ \frac{d}{dS}\bar{e}_R &= \theta'\bar{e}_\theta\end{aligned}\tag{3.6}$$

$$\begin{aligned}\left(\frac{d\bar{T}}{dS}\right)_n &= (T_n R_n')\bar{e}_R + (TR'\theta')\bar{e}_\theta + (TR\theta')'\bar{e}_\theta \\ &\quad - (TR\theta'\theta')\bar{e}_R + (TZ')\bar{e}_K\end{aligned}\tag{3.7}$$

$$\begin{aligned}\left(\frac{d\bar{T}}{dS}\right)_n &= [(TR')' - TR(\theta')^2]\bar{e}_R \\ &\quad + [(TR\theta')' + TR'\theta']\bar{e}_\theta + (TZ')\bar{e}_K\end{aligned}\tag{3.8}$$

In the next step, the grid structure depicted in Figure 3.4 was examined and used to write the central difference

approximation of equation (3.8). Two versions of the approximation were eventually required as will be explained at the end of this section. These are provided as equations (3.9) and (3.10). Several of the first derivative with respect to  $S$  terms were left in equation (3.10). The reason for not expanding these particular derivatives in terms of central difference approximations will be seen when the equations are written in their final forms at the end of this section.

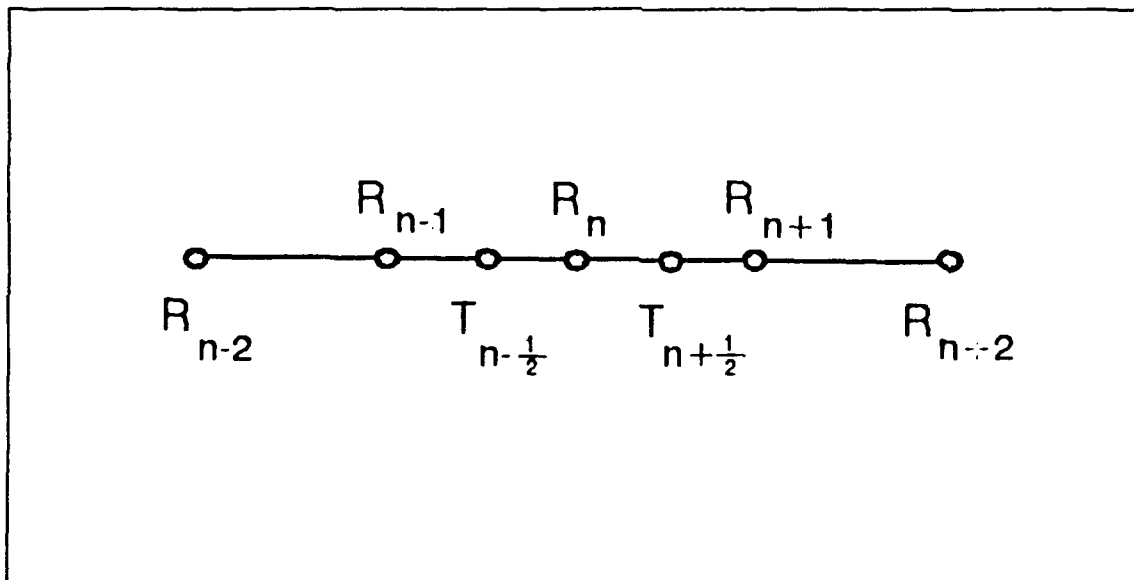


**Figure 3.4:** Central Difference Gridpoint Scheme for Change in Tension

$$\begin{aligned}
& \left( \frac{dT}{dS} \right)_n = \frac{T_{n+\frac{1}{2}} - T_{n-\frac{1}{2}}}{\Delta S} = \\
& \frac{\frac{T_{n+\frac{1}{2}}(R_{n+1} - R_n)}{\Delta S} - \frac{T_{n-\frac{1}{2}}(R_n - R_{n-1})}{\Delta S}}{\Delta S} - \left( \frac{T_{n+\frac{1}{2}} + T_{n-\frac{1}{2}}}{2} \right) R_n \left( \frac{\theta_{n+1} - \theta_{n-1}}{2\Delta S} \right)^2 \overline{e_R^+} \\
& \frac{T_{n+\frac{1}{2}} \left( \frac{R_{n+1} + R_n}{2} \right) \left( \frac{\theta_{n+1} - \theta_n}{\Delta S} \right) - T_{n-\frac{1}{2}} \left( \frac{R_n + R_{n-1}}{2} \right) \left( \frac{\theta_n - \theta_{n-1}}{\Delta S} \right)}{\Delta S} + \quad (3.9) \\
& \left( \frac{T_{n+\frac{1}{2}} + T_{n-\frac{1}{2}}}{2} \right) \left( \frac{R_{n+1} - R_{n-1}}{2\Delta S} \right) \left( \frac{\theta_{n+1} - \theta_{n-1}}{2\Delta S} \right) \overline{e_\theta} \\
& \frac{T_{n+\frac{1}{2}} \left( \frac{Z_{n+1} - Z_n}{\Delta S} \right) - T_{n-\frac{1}{2}} \left( \frac{Z_n - Z_{n-1}}{\Delta S} \right)}{\Delta S} \overline{e_K}
\end{aligned}$$

$$\begin{aligned}
& \left( \frac{dT}{dS} \right)_n = \frac{T_{n+\frac{1}{2}} - T_{n-\frac{1}{2}}}{\Delta S} = \\
& \left( \frac{T_{n+\frac{1}{2}} R'_{n+\frac{1}{2}} - T_{n-\frac{1}{2}} R'_{n-\frac{1}{2}}}{\Delta S} \right) \overline{e_R^+} \\
& \left( \frac{T_{n+\frac{1}{2}} \left( \frac{R_{n+1} + R_n}{2} \right) \theta'_{n+\frac{1}{2}} + T_{n-\frac{1}{2}} \left( \frac{R_{n+1} + R_n}{2} \right) \theta'_{n-\frac{1}{2}}}{\Delta S} \right) \overline{e_\theta^+} \quad (3.10) \\
& \left( \frac{T_{n+\frac{1}{2}} Z'_{n+\frac{1}{2}} - T_{n-\frac{1}{2}} Z'_{n-\frac{1}{2}}}{\Delta S} \right) \overline{e_K}
\end{aligned}$$

Equations (3.9) and (3.10) were the central difference approximations of the first term in equation (3.1). Eventually, central difference approximations were substituted for all of the terms of equation (3.1). The three orthogonal components of this vector equation were then solved as a coupled set.

Equations (3.9) and (3.10) included four unknowns ( $R_n$ ,  $\theta_n$ ,  $Z_n$  and  $T_n$ ) in three components ( $\bar{e}_R$ ,  $\bar{e}_\theta$ ,  $\bar{e}_z$ ). A fourth compatibility equation was required to complete the problem statement. Compatibility was established in two separate ways. In the first case, compatibility was established using the assumption that the wire was essentially inextensible with the result that the distance between each gridpoint remained invariant. The equation in rectangular coordinates was initially stated as in (3.11).

$$\Delta S^2 = (X_n - X_{n-1})^2 + (Y_n - Y_{n-1})^2 + (Z_n - Z_{n-1})^2 \quad (3.11)$$

Equation (3.11) was converted to cylindrical coordinates in equation (3.12). Expanding (3.12) and simplifying led to (3.13). Solving (3.13) for  $Z_n$  left (3.14) which was the final form of the first compatibility relation.

$$\Delta S^2 = (R_n \cos \theta_n - R_{n-1} \cos \theta_{n-1})^2 + (R_n \sin \theta_n - R_{n-1} \sin \theta_{n-1})^2 + (Z_n - Z_{n-1})^2 \quad (3.12)$$

$$\Delta S^2 = R_n^2 + R_{n-1}^2 - 2R_n R_{n-1} \cos(\theta_n - \theta_{n-1}) + (Z_n - Z_{n-1})^2 \quad (3.13)$$

$$Z_n = Z_{n-1} \pm \sqrt{\Delta S^2 - R_n^2 - R_{n-1}^2 + 2R_n R_{n-1} \cos(\theta_n - \theta_{n-1})} \quad (3.14)$$

The compatibility equation in (3.14) had the distinct advantage that it required knowledge of only the previous gridpoint as well as the  $R$  and  $\theta$  at the current gridpoint to calculate  $Z_{n+1}$ . It had the disadvantage that it was not



very accurate in the general case where the curvature of the wire may account for a lessening of the direct length between gridpoints. This relation had utility for one time calculations to obtain the first internal gridpoints. The inaccuracies accrued in a single grid segment were small and the need to start the computations at the boundary greatly override their magnitude. The negative case of the  $\pm$  term in equation (3.14) was excluded since the final steady-state solution was monotonically increasing in  $Z$  from the drogue to the towplane.

The second formulation of the compatibility equation made use of the definition of the unit tangent vector provided in equation (3.3). The expression is rewritten in (3.15) with the indices as required for this application. Equation (3.16) is the central difference approximation of (3.15). The central difference approximation in (3.16) was second order accurate and more precise than equation (3.14) but required the two previous gridpoint locations as a start.

$$\begin{aligned} R'_{n+\frac{1}{2}} + R_{n+\frac{1}{2}} \theta'_{n+\frac{1}{2}} + Z'_{n+\frac{1}{2}} = \\ R'_{n+\frac{1}{2}} + \left( \frac{R_{n+1} + R_n}{2} \right) \theta'_{n+\frac{1}{2}} + Z'_{n+\frac{1}{2}} = 1 \end{aligned} \quad (3.15)$$

$$\left( \frac{R_{n+1} - R_{n-1}}{2\Delta S} \right)^2 + R_n^2 \left( \frac{\theta_{n+1} - \theta_{n-1}}{2\Delta S} \right)^2 + \left( \frac{Z_{n+1} - Z_{n-1}}{2\Delta S} \right)^2 = 1 \quad (3.16)$$

For the steady-state, no-wind solution, the radial and vertical coordinates of each gridpoint were constant.  $\dot{\psi}$  was defined as the orbit rate of the airplane. The velocity at gridpoint  $n$  was written as a vector cross product, in equation (3.17). For the case of constant  $R_n$  and  $Z_n$ , equation (3.18) was written at each gridpoint. Finally, for steady-state conditions where no wind was allowed,  $\dot{\psi} = \dot{\theta}_n = \dot{\theta}$ , resulting in equation (3.19).

$$\overline{V}_n = \dot{\psi} \times \overline{R}_n \quad (3.17)$$

$$\overline{V}_n = R_n \dot{\psi} \overline{e}_{\theta n} \quad (3.18)$$

$$\overline{V}_{rel n} = R_n \dot{\theta} \overline{e}_{\theta n} \quad (3.19)$$

The magnitude of the relative velocity at each gridpoint, a term needed later in the derivation, was expressed by equation (3.20).

$$|\overline{V}_{rel n}| = |R_n \dot{\theta}| \quad (3.20)$$

The central difference approximation of the unit vector, tangent to the wire at each gridpoint was also required later in the derivation. Applying a second order accurate central difference approximation to equation (3.3) resulted in equation (3.21).

$$\overline{e_{sn}} = \left( \frac{R_{n+1} - R_{n-1}}{2\Delta S} \right) \overline{e_R} + \frac{R_n(\theta_{n+1} - \theta_{n-1})}{2\Delta S} \overline{e_\theta} + \left( \frac{Z_{n+1} - Z_{n-1}}{2\Delta S} \right) \overline{e_K} \quad (3.21)$$

It was desirable to resolve the  $\overline{V}_{reln}$  vector into components normal and axial to the wire at each control point. This was done to facilitate the application of the characteristic aerodynamic coefficients for a cylindrical wire as outlined by Hoerner [Ref.10: pp.3.11-3.12,4.5]. Defining  $\overline{V}_{relparn}$  as the component of  $\overline{V}_{reln}$  parallel to the wire, equation (3.22) was written by noting that the magnitude of  $\overline{V}_{relparn}$  was equal to the dot product of  $\overline{V}_{reln}$  and the wire unit tangent vector and it was coincident with the unit tangent vector. The dot product was expanded using (3.19) and (3.21) and then simplified to the form of (3.23).

$$\overline{V_{relparn}} = (\overline{V_{reln}} \cdot \overline{e_{sn}}) \overline{e_{sn}} \quad (3.22)$$

$$\overline{V_{relparn}} = (\overline{V_{reln}} \cdot \overline{e_{sn}}) \overline{e_{sn}} = \frac{-R_n^2 \dot{\theta}}{2\Delta S} (\theta_{n+1} - \theta_{n-1}) \overline{e_{sn}} \quad (3.23)$$

Defining  $\overline{V}_{relpern}$  as the component of  $\overline{V}_{reln}$  perpendicular to the flow, (3.24) was written by noting that  $\overline{V}_{relpern}$  was the orthogonal component of  $\overline{V}_{reln}$  remaining after  $\overline{V}_{relparn}$  was developed. Equations (3.19), (3.21) and (3.23) were substituted into (3.24) to derive (3.25) and (3.25) was simplified to get (3.26).

$$\overline{V_{relpern}} = \overline{V_{reln}} - (\overline{V_{reln}} \cdot \overline{e_{sn}}) \overline{e_{sn}} \quad (3.24)$$

$$\begin{aligned} \overline{V_{relpern}} = & -R_n \dot{\theta} \overline{e_{\theta}} + \left( R_n^2 \dot{\theta} \left( \frac{\theta_{n+1} - \theta_{n-1}}{2\Delta S} \right) \right) \\ & \left[ \left( \frac{R_{n+1} - R_{n-1}}{2\Delta S} \right) \overline{e_R} + R_n \left( \frac{\theta_{n+1} - \theta_{n-1}}{2\Delta S} \right) \overline{e_{\theta}} + \left( \frac{Z_{n+1} - Z_{n-1}}{2\Delta S} \right) \overline{e_K} \right] \end{aligned} \quad (3.25)$$

$$\begin{aligned} \overline{V_{relpern}} = & R_n \dot{\theta} \left[ R_n \frac{(\theta_{n+1} - \theta_{n-1})(R_{n+1} - R_{n-1})}{4\Delta S^2} \overline{e_R} + \right. \\ & \left. \left( R_n^2 \frac{(\theta_{n+1} - \theta_{n-1})^2}{4\Delta S^2} - 1 \right) \overline{e_{\theta}} + \left( \frac{R_n(\theta_{n+1} - \theta_{n-1})(Z_{n+1} - Z_{n-1})}{4\Delta S^2} \right) \overline{e_K} \right] \end{aligned} \quad (3.26)$$

The magnitude of  $\overline{V_{relpern}}$ , used in several of the later relationships and shown in equation (3.27), was obtained from (3.26).

$$\begin{aligned} |\overline{V_{relpern}}| = & R_n \dot{\theta} \left[ \frac{R_n^2(\theta_{n+1} - \theta_{n-1})^2(R_{n+1} - R_{n-1})^2}{16\Delta S^4} + \frac{R_n^4(\theta_{n+1} - \theta_{n-1})^4}{16\Delta S^4} \right. \\ & \left. - \frac{2R_n^2(\theta_{n+1} - \theta_{n-1})^2}{4\Delta S^2} + 1 + \frac{R_n^2(\theta_{n+1} - \theta_{n-1})^2(Z_{n+1} - Z_{n-1})^2}{16\Delta S^4} \right]^{\frac{1}{2}} \end{aligned} \quad (3.27)$$

Applying the definition of  $\overline{e_{sn}}$  given in equation (3.21) and noting that  $|\overline{e_{sn}}| = 1$ , it was possible to factor (3.28) from each term and then apply the substitution for  $|\overline{e_{sn}}|$  to obtain equation (3.29).

$$\frac{R_n^2(\theta_{n+1} - \theta_{n-1})^2}{4\Delta S^2} \quad (3.28)$$

$$|\overline{V_{relpern}}| = R_n \dot{\theta} \sqrt{1 - \frac{R_n^2 (\theta_{n+1} - \theta_{n-1})^2}{4 \Delta S^2}} \quad (3.29)$$

The Hoerner model defined a friction dominated coefficient,  $C_f$ , which was a measure of the force component along the direction of the relative velocity and was defined using the relative velocity as provided above. In addition, a second coefficient,  $C_D$ , was defined. This term was dominated by the significant separation drag associated with the bluff shape of the cylinder-like wire.  $C_D$  was a measure of the aerodynamic force normal to the cylinder and in the direction of the velocity component normal to the cylinder. The force was defined in terms of the normal component of velocity vice the full relative velocity.  $C_D$  was a measure of what would be called lift in the classic sense as well as form and separation drag, while  $C_f$  was a measure of the skin friction drag and was always oriented in the direction of the relative flow. Both coefficients used the diameter of the cylinder as the characteristic length, however, as mentioned above, the  $C_f$  coefficient used the full relative velocity to define the coefficient and the  $C_D$  coefficient used only that portion of the relative velocity normal to the wire. A third coefficient will be introduced later, which will account for the possibility of a sideforce perpendicular to the wire and the steady-state  $\bar{e}_R$ ,  $\bar{e}_R$  plane.

Using both of these coefficients ( $C_D$  and  $C_f$ ), the total aerodynamic force upon a segment of the wire was characterized as in equation (3.30). Note that this is not a magnitude but a true force vector. Substituting equations (3.26) and (3.29) into (3.30) resulted in (3.31). Finally, rearranging (3.31) provided equation (3.32).

$$\frac{\overline{F_{an}}}{\Delta S} = \frac{1}{2} \rho_n |\overline{V_{relpern}}| \overline{V_{relpern}} D C_D + \frac{1}{2} \rho_n |\overline{V_{reln}}| \overline{V_{reln}} D C_f \quad (3.30)$$

$$\begin{aligned} \frac{\overline{F_{an}}}{\Delta S} = & \left( \frac{1}{2} \rho_n D C_D \right) R_n \dot{\theta} \sqrt{1 - \frac{R_n^2 (\theta_{n+1} - \theta_{n-1})^2}{4 \Delta S^2}} (R_n \dot{\theta}) \left[ \frac{R_n (\theta_{n+1} - \theta_{n-1}) (R_{n+1} - R_{n-1})}{4 \Delta S^2} \overline{e_R} \right. \\ & \left. + \left[ \frac{R_n^2 (\theta_{n+1} - \theta_{n-1})^2}{4 \Delta S^2} - 1 \right] \overline{e_\theta} + \left[ \frac{R_n (\theta_{n+1} - \theta_{n-1}) (Z_{n+1} - Z_{n-1})}{4 \Delta S^2} \right] \overline{e_K} \right] - \frac{1}{2} \rho_n D C_f (R_n \dot{\theta})^2 \overline{e_\theta} \end{aligned} \quad (3.31)$$

$$\begin{aligned} \frac{\overline{F_{an}}}{\Delta S} = & \frac{1}{2} \rho_n D C_D (R_n \dot{\theta})^2 \sqrt{1 - \frac{R_n^2 (\theta_{n+1} - \theta_{n-1})^2}{4 \Delta S^2}} \frac{R_n (\theta_{n+1} - \theta_{n-1}) (R_{n+1} - R_{n-1})}{4 \Delta S^2} \overline{e_R} \\ & + \frac{1}{2} \rho_n D (R_n \dot{\theta})^2 \left[ -C_f + C_D \sqrt{1 - \frac{R_n^2 (\theta_{n+1} - \theta_{n-1})^2}{4 \Delta S^2}} \frac{R_n^2 (\theta_{n+1} - \theta_{n-1})^2}{4 \Delta S^2} - 1 \right] \overline{e_\theta} \\ & + \frac{1}{2} \rho_n D C_D (R_n \dot{\theta})^2 R_n \sqrt{1 - \frac{R_n^2 (\theta_{n+1} - \theta_{n-1})^2}{4 \Delta S^2}} \frac{(\theta_{n+1} - \theta_{n-1}) (Z_{n+1} - Z_{n-1})}{4 \Delta S^2} \overline{e_K} \end{aligned} \quad (3.32)$$

Equation (3.32) was the finite difference approximation of the second term in equation (3.1). The remaining terms were derivable in a straight forward manner. The right hand

side of equation (3.1) was the inertial term of the wire segment. For the static case, the inertial force was due solely to the centrifugal force. Further, the force was constant at each wire segment and dependent solely upon the tangential component of velocity, radial position and mass. Defining  $\mu$ =mass per unit length and noting that in steady-state the tangential component of velocity at each gridpoint was equal to the magnitude of  $\bar{V}_{reln}$  as in equation (3.20) allowed equation (3.33) to be stated.

$$\frac{\bar{F}_{In}}{\Delta S} = -\mu \frac{[\bar{V}_{reln}]^2}{R_n} \bar{e}_R = -\mu \dot{\theta}^2 R_n \bar{e}_R \quad (3.33)$$

The final term in equation (3.1) was the contribution due to the weight of the wire segment. The equation was again in terms of per unit length and  $g$  was defined as the acceleration due to gravity resulting in equation (3.34).

$$\frac{\bar{F}_g}{\Delta S} = -\mu g \bar{e}_x \quad (3.34)$$

All of the components of equation (3.1) were thus formulated. It was then possible to substitute these components into (3.1), to derive a single vector equation. This equation consisted of three orthogonal vector components which could be solved simultaneously. Performing the substitution and using (3.9) vice (3.10) allowed equations (3.35) to (3.37) to be immediately written. The

compatibility relation, equation (3.17), was rewritten in (3.38) for convenience.

$$\begin{aligned} & \frac{T_{n+\frac{1}{2}}(R_{n+1}-R_n)-T_{n-\frac{1}{2}}(R_n-R_{n-1})}{\Delta S^2} - \left( \frac{T_{n+\frac{1}{2}}+T_{n-\frac{1}{2}}}{2} \right) R_n \left( \frac{\theta_{n+1}-\theta_{n-1}}{2\Delta S} \right)^2 \\ & + \frac{1}{2} \rho_n D C_D (R_n \dot{\theta})^2 \sqrt{1 - \frac{R_n^2 (\theta_{n+1}-\theta_{n-1})^2}{4\Delta S^2}} \left( \frac{R_n (\theta_{n+1}-\theta_{n-1}) (R_{n+1}-R_{n-1})}{4\Delta S^2} \right) = -\mu \dot{\theta}^2 R_n \end{aligned} \quad (3.35)$$

$$\begin{aligned} & \frac{T_{n+\frac{1}{2}}(R_{n+1}+R_n)(\theta_{n+1}-\theta_n)-T_{n-\frac{1}{2}}(R_n+R_{n-1})(\theta_n-\theta_{n-1})}{2\Delta S^2} \\ & + \frac{\left( \frac{T_{n+\frac{1}{2}}+T_{n-\frac{1}{2}}}{2} \right) (R_{n+1}-R_{n-1})(\theta_{n+1}-\theta_{n-1})}{8\Delta S^2} + \\ & \frac{1}{2} \rho_n D (R_n \dot{\theta})^2 \left[ -C_F + C_D \sqrt{1 - \frac{R_n^2 (\theta_{n+1}-\theta_{n-1})^2}{4\Delta S^2}} \left( \frac{R_n^2 (\theta_{n+1}-\theta_{n-1})^2}{4\Delta S^2} - 1 \right) \right] = 0 \end{aligned} \quad (3.36)$$

$$\begin{aligned} & \frac{T_{n+\frac{1}{2}}(Z_{n+1}-Z_n)-T_{n-\frac{1}{2}}(Z_n-Z_{n-1})}{\Delta S^2} + \\ & \frac{1}{2} \rho_n D C_D (R_n \dot{\theta})^2 R_n \sqrt{1 - \frac{R_n^2 (\theta_{n+1}-\theta_{n-1})^2}{4\Delta S^2}} \left( \frac{(\theta_{n+1}-\theta_{n-1})(Z_{n+1}-Z_{n-1})}{4\Delta S^2} \right) - \mu g = 0 \end{aligned} \quad (3.37)$$

$$\left( \frac{R_{n+1}-R_{n-1}}{2\Delta S} \right)^2 + R_n^2 \left( \frac{\theta_{n+1}-\theta_{n-1}}{2\Delta S} \right)^2 + \left( \frac{Z_{n+1}-Z_{n-1}}{2\Delta S} \right)^2 = 1 \quad (3.38)$$



Using (3.35) to (3.37) with the  $\Delta S$  compatibility equation in the form of equation (3.14) for the first internal gridpoint and (3.38) for all subsequent gridpoints, there existed four finite difference equations in the four unknowns  $R_n$ ,  $\theta_n$ ,  $Z_n$  and  $T_n$ . The task was then to devise a numerical scheme to solve these coupled finite difference equations along the entire wire. The logical choice was to iteratively solve for  $R_{n+1}$ ,  $\theta_{n+1}$ ,  $T_{n+1}$  and  $Z_{n+1}$  using the four equations and knowledge of the location and tensions of the previous two gridpoints. Examination of the three equations above, as well as (3.38), indicated that there were numerous formulations of the equations that would allow the  $T_{n+1}$ ,  $R_{n+1}$ ,  $\theta_{n+1}$  and  $Z_{n+1}$  to be explicitly or implicitly broken out from the equations. Gerald and Wheatley explained that a sufficient condition for convergence of coupled equations using the iterative technique was that the sum of the partial derivatives with respect to each variable had to be less than one for each equation [Ref 11:pp.142-143]. Note that this was a sufficient and not a necessary condition, which was fortuitous since there were no formulations found which fit this requirement. This led to a trial and error search through the various formulations. Upon examining (3.35) through (3.37) and (3.38), an obvious candidate was to solve (3.35) for  $R_{n+1}$ , (3.36) for  $T_{n+1}$ , (3.37) for  $Z_{n+1}$  and (3.38) for  $\theta_{n+1}$  as in equations (3.39) to (3.42). This set of equations had the obvious advantage of

being entirely explicit. Examination of this equation set is representative of the problems with convergence instability encountered in the other combinations which were attempted. The difficulty with this set lies in equation (3.40). Note that both the terms in the denominator of the multiplicative factor were small and when their sum was inverted, the multiplicative factor became very large, on the order of around 500 for a typical scenario at the bottom of the wire grid. This meant that small errors in the variables within the bracketed sections were greatly amplified. This amplification drove the set of equations unstable for most scenarios.

$$R_{n+1} = \left[ \frac{1}{\frac{T_{n+\frac{1}{2}}}{\Delta S^2} + \frac{1}{2} \rho_n DC_D (R_n \dot{\theta})^2 \sqrt{1 - \frac{R_n(\theta_{n+1} - \theta_{n-1})^2}{4\Delta S^2}} \frac{R_n(\theta_{n+1} - \theta_{n-1})}{4\Delta S^2}} \right. \\ \left. \left[ \frac{T_{n+\frac{1}{2}} R_n - T_{n-\frac{1}{2}} (R_n - R_{n-1})}{\Delta S^2} + \left( \frac{T_{n+\frac{1}{2}} + T_{n-\frac{1}{2}}}{2} \right) R_n \left( \frac{\theta_{n+1} - \theta_{n-1}}{2\Delta S} \right)^2 \right. \right. \\ \left. \left. + \frac{1}{2} \rho_n DC_D (R_n \dot{\theta})^2 \sqrt{1 - \frac{R_n^2(\theta_{n+1} - \theta_{n-1})^2}{4\Delta S^2}} \frac{R_n(\theta_{n+1} - \theta_{n-1}) R_{n-1}}{4\Delta S^2} - \mu \dot{\theta}^2 R \right] \right] \quad (3.39)$$

$$\begin{aligned}
T_{n+\frac{1}{2}} = & \left( \frac{2\Delta S^2}{(R_{n+1}+R_n)(\theta_{n+1}-\theta_n) + \frac{(R_{n+1}-R_{n-1})(\theta_{n+1}-\theta_{n-1})}{4}} \right) \\
& \left[ \frac{T_{n-\frac{1}{2}}(R_n+R_{n-1})(\theta_n-\theta_{n-1})}{2\Delta S^2} - \frac{T_{n-\frac{1}{2}}(R_{n+1}-R_{n-1})(\theta_{n+1}-\theta_{n-1})}{8\Delta S^2} \right. \\
& \left. - \frac{1}{2} \rho_n D (R_n \dot{\theta})^2 \left[ -C_f + C_D \sqrt{1 - \frac{R_n^2(\theta_{n+1}-\theta_{n-1})^2}{4\Delta S^2}} \left( \frac{R_n^2(\theta_{n+1}-\theta_{n-1})^2}{4\Delta S^2} - 1 \right) \right] \right]
\end{aligned} \tag{3.40}$$

$$\begin{aligned}
Z_{n+1} = & \left[ \frac{1}{\frac{T_{n+\frac{1}{2}}}{\Delta S^2} + \frac{1}{2} \rho_n D C_D (R_n \dot{\theta})^2 R_n \sqrt{1 - \frac{R_n^2(\theta_{n+1}-\theta_{n-1})^2}{4\Delta S^2}} \frac{(\theta_{n+1}-\theta_{n-1})}{4\Delta S^2}} \right. \\
& \left. \left[ \frac{T_{n+\frac{1}{2}} Z_n + T_{n-\frac{1}{2}}(Z_n - Z_{n-1})}{\Delta S^2} \right. \right. \\
& \left. \left. + \frac{1}{2} \rho_n D C_D (R_n \dot{\theta})^2 R_n \sqrt{1 - \frac{R_n^2(\theta_{n+1}-\theta_{n-1})^2}{4\Delta S^2}} \frac{(\theta_{n+1}-\theta_{n-1}) Z_{n-1}}{4\Delta S^2} + \mu g \right] \right]
\end{aligned} \tag{3.41}$$

$$\theta_{n+1} = \theta_{n-1} + \frac{1}{R_n} \sqrt{4\Delta S^2 - (R_{n+1} - R_{n-1})^2 - (Z_{n+1} - Z_{n-1})^2} \tag{3.42}$$

The problem of iterative convergence was solved by changing the set of convergence variables. Equations (3.35) through (3.37) were rewritten using equation (3.10) vice (3.9) in equations (3.43) through (3.45). Then a new set of convergence variables were defined as in equation (3.46) where the  $n+\frac{1}{2}$  index was used for illustration.

$$\begin{aligned}
& \left( \frac{T_{n+\frac{1}{2}} R'_{n+\frac{1}{2}} - T_{n-\frac{1}{2}} R'_{n-\frac{1}{2}}}{\Delta S} \right) - \left( \frac{T_{n+\frac{1}{2}} + T_{n-\frac{1}{2}}}{2} \right) R_n \left( \frac{\theta_{n+1} - \theta_{n-1}}{2\Delta S} \right)^2 \\
& + \frac{1}{2} \rho_n D C_D (R_n \dot{\theta})^2 \sqrt{1 - \frac{R_n^2 (\theta_{n+1} - \theta_{n-1})^2}{4\Delta S^2}} \left( \frac{R_n (\theta_{n+1} - \theta_{n-1}) (R_{n+1} - R_{n-1})}{4\Delta S^2} \right) = -\mu \dot{\theta}^2 R_n
\end{aligned} \tag{3.43}$$

$$\begin{aligned}
& \frac{T_{n+\frac{1}{2}} \left( \frac{R_{n+1} + R_n}{2} \right) \theta'_{n+\frac{1}{2}} - T_{n-\frac{1}{2}} \left( \frac{R_n + R_{n-1}}{2} \right) \theta'_{n-\frac{1}{2}}}{\Delta S^2} \\
& + \frac{\left( T_{n+\frac{1}{2}} + T_{n-\frac{1}{2}} \right) (R_{n+1} - R_{n-1}) (\theta_{n+1} - \theta_{n-1})}{8\Delta S^2} + \\
& \frac{1}{2} \rho_n D (R_n \dot{\theta})^2 \left[ -C_F + C_D \sqrt{1 - \frac{R_n^2 (\theta_{n+1} - \theta_{n-1})^2}{4\Delta S^2}} \left( \frac{R_n^2 (\theta_{n+1} - \theta_{n-1})^2}{4\Delta S^2} - 1 \right) \right] = 0
\end{aligned} \tag{3.44}$$

$$\begin{aligned}
& \left( \frac{T_{n+\frac{1}{2}} Z'_{n+\frac{1}{2}} - T_{n-\frac{1}{2}} Z'_{n-\frac{1}{2}}}{\Delta S} \right) + \\
& \frac{1}{2} \rho_n D C_D (R_n \dot{\theta})^2 R_n \sqrt{1 - \frac{R_n^2 (\theta_{n+1} - \theta_{n-1})^2}{4\Delta S^2}} \left( \frac{(\theta_{n+1} - \theta_{n-1}) (Z_{n+1} - Z_{n-1})}{4\Delta S^2} \right) - \mu g = 0
\end{aligned} \tag{3.45}$$

$$\begin{aligned}
A_{n+\frac{1}{2}} &= T_{n+\frac{1}{2}} R'_{n+\frac{1}{2}} = T_{n+\frac{1}{2}} \left( \frac{R_{n+1} - R_n}{\Delta S} \right) \\
B_{n+\frac{1}{2}} &= T_{n+\frac{1}{2}} \left( \frac{R_{n+1} + R_n}{2} \right) \theta'_{n+\frac{1}{2}} = T_{n+\frac{1}{2}} \left( \frac{R_{n+1} + R_n}{2} \right) \left( \frac{\theta_{n+1} - \theta_{n-1}}{\Delta S} \right) \\
C_{n+\frac{1}{2}} &= T_{n+\frac{1}{2}} Z'_{n+\frac{1}{2}} = T_{n+\frac{1}{2}} \left( \frac{Z_{n+1} - Z_n}{\Delta S} \right)
\end{aligned} \tag{3.46}$$

Equations (3.47) through (3.49) were developed by substituting (3.46) into (3.47) through (3.49).

$$A_{n+\frac{1}{2}} = A_{n-\frac{1}{2}} + \left[ \left( \frac{T_{n+\frac{1}{2}} + T_{n-\frac{1}{2}}}{2} \right) R_n \left( \frac{\theta_{n+1} - \theta_{n-1}}{2\Delta S} \right)^2 - \frac{1}{2} \rho_n D C_D (R_n \dot{\theta})^2 \sqrt{1 - \frac{R_n^2 (\theta_{n+1} - \theta_{n-1})^2}{4\Delta S^2}} \left( \frac{R_n (\theta_{n+1} - \theta_{n-1}) (R_{n+1} - R_{n-1})}{4\Delta S^2} \right) - \mu \dot{\theta}^2 R_n \right] \Delta S \quad (3.47)$$

$$B_{n+\frac{1}{2}} = B_{n-\frac{1}{2}} - \left[ \frac{\left( \frac{T_{n+\frac{1}{2}} + T_{n-\frac{1}{2}}}{2} \right) (R_{n+1} - R_{n-1}) (\theta_{n+1} - \theta_{n-1})}{8\Delta S^2} + \frac{1}{2} \rho_n D (R_n \dot{\theta})^2 \left[ -C_F + C_D \sqrt{1 - \frac{R_n^2 (\theta_{n+1} - \theta_{n-1})^2}{4\Delta S^2}} \left( \frac{R_n^2 (\theta_{n+1} - \theta_{n-1})^2}{4\Delta S^2} - 1 \right) \right] \right] \Delta S \quad (3.48)$$

$$C_{n+\frac{1}{2}} = C_{n-\frac{1}{2}} + \left[ -\frac{1}{2} \rho_n D C_D (R_n \dot{\theta})^2 R_n \sqrt{1 - \frac{R_n^2 (\theta_{n+1} - \theta_{n-1})^2}{4\Delta S^2}} \left( \frac{(\theta_{n+1} - \theta_{n-1}) (Z_{n+1} - Z_{n-1})}{4\Delta S^2} \right) + \mu g \right] \Delta S \quad (3.49)$$

Equations (3.47) through (3.49) were the iterative equations in their implemented form. Equation (3.50) illustrated the relationship of the variables defined in (3.46) to the unit tangent vector and allowed a simple solution for  $T_{n+\frac{1}{2}}$  given  $A_{n+\frac{1}{2}}$ ,  $B_{n+\frac{1}{2}}$  and  $C_{n+\frac{1}{2}}$  in equation (3.51). A central difference approximation of the primed derivatives with respect to  $S$  listed in equation (3.46)

allowed for the iterative equation variables to be used to solve for  $R_{n+1}$ ,  $\theta_{n+1}$  and  $Z_{n+1}$  in equations (3.52) through (3.54) which were then used along with  $T_{n+\frac{1}{2}}$  in the next iteration.

$$A_{n+\frac{1}{2}}^2 + B_{n+\frac{1}{2}}^2 + C_{n+\frac{1}{2}}^2 = T_{n+\frac{1}{2}}^2 \left( R'_{n+\frac{1}{2}} \right)^2 + T_{n+\frac{1}{2}}^2 \left( R_{n+\frac{1}{2}} \theta'_{n+\frac{1}{2}} \right)^2 + T_{n+\frac{1}{2}}^2 \left( Z'_{n+\frac{1}{2}} \right)^2 = \left( T_{n+\frac{1}{2}} \right)^2 (1) \quad (3.50)$$

$$T_{n+\frac{1}{2}} = \sqrt{A_{n+\frac{1}{2}}^2 + B_{n+\frac{1}{2}}^2 + C_{n+\frac{1}{2}}^2} \quad (3.51)$$

$$R_{n+1} = R_n + \frac{A_{n+\frac{1}{2}} \Delta S}{T_{n+\frac{1}{2}}} \quad (3.52)$$

$$\theta_{n+1} = \theta_n + \frac{B_{n+\frac{1}{2}} 2 \Delta S}{T_{n+\frac{1}{2}} (R_{n+1} + R_n)} \quad (3.53)$$

$$Z_{n+1} = Z_n + \frac{C_{n+\frac{1}{2}} \Delta S}{T_{n+\frac{1}{2}}} \quad (3.54)$$

Equations (3.47) through (3.49), (3.52) through (3.54) and (3.51) are solved iteratively at each internal gridpoint. As mentioned above, and as seen in the

equations, a solution at the two previous gridpoints are required in order to solve the current gridpoint. This is only a problem when first starting the algorithm at the bottom of the wire. The first internal gridpoint was solved by defining the boundary condition of this coupled set of equations in terms of moment and force equilibrium at the drogue attachment point.

## B. FORMULATION OF THE DROGUE EQUATIONS

Figure 3.5 is a depiction of the forces and moments upon the drogue in the vertical plane. Using this diagram, the moments around the nose of the drogue were summed. The nose was chosen as a reference point since it allowed elimination of the tension term and enabled the resulting equation to be solved without knowledge of the next gridpoint. The moment summation is provided in equation (3.55) where  $L_D$  and  $D_D$  were the lift and drag of the drogue,  $MAC_D$  was the moment around the aerodynamic center,  $\alpha_D$  was the angle of attack of the drogue,  $W_D$  was the drogue weight and  $cg$  and  $ac$  were the center of gravity and aerodynamic center of the drogue respectively.

$$\sum M_{LE} = -L_D ac \cos(\alpha_D) + W_D cg \cos(\alpha_D) + MAC_D = 0 \quad (3.55)$$

It was assumed that the drogue coefficient of drag,  $C_{DD}$ , and moment coefficient,  $C_{MACD}$ , were approximately constant and that the drogue lift curve slope,  $C_{L\alpha D}$ , conformed to the

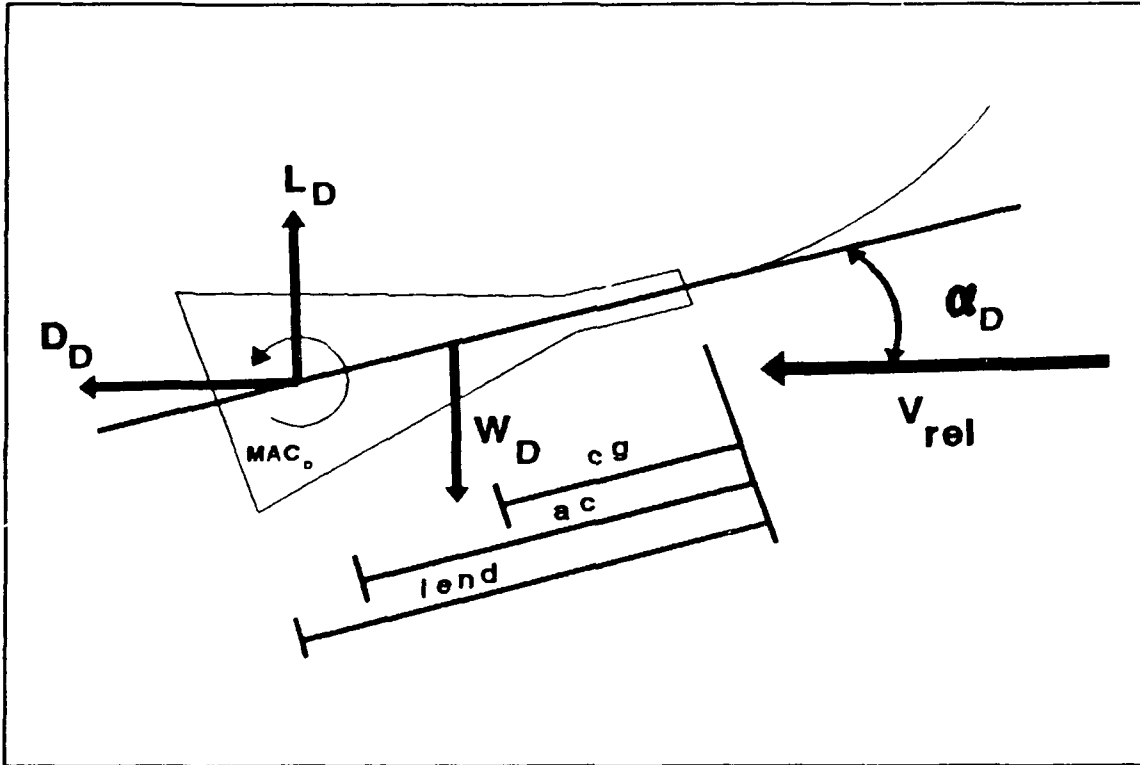


**Figure 3.5:** Forces and Moments Upon the Drogue in Vertical Plane

model in equation (3.56). Expanding the components of equation (3.55) resulted in (3.57) to (3.59), where  $n$  equaled the drogue gridpoint number,  $S_D$  was the drogue maximum cross sectional area and  $LEND$  was the length of the drogue as seen in Figure 3.5. Substituting these relations into equation (3.55) resulted in equation (3.61), a solvable transcendental relation in  $\alpha_D$ .

$$\begin{aligned}
 C_{LSD} &= 0 & \alpha_D &\neq 0 - \frac{\pi}{2} \\
 C_{LSD} &= C_{LSDmax} \left( \frac{\frac{\pi}{2} - \alpha_D}{\frac{\pi}{2}} \right) & \alpha_D &= 0 - \frac{\pi}{2}
 \end{aligned}
 \tag{3.56}$$



$$q_n = \frac{1}{2} \rho_n V_{reln}^2 = \frac{1}{2} \rho_n (R_n \dot{\theta})^2 \quad (3.57)$$

$$L_D = C_{L\alpha D} \alpha_D q_n S_D \quad (3.58)$$

$$D_D = C_{DD} \alpha_D q_n S_D \quad (3.59)$$

$$MAC_D = C_{MACD} q_n S_D L_{END} \quad (3.60)$$

$$-C_{L\alpha D} \alpha_D q_n S_D ac \cos \alpha_D - C_{DD} q_n S_D ac \sin \alpha_D + W_D cg \cos \alpha_D + C_{MACD} q_n S_D L_{END} = 0 \quad (3.61)$$

A very similar technique was applied in the horizontal plane to determine the drogue sideslip angle,  $\beta_D$ . Figure 3.6 is a depiction of the forces and moments upon the drogue in the horizontal plane. The summation of forces in the horizontal plane about the nose of the drogue was written in equation (3.62) by examining Figure 3.6 and noting that  $F_{ID}$  was the centrifugal force upon the drogue mass and that  $ASFD$  was the aerodynamic side force due to  $\beta_D$ . Making similar substitutions as were made in the summation of forces in the vertical plane and again noting that  $n$  was the drogue gridpoint number, resulted in equation (3.63).  $ASFD$  and  $F_{ID}$  were required later, where  $ASFD$  was as defined in equation (3.64) and  $F_{ID}$  as in (3.65).

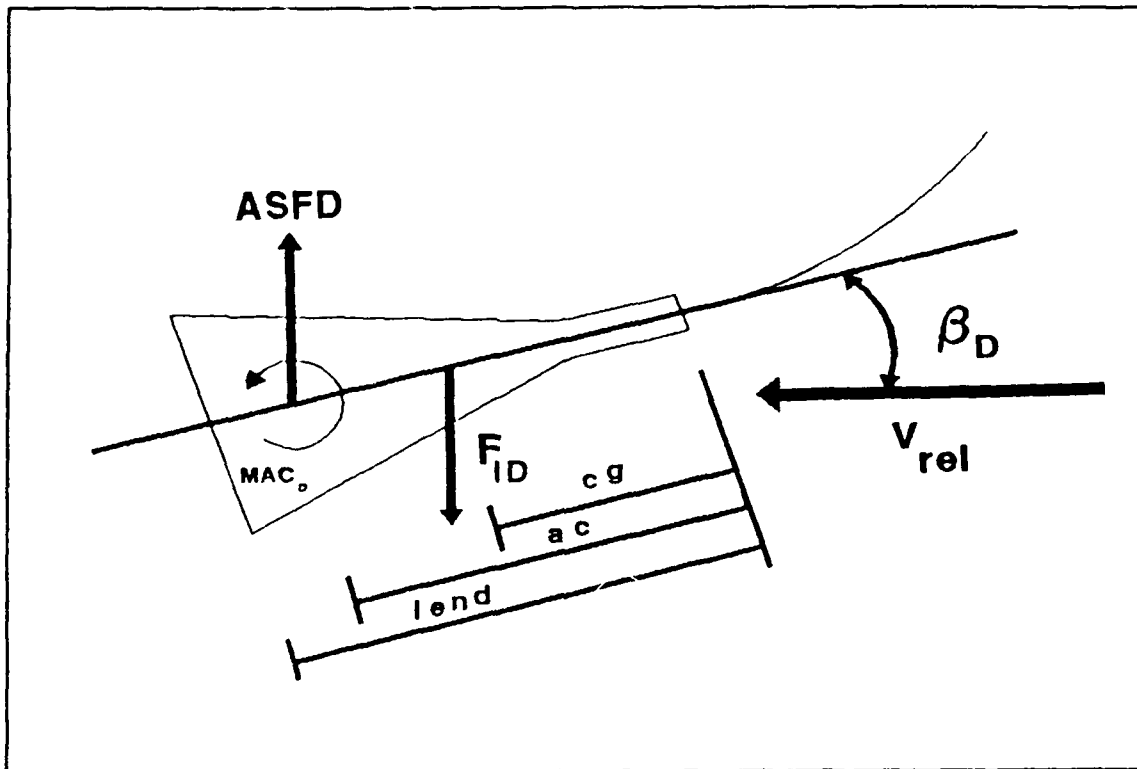


**Figure 3.6:** Forces and Moments Upon the Drogue in the Horizontal Plane

$$\sum M_{LE} = F_{ID} - ASFD + MAC_D \quad (3.62)$$

$$\frac{W_D}{g} \ddot{\theta}^2 R_n \, cg \cos \beta_D - C_{LAD} \beta_D q_n S_D \, ac \cos \beta_D + C_{MACD} q_n S_D LEND = 0 \quad (3.63)$$

$$ASFD = C_{LAD} \beta_D q_n S_D \quad (3.64)$$

$$F_{ID} = \frac{W_D \dot{\theta}^2 R_1}{g} \quad (3.65)$$

The horizontal components of the forces upon the drogue in their vector form were rewritten in equation (3.66) by re-examining Figure 3.6 and remembering that the drogue was in a steady-state orbit. For static force equilibrium, the tension magnitude at the drogue had to equal the magnitude of the vector sum of all of the forces listed in (3.66). The tension at gridpoint 1 was thus as written in equation (3.67). Only the tension magnitude as in equation (3.68) was required.

$$\begin{aligned} L_D &\rightarrow L_D \overline{e_K} \\ D_D &\rightarrow -D_D \overline{e_\theta} \\ W_D &\rightarrow -W_D \overline{e_K} \\ F_{ID} &\rightarrow F_{ID} \overline{e_R} \\ ASFD &\rightarrow -ASFD \overline{e_R} \end{aligned} \quad (3.66)$$

$$\overline{T_1} = (F_{ID} - ASFD) \overline{e_R} - D_D \overline{e_\theta} + (L_D - W_D) \overline{e_K} \quad (3.67)$$

$$T_1 = \sqrt{(F_{ID} - ASFD)^2 + D_D^2 + (L_D - W_D)^2} \quad (3.68)$$

It was assumed that the forces upon the first wire segment were small compared to the forces upon the drogue. Later analysis showed that the forces upon the first segment of the wire were at least an order of magnitude less than those acting upon the drogue. It was thus said that  $T_1 = T_2$ .

A further requirement of static equilibrium was that the  $T_1$  tension had to be directed in the reciprocal direction to the resultant vector at the drogue. This in turn defined the unit tangent vector of the first segment of the wire and together with the assumption that the wire forces on the first segment were small relative to the drogue forces and the two gridpoint  $\Delta S$  constraint of equation (3.14), the gridpoint 2 positions were written in equation (3.69). At this point, given a guess at the location of the drogue, the location of the second gridpoint, as well as the tension at both points were determined.

$$\begin{aligned}
 R_2 &= R_1 - \left( \frac{F_{ID} - \Delta S F_D}{T_1} \right) \Delta S \\
 \theta_2 &= \theta_1 + \frac{D_D \Delta S}{T_1 \left( \frac{R_2 + R_1}{2} \right)} \\
 Z_2 &= Z_1 + \sqrt{\Delta S^2 - R_n^2 - R_{n-1}^2 + 2R_n R_{n-1} \cos(\theta_n - \theta_{n-1})}
 \end{aligned} \tag{3.69}$$

Atmospheric density was required for each gridpoint. The computer code, to be described later, permits the use of either standard atmosphere or radiosonde data in the form of input data files indexed at 1,000 feet intervals. The  $Z_n$  value at each point was rounded up to the next higher 1,000 feet interval and the density was assigned from the radiosonde data table. The standard atmosphere model used is presented in equation (3.70).

$$\begin{aligned}
\rho_n &= \rho_1 \left[ \frac{T_1 + a Z_n}{T_1} \right]^{-\left[ \frac{1}{aR} + 1 \right]} \\
\rho_1 &= 0.0023769 \frac{\text{lb}_f \text{ sec}^2}{\text{ft}^3} \\
a &= -0.0035662 \frac{\text{ft}^4}{\text{lb}_m^\circ R} \\
R &= 53.3 \frac{\text{ft lb}_f}{\text{lb}_m^\circ R} \\
T_1 &= 518.69^\circ R
\end{aligned} \tag{3.70}$$

The input conditions for the towplane will be bank angle (degrees) and airspeed (equivalent, knots) when determining aircraft steady-state orbit radius (feet) and rate (rad/sec). The derivation of these quantities was begun by converting aircraft airspeed from knots to ft/sec and then converting from equivalent airspeed,  $V_{EAS}$ , to true airspeed,  $V_{true}$  as in equation (3.71), where  $\rho_{SL}$  was the atmospheric density at sea level. Next, the aircraft bank angle,  $\phi$ , was converted from degrees to radians, the aircraft acceleration,  $n_{ac}$ , was calculated, and all of this was used to calculate the towplane orbit radius,  $R_n$  and the orbit rate,  $\dot{\theta}$  in equation (3.72).

$$\begin{aligned}
V_{EAS} \left( \frac{\text{ft}}{\text{sec}} \right) &= V_{EAS}(\text{KTS}) \frac{6076.1}{3600} \\
V_{true} &= \frac{V_{EAS}}{\sqrt{\sigma}} = \frac{V_{EAS}}{\sqrt{\frac{\rho_n}{\rho_{SL}}}}
\end{aligned} \tag{3.71}$$

$$\begin{aligned}
\phi(\text{rad}) &= \phi(\text{deg}) \left( \frac{2\pi}{360} \right) \\
n_{ac} &= \frac{1}{\cos \phi} \\
R_n &= \frac{V_{true}^2}{g \sqrt{n_{ac}^2 - 1}} \\
R_n &= \frac{V_{true}^2}{\left( g \sqrt{\left( \frac{1}{\cos \phi} \right)^2 - 1} \right)} \\
\dot{\theta} &= \frac{V_{true}}{R_n}
\end{aligned}
\tag{3.72}$$

### C. THE SHOOTING PROBLEM

Finally, all the components were available that were necessary to solve the steady-state wire position and tension distribution given a guess at the drogue location. The last task was to develop the iterative scheme needed to find the correct drogue location. Shooting the boundary condition was the technique chosen. An initial estimate was made of the correct drogue location. The algorithm described above was then used to propagate a solution to the top of the wire where the position of the top gridpoint was compared to the known location of the towplane (radial position and the vertical position). A simple approach to the update was used. The update to the bottom position was based upon a fraction of the miss distance at the top. The fraction used had the appearance of an update "gain".  $Z_1$  and  $R_1$  were updated each time the boundary condition was

shot. The update equations are presented in (3.86) with the gains represented as  $g_1$  and  $g_2$  and where  $Z_{1new}$  and  $R_{1new}$  were the updated drogue position estimates,  $Z_{1old}$  and  $R_{1old}$  were the last drogue position estimates, ALTTP was the towplane altitude, RADTP was the towplane radial position during the steady-state orbit and  $Z_{topnew}$  and  $R_{topnew}$  were the latest position coordinates of the top gridpoint position as calculated on the last boundary condition shot.

$$\begin{aligned} Z_{1new} &= Z_{1old} + g_1(ALTTP - Z_{topnew}) \\ R_{1new} &= R_{1old} + g_2(RADTP - R_{topnew}) \end{aligned} \quad (3.73)$$

The process of shooting the boundary condition became more sensitive as the bottom point approached the origin. For this reason, tailored, or adaptive, gains were used in the update equations which were made as large as possible to facilitate quick convergence. Care had to be taken, however, to ensure that the gains did not cause the updates to be so large that they never converged. The gains in the more sensitive radial positions, where the drogue was close to the origin, were thus necessarily small, while those farther out were larger. The best gains were developed through experimentation with the algorithm. Note that occasionally, for towplane angles of bank above forty degrees and below five degrees and in the vicinity of the jump phenomenon (to be explained later), the gains, as currently implemented, may fail to converge. The program

then suggests corrections to be made to the gain values. Very small gain values would ensure convergence in all relatable conditions but would unnecessarily slow the convergence process for the majority of cases. The tradeoff between the need to occasionally change the gains and the run time saved for the majority of cases was deemed appropriate.

The steady-state model, with the 3X7 wire, the standard TACAMO drogue, the textbook derived aerodynamic coefficients [Ref. 10:pp. 3-18,4-5] and making the sideforce coefficient (to be explained in Section E of this chapter) an operator input, is provided in Appendix A. The details of implementation and of the numerical techniques are explained within the program code. A number of outputs are available from the program. As examples, the angle of attack of the wire at each grid segment, drogue and aircraft flight parameters, as well as position and tension data for each gridpoint are available. The inputs and outputs are fully documented within the code. The outputs are conditioned to facilitate input into the dynamic model program as well as various plotting routines.

The static model algorithm may be summarized as follows:

- \* The process begins by guessing at the drogue location.
- \* Equations (3.61) and (3.63) are then solved iteratively for  $\alpha_D$  and  $\beta_D$ .
- \* (3.58) and (3.59) provide  $L_D$  and  $D_D$  and (3.68) provides  $T_{1+\frac{1}{2}}$ . Note that  $T_1=T_2=T_{1+\frac{1}{2}}$  in equation (3.68) and all subsequent tension calculations are shifted forward  $\frac{1}{2}$



of an index.

- \* (3.69) defines  $R_2$ ,  $\theta_2$  and  $Z_2$  and  $T_{2+\frac{1}{2}}=T_{1+\frac{1}{2}}$ .
- \* (3.47) through (3.49) and (3.51) to (3.54) are solved iteratively for the  $R_n$ ,  $\theta_n$ ,  $Z_n$  and  $T_{n+\frac{1}{2}}$  at each subsequent gridpoint.
- \* When the upper gridpoint,  $N$ , is reached, its  $R_N$  and  $Z_N$  positions are compared to the position of the towplane and a fraction of the difference between the two is used to update the drogue position for the next shot to the upper boundary condition.
- \* The position and tension values are used to derive several off-line quantities of interest described within the program.

Convergence is quite fast for a typical run, taking 10 to 45 seconds on a 486 DX 33 MHZ microcomputer.

#### D. VALIDATION, VERIFICATION AND ANALYSIS

The code was validated by several techniques. First, the program was run using the aerodynamic coefficients and physical parameters used to generate the plots in the 1969 NADC report. [Ref. 7] These coefficients and parameters are listed below in (3.74).

$$\begin{aligned} \text{WIRE: } C_D &= 1.03 \quad C_f = 0.022 \quad D = 0.21 \text{ inches} \\ &\quad \mu g = 0.1095 \frac{\text{lb}_f}{\text{ft}} \\ \text{DROGUE: } C_{D_0} &= 0.6 \quad C_{L_{\text{aD}}} = 2.0 \quad ac = 2.31 \text{ feet} \quad cg = 1.34 \text{ feet} \\ &\quad W_D = 100.0 \text{ lb}_f \quad S_D = 3.68 \text{ feet}^2 \end{aligned} \tag{3.74}$$

The benchmark flight profile of 200 KTAS and 29,000 feet and a wire length of 33,800 feet used for the NADC report was run at various bank angles/turn radii. In keeping with the assumptions of the steady-state model, a constant bank

angle, circular orbit was assumed. Figures 3.7 and 3.8 are plots of the NADC data with the NPS model's towplane/drogue separation and towpoint tension data overlaid [Ref. 7:p. 23]. The plots showed extremely close correlation. Figure 3.9 is a plot of the radial coordinate versus the location along the wire's length as calculated using the NADC and the NPS models starting from the same drogue locations. Again, the models were very close. The program was then modified to allow for the cases of a massless wire and drogue and for zero aerodynamic coefficients on the wire and drogue. When the simulation was run at a very low towplane angle of bank, the massless wire and drogue trailed straight back from the towplane. When simulated with zeroed aerodynamic coefficients, the wire fell straight down from the aircraft. Plots of these simulations are not provided since they merely show straight lines and add nothing to the understanding of the outcome. Finally, the static model, as a subset of the dynamic model, was compared to actual TACAMO flight test data. The outcome of this comparison will be discussed following the development of the dynamic model.

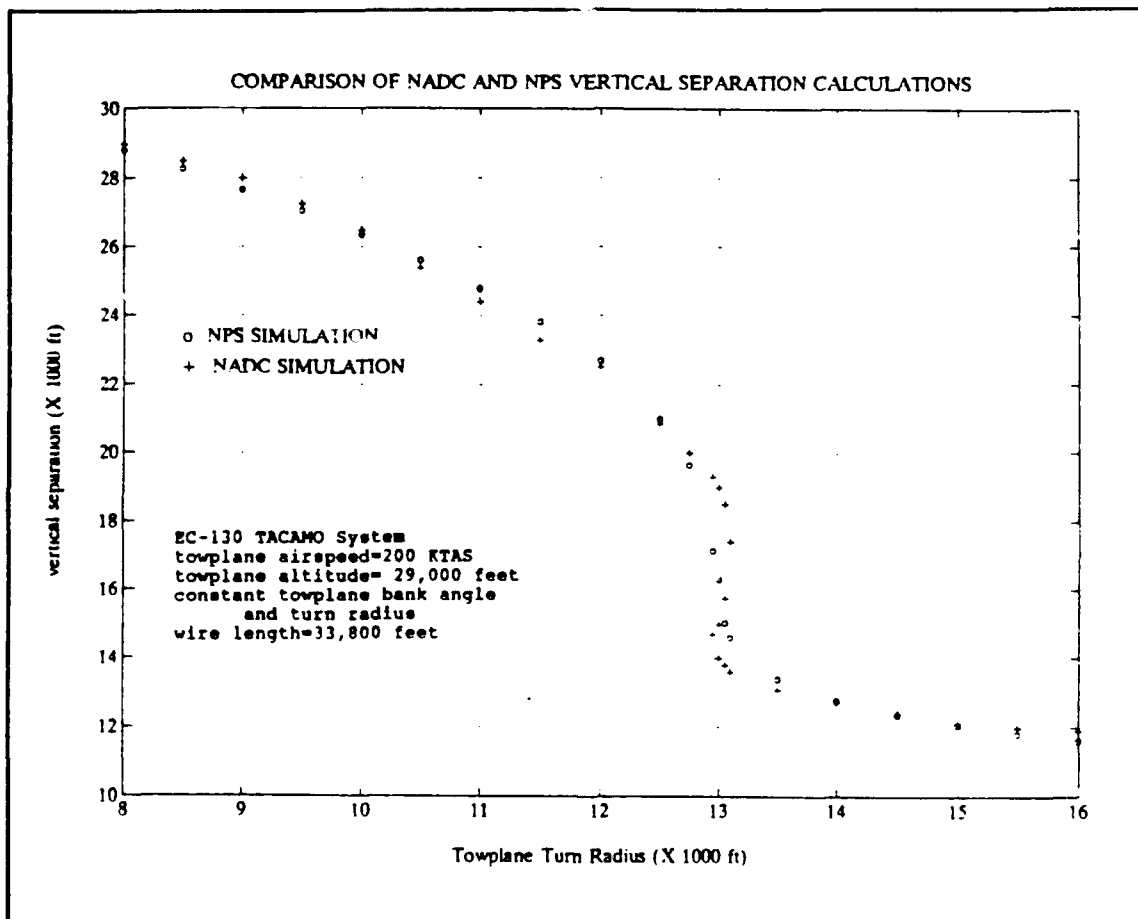


**Figure 3.7: Comparison of NADC and NPS Vertical Separation Calculations**

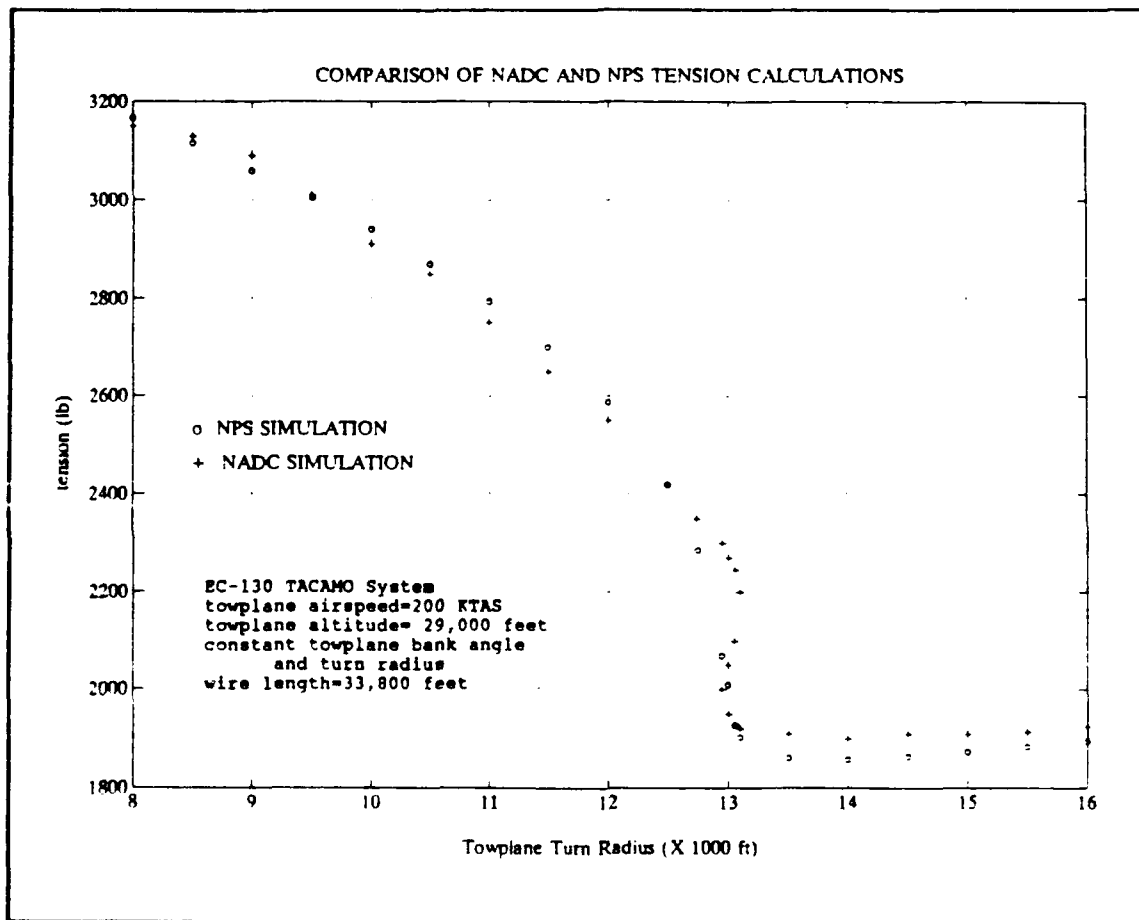


**Figure 3.8:** Comparison of NADC and NPS Towpoint Tension Calculations

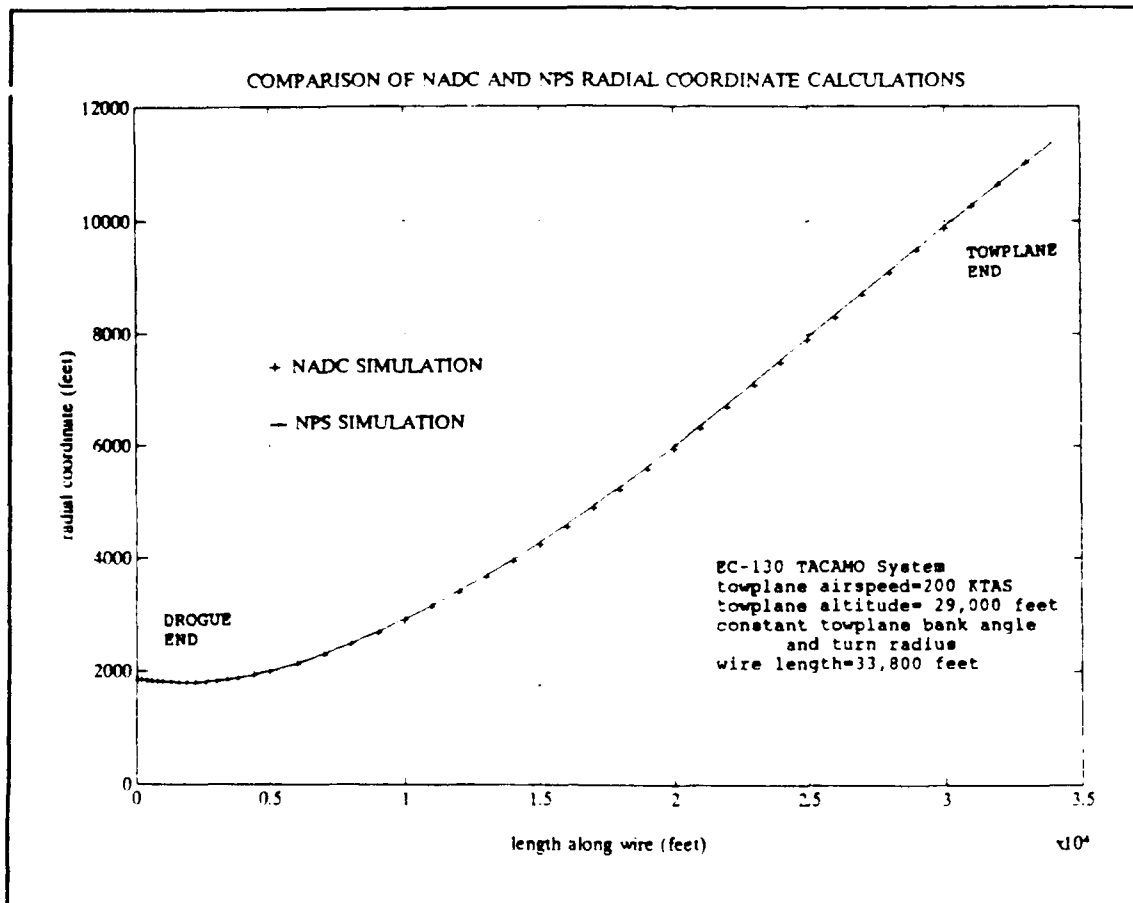


**Figure 3.9:** Comparison of NADC and NPS Radial Coordinate Calculations

Figures 3.10 to 3.13 are plots of  $R_n$ ,  $\theta_n$ ,  $Z_n$  and  $T_n$  versus the distance along the wire for a representative run of the static model. A plot of the true angle of attack along the wire at the same conditions is provided for information in Figure 3.14. The origin of the horizontal axis represents the drogue position. The 3X7 wire with a zero sideforce coefficient was used with the standard TACAMO drogue and the towplane was at 18,325 feet altitude, 156 KEAS and a bank angle of 34 degrees. The 3X7 wire and the standard drogue parameters are provided in (3.75). Note

that the slopes of the  $R_n$ ,  $\theta_n$ ,  $z_n$  and  $T_n$  plots were fairly constant from one gridpoint to the next and thus the second and higher derivatives were small. As seen in equations (3.8), (3.9), (3.24) and (3.25), the derivatives in this chapter were approximated using a central difference technique. Gerald and Wheatley show that for the first derivative approximations used in this chapter, the truncation error was as shown in equation (3.76). [Ref. 11:p. 284] The resulting errors for each of the central difference approximations were calculated at each gridpoint for the conditions of Figures 3.10 through 3.14 and then averaged over each gridpoint. The resulting average truncation errors as a percentage of the calculated derivatives are shown in equation (3.77).

$$\begin{aligned}
 \text{WIRE: } C_D &= 1.02 \quad C_f = 0.022 \quad D = 0.1582 \text{ inches} \\
 \mu g &= 0.062 \frac{\text{lb}_f}{\text{ft}} \\
 \text{DROGUE: } C_{DD} &= 0.41 \quad C_{L\&D} = 2.0 \quad ac = 1.95 \text{ feet} \quad cg = 1.15 \text{ feet} \\
 W_D &= 81.95 \text{ lb}_f \quad S_D = 3.14 \text{ feet}^2
 \end{aligned}
 \tag{3.75}$$

$$f'_o \text{ truncation error} = \frac{\Delta S^2}{6} F_o''' + \frac{\Delta S^4}{120} f_o^{IV} + \dots \tag{3.76}$$

$$\begin{aligned}
\left(\frac{dR}{dS}\right)_n &\rightarrow 0.07\% \\
\left(\frac{d\theta}{dS}\right)_n &\rightarrow 0.02\% \\
\left(\frac{dZ}{dS}\right)_n &\rightarrow 0.002\% \\
\left(\frac{dT}{dS}\right)_n &\rightarrow 0.04\% \\
\left(\frac{d\left(T_n\left(\frac{dR}{dS}\right)_n\right)}{dS}\right)_n &\rightarrow 0.1\% \\
\left(\frac{d\left(T_n R_n\left(\frac{d\theta}{dS}\right)_n\right)}{dS}\right)_n &\rightarrow 0.02\% \\
\left(\frac{d\left(T_n\left(\frac{dZ}{dS}\right)_n\right)}{dS}\right)_n &\rightarrow 0.01\%
\end{aligned}
\tag{3.77}$$

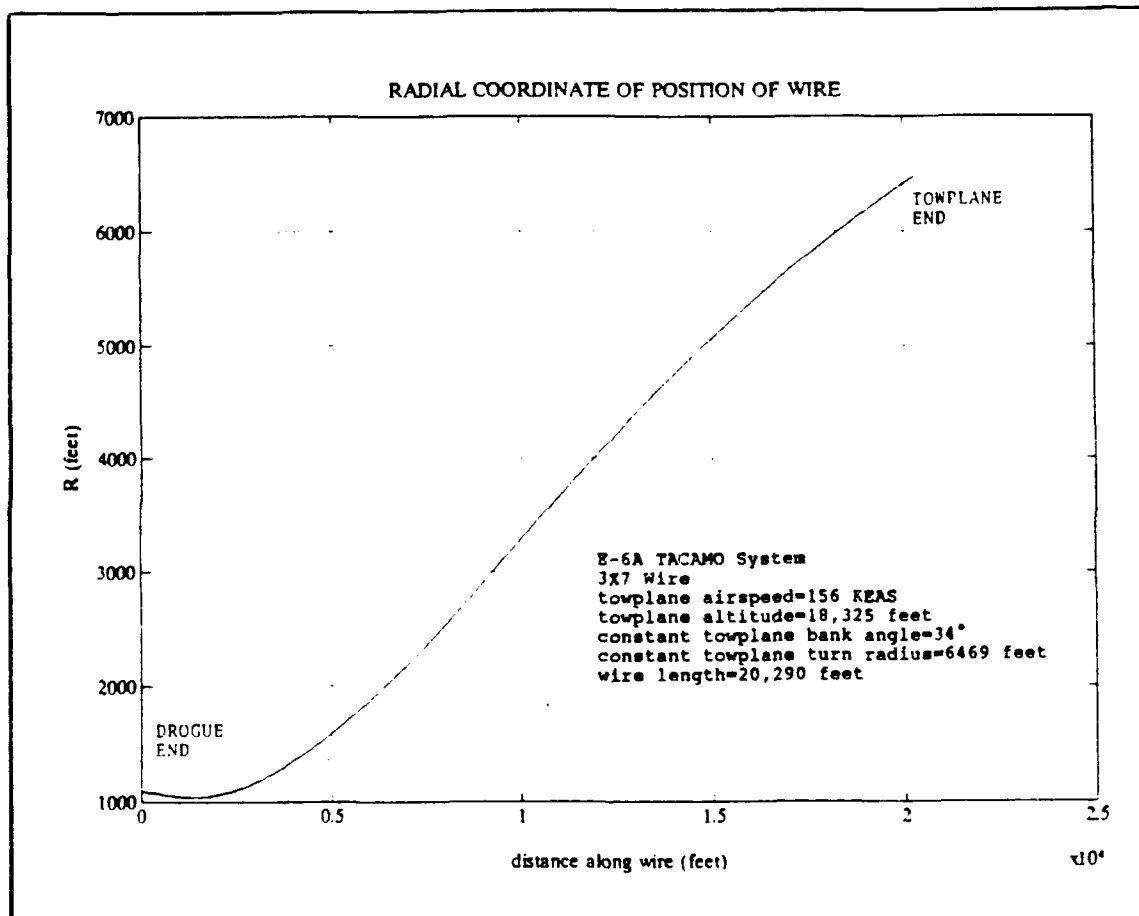
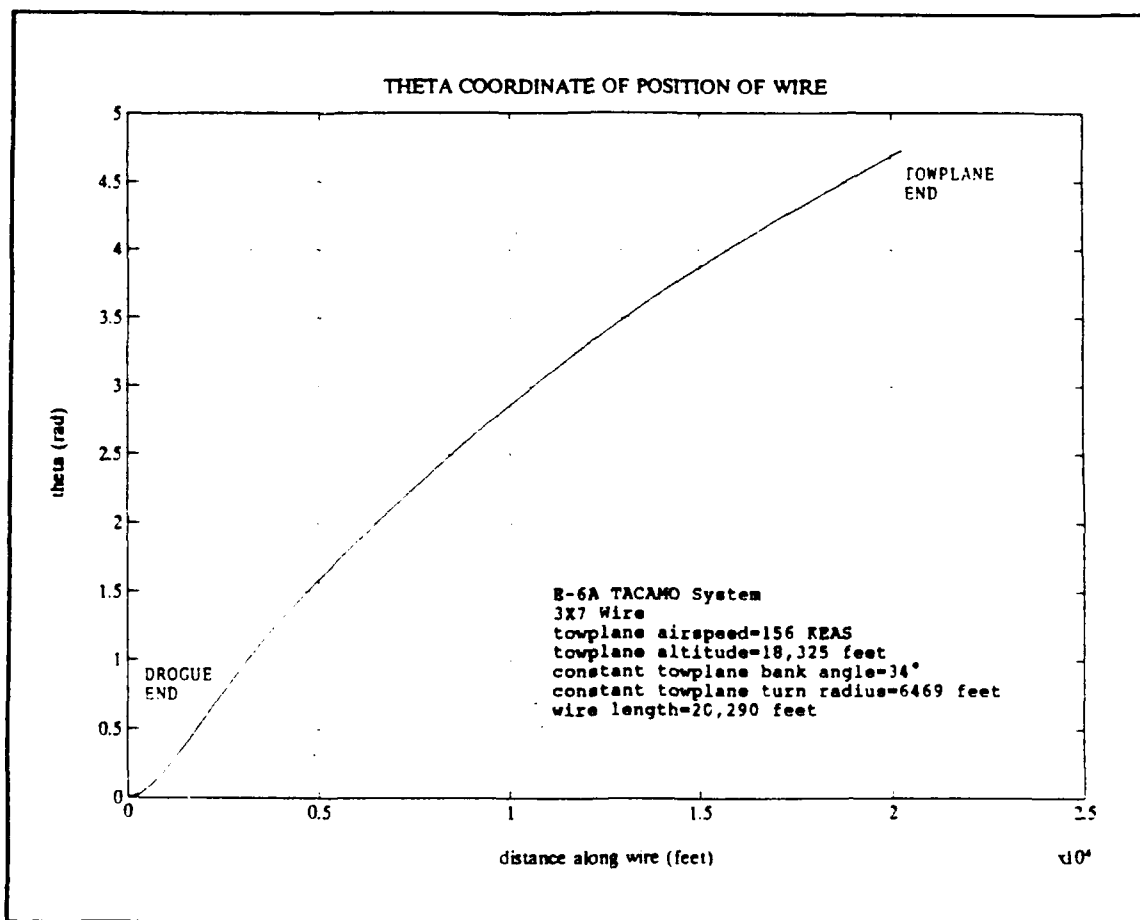
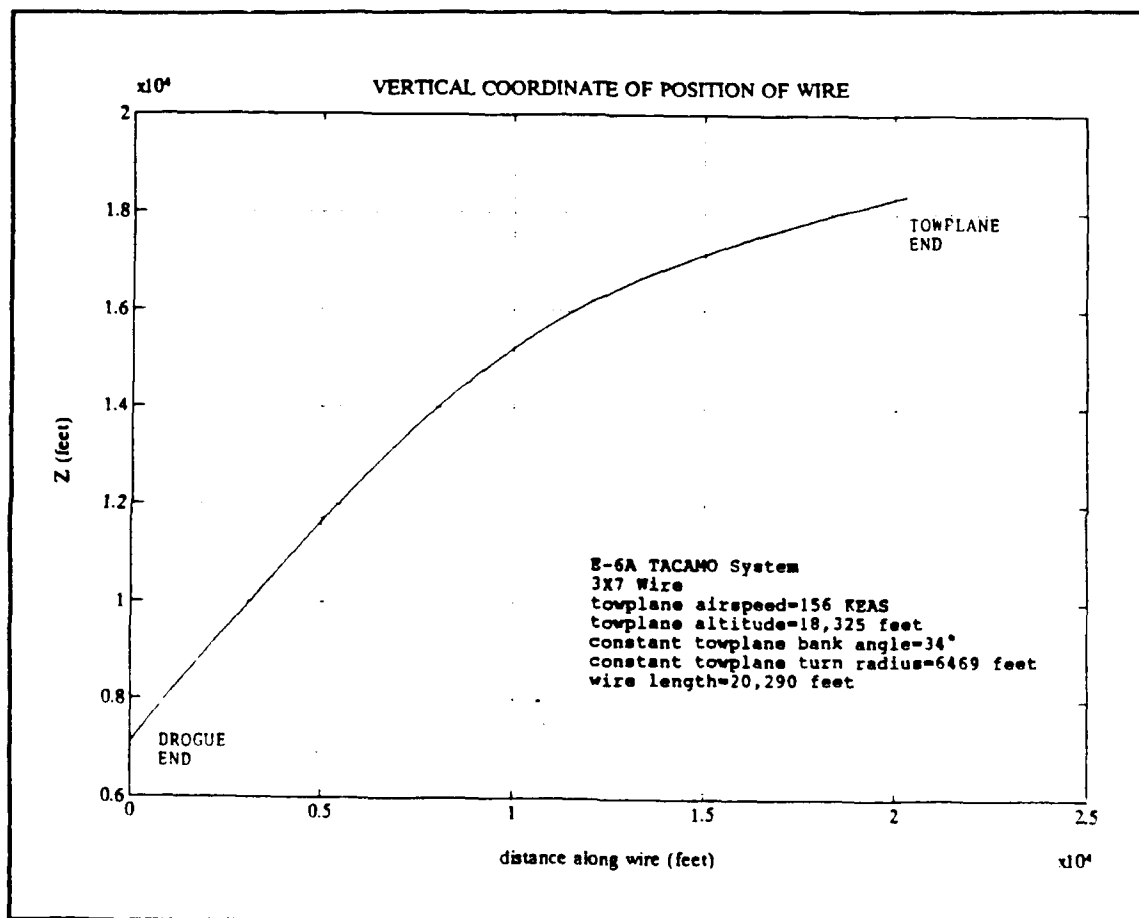


Figure 3 10. Radial Coordinate of Position of Wire





**Figure 3.11:  $\theta$  Coordinate of Position of Wire**



**Figure 3.12: Vertical Coordinate of Position of Wire**

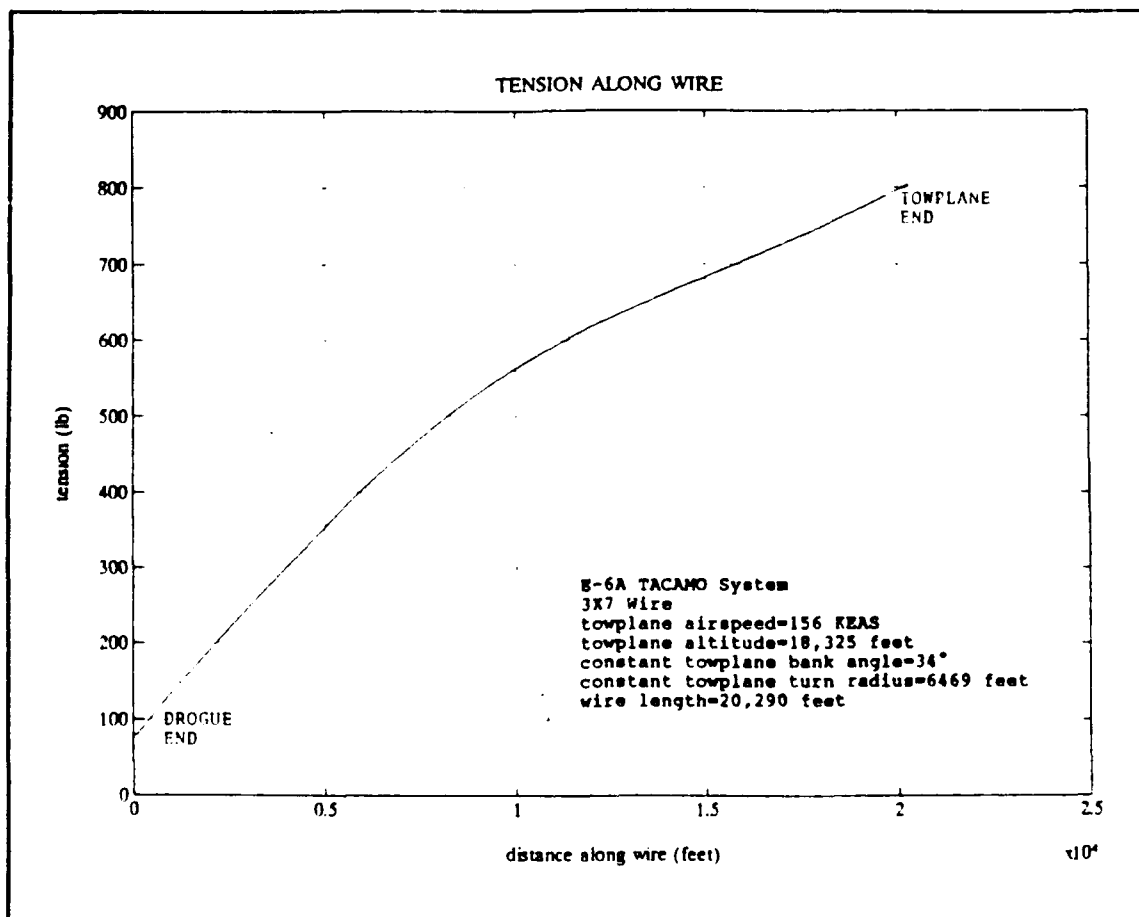


**Figure 3.13: Tension Along Wire**

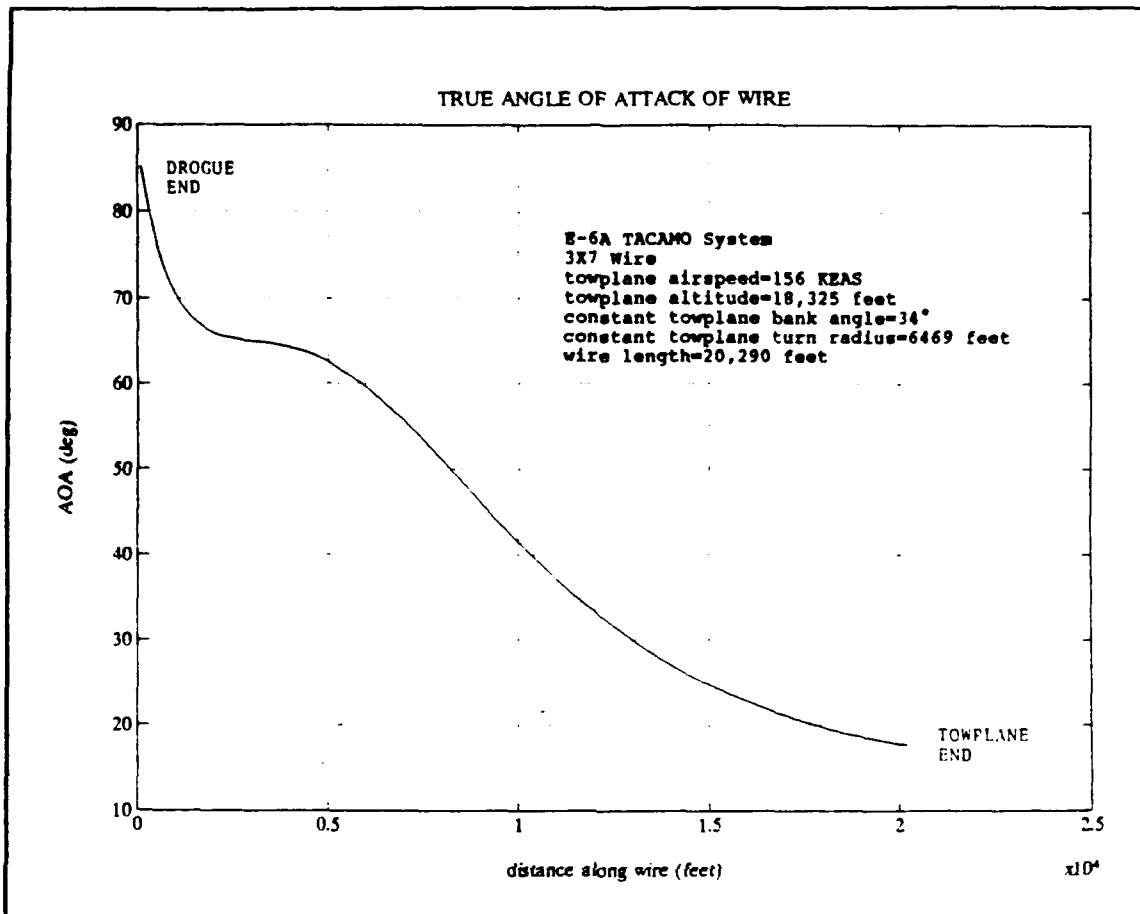


**Figure 3.14: True Angle of Attack of the Wire**

The independence of the static model from the choice of the grid was established by running the model using 200 grid segments and again using 400 segments and then comparing the results. The  $R_n$ ,  $\theta_n$ ,  $Z_n$  and  $T_n$  values were compared and found to be virtually identical. Figure 3.15 is a sample of the results where the 200 and 400 grid segment R coordinate values are plotted as a function of distance along the wire. The plots overlay, differing only by a portion of the upper boundary condition convergence criterion. The static model was thus grid independent as desired.

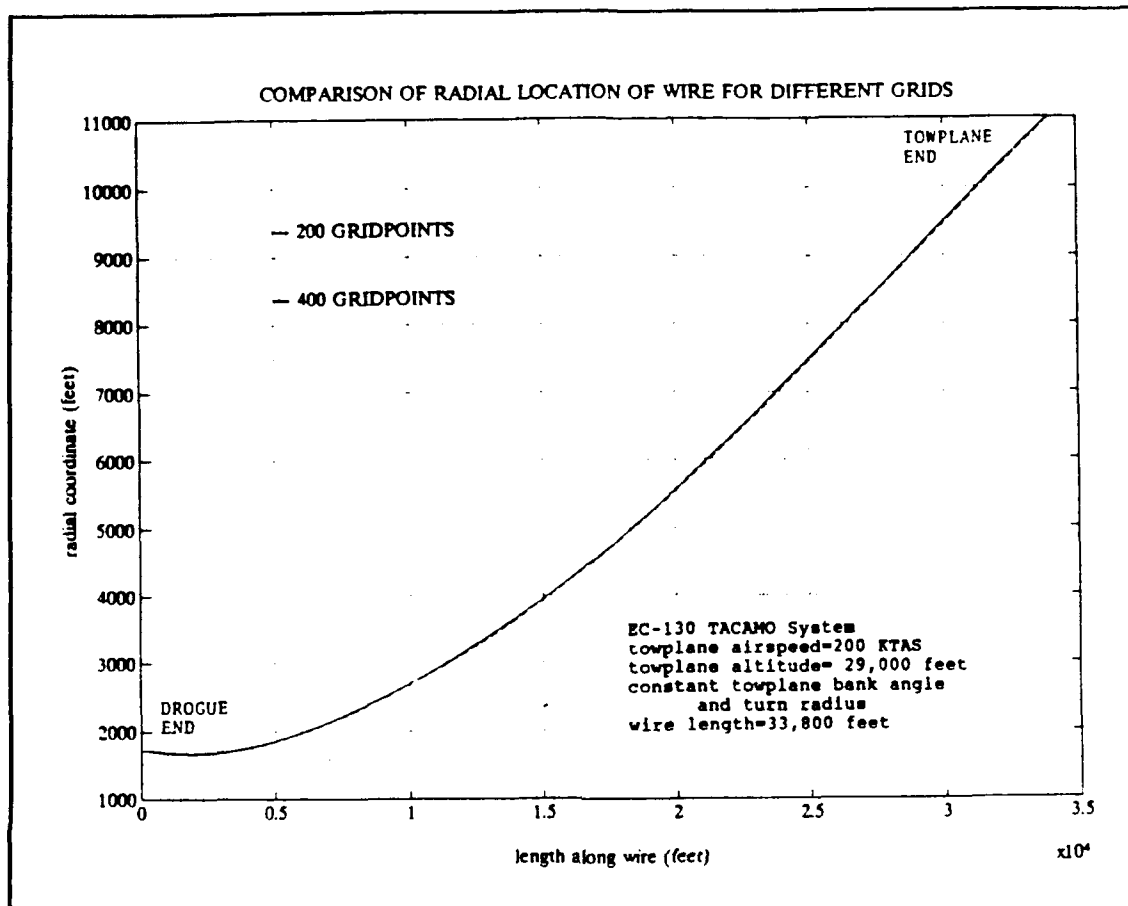


**Figure 3.15:** Comparison of Radial Location of Wire for Different Grids

The derivation of the static model assumed that the shear forces upon the wire were negligible when compared to the tension forces. The shear forces were dominated by the perpendicular component of the aerodynamic force. Figure 3.14 showed that the angle of attack was greatest at the bottom of the wire near the drogue and Figure 3.13 showed that the tension was least at the drogue gridpoint, leading to the largest ratio of shear forces to tension. The ratio of the shear forces to tension at the drogue were calculated to be less than 6% for the conditions of Figure 3.13. This

value decreased drastically along the wire as the angle of attack decreased to half and the tension increased to over ten times the value at the drogue.

Figure 3.16 is a plot of the verticality versus the towplane angle of bank for the 3X7 wire with a zero sideforce coefficient, standard drogue and flight conditions of 18,325 feet altitude, 156 KEAS and a wire length of 20,290 feet. The towplane flight path varied from level flight to a circular radius of 3100 feet at 50 degrees angle of bank. This plot was interesting in that it highlighted the "jump" phenomenon where, in a certain range of angles of bank, there were drastic changes in verticality and even multiple values of verticality. In Figure 3.16, the verticality changed over 20% between multiple solutions. The dashed-line fairing denotes a verticality solution that could not be obtained due to an apparent local solution instability. Analysis of the balance between the weight of each wire segment and the aerodynamic force and the tension, provided a physical explanation for this phenomenon and a comparison of the high and low verticality cases provided much support for the following hypothesis.

The analysis of the jump phenomenon began by remembering the definition of the aerodynamic coefficients for the wire. The model indicated that the classical lift for the wire was essentially zero whenever the wire was oriented vertically and, for the steady-state condition, whenever the wire was

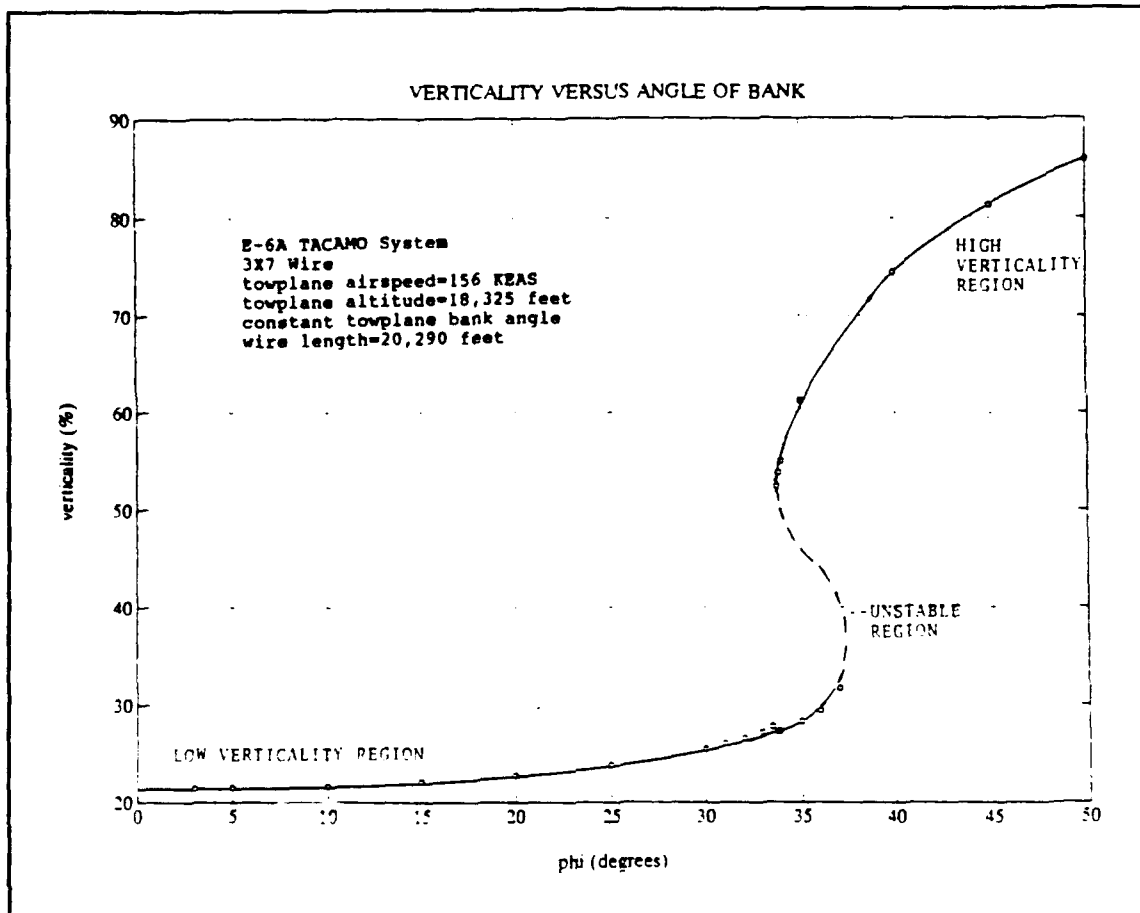


**Figure 3.16: Verticality Versus Angle of Bank**

oriented in the  $\bar{e}_R, \bar{e}_\theta$  plane. The lift was, in general, finite for orientations between these two extremes. As a two-dimensional analogy, where the wire was oriented in the  $\bar{e}_\theta, \bar{e}_z$  plane and was in a steady-state orbit, the lift varied from zero at a zero true angle of attack, grew to a maximum as the true angle of attack was increased and then decreased again to zero as the true angle of attack approached 90 degrees. Concurrently, as the wire varied from 0 degrees to 90 degrees true angle of attack under steady-state assumptions, the orientation of the wire with the vertical  $\bar{e}_z$  vector changed approximately from

perpendicular to tangential. That is, the  $\bar{e}_z$  component of the unit tangent vector changed from a magnitude of approximately  $e_z=0$  to  $e_z=1$ . As this occurred, the tension vector, which was aligned with the unit tangent vector, varied from an orientation which was approximately orthogonal to an orientation that was parallel to the weight vector. Noting in Figure 3.13 that the tension was typically monotonically increasing from the drogue to the towplane, the change in tension over the grid segment was always positive, and thus any positive,  $\bar{e}_z$  component of the unit tangent vector resulted in the change in tension supporting the weight of the wire segment. Figure 3.14 showed that the angle of attack was also positive along the wire and so the lift which was produced also aided in balancing the weight term. Thus, the weight term was balanced by the vertical component of the tension change over each grid segment which varied from approximately zero to a maximum and by the lift of the grid segment which varied from approximately zero, through some range of values and then back to zero. Knowing that the wire could produce the same amount of lift at more than one angle of attack, it seemed not only possible, but likely, that a range of flight conditions existed where at least two orientations of the wire resulted in a balancing of the weight term. One orientation required a high inclination on the wire where the lift was small while the vertical component of the



tension provided much of the vertical force necessary to balance the weight and another orientation required a lower inclination where the lift was higher and the vertical component of the change in tension was small. Note also that as the lift increased, the tangential component of the lift tended to decrease the change in tension over the grid segment due to the segment weight. It thus also seemed likely that the low verticality case would have a lower towpoint tension than the high verticality case.

Figures 3.17 through 3.21 are plots of  $R_n$ ,  $\theta_n$ ,  $Z_n$ ,  $T_n$  and  $\alpha_n$  for the same configuration and flight conditions used to develop Figure 3.16. The plots were for bank angles of 10 degrees, 20 degrees, 40 degrees, 50 degrees and for two multiple solutions at a bank angle of 35 degrees. Figure 3.22 is a plot of the towpoint tension versus the bank angle for the same conditions. Figure 3.21 provided graphic support for the previous explanation of the jump phenomenon. The angle of attack in the low verticality case was small and reasonably constant along the wire length, but once in the high verticality region, the angle of attack dramatically increased, particularly in the lower part of the wire. The change in tension was thus contributing much more in the lower part of the wire to the support of the weight vector in the high verticality case. Figure 3.19 showed that the slope of the wire in the  $\bar{e}_z$  coordinate direction was decidedly higher in the bottom half of the

wire in the higher verticality multiple solution than the low verticality multiple solution. Something dramatic happened in the lower half of the wire which caused this. The answer came from Figure 3.17. As can be seen, the radial coordinate of the wire in the low verticality case was reasonably constant and approached the towplane coordinate all along the wire length. This meant that each gridpoint's dynamic pressure was high, since in the steady-state condition it was proportional to  $R_n^2$  and thus the magnitudes of the aerodynamic forces were high. The wire was then able to generate the lift forces necessary to counter the weight term without the use of the vertical component of the change in tension available in the high verticality case. The opposite was true in the high verticality case where in the lower portions of the wire, the radial coordinate became very small, the dynamic pressure reduced proportional to  $R_n^2$  and the lift generating capability of the wire decreased dramatically. The wire had to be at the high verticality solution to allow the change in tension to counter the weight because the aerodynamic forces achievable with the dynamic pressure available were not large enough. Furthermore, as long as the radial position was close to the center of the orbit, the dynamic pressure was so small that the wire could not produce enough force to move itself out of the low radial/high verticality position. This was critical since it indicated that control

of the radial position was crucial to the prevention of a transition from the high to the low verticality solutions.

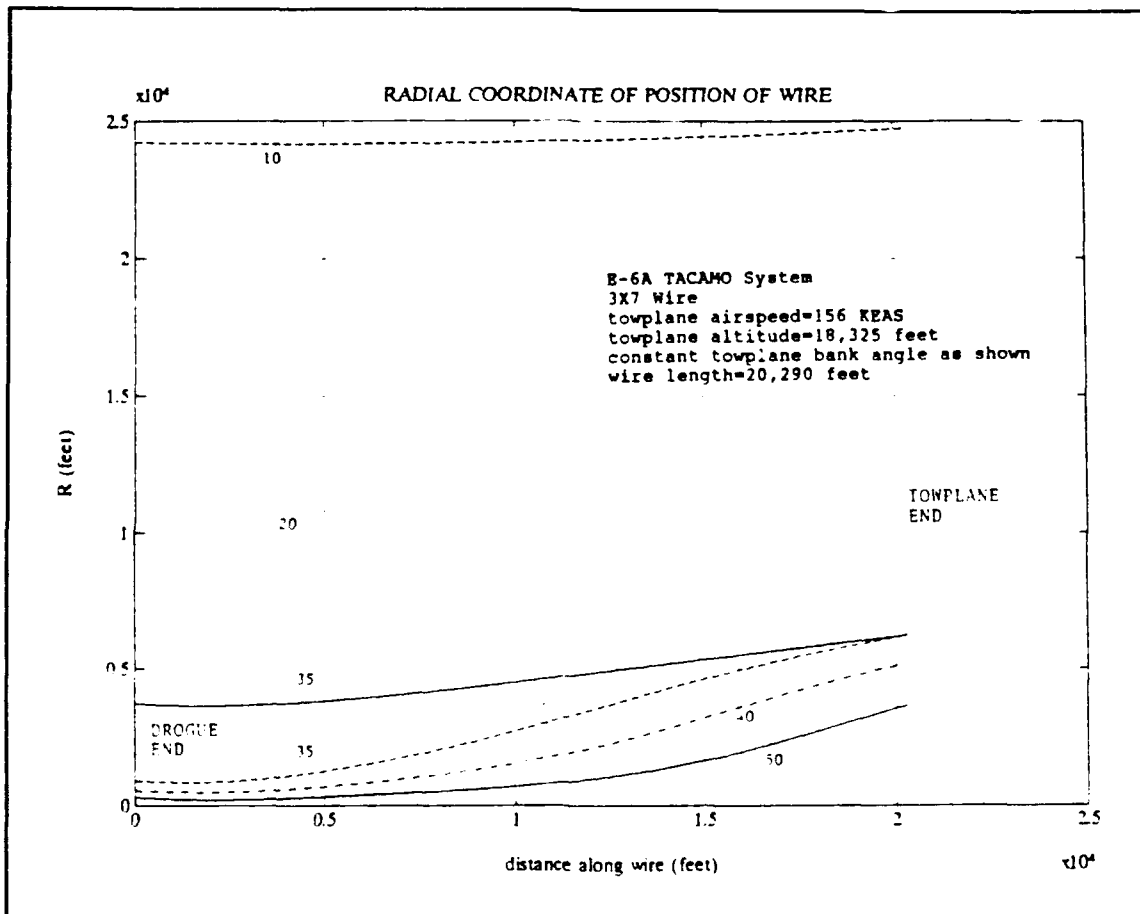


**Figure 3.17: Radial Coordinate of Position of Wire for Various Bank Angles**

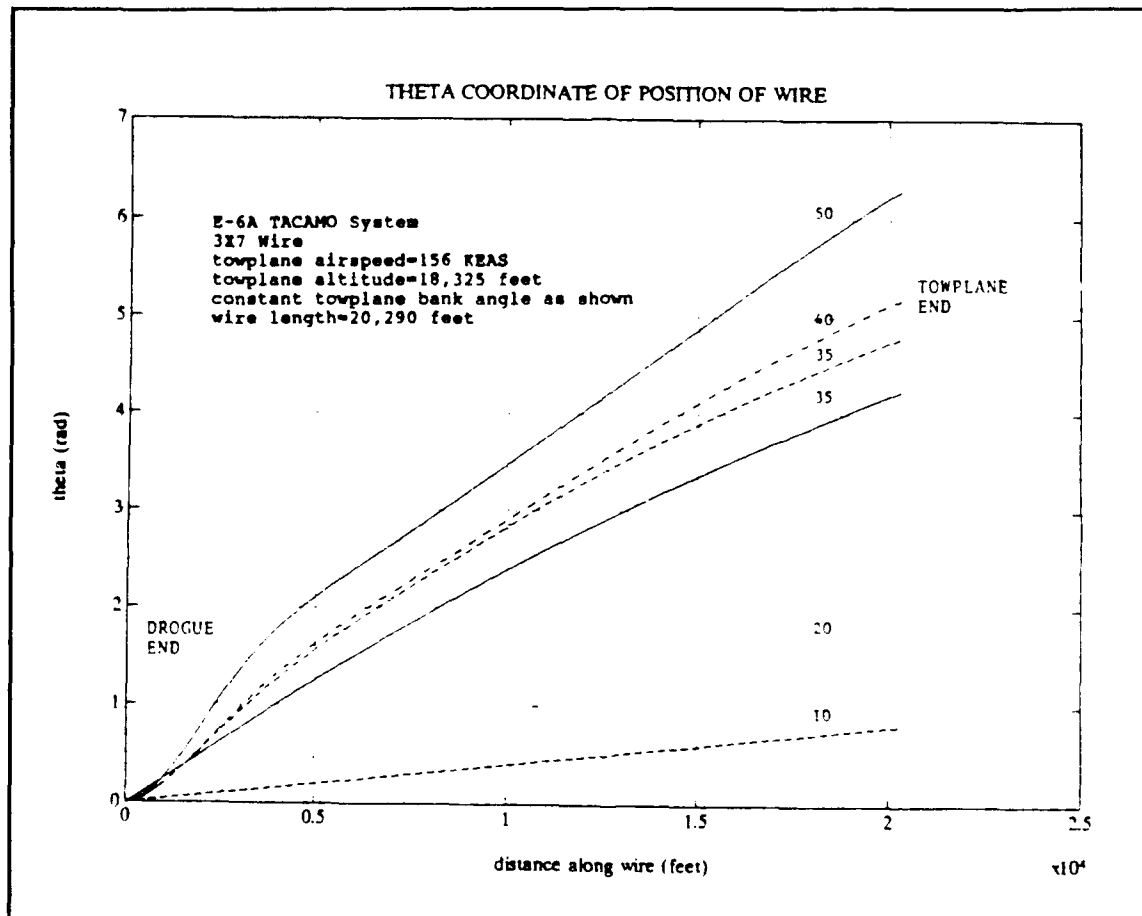


**Figure 3.18:**  $\theta$  Coordinate of Position of Wire for Various Bank Angles

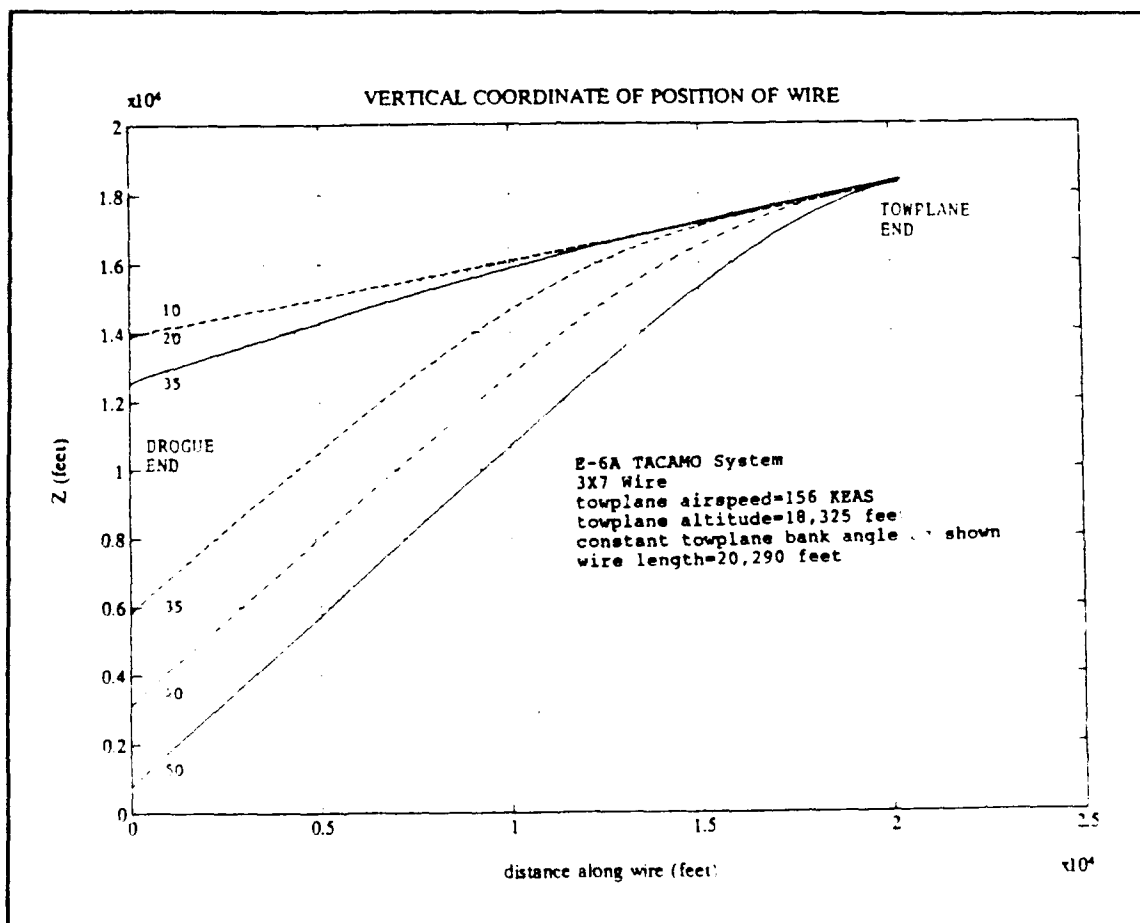


**Figure 3.19: Vertical Coordinate of Position of Wire for Various Bank Angles**

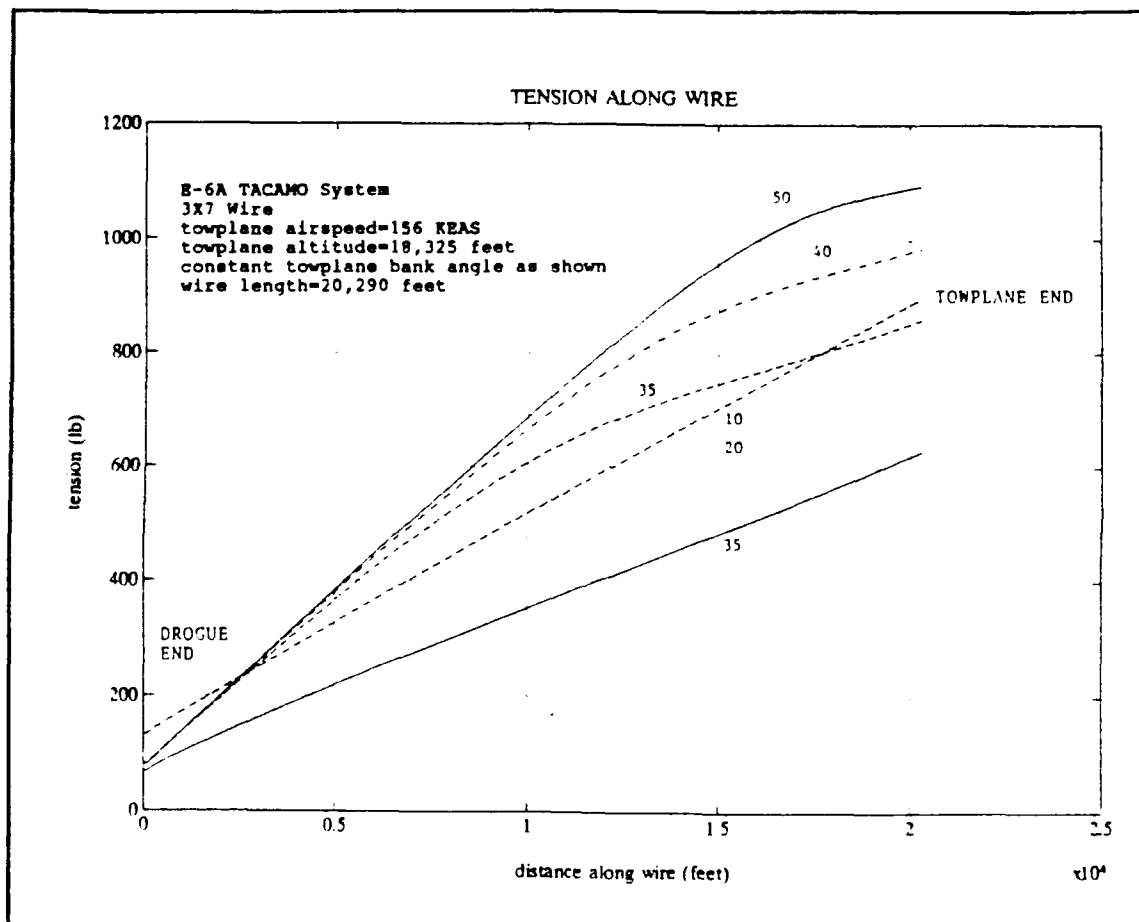


**Figure 3.20: Tension Along Wire for Various Bank Angles**

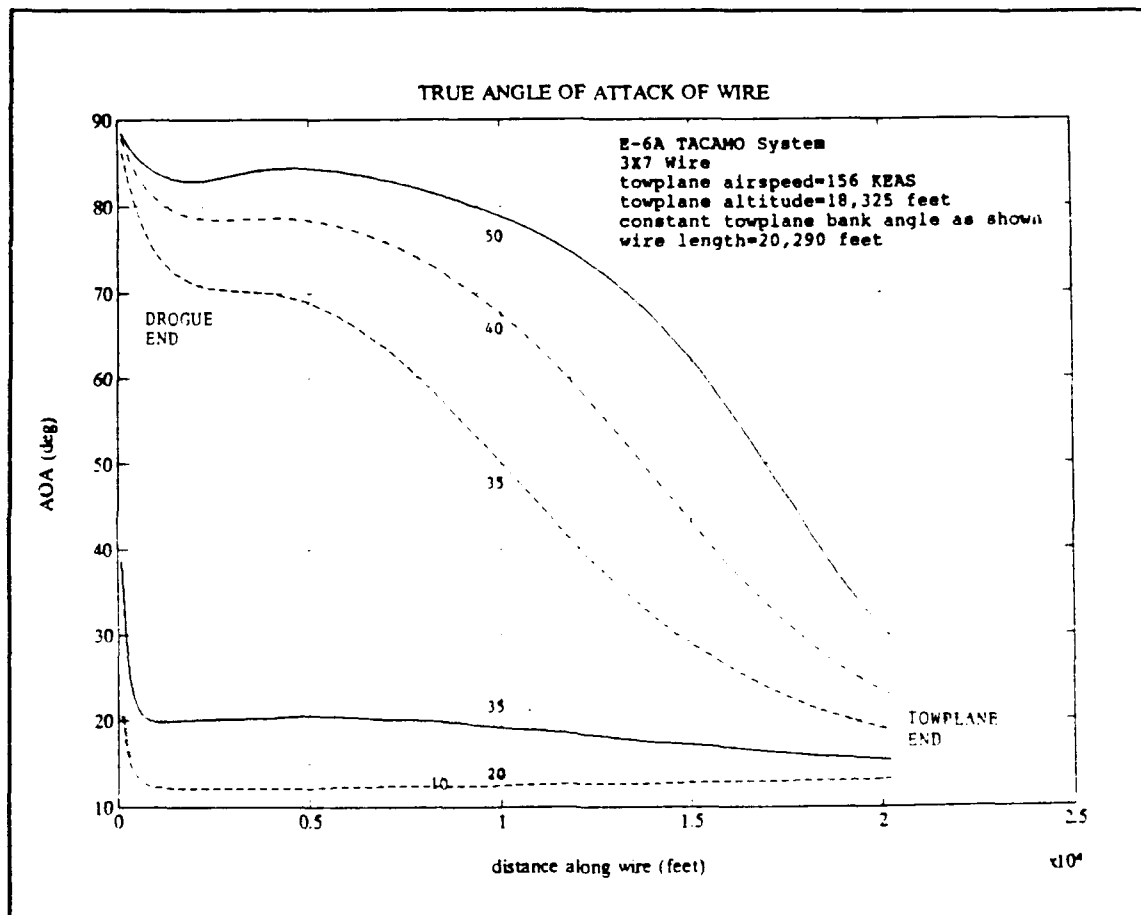


**Figure 3.21: The  $\alpha$  Along the Wire for Various Bank Angles**

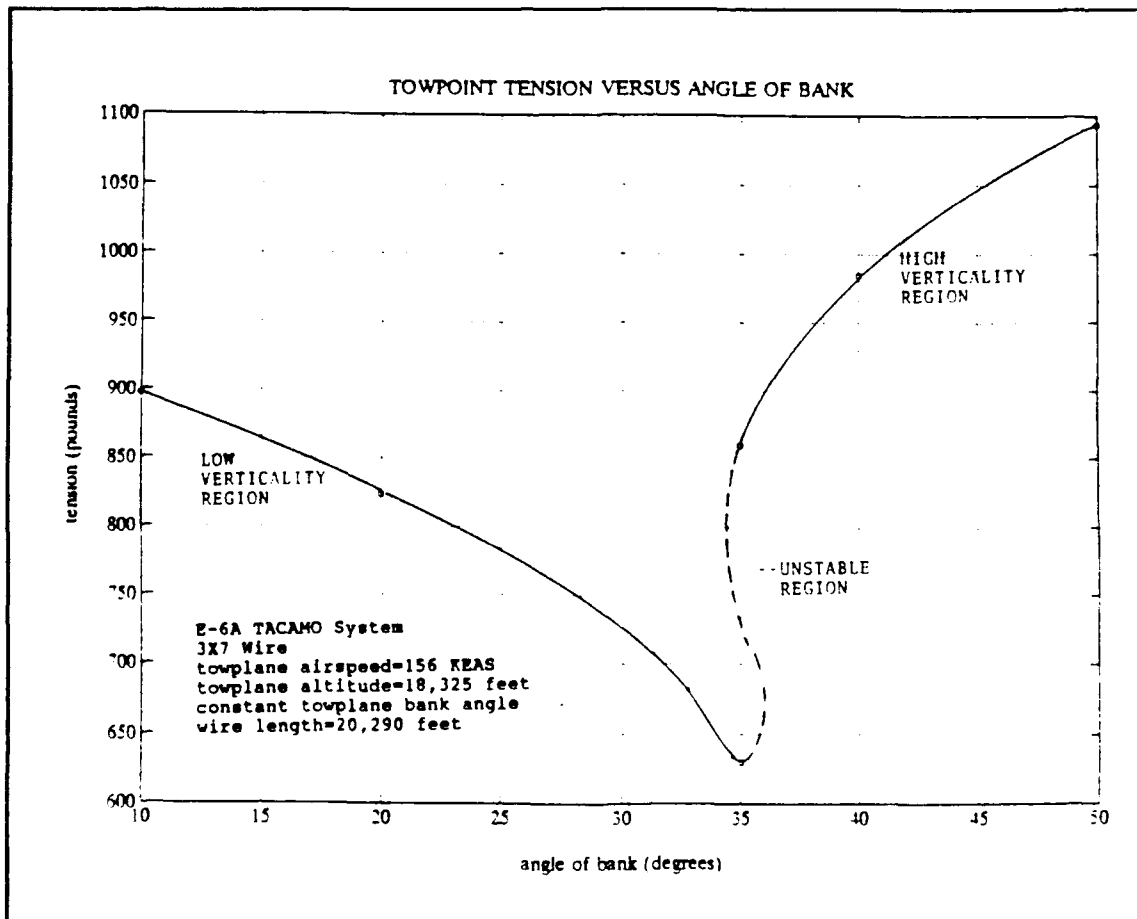


**Figure 3.22: Towpoint Tension Versus Angle of Bank**



As further support of the explanation of the jump phenomenon, decreasing the wire's drag coefficient and/or increasing the wire's density a sufficient amount would result in the disappearance of the jump phenomenon. Figure 3.23 is a repeat of the verticality variation with towplane bank angle (Figure 3.16) but this time modified to include conditions of wire drag,  $C_D=0.2$  and for a wire mass density of  $\mu=0.5$ . Note that for all reasonable bank angles, the jump phenomenon and multiple solutions were gone. The radial positions of the bottom segments of the wire were thus crucial to the maintenance of the wire in the high verticality geometry and the jump phenomenon existed because of the interplay between the aerodynamic lift and the vertical component of the tension as they balanced the weight of the wire. As a final note, Figure 3.22 showed a sharp increase in tension as the wire transitioned from the low verticality to the high verticality solution as hypothesized earlier in the discussion.

#### **E. SIDEFORCE MODEL**

When trailing the 3X7 wire in straight and level flight and looking back from the aircraft at the wire, the wire distinctly trails off to the right. As mentioned earlier, the 3X7 wire is made of three sets of seven wires in a copper matrix. The three sets are twisted at a pitch of 1.87 inches. The twisting causes three spiraling grooves in

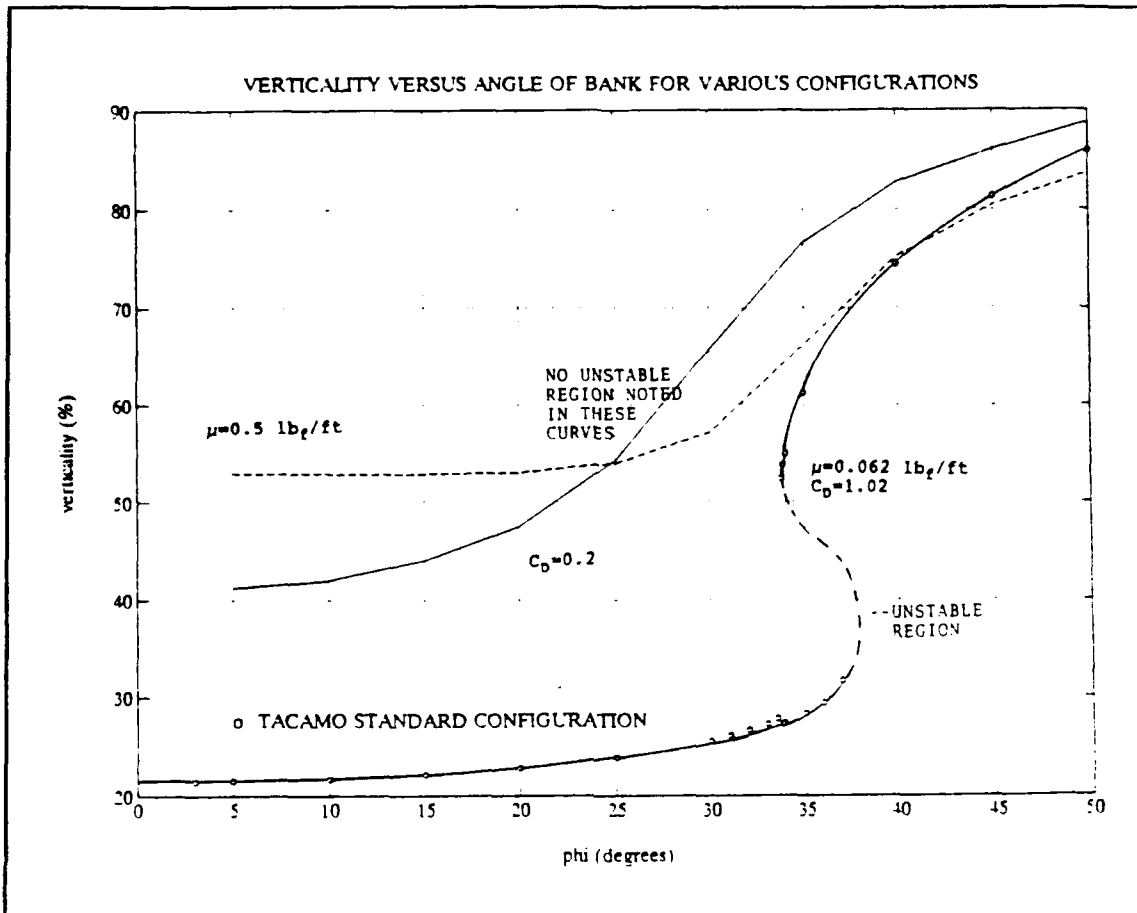


**Figure 3.23:** Verticality Versus Angle of Bank for Various Wire Configurations

the wire surface. It was hypothesized that the grooves entrain the flow and cause it to swirl around the wire surface. A cross flow then produces a sideforce due to asymmetric vortex shedding. Since axial flow is required for the swirl and normal flow to generate the side force, the effect is not exhibited at zero and ninety degrees of angle of attack and is a maximum at some value in between. [Ref. 12] As an approximation, a coefficient of side force,  $C_{fside}$ , was proposed which varied sinusoidally from zero at an angle of attack of zero to the maximum value at 45

degrees and again zero by ninety degrees of angle of attack.  $F_{side}$  was defined as the force due to this sideforce effect and  $\alpha_n$  was defined as the true angle of attack of the wire segment. The relation for  $\alpha_n$  was most easily derived by looking at the definition of the dot product between the relative velocity and the unit tangent vector at the given gridpoint. This was done in equation (3.78). The central difference approximation of the definition of the unit tangent vector at gridpoint  $n$  is repeated in (3.79). Note that this vector was already normalized. A normalized version of the relative velocity was also required and is provided in equation (3.80). This expression was very simple due to the steady-state condition. Substituting the above two expressions into the dot product resulted in (3.81) and since both the relations substituted above were already normalized, equation (3.82) was written.

$$\overline{V_{reln}} \cdot \overline{e_{sn}} = |\overline{V_{reln}}| |\overline{e_{sn}}| \cos \alpha \quad (3.78)$$

$$\overline{e_{sn}} = \left( \frac{R_{n+1} - R_{n-1}}{2\Delta S} \right) \overline{e_R} + \left( \frac{R_n(\theta_{n+1} - \theta_{n-1})}{2\Delta S} \right) \overline{e_\theta} + \left( \frac{Z_{n+1} - Z_{n-1}}{2\Delta S} \right) \overline{e_Z} \quad (3.79)$$

$$\frac{\overline{V_{reln}}}{|\overline{V_{reln}}|} = \left( \frac{R_n \dot{\theta}}{R_n \dot{\theta}} \right) \overline{e_{\theta n}} = \overline{e_{\theta n}} \quad (3.80)$$

$$\overline{V_{reln}} \cdot \overline{e_{sn}} = \frac{R_n(\theta_{n+1} - \theta_{n-1})}{2\Delta S} \quad (3.81)$$

$$\left| \frac{\overline{V_{reln}}}{|\overline{V_{reln}}|} \right| = |\overline{e_{sn}}| = 1 \quad (3.82)$$

Equation (3.78) was solved for  $\alpha$ , the central difference approximation in (3.81) was substituted into the left hand side of (3.78) and (3.82) substituted into (3.78) to obtain (3.83). Using with the  $\alpha_n$  value and the definition of  $C_{fside}$ , an expression for the change in sideforce over an increment of wire was written as in equation (3.83) where  $\Delta S$  was canceled from both sides. Substituting for  $\alpha_n$  from equation (3.83) resulted in equation (3.85). Equation (3.85) provided a radial force component which was pointed inward toward the center of the orbit for a positive coefficient and was in the same form as the components of the forces added together in equation (3.1). Since (3.85) was in terms of the radial component alone, it was added directly to equation (3.35), the central difference approximation of the orthogonal radial component of equation (3.1). A new expression for  $A_{n+1/2}$ , similar to equation (3.47) was then written as in equation (3.86).

$$\alpha_n = a \cos \left[ \frac{R_n(\theta_{n+1} - \theta_{n-1})}{2\Delta S} \right] \quad (3.83)$$

$$\left(\frac{\partial F_{side}}{\partial S}\right)_n \Delta S = -\sin(2\alpha_n) C_{fside} \frac{1}{2} \rho_n V_{reln}^2 D \Delta S \quad (3.84)$$

$$\left(\frac{\partial F_{side}}{\partial S}\right)_n = -\sin\left(\frac{Z_{n+1} - Z_{n-1}}{\Delta S}\right) C_{fside} \frac{1}{2} \rho_n D (R_n \dot{\theta})^2 e_R \quad (3.85)$$

$$\begin{aligned} A_{n+\frac{1}{2}} = A_{n-\frac{1}{2}} + & \left[ \left( \frac{T_{n+\frac{1}{2}} + T_{n-\frac{1}{2}}}{2} \right) R_n \left( \frac{\theta_{n+1} - \theta_{n-1}}{2\Delta S} \right)^2 \right. \\ & - \frac{1}{2} \rho_n D C_D (R_n \dot{\theta})^2 \sqrt{1 - \frac{R_n^2 (\theta_{n+1} - \theta_{n-1})^2}{4\Delta S^2}} \left( \frac{R_n (\theta_{n+1} - \theta_{n-1}) (R_{n+1} - R_{n-1})}{4\Delta S^2} \right) - \mu \dot{\theta}^2 R_n \\ & \left. + \sin\left(\frac{Z_{n+1} - Z_{n-1}}{\Delta S}\right) C_{fside} \frac{1}{2} \rho_n D (R_n \dot{\theta})^2 \right] \Delta S \end{aligned} \quad (3.86)$$

The above analysis was required to model the sideforce in a class of wires. An experimentally derived knowledge of the sideforce coefficient is required to apply this model. In the absence of a known sideforce or a valid coefficient, it is best to make the sideforce coefficient zero which causes the equations to revert to the form of the original equation which neglected sideforces. This is the approach used for all later analysis. The model is provided to allow the flexibility necessary to implement sideforce effects for trailing wires for which the coefficient has been

determined. The most general case is thus preserved for later application.

#### IV. DYNAMIC MODEL

##### A. FORMULATION OF THE DYNAMIC MODEL EQUATIONS

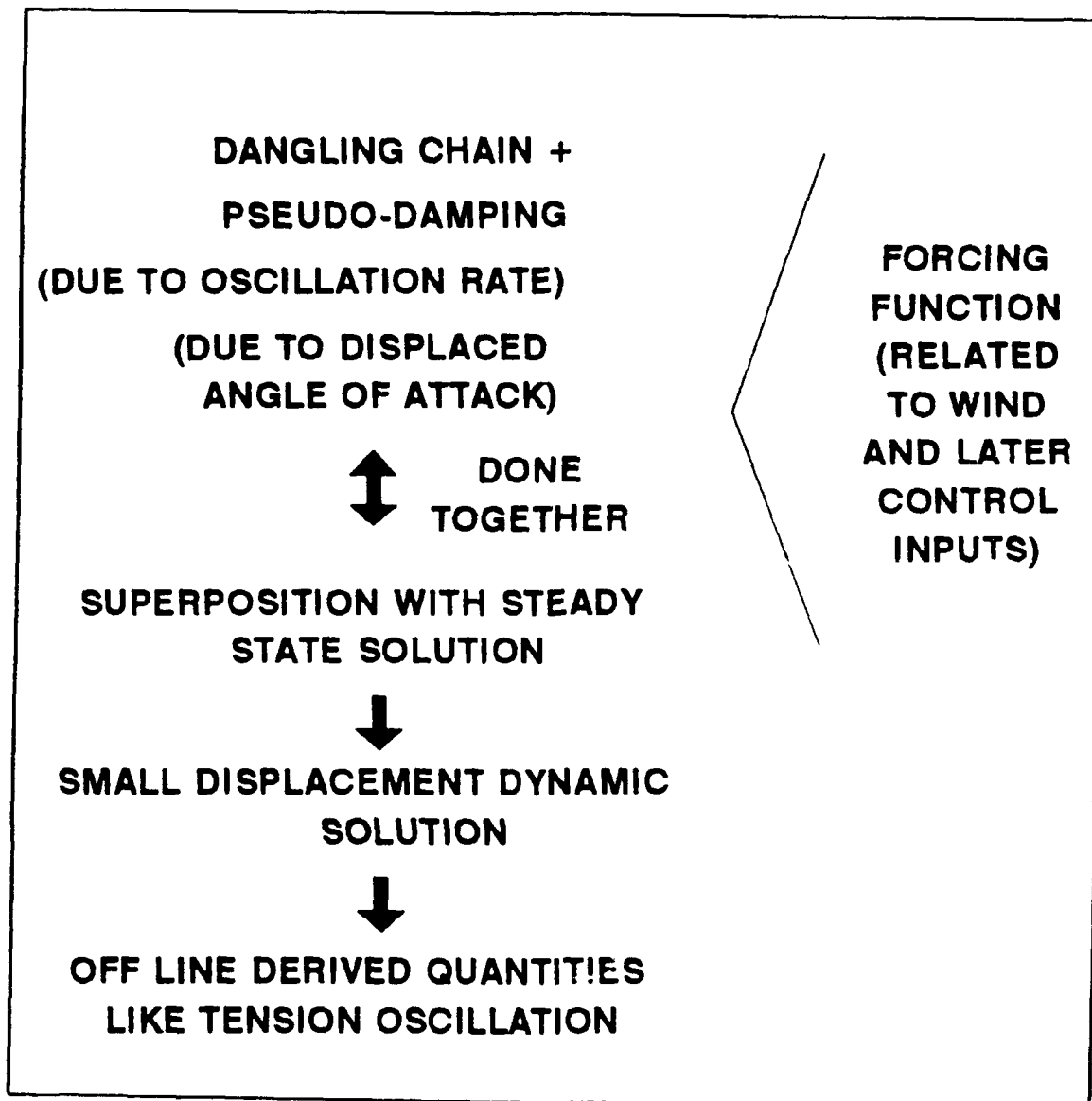
The dynamic model was developed under the assumption that all displacements from the steady-state equilibrium condition were small. The static model was used as the definition of the initial condition and the dynamics, which were modeled as a classical "dangling chain", were superimposed upon this solution. The towplane was assumed to be flying a constant circular orbit. It was assumed that the dangling chain model was the source of all significant wire dynamics. Wire torsion, stretching and bending effects, as well as the effects of towplane pitch bank and yaw transients were ignored. The validity of these assumptions is discussed at the end of this chapter. The dangling chain displacement calculations were then validated by comparison with analytical solutions. Finally, the complete model was compared to actual flight test data as an end-to-end validity check. It will be seen that this procedure validated the application of superposition of small displacement vibrations upon the steady-state solution for the problem of a long cable suspended from a towplane in a circular orbit.

Figure 4.1 is a graphical representation of the algorithm used in the dynamic model development. A

classical dangling chain, with one end fixed and one free boundary with a dead weight attached was first developed. Once this classical problem was developed, pseudo-damping was applied to the model. The term pseudo-damping was chosen because the restorative and dissipative forces were not related linearly to velocity but had an effect similar to damping. Two forms of pseudo-damping were hypothesized and modeled. The first was due to the drag caused by the lateral oscillatory motion. The second was due to the change in the angle of attack of the gridpoint segments in the displaced condition. At this point, superposition onto the steady-state model was performed. The superimposed geometry was required to establish the pseudo-damping and vice-versa and so the process had to be performed iteratively. Following the superposition process, a number of quantities, such as the tension oscillation value, were calculated off-line from the model algorithm. At various points within the process, the forcing function was applied. The forcing function was based upon the pattern of the winds along the entire length of the wire.

The governing partial differential equation of the dangling chain with one end fixed and one free boundary condition and with a concentrated mass on the free end of the chain was derived in Appendix B. This equation was derived assuming that the equilibrium distribution was the vertically hanging chain. The equation was modified to





**Figure 4.1:** Dynamic Model Algorithm

calculate the displacements from the steady-state distribution in equation (4.1). A time independent tension distribution,  $T(S)$ , derived from the steady-state solution vice a fully time dependent  $T(S,t)$  was used. An analysis of the validity of this assumption will be presented in the validation and verification section of this chapter. Note that the independent variable,  $v(S,t)$ , which was the

displacement due to the dangling chain vibration, was referenced from the top, at the towplane, to the bottom, at the drogue. This was opposite to the steady-state model and was the convention for the entire dynamic model development. The expression was developed assuming that the displacements were "small" and defined as being perpendicular to the wire equilibrium position. The validity of this assumption of "small" displacements will also be discussed in the validation and verification section of this chapter. Note again that  $S$  was the distance along the wire length.  $Q(S,t)$  was defined as an arbitrary forcing function, which was perpendicular to the wire at any point and was in terms of force per unit length at time  $t$ . The origin of the forcing function is discussed in detail in Appendix C. As indicated in (4.1) it was further assumed that the initial condition corresponded to the wire being located at the steady-state no-wind position, defined as  $f(S)$ . Further, the initial displacement rate was assumed to be zero. It will be seen later, that this assumption led to a short starting transient at the beginning of the dynamic model simulation. Two separate, orthogonal solutions to equation (4.1) were required to model the two-dimensional displacement of each point around the equilibrium position. The  $\Delta S$  compatibility condition for the first internal gridpoint and the definition of the unit tangent vector for all subsequent gridpoints were then used to make the solution into a three-

dimensional model using the R,  $\theta$  and Z coordinates described in the steady-state wire analysis. The procedure is fully discussed later when the superposition formulas are developed.

$$\begin{aligned}
 \mu \frac{\partial^2 v(S, t)}{\partial t^2} &= \frac{\partial}{\partial S} \left( T(S) \frac{\partial v(S, t)}{\partial S} \right) + Q(S, t) \\
 B.C. \quad v(0, t) &= 0 \quad v(L, t) \rightarrow \text{Bounded} \\
 T(L) \frac{\partial v(L, t)}{\partial S} + Q(S, t) &= m \frac{\partial^2 v(L, t)}{\partial t^2} \\
 I.C. \quad v(S, 0) &= f(S) \quad \frac{\partial v}{\partial t}(S, 0) = 0
 \end{aligned} \tag{4.1}$$

As in the steady-state problem, the partial differential equation in (4.1) was approximated using a second order accurate central difference scheme. The central difference approximation of the time derivative component of equation (4.1) was written as in equation (4.2) by first defining  $n$  as the spatial gridpoint number indexed from the top of the wire at the towplane down to the drogue at the bottom,  $m$  as the time step index and  $T(n) = T_n$  = the steady-state tension distribution. The central difference approximation of the derivative of  $v$  with respect to  $S$  was written, as in equation (4.3) by referring to Figure 4.2 and again choosing  $\Delta S$  as the spatial distance between the gridpoints. Again,  $S$  was the distance along the wire length. The process was then repeated for the derivative with respect to  $S$  of the product of  $T(S)$  and the derivative of  $v$  with respect to  $S$  as shown in (4.4) and the result simplified in (4.5). [Ref. 14]

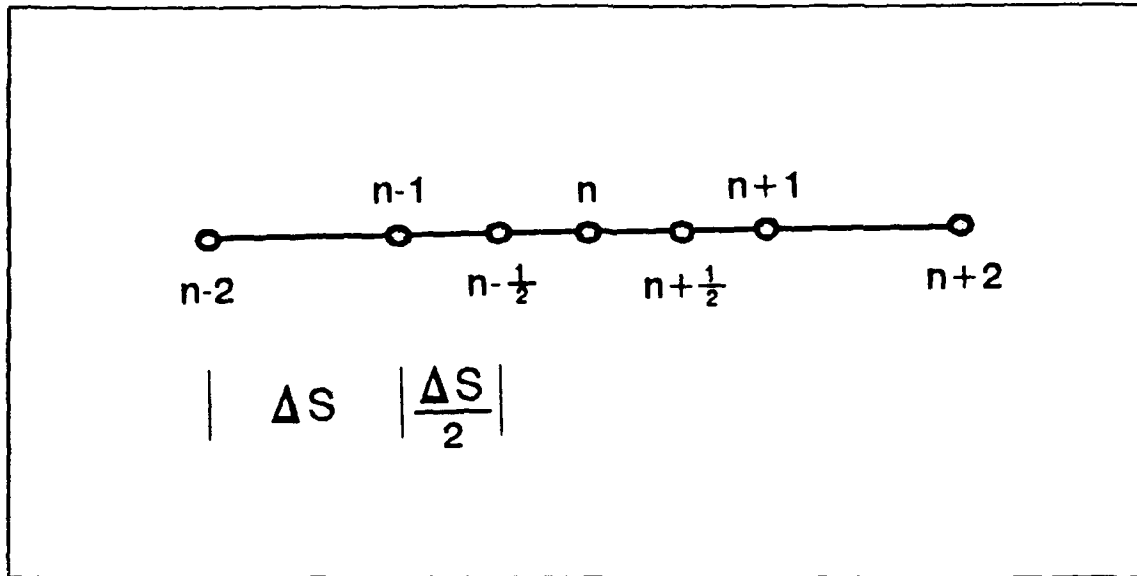


**Figure 4.2:** Central Difference Gridpoint Scheme for Dynamic Model Spatial Dimension

$$\frac{\partial^2 v_{n,m}}{\partial t^2} = \frac{v_{n,m+1} - v_{n,m} + v_{n,m-1}}{\Delta t^2} \quad (4.2)$$

$$\frac{\partial v_{n+\frac{1}{2},m}}{\partial S} = \left( \frac{v_{n+1,m} - v_{n,m}}{2\left(\frac{1}{2}\Delta S\right)} \right) \quad (4.3)$$

$$\frac{\partial}{\partial S} \left( \pi S \frac{\partial v_{n,m}}{\partial S} \right) = \frac{T_{n+\frac{1}{2}} \left( \frac{v_{n+1,m} - v_{n,m}}{\Delta S} \right) - T_{n-\frac{1}{2}} \left( \frac{v_{n,m} - v_{n-1,m}}{\Delta S} \right)}{2\left(\frac{1}{2}\Delta S\right)} \quad (4.4)$$

$$\frac{\partial}{\partial S} \left( \pi S \frac{\partial v_{n,m}}{\partial S} \right) = \frac{T_{n+\frac{1}{2}} (v_{n+1,m} - v_{n,m}) - T_{n-\frac{1}{2}} (v_{n,m} - v_{n-1,m})}{\Delta S^2} \quad (4.5)$$

The central difference approximation shown in equation (4.5) was taken about the half step. This technique had the distinct advantage of requiring only three gridpoint positions and allowed the use of the average of the tension at each gridpoint at the half step tension gridpoint. This in turn facilitated the solving of the first internal gridpoints explicitly without resorting to the use of iteration. As is seen later, the form of the boundary conditions then make the entire process explicit.

Substituting equations (4.2) and (4.5) into (4.1) resulted in the finite difference approximation of the entire wire dynamics expression presented in equation (4.6). The forcing function,  $Q_{n,m}$ , with the indices at  $n,m$  was used since the entire central difference scheme was taken about the point  $n,m$ . Since  $T_n$  was a constant over time, the expression was explicit in the variable  $v_{n,m+1}$ . It was then possible to envision a fully explicit marching scheme requiring only knowledge of the two end gridpoints and the two previous time step solutions. This is graphically depicted in Figure 4.3. Equation (4.7) resulted when  $v_{n,m+1}$  was broken out from equation (4.6).

$$\mu \left[ \frac{v_{n,m+1} - 2v_{n,m} + v_{n,m-1}}{\Delta t^2} \right] = \frac{T_{n+\frac{1}{2}}(v_{n+1,m} - v_{n,m}) - T_{n-\frac{1}{2}}(v_{n,m} - v_{n-1,m})}{\Delta S^2} + Q_{n,m} \quad (4.6)$$

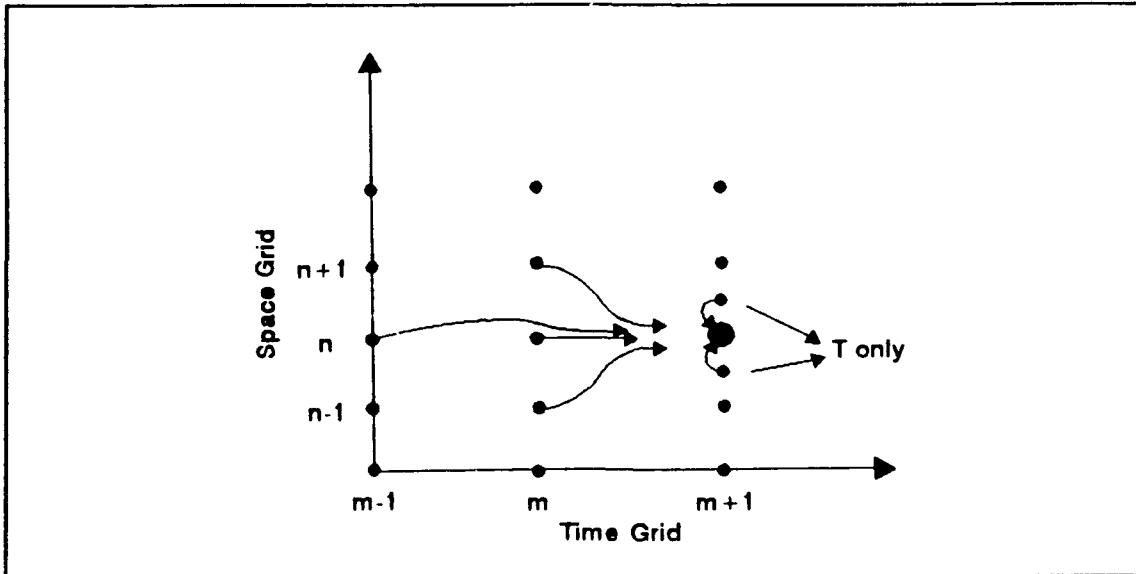


Figure 4.3: Dangling Chain Time and Space Grid

$$v_{n,m+1} = \frac{\Delta t^2}{\mu} \left[ \frac{T_{n+\frac{1}{2}}(v_{n+1,m} - v_{n,m}) - T_{n-\frac{1}{2}}(v_{n,m} - v_{n-1,m})}{\Delta S^2} + Q_{n,m} \right] + 2v_{n,m} - v_{n,m-1} \quad (4.7)$$

Examining the boundary conditions, the wire at the top was pinned and thus  $v_{1,m}$  equaled 0 and for this physical system, the solution had to be bounded. Neither of these boundary conditions aided in determining  $v_{n,m+1}$  at the bottom of the wire. Examination of equation (4.7) showed , that in order to determine  $v_{n,m+1}$ ,  $v_{n+1,m}$  was required. The solution of this dilemma was derived by application of the third boundary condition listed in (4.1). This boundary condition ensured force equilibrium at the drogue gridpoint,  $n=N$ , and was written in a central difference form in equation (4.8).

$$T_N \left( \frac{V_{N-1,m} - V_{N+1,m}}{2\Delta S} \right) + Q_{N,m} = \frac{W_D}{g} \left( \frac{V_{N,m+1} - 2V_{N,m} + V_{N,m-1}}{\Delta t^2} \right) \quad (4.8)$$

Equation (4.8) described the balance between the tension and forcing function forces and the lateral acceleration of the drogue (remember that all motion was defined as lateral in the dangling chain problem). It was next assumed that the forces upon the drogue were much greater than the forces on the last bit of the wire. Later analysis showed that the forces differ by approximately two orders of magnitude. Based upon this assumption, it was possible to visualize that at the drogue attachment point, the wire slope was nearly a constant since the shape of the wire was determined by the drogue forces and not the distributed wire forces. This condition was approximated by defining an  $N+1$  point beyond the drogue and equating the central difference approximations of the slope at the half step before and after the drogue as in equation (4.9).

$$\frac{V_{N,m} - V_{N-1,m}}{\Delta S} = \frac{V_{N+1,m} - V_{N,m}}{\Delta S} \quad (4.9)$$

Under the assumption that the forces on the drogue were much greater than the wire, it was seen that  $T_N = T_{N-1} = T_{N-1/2}$ . Finally, solving (4.9) for  $v_{N+1,m}$  and substituting this result into (4.8), replacing  $T_N$  in (4.8) with  $T_{N-1/2}$  and solving for  $v_{N,m+1}$  resulted in (4.10). (4.10) was the solution of  $v_{N,m+1}$  in terms of previously known quantities. Note that this equation showed that the updated displacement

was larger for a bigger tension value and smaller for a lighter drogue which corresponded with physical intuition.

$$v_{N,m+1} = \frac{\Delta t^2 g}{W_D} \left[ T_{N-\frac{1}{2}} \left( \frac{v_{N-1,m} - v_{N,m}}{\Delta S} \right) + Q_{N,m} \right] + 2v_{N,m} - v_{N,m-1} \quad (4.10)$$

Now to summarize, the marching scheme is started from the steady-state condition so that the two previous time step position sets are known. The boundary condition of  $v_{1,m}$  and equation (4.10) are used to provide the endpoints. Equation (4.7) is used to get the internal gridpoints. For the purposes of bookkeeping, the two orthogonal components of displacement were defined as  $X_{n,m}$  and  $Y_{n,m}$  vice the generic  $v_{n,m}$  chosen for the development above.

## B. FORCING FUNCTION DEVELOPMENT

In applying the wind as a forcing function to the wire dynamics problem, it was important to first note that under the assumption of a steady-state angle of bank turn, the towplane moved with the airmass, and so the forcing function due to the wind was in fact zero at the towplane. The drifting towplane, in a constant angle of bank orbit, is depicted in Figure 4.4. The required apparent forcing wind was then derived by adding the negative of the wind vector at altitude to the winds at each gridpoint including the towplane end gridpoint.

With the apparent forcing wind defined, an arbitrary reference system was set up such that the towplane was



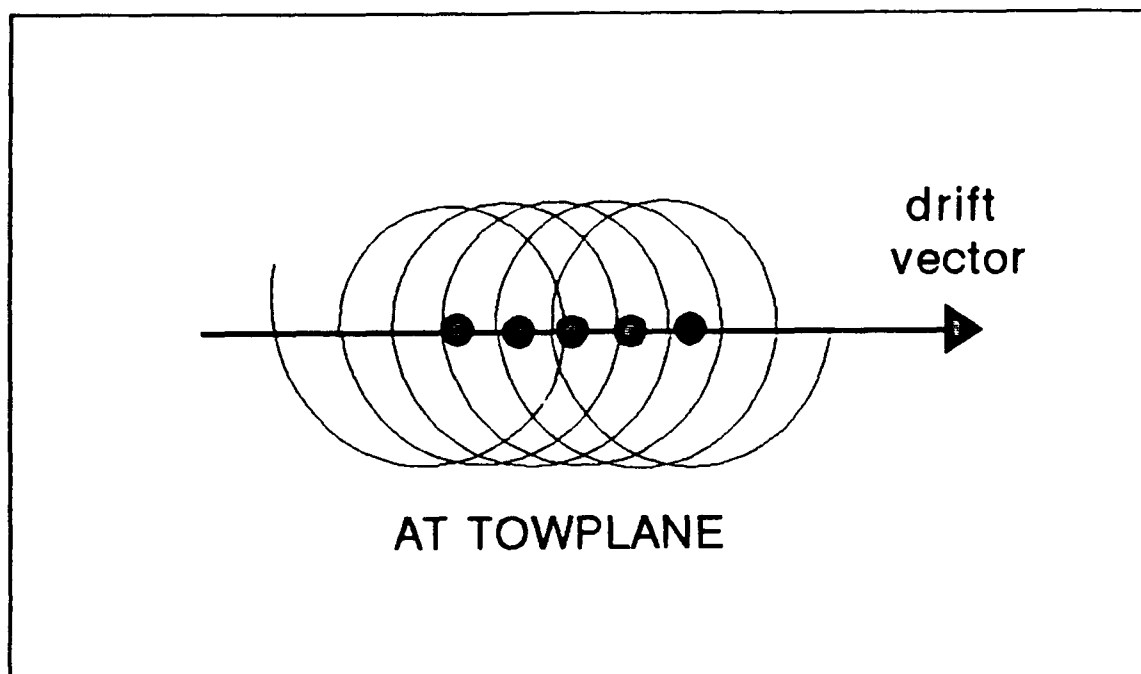


**Figure 4.4:** Towplane Drift Due to Wind During Steady State Turn

aligned with the heading of 000 at time zero. This was possible because the correlation between the defined cylindrical coordinate system and the compass direction was completely arbitrary. The convention chosen for the definition of the wind heading was that the wind direction was the heading from which the wind came from vice the actual direction that the wind vector pointed. This was the normal aeronautical definition used in the flight test data that will be discussed later. Equation (4.1), the governing equation of the dangling chain model, was derived assuming that all displacements, as well as the forcing function,  $Q_{n,m}$ , were perpendicular to the chain.  $Q_{n,m}$  was thus defined as perpendicular to the wire tangent vector. The forcing function was derived from the apparent forcing wind. Since

the forcing function was defined perpendicular to the wire, only that component of the apparent forcing wind perpendicular to the wire was used to calculate the forcing function. The orientation of the apparent forcing wind with the wire varied harmonically as the wire orbited within the airmass. The calculations were performed for each orthogonal component of the oscillation and so one harmonically varying wind induced forcing component was described using a sine function while the second was described using a cosine function. Two adjustments in phasing were required to the harmonic functions. As mentioned above, the apparent forcing wind was resolved into components perpendicular to the wire. These calculations were performed for the case where the gridpoint  $\bar{e}_0$  vector was oriented along the 000 heading described earlier in this paragraph and assuming that the apparent forcing wind was coming from the 000 direction. The first phase correction was the  $\theta$  coordinate at each gridpoint to account for the fact that for every gridpoint except the towplane's, the wire shape had to rotate through the  $\theta$  angle for  $\bar{e}_0$  to be aligned with the 000 heading. The second phase correction accounted for the wind heading at each gridpoint being in general, different from 000. Finally, the aerodynamic coefficients of the wire were used to convert the forcing wind into a force vector, which was the true forcing function desired. The forcing function equations were

developed in detail in Appendix C. Wind data may be contrived or radiosonde derived flight test data may be used. The simulation programs allow for winds to be defined internally to the program or imported as data files.

### C. SUPERPOSITION

The next task was to derive the algorithm used to superimpose  $X_{n,m}$  and  $Y_{n,m}$ , the orthogonal components of the dangling chain oscillation, onto the steady-state solution. The development of the superposition equation for the  $X_{n,m}$  component of the oscillation was begun by arbitrarily defining the  $X_{n,m}$  displacements as being in the  $\bar{e}_R, \bar{e}_\theta$  plane and thus orthogonal to the  $\bar{e}_K$  vector. Next, the governing equation for the dangling chain oscillations presented in (4.1) was derived assuming that the displacements were perpendicular to the chain. The  $X_{n,m}, Y_{n,m}$  orthogonal components of the dangling chain displacements were thus orthogonal to the unit tangent vector at each gridpoint. The cross product of the  $\bar{e}_K$  vector and the unit tangent vector in cylindrical coordinates then defined the direction of the  $X_{n,m}$  component of displacement in the cylindrical coordinate system used for the superimposed model. The  $Y_{n,m}$  component of displacement was orthogonal to the unit tangent vector and to the  $X_{n,m}$  displacement. The direction of the  $Y_{n,m}$  displacement in cylindrical coordinates was then derived using the cross product of the vector in the direction of the  $X_{n,m}$  displacement and the unit tangent

vector at each gridpoint. The  $\bar{e}_R$  and  $\bar{e}_\theta$  components of the displacements were added to the  $R_n$  and  $\theta_n$  coordinates of the steady-state gridpoint locations to derive the time dependent superimposed locations  $RS_{n,m}$  and  $\theta S_{n,m}$ . The time dependent, superimposed  $ZS_{n,m}$  location was calculated using the compatibility equation in the form of (3.14) for the first internal gridpoint and (3.16) for all subsequent gridpoints. The superposition equations were derived in detail in Appendix D.

#### D. PSEUDO-DAMPING

As implemented up to this point, the modeled oscillations tended to be larger than expected when compared to experimental data. What was needed was to identify a "damping-like" set of restorative and/or dissipative forces. The term "damping-like" was chosen because the hypothesized forms of the pseudo-damping involved both restorative and dissipative forces and none of the contributions were directly proportional to rate. Two forms of the pseudo-damping were modeled. Both were defined as  $D'$  since their effects were additive and made up the total pseudo-damping term. The first was due to the increment in drag caused by the lateral oscillation rate. In keeping with the small displacement assumptions, it was assumed that the lateral oscillations remained perpendicular to the steady-state positions of the wire and thus this dissipative force remained perpendicular also. It was thus always orthogonal

to the steady-state wire shape and opposite in direction to the lateral velocity of the wire gridpoints. This was because the lateral oscillations were also calculated based upon the assumption that they remained orthogonal to the steady-state wire. Equation (4.11) was the contribution to the total pseudo-damping of the lateral oscillation rate. The unprimed D is the wire diameter. Equation (4.12) was the central difference approximation describing the displacement rate from the equilibrium position and (4.13) was the central difference approximation of (4.11).

$$D' = (C_D + \pi C_f) D \frac{1}{2} \rho_n \left( \frac{\partial v_{n,m}}{\partial t} \right)^2 \quad (4.11)$$

$$\frac{\partial v_{n,m}}{\partial t} = \left( \frac{v_{n,m+1} - v_{n,m-1}}{2 \Delta t} \right) \quad (4.12)$$

$$D'_{n,m} = (C_D + \pi C_f) D \frac{1}{2} \rho_n \left( \frac{v_{n,m+1} - v_{n,m-1}}{2 \Delta t} \right) \left\| \frac{v_{n,m+1} - v_{n,m-1}}{2 \Delta t} \right\| \quad (4.13)$$

Note that  $v_{n,m+1}$  was required to calculate  $D'_{n,m}$ .  $D'_{n,m}$  was also required in the calculation of  $v_{n,m+1}$  and so there was a requirement to iterate at each gridpoint for the new position in time. In implementation, the equations converged in two to three iterations and this requirement did not slow the process excessively. This pseudo-damping

force dominated when the rate was highest, which usually occurred as the wire was swinging through equilibrium.

The next task was to examine the restorative force due to the change in angle of attack of the wire in the displaced condition. On the average, as the wire moved above equilibrium, the angle of attack reduced and conversely, on the average, as the wire moved below the equilibrium position, the average angle of attack increased. For this reason, the effect of angle of attack changes during oscillations was, on the average, restorative. There will of course be times when the angle of attack is less when above equilibrium and vice versa. The change in the angle of attack from equilibrium to the displaced position was the key. As in the steady-state model,  $\alpha_n$  was defined as the steady-state angle of attack and  $\alpha_{S_{n,m}}$  was defined as the displaced angle of attack. The finite difference approximation of  $\alpha_n$  is repeated in equation (4.14) but this time the inverted grid coordinate system used in the dynamic model was applicable.  $\alpha_{S_{n,m}}$  was defined in (4.15) and the difference between the two angles was defined as  $\Delta\alpha_{n,m}$  in (4.16).

$$\alpha_n = \arccos \left[ R_n \frac{(\theta_{n-1} - \theta_{n+1})}{2\Delta S} \right] \quad (4.14)$$

$$\alpha_{S_{n,m}} = \arccos \left[ \frac{RS_{n,m}(\theta_{S_{n-1,m}} - \theta_{S_{n+1,m}})}{2\Delta S} \right] \quad (4.15)$$

$$\Delta\alpha_{n,m} = \alpha_n - \alpha_{S_{n,m}} \quad (4.16)$$

Figure 3.14 showed that for typical TACAMO flight conditions, the high verticality wire distribution had an  $\alpha_{n,m}$  that varied from about 30 degrees to 60 degrees for the great majority of the wire length. Knowing the approximate value of the angle of attack, it was possible to compare the relative magnitudes of the  $C_f$  and  $C_D$  drag due to  $\Delta\alpha_{n,m}$ , both of which varied with  $\sin(\Delta\alpha_n)$ . Note that for  $\alpha_n$  on the order of 30 degrees to 60 degrees  $V_{relpern}$  and  $V_\infty$  compared to approximately a factor of two and  $C_D$  and  $C_f$  differed by a factor of 20 to 50. Examining equation (4.17) showed that the effect due to  $C_D$  greatly dominated the effect of  $C_f$  and thus the  $C_f$  effects were neglected. The  $C_D$  drag was already defined perpendicular to the wire. The relative perpendicular velocity,  $V_{relpern}$ , was developed in the steady-state model section as equation (3.29). The change in the relative perpendicular velocity in the displaced geometry,  $\Delta V_{relpern,m}$ , was defined in equation (4.18) and finally,  $D'_{n,m}$  was written as in equation (4.19).

$$\begin{aligned} D'_{n,m} &= \left( \frac{1}{2} \rho_n V_{\infty}^2 D \right) C_D \\ D'_{n,m} &= \left( \frac{1}{2} \rho_n V_{relpern}^2 D \right) C_f \end{aligned} \quad (4.17)$$

( ) terms same order of magnitude  
 $C_D$  and  $C_f$  orders different

$$\Delta V_{relpern,m} = V_{relpern} \sin(\Delta \alpha_{n,m}) \quad (4.18)$$

$$D'_{n,m} = C_D D \frac{1}{2} \rho_n (\Delta V_{relpern,m}) |\Delta V_{relpern,m}| \quad (4.19)$$

The force derived above and presented in equation (4.19) was resolved into components that were applied to the  $X_{n,m}$  and  $Y_{n,m}$  calculations by examining Figure 4.5. The coordinate transformation was written by noting that  $C_D$  drag was already perpendicular to the steady-state wire position and so under the small displacement assumptions, use was made of the steady-state geometry. The transformation equations are provided in equations (4.20) and (4.21). All of the calculations for the pseudo-drag due to angle of attack changes were in terms of time step  $m$  and so this force was calculated explicitly at time  $M+1$  without resorting to an iterative scheme.



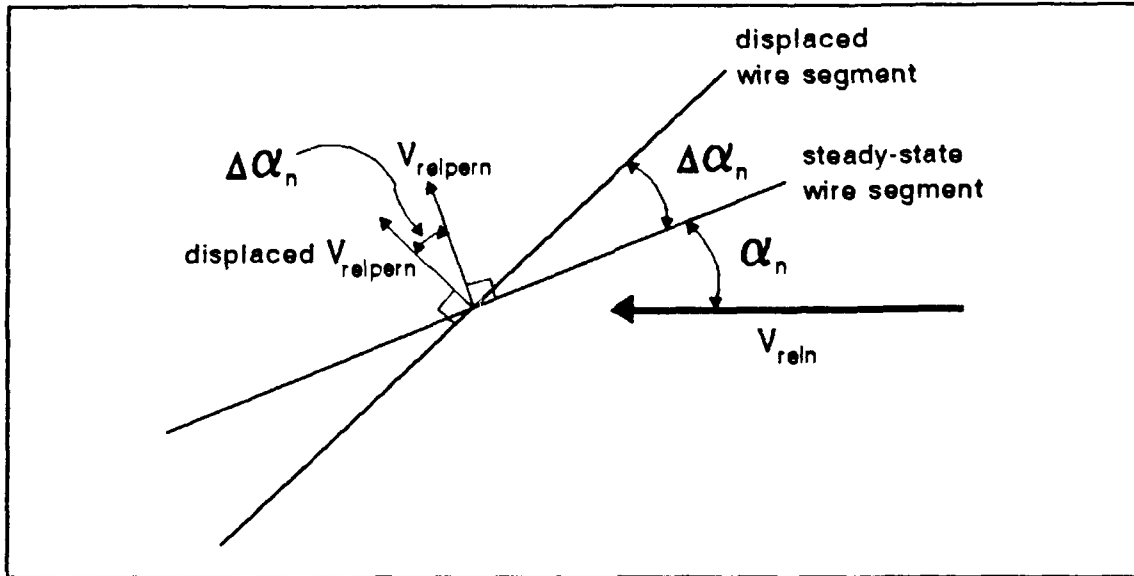


**Figure 4.5:** Dynamic Model Displaced Angle of Attack Geometry

$$D'_{xn,m} = \frac{|X_{n,m}|D'_{n,m}}{\sqrt{X_{n,m}^2 + Y_{n,m}^2}} \quad (4.20)$$

$$D'_{yn,m} = \frac{|Y_{n,m}|D'_{n,m}}{\sqrt{X_{n,m}^2 + Y_{n,m}^2}} \quad (4.21)$$

#### **E. TENSION OSCILLATION**

As mentioned at the beginning of this chapter and shown in Figure 4.1, the tension oscillation was modeled separately from the dangling chain calculations discussed in sections A through D. The dangling chain model assumed a constant tension distribution provided by the steady-state solution. The tension oscillation estimations were not used

in the dangling chain calculations. As will be seen in the following pages, the estimate of the tension oscillation magnitude at the towplane required the axial wavespeed in order to calculate the time required for a tension variation along the wire length to propagate to the towplane attachment point. At the beginning of this chapter, it was assumed that axial waves did not contribute to the wire dynamics and that the tension distribution was constant. Since the axial wavespeed was used only in the off-line tension calculations and not the dangling chain calculation for wire displacement, this assumption was not violated.

In modeling the tension oscillation, four sources were hypothesized. The first source was due to the acceleration of the drogue. A fourth order accurate, five gridpoint scheme was used to calculate the acceleration of the drogue. The drogue acceleration finite difference approximation is provided in equation (4.22) and the contribution of the drogue to the tension variation, defined as  $\Delta T_{n,m}$ , is in equation (4.23).

$$\begin{aligned}
 accel_D^2 = & \left( \frac{-RS_{200,m+2} + 16RS_{200,m+1} - 30RS_{200,m} + 16RS_{200,m-1} - RS_{200,m-2}}{\Delta t^2} \right)^2 + \\
 & \left( \frac{-RS_{200,m+2}\theta S_{200,m+2} + 16RS_{200,m+1}\theta S_{200,m+1} - 30RS_{200,m}\theta S_{200,m}}{\Delta t^2} \right. \\
 & \quad \left. + \frac{16RS_{200,m-1}\theta S_{200,m-1} - RS_{200,m-2}\theta S_{200,m-2}}{\Delta t^2} \right)^2 \\
 & + \left( \frac{-ZS_{200,m+2} + 16ZS_{200,m+1} - 30ZS_{200,m} + 16ZS_{200,m-1} - ZS_{200,m-2}}{\Delta t^2} \right)^2
 \end{aligned}
 \tag{4.22}$$

$$\Delta T_{n,m} = \left( \frac{W_D}{g} \right) accel_D \quad (4.23)$$

The drogue force was applied at the very end of the wire; however, as mentioned above, the tension oscillation at the towplane was the quantity of interest. A finite amount of time was required for the tension oscillation that occurred at a given gridpoint to propagate and take effect at the towplane. This amount of time was calculated knowing the wave speed of the wire medium. The wave speed was defined via the classical axial wave equation, written in (4.24), where  $c_1$  was the wavespeed,  $E$  was Young's modulus and  $\rho$  was the rod density.  $\rho$  was then written in terms of  $\mu$  in (4.25) and the definition of  $c_1$  written in terms of the wire parameters in (4.26).

$$c_1 = \sqrt{\frac{E}{\rho}} \quad (4.24)$$

$$\rho = \frac{\mu}{\pi \left( \frac{D}{2} \right)^2 g} \quad (4.25)$$

$$c_1 = \sqrt{\frac{\pi \left( \frac{D}{2} \right)^2 E g}{\mu}} \quad (4.26)$$

The time required for a tension disturbance at a given gridpoint  $n$  to propagate to the towplane was defined as

$t_{\text{delay}}$  and developed in (4.27). Substituting (4.24) into (4.27) resulted in (4.28). Next,  $\Delta m$ , the time delay in terms of the nearest program time step, was calculated in (4.29). Finally, substituting (4.28) into (4.29) resulted in (4.30).  $\Delta m$  was the value required by the program in that it determined how many time steps in the future a contribution to the tension oscillation at a given gridpoint had to be applied at the towplane. [Ref. 15]

$$t_{\text{delay}} = \frac{n\Delta S}{C_1} \quad (4.27)$$

$$t_{\text{delay}} = \frac{n\Delta S}{\frac{D}{2}} \sqrt{\frac{\mu}{\pi E}} \quad (4.28)$$

$$\Delta m = NINT \left[ \frac{t_{\text{delay}}}{\Delta t} \right] \quad (4.29)$$

$$\Delta m = NINT \left[ \frac{\frac{n\Delta S}{\frac{D}{2}} \sqrt{\frac{\mu}{\pi E g}}}{\Delta t} \right] \quad (4.30)$$

At each wire section, as the wire oscillated and changed shape, the angle with the relative wind changed. Since the  $C_f$  drag was defined in the direction of the relative wind, the oscillations caused a change in the component of  $C_f$  drag

tangential to the wire and thus changed the tension value. This was the second contribution to the tension oscillation. A formulation of this contribution is presented in equation (4.31) where  $\alpha_n$  was as defined in equation (4.14) but  $\Delta\alpha_{n,m}$  was modified slightly from the definition of equation (4.16). The modification was necessary since the  $\Delta T_{n,m}$  contributed from the  $C_f$  was not affected by whether the superimposed angle of attack was positive or negative. The modified relation is presented in equation (4.32).

$$\Delta T_{n,m} = \frac{1}{2} \rho_n (R_n \dot{\theta})^2 D \Delta S C_f \cos(\alpha_n) \Delta \alpha_{n,m} \quad (4.31)$$

$$\Delta \alpha_{n,m} = (\alpha_n - |\alpha_{S_{n,m}}|) \quad (4.32)$$

The third source of the tension oscillation was due to the variation in the orientation of the  $C_D$  drag in the displaced geometry. In all the previous discussions, the  $C_D$  drag was assumed to be perpendicular to the steady-state position of the wire. In the disturbed state, a component of the  $C_D$  drag was, in general, tangential to the steady-state tangent vector. This force variation was accounted for in equation (4.33).

$$\Delta T_{n,m} = \frac{1}{2} \rho_n V_{rel}^2 D \Delta S C_D \sin(\alpha_n - \alpha_{S_{n,m}}) \quad (4.33)$$

The fourth and final contributor to the tension oscillation was due to the variation in the tangential

component of the forcing function as the grid segments changed orientation with the wind during orbit. Since this contribution was related to the tangential wind velocity, which was small compared to the orbit velocity over most of the wire and was defined in terms of the small  $C_f$  aerodynamic force coefficient, this contribution was small and it was reasonable to define its value based completely upon the steady-state geometry. A simple model was constructed by recognizing that, based upon the steady-state geometry, the force oscillation varied sinusoidally at a frequency equal to the orbit rate and that the maximum value was readily defined in terms of the steady-state geometry. A phase adjustment was made to account for the wire position relative to the wind direction at each gridpoint. This procedure was identical to the algorithm used in the forcing function calculation. The relation is provided in equation (4.34). A modified expression was required at the drogue and is provided in equation (4.36) where  $\theta'_n$  was as defined in (4.35).

$$\Delta T_{n,m} = \frac{1}{2} \rho_n V_{wn}^2 D \Delta S \sin(\alpha_n) C_f \sin(\dot{\theta} t - \theta'_n) \quad (4.34)$$

$$\theta'_n = \theta_n - \theta_{wn} \quad (4.35)$$

$$\Delta T_{n,m} = \left( \frac{\frac{1}{2} \rho_n V_{wn}^2 S_D}{\Delta S} \right) C_{DD} \sin(\dot{\theta} t - \theta'_n) \quad (4.36)$$

#### F. VALIDATION, VERIFICATION AND ANALYSIS

A Von Neumann's stability analysis was performed for the dangling chain problem. The homogeneous form of the dangling chain partial differential equation was provided in equation (4.37). For the stability analysis, a constant tension value was assumed and so the equation was rewritten in (4.38). A new variable,  $\lambda$ , was defined as  $\lambda^2 = \Delta t^2 c^2 / \Delta S^2$  and the central difference approximation of (4.38) written as in (4.39).

$$\mu \frac{\partial^2 v(S, t)}{\partial t^2} = \frac{\partial}{\partial S} \left( T(S) \frac{\partial v(S, t)}{\partial S} \right) \quad (4.37)$$

$$\mu \frac{\partial^2 v(S, t)}{\partial t^2} = T \frac{\partial^2 v(S, t)}{\partial S^2} \quad (4.38)$$

$$v^{n+1} - 2v^n + v^{n-1} = \frac{\Delta t^2 c^2}{\Delta S^2} [v_{i+1} - 2v_i + v_{i-1}] \quad (4.39)$$

In keeping with the usual Von Neumann's stability analysis procedure, it was assumed that the error function solved the original partial differential equation and that it took the form of equation (4.40). Substituting (4.40) into (4.39) resulted in (4.41) and simplifying provided

(4.42). Applying Euler's identity to (4.42) and multiplying through by  $e^{a\Delta t}$  and rearranging, resulted in (4.43).

$$e(S, t) = e^{at} e^{i\pi m S} \quad (4.40)$$

$$\frac{e^{i\pi m S} [e^{a(t+\Delta t)} - 2e^{at} + e^{a(t-\Delta t)}]}{\lambda^2 e^{at} [e^{i\pi m(S+\Delta S)} - 2e^{i\pi m S} + e^{i\pi m(S-\Delta S)}]} = \quad (4.41)$$

$$[e^{a\Delta t} - 2 + e^{-a\Delta t}] = [e^{i\pi m \Delta S} - 2 + e^{-i\pi m \Delta S}] \quad (4.42)$$

$$e^{2a\Delta t} - e^{a\Delta t} [2 + c^2(-2 + 2\cos(i\pi m \Delta S))] + 1 = 0 \quad (4.43)$$

Note that in general for (4.43) to be true, the roots of (4.43) had to be complex conjugates. This was required because for roots  $r_1$  and  $r_2$ , the product of  $r_1$  and  $r_2$  equaled 1 which in turn required either  $r_1 = 1/r_2$  or the norm of  $r = 1$  and  $r_1 = r_2^*$  [Ref. 14]. Application of the quadratic formula and the knowledge that the roots were complex led to the conclusion that  $b^2 - 4ac < 1$  and thus (4.44) was written. Rearranging (4.44) and applying the double angle formula resulted in (4.55).

$$-2 \leq 2 + \lambda^2(-2 + 2\cos(i\pi m \Delta S)) \leq 2 \quad (4.44)$$



$$-\frac{2}{\lambda^2} \leq -2 \sin^2 \left( \frac{i\pi m \Delta S}{2} \right) \leq 0 \quad (4.45)$$

Since the center part of the inequality in (4.45) was limited to 0 to -2, the right hand side inequality was discarded and rearranging resulted in (4.46). The worst case occurred when the denominator of the right hand side of equation (4.46) was equal to one. Substituting one into the right hand side of (4.46) and for the definition of  $\lambda$  in the left hand side, produced (4.47), the final result. [Ref. 16: pp. 71-77]

$$\lambda^2 \leq \frac{1}{\sin^2 \left( \frac{\Delta S \pi m}{2} \right)} \quad (4.46)$$

$$\frac{\Delta t^2 T}{\Delta S^2 \mu} \leq 1 \quad (4.47)$$

A 200 segment grid pattern was chosen with a  $\Delta t = 0.1$  second. The most restrictive case was with a wire of the smallest reasonable length and the largest expected tension for this wire length. As shown in (4.48), the criterion was met under these extreme conditions.

$$\frac{(0.1)^2(1000)}{(75)^2 \left( \frac{0.062107}{32.2} \right)} = 0.92 \leq 1 \quad (4.48)$$

Rewriting equation (4.47) by moving  $T$  and  $\mu$  to the right hand side resulted in  $\Delta t^2 \Delta S^2 \leq \mu/T$ . An analysis of this equation provided a physical insight into the stability

criterion. In words, this criterion indicated that as the mass of the wire decreased while the tension increased, the  $\Delta t$  had to decrease in order to retain numerical stability. This made sense when using the analogy of a guitar string. The smaller strings are used to generate higher notes at higher frequencies and as the tension is increased while tuning, the plucked string also renders a higher frequency sound. The discretized model of the string must then sample more often to adequately model the higher frequency.

The dynamic model was implemented in the program TAC29 which is included in Appendix E. As with the static model, TAC29 was written using the parameters applicable to the 3X7 wire and the normal mission drogue. The program requires a number of files which are generated by TAC17. The only operator inputs are the number of time steps required and whether the anti-yoyo subroutines are to be used. The anti-yoyo algorithm will be discussed in Chapter V. As implemented, the program uses the 200 segment spatial grid and the tenth of a second time step size selected above. The program runs at about  $1\frac{1}{2}$  real time on a 486 33 MHZ computer. As explained in the static model section, the program may use either standard atmosphere or externally provided atmospheric data. Wind data is provided by external files. The details of implementation and of the numerical techniques are explained within the program code. Examples of program outputs include  $X_{n,m}$  and  $Y_{n,m}$

displacement snapshots and time plots of verticality, towpoint tension, drogue position and the wire position 45 feet aft of the towpoint.

Validation of the dangling chain portion of the model was performed by comparing the program displacement calculations to the analytical solution of the dangling chain without a concentrated mass on the end of the wire. The homogeneous response of the dangling chain model with the concentrated mass removed and the restorative and dissipative forces deleted was checked when the initial condition was in the shape of an eigenvector. The resulting oscillation repeated the eigenvector shape at the eigenfrequency, thus validating the simulation. The details of the procedure are discussed after the development of the dangling chain problem in Appendix B.

Figure 4.6 shows snapshot plots of one of the orthogonal components of the displacement value for the superimposed problem with the drogue attached and with pseudo-damping. The ten plots are evenly spaced over a single orbit period. The 3X7 wire with a zero sideforce coefficient was used with the standard TACAMO drogue and the towplane at 18,325 feet, 156 KEAS and 34 degrees angle of bank. A moderate apparent forcing wind was used. The plots had, at most, three slope reversals and the changes were fairly gentle noting the relative magnitudes of the two scales.

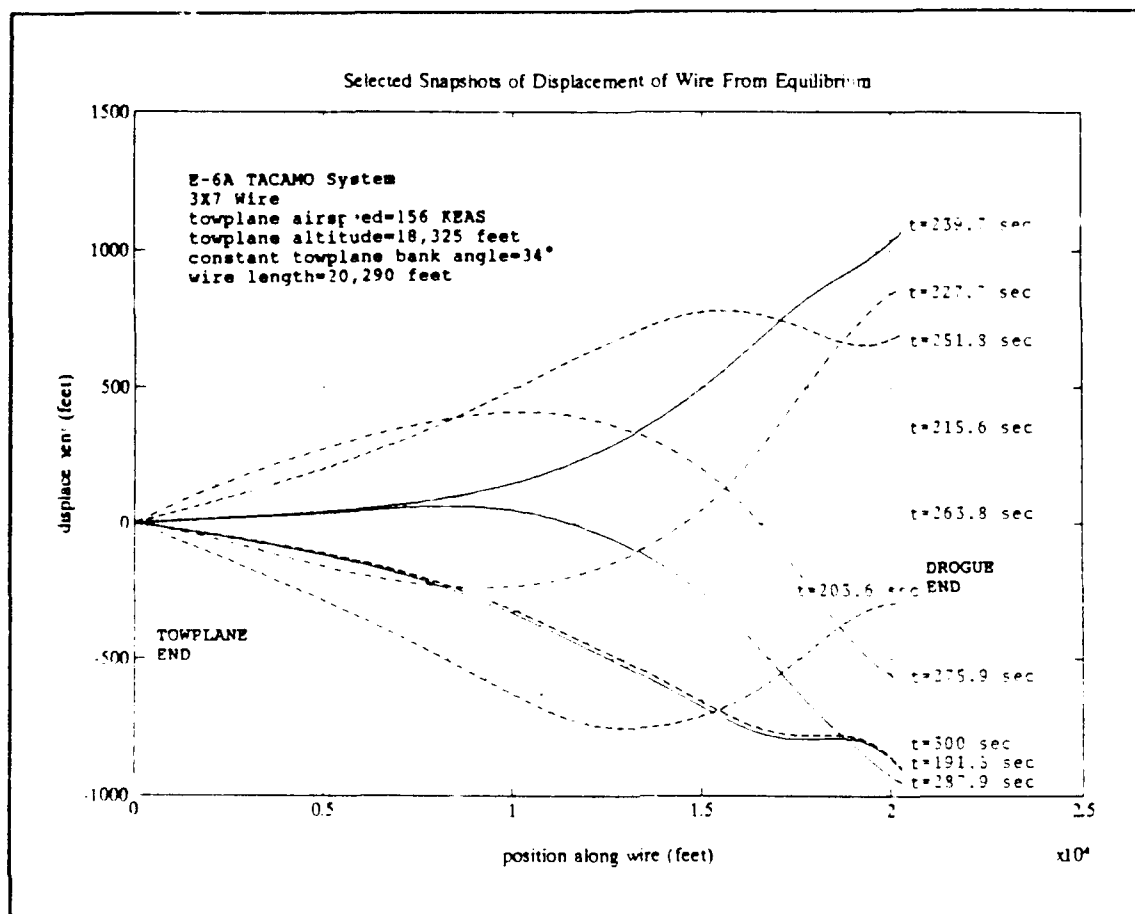


**Figure 4.6:** Selected Snapshots of Displacement of Wire From Equilibrium

As seen in equations (4.1) and (4.6), the first and second partial derivatives used in the dangling chain simulation were approximated using a central differencing technique. Gerald and Wheatley show that for the first derivative approximation, the truncation error was as shown in equation (3.76) and for the second derivative, as shown in equation (4.49). [Ref 11: p. 284] The resulting error for the central difference approximations of the dangling chain derivatives were calculated at each gridpoint for the  $t=263.8$  second curve of Figure 4.6 and then averaged over

each gridpoint. The resulting average truncation errors as a percentage of the calculated derivatives are shown in equation (4.50).

$$f''_o \text{ truncation error} = \frac{\Delta t^2}{12} f''_o + \frac{\Delta t^4}{360} f''_o + \dots \quad (4.49)$$

$$\begin{aligned} \left( \frac{\partial^2 v}{\partial t^2} \right)_n &= 0.001\% \\ \left( \frac{\partial \left( T_n \left( \frac{\partial v}{\partial S} \right)_n \right)}{\partial S} \right)_n &= 0.1\% \end{aligned} \quad (4.50)$$

A check of the choice of both the spatial and the time grid was performed as in Chapter III for the static model. The dynamic model was run using a 0.1 second time step and a 200 point spatial grid and then using a 0.05 second time step and a 400 point spatial grid. The time histories were then compared. As an example, Figure 4.7 is a plot of the verticality time histories for the two runs. The plots overlay, thus validating the choice of spatial and time grids.

As expressed at the beginning of this chapter, mention had to be made of the validity of the use of the steady-state tension distribution vice the fully time dependent tension distribution in the dangling chain displacement calculations. The fully time dependent tension value was defined at each gridpoint as in equation (4.51). Substituting (4.51) for  $T(S)$  in equation (4.1) and expanding

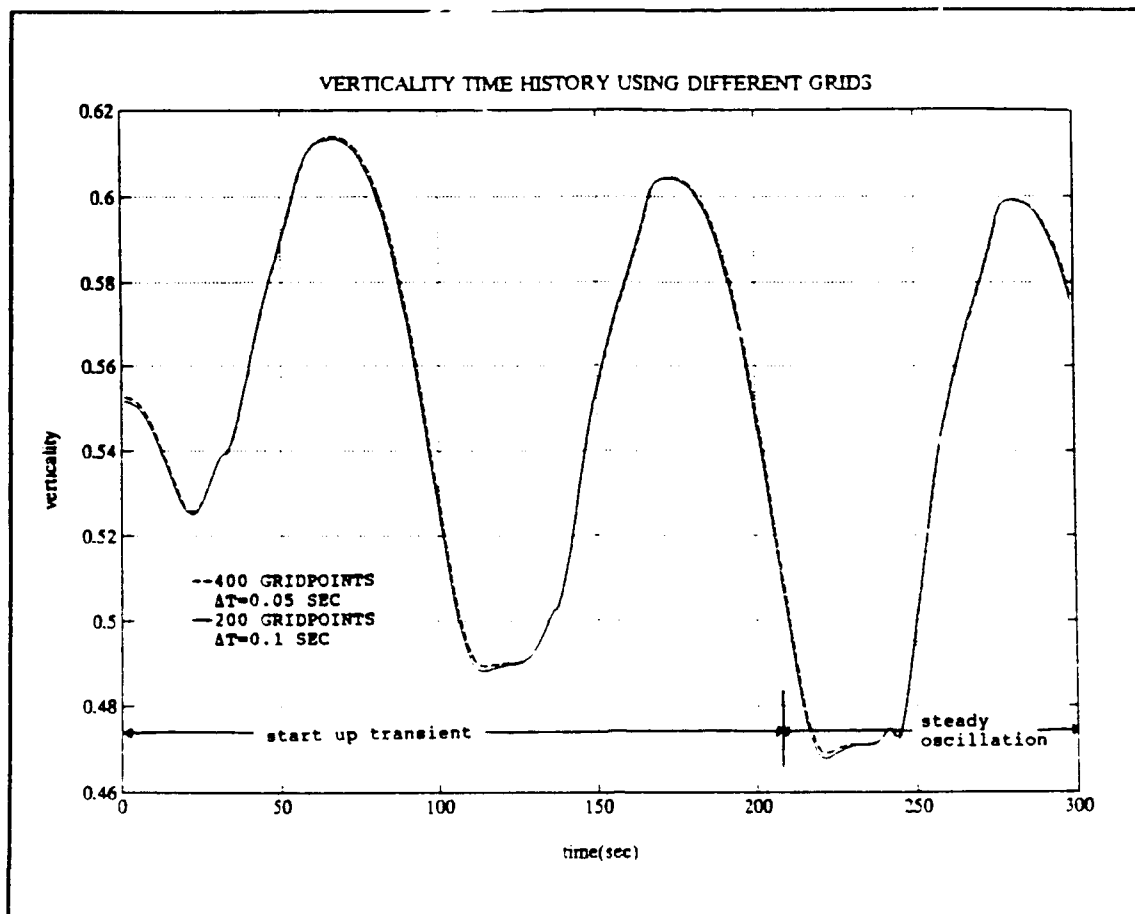


**Figure 4.7: Verticality Time Histories Using Different Grids**

the derivative with respect to  $S$  resulted in equation (4.52). Equation (4.53) is each term of (4.52) written separately with its order of magnitude. The order of magnitude was calculated by averaging the absolute value of each term along the entire wire length at a single point in time for a representative test case. Figure 4.8 is a plot of each term at each gridpoint along the wire at one point in time for the same test case. Terms 3 and 5 are the  $\Delta T$  terms which were truncated when it was decided to use the constant  $T(S)$  distribution vice the fully time dependent  $T(S,t)$  term. As shown in (4.53), these terms were

significantly smaller than the ones which were retained. Terms 3 and 5 were barely distinguishable from the S axis in Figure 4.8. The use of  $T(S)$  vice  $T(S,t)$  greatly simplified the simulation code and based upon the size of the truncated terms, the approximation was warranted.

$$T(S, t) = T(S) + \Delta T(S) \quad (4.51)$$

$$\begin{aligned} \mu \frac{\partial^2 v(S, t)}{\partial t^2} = & (\pi(S) + \Delta \pi(S)) \frac{\partial^2 v(S, t)}{\partial S^2} + \\ & \left( \frac{\partial \pi(S)}{\partial S} + \frac{\partial \Delta \pi(S)}{\partial S} \right) \frac{\partial v(S, t)}{\partial S} + Q(S, t) \end{aligned} \quad (4.52)$$

$$\begin{aligned} \text{Term 1: } & \mu \frac{\partial^2 v(S, t)}{\partial t^2} & \alpha(0.0025) \\ \text{Term 2: } & \pi(S) \frac{\partial^2 v(S, t)}{\partial S^2} & \alpha(0.0055) \\ \text{Term 3: } & \Delta \pi(S) \frac{\partial^2 v(S, t)}{\partial S^2} & \alpha(0.000015) \\ \text{Term 4: } & \frac{\partial}{\partial S} \pi(S) \frac{\partial v(S, t)}{\partial S} & \alpha(0.0021) \\ \text{Term 5: } & \frac{\partial}{\partial S} \Delta \pi(S) \frac{\partial v(S, t)}{\partial S} & \alpha(0.00023) \end{aligned} \quad (4.53)$$

The development of the dynamic model assumed that the towplane flew a constant, circular orbit and thus the effects of towplane pitch, bank and yaw transients were ignored. This assumption was made because on days when the winds were calm at all altitudes along the wire and the crew was flying a normal mission profile, the wire maintained a constant shape without oscillations in verticality or

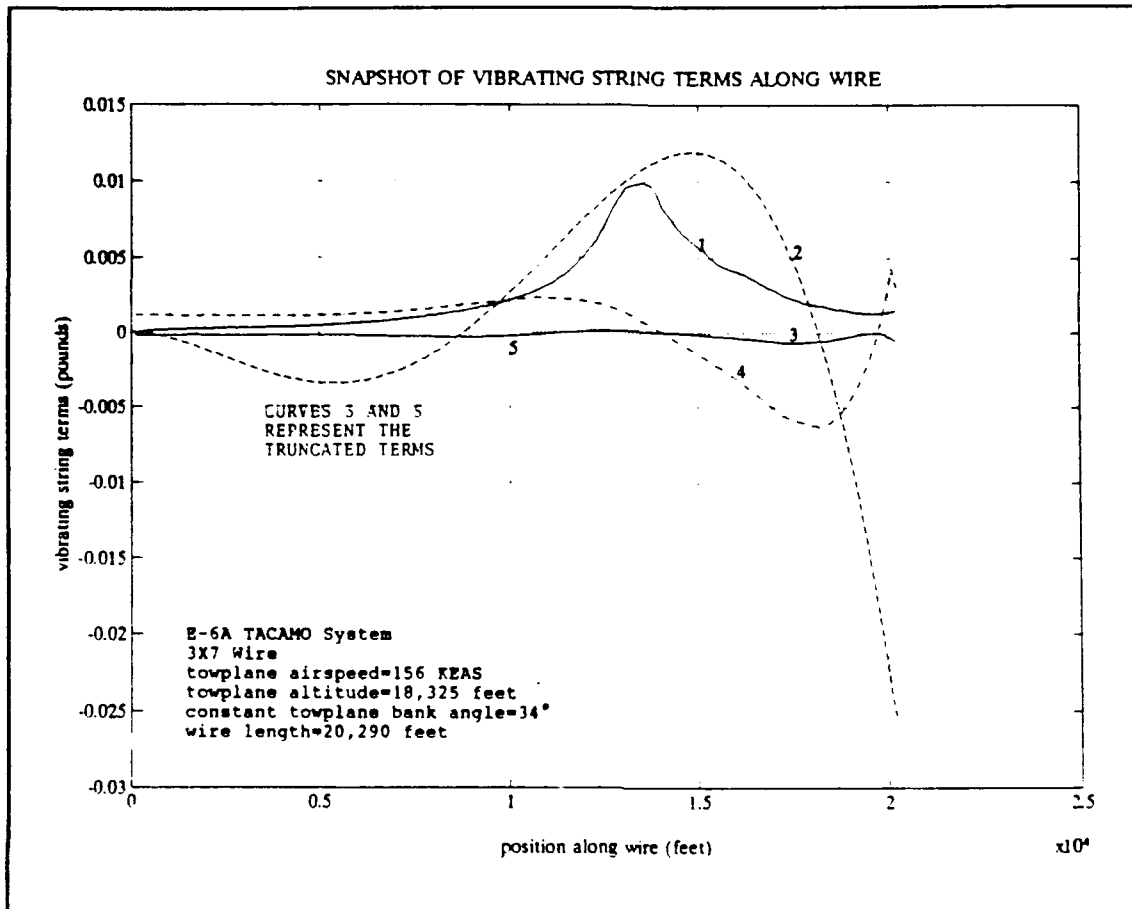


**Figure 4.8:** Snapshot of Vibrating String Terms Along Wire

towpoint tension. Thus, normal aircraft maneuvering transients do not induce significant oscillations in the wire.

The development of the dynamic model also assumed that wire bending, torsion and stretching effects did not contribute to the wire oscillations. Beer and Johnston define the end-of-beam deflection of a cantilevered beam with a distributed load as in equation (4.54) [Ref. 13:p. 598] where, in the case of the wire, the distributed load was the wire weight. The maximum cantilevered wire segment that could support its own weight with at most a 10 percent



deflection was calculated in equation (4.56) to be 3.2 feet by applying equation (4.54) and using the 3X7 wire parameters as listed in (4.55) and assuming a maximum deflection of 10 percent of the wire length. The discretized wire problem used wire segment lengths of approximately one to two orders of magnitude more than this length. Since the wire was unable to support its own weight, it was reasonable to assume that the wire bending forces did not contribute significantly to the oscillations.

$$\delta = \frac{\mu g L^4}{8EI} \quad (4.54)$$

$$\begin{aligned} \mu g &= 0.005176 \frac{\text{lb} \cdot \text{f}}{\text{in}} \\ E &= 12.0 \times 10^6 \frac{\text{lb} \cdot \text{f}}{\text{in}^2} \\ I &= 3.075 \times 10^{-5} \text{ in}^4 \end{aligned} \quad (4.55)$$

$$\begin{aligned} \delta &= 0.1 L \\ L &= \left( \frac{0.8EI}{\mu g} \right)^{\frac{1}{3}} = 3.2 \text{ ft} \end{aligned} \quad (4.56)$$

The axial wavespeed within the 3X7 wire solid mass was calculated as shown in equation (4.57) where  $\rho$ , the wire density, was derived from  $\mu g$  in (4.55). The axial wavespeed was 11,000 ft/sec. for a 20,000 feet wire, tension waves would then propagate the wire length in approximately two seconds. This was approximately two orders of magnitude less than the period of the experimentally determined wire

dynamics. It was thus reasonable to assume that tension waves would dissipate before contributing to the wire oscillations and their effects were neglected. Similarly, for  $G=4.6 \times 10^6 \text{ lb}_f/\text{in}^2$  for the new 3X7 wire, the torsional wavespeed was calculated using equation (4.58) to be 6800 ft/sec. For a 20,000 feet wire, the torsion waves would then propagate the wire length in approximately 3 seconds. Additionally, the drogue on the end of the wire is axisymmetric, allowing torsion disturbances to merely cause a rotation of the drogue on the free end. It was thus assumed that the torsion waves would result in a rotation of the drogue and would dissipate before contributing to the wire dynamics.

$$c_1 = \sqrt{\frac{E}{\rho}} \quad (4.57)$$

$$c_2 = \sqrt{\frac{G}{\rho}} \quad (4.58)$$

The dynamic model was run using a wind profile of zero at the bottom, increasing linearly to a maximum at the towplane, all from a constant bearing. The simulation was run for magnitudes of the wind vector at the towplane from zero to 100 knots. The resulting verticality oscillations reached a steady oscillation magnitude for oscillations less than approximately 20%. For oscillation magnitudes above

20%, the verticality history often diverged in magnitude and the envelope of verticality oscillations diverged away from the steady-state verticality, indicating a break down of the assumptions of the model.

An analysis of the cause of the divergence of the model was begun by non-dimensionalizing the vibrating string governing partial differential equation. Dividing equation (4.1) through by  $\mu$  and then multiplying each term by  $T^2/L$  where  $T$  equaled characteristic time and  $L$  equaled characteristic length resulted in a non-dimensionalized equation. Given an appropriate choice of  $L$ , the "largeness" or "smallness" of displacement was then based upon its fraction of  $L$ . The best choice for  $L$  was the total wire length for two reasons. First, the wire was described by only two dimensions, its length and diameter. The diameter was on the order of 0.1 inch and was obviously not the correct choice to characterize the dynamics of a wire on the order of four miles in length. This left the length of the wire as the choice for characteristic length. The second reason was derived from examination of Figure 4.6 which is a plot of the wire displacements in the  $X_{n,m}$  direction of each point along the wire at ten different points in time. These snapshots of wire displacement showed at most two slope reversals over the entire wire length. The shape of these oscillations were then characterized on a scale approaching the length of the wire. If a second set of waves, of much

smaller scale, were shown in the plots then a smaller characteristic length would have been implied. As discussed above, verticality oscillations above approximately 20% resulted in divergence of the model, which was based upon the assumption that the displacements from the steady-state solution were small. For a 20% verticality oscillation the maximum displacement from the steady-state location was approximately 5% of the characteristic length. Thus, for the scenarios tested, the assumption of small displacements from steady-state breaks down for  $X_{n,m}$  or  $Y_{n,m}$  displacements of greater than 5% of the length of the wire resulting in verticality oscillations of approximately 20%.

The dynamic model was also run using a wind profile of zero along the entire wire length except at the three gridpoints located half-way along the wire. The simulation was run for magnitudes of wind from zero to 200 knots. The verticality oscillation magnitude and the magnitude of the oscillations in the radial position at the drogue after the initial start up transient period had passed were recorded for each simulation. The time history of the drogue radial position was also recorded. Figure (4.9) is a plot of the time history of the radial position of the drogue for wind magnitudes of 10 knots to 180 knots. The model diverged at 200 knots of wind. Note the symmetry of the oscillations about the steady-state drogue position for all but the very large wind inputs. Figure (4.10) is a plot of the

displacement of the mean value of the radial oscillation of the drogue from the steady-state drogue position. The application of superposition required that the mean oscillation value remain close to the steady-state value. Figure (4.10) showed that as the oscillation magnitude approached the region where divergence occurred, the mean radius began to depart from the steady-state value. For verticality oscillations of less than 20%, the mean radius shifted from the steady-state value less than 0.5%. For all conditions tested, the superposition of the dangling chain vibrations upon the steady-state model was valid and resulted in a non-divergent simulation for verticality oscillations of less than 20%.

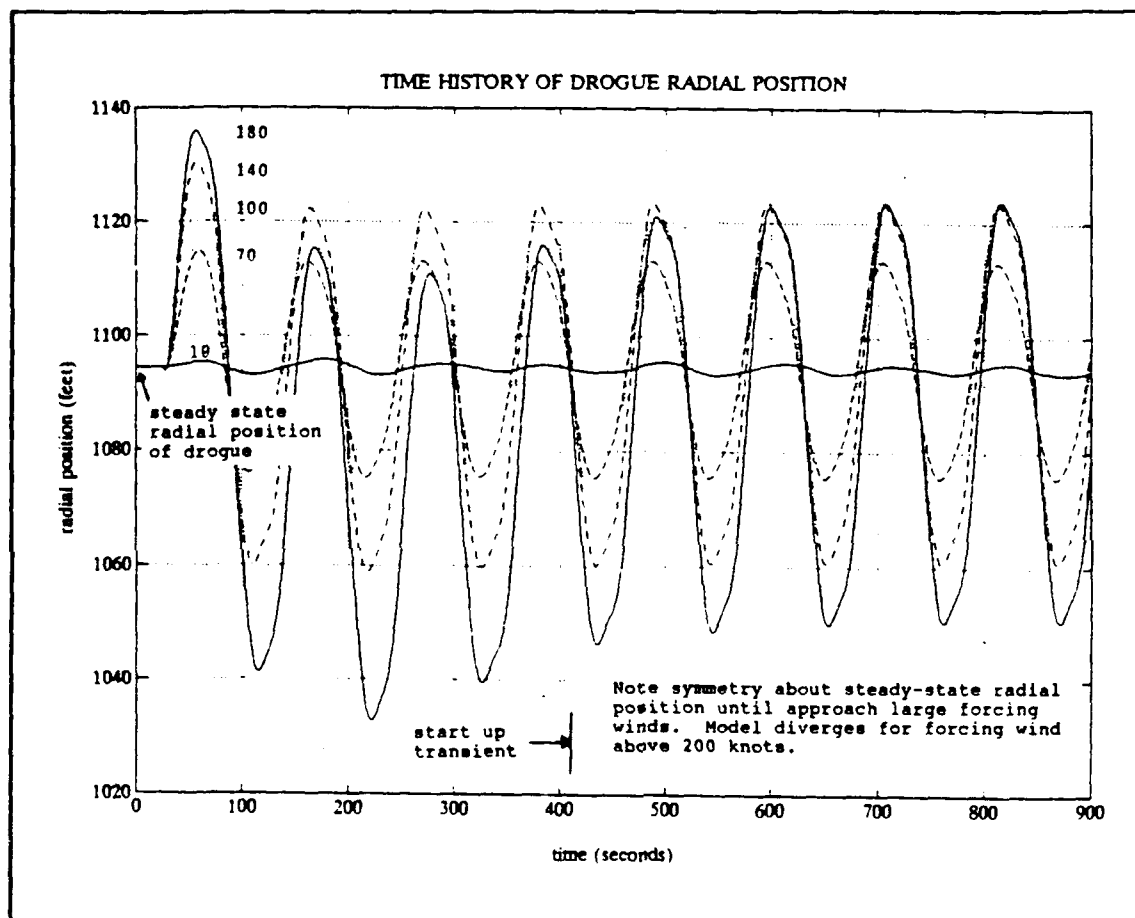


**Figure 4.9:** Time History of Drogue Radial Position for Various Wind Profiles

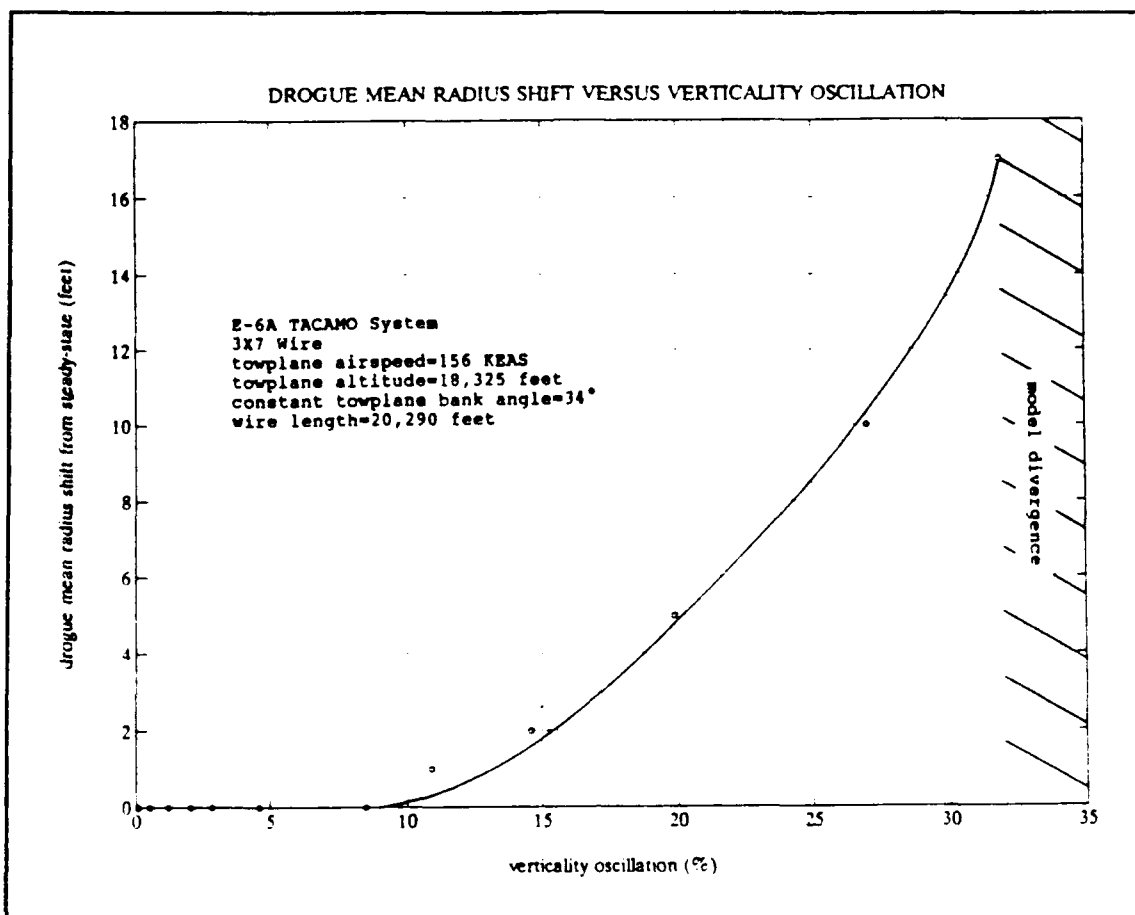


**Figure 4.10:** Drogue Mean Radius Shift Versus Verticality Oscillation Magnitude

As a final check of the fidelity of the static and dynamic models, the simulation output was compared to flight test data taken 1 June 1991 during TACAMO flight number 27-05 under the same flight and atmospheric conditions. In Figure 4.11, the solid line is a plot of the simulated verticality time history and the stars are flight test data taken for a towplane airspeed of 156 KEAS, an altitude of 18,325 feet and a bank angle of 34 degrees. Keeping in mind that the textbook derived aerodynamic coefficients were used, the difference between the modeled and the

experimentally measured verticality was approximately 5%. More importantly for this comparison, the magnitude of the oscillation, frequency and phasing were very close. The spike at the bottom of the simulation plot was caused by the effect of the pseudo-damping due to the change in wire angle of attack. The model shows very good fidelity when compared to TACAMO flight test data despite the use of rough, textbook derived aerodynamic coefficients.



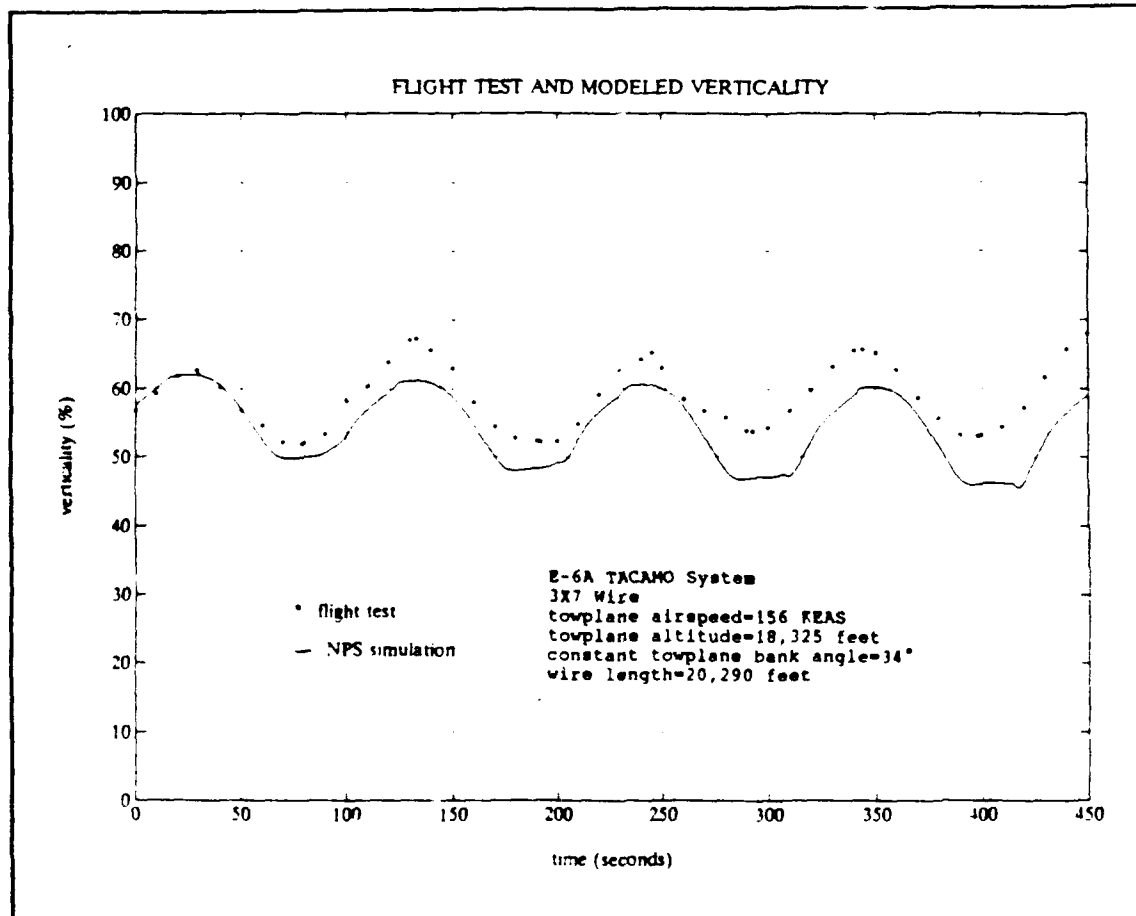


**Figure 4.11:** Comparison of Flight Test and Modeled Verticality Measurements

## V. CONTROL OF WIRE OSCILLATIONS

### A. ANTI-YOYO

Anti-yoyo maneuvers receive their name from their stated goal of eliminating the verticality oscillations using the aircraft as a wire control device. As will be seen later, flight test derived data indicate that changes in the aircraft bank angle can have significant effects upon the wire oscillations. At the slow speed, high angle of bank conditions required for good wire verticality, the TACAMO airplane cannot be safely maneuvered in pitch or yaw. Small inputs in bank angle around the steady-state condition are the only safe inputs at the aircraft. The determination of a satisfactory anti-yoyo bank angle schedule has been limited by the lack of a mathematically founded and rigorous definition of the phenomenon.

The key to understanding the anti-yoyo maneuver was to think of the winds along the length of the wire in terms of a forcing function applied to the dangling chain partial differential equations outlined in Appendix B. In this context, the goal of the anti-yoyo maneuver was stated as the mitigation of the forcing function along the wire. The problem was broken into two parts, first, the definition of the anti-yoyo maneuver once an anti-yoyo drift vector was chosen and second, the choice of the "best" drift vector.

The derivation was most clearly presented by beginning with the definition of the maneuver once a drift vector was chosen.

The anti-yoyo analysis was begun by remembering that the apparent forcing wind was defined in Chapter IV as the sum of the wind vector at the current altitude and the negative of the wind vector at the towplane altitude. Reduction of this apparent forcing wind at various gridpoint altitudes resulted in the component of the apparent forcing wind perpendicular to the wire being reduced and this in turn meant that the aerodynamic force, which was the true forcing function, was also mitigated. The apparent center of orbit was controlled (caused to drift) by modulating the bank angle, which in turn reduced this apparent forcing wind at the desired gridpoints. The bank angle of the towplane was varied around the steady-state value such that the apparent center of orbit of the chosen gridpoint translated exactly at the same rate and in the same direction as the component of the apparent forcing wind vector which was to be eliminated [Ref. 9:p.17-20].

A little thought concerning the effect that the bank angle modulation had to have on the apparent center of orbit led to the conclusion that the desired results could only exactly be derived by sinusoidally varying the bank angle at the orbit rate around the steady-state value. As shown in Figure 5.1, the sinusoidal bank angle modulation was phased

such that the bank angle was a maximum when the towplane was heading in the direction of the component of the apparent forcing wind to be eliminated, a minimum when headed in the opposite direction and equal to the steady-state bank angle when perpendicular to the eliminated wind.

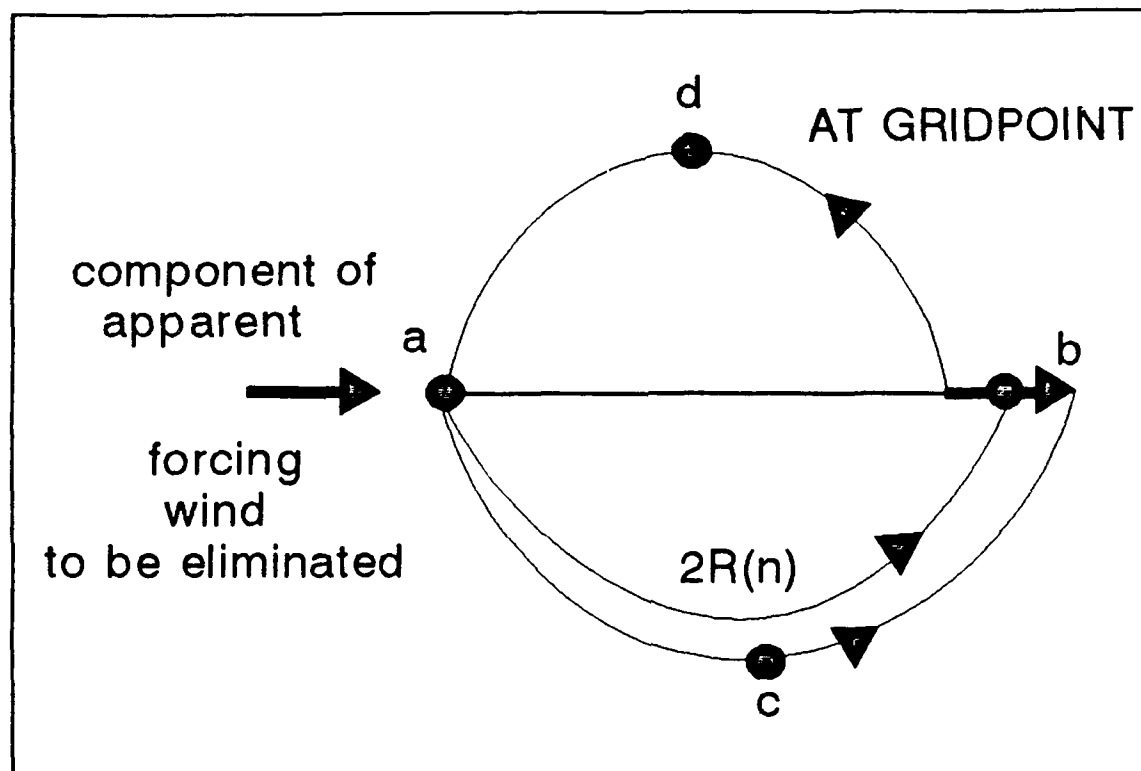


Figure 5.1: Anti-Yoyo Orbit Changes at a Given Gridpoint

The production of the required drift vector actually required the tailoring of the orbit radius of the towplane vice the bank angle. The bank angle modulation scheme was chosen in order to emphasize the effects of the anti-yoyo scheme upon the towplane. The analysis thus assumed that a bank angle input immediately translated into a change in the instantaneous orbit radius. The bank angle modulation of the aircraft required a lateral control input. The aircraft

bank angle response to a roll command was similar to a first order system with an approximate time constant of  $\tau=1$  second. The frequency of the roll input was equal to the orbit rate and was on the order of  $\dot{\theta}=0.05$  radians/second. The phase shift involved in developing a bank angle by lateral control was estimated as  $\Delta_{\text{phase}}=-\tan^{-1}(-\dot{\theta}\tau)=-\tan^{-1}(0.05)$  or  $\Delta_{\text{phase}}=-2.9$  degrees, a value that was small enough to neglect. The effect of modulating the instantaneous center of orbit was thus considered as equivalent to modulation by lateral control command. Three other assumptions were made. First, it was assumed that the required bank angle modulation was small, on the order of one or two degrees. It will be seen later in this chapter that the required bank angle modulation was less than three degrees for a typical scenario. Second, the period of time between when the anti-yoyo maneuver was begun and when the desired drift vector was fully established along the entire wire was ignored. This assumption will be addressed when the experimental flight test data is presented later in this chapter. Finally, the sinusoidally varying towplane radius provided a harmonic input at the top of the wire. It was assumed that this input did not contribute to the wire oscillations. The validity of this last assumption was established in Appendix F.

The key to deriving the maximum bank angle change required to eliminate the desired component of the forcing

function at a given gridpoint was contained in Figure 5.1. The change in the orbit radius between the two sides of the orbit split by the component vector divided by the orbit rate was required to equal the magnitude of the rate of the component of the apparent forcing wind to be eliminated. Figure 5.2 and equation (5.1) reiterated this point.

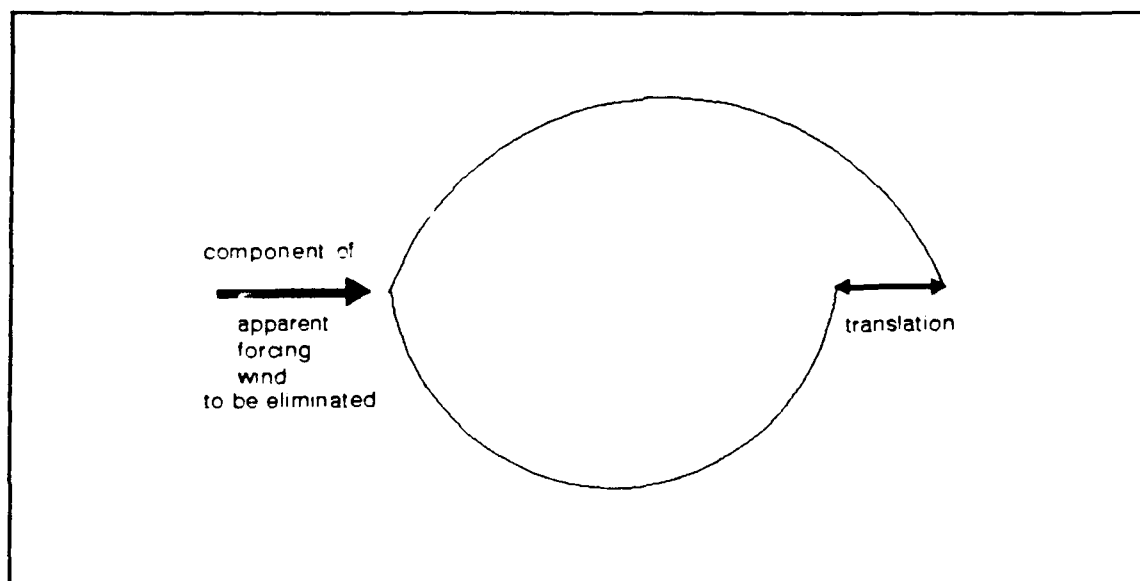


**Figure 5.2:** Translation of the Apparent Center of Orbit of the Towplane

$$\begin{aligned}
 \frac{\text{translation}}{\text{orbit period}} &= \text{speed of center of orbit} \\
 &= \text{magnitude of component of} \\
 &\quad \text{apparent forcing wind} \\
 &\quad \text{vector eliminated}
 \end{aligned}
 \tag{5.1}$$

Equations (5.2) and (5.3) were a repeat of the definition of the true airspeed of the towplane and the orbit rate. Equation (5.4) was an expression for the

instantaneous radius of orbit of the towplane,  $R_{1,m}$ , given the true airspeed and the instantaneous bank angle,  $\phi(t)$ .

$$V_T = \frac{V_{EAS}}{\sqrt{\frac{\rho_{alt}}{\rho_{ssl}}}} \quad (5.2)$$

$$\dot{\theta} = \frac{V_T}{R_1} \quad (5.3)$$

$$R_{1,m} = \frac{V_T^2}{g \sqrt{\left(\frac{1}{\cos(\phi(t))}\right)^2 - 1}} \quad (5.4)$$

Figure 5.3 is a depiction of the model used to develop the integral that defined the diameter of a half orbit transcribed by the towplane flying an anti-yoyo profile with varying bank angle.  $\eta$  was defined as a dummy variable of integration and RAD as the radius of the half orbit. A differential segment of RAD was found as in equation (5.5) and the entire diameter was defined as in equation (5.6).

$$R_{1,m} d\eta \sin \eta = dRAD \quad (5.5)$$

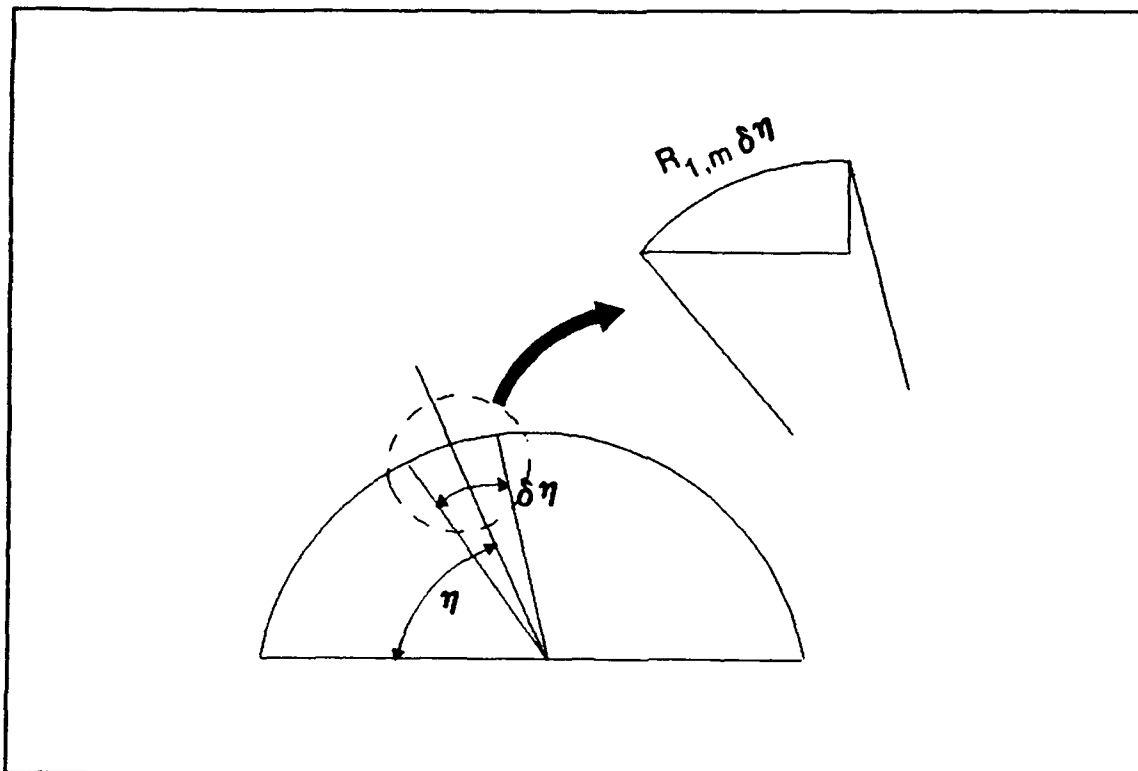


**Figure 5.3:** Calculation of the Radius of a Tailored Half Orbit

$$2 \text{ RAD} = \int_0^{\pi} R_{1,m} \sin \eta d\eta \quad (5.6)$$

Equation (5.8) was written by substituting equation (5.4) into (5.6) and noting the definition of  $\phi$  in equation (5.7) where  $\phi_{\text{nom}}$  was the steady-state or nominal bank angle and  $\phi_{\text{varmax}}$  was the maximum bank angle change (the desired value).

$$\phi = \phi_{\text{nom}} - \phi_{\text{varmax}} \sin \eta \quad (5.7)$$



$$2 \text{ RAD} = \int_0^\pi \frac{V_T^2 \sin \eta}{g \sqrt{\left( \frac{1}{\cos(\phi_{nom} - \phi_{varmax} \sin \eta)} \right)^2 - 1}} d\eta \quad (5.8)$$

The single equation (5.8) was in terms of two unknown variables, RAD and  $\phi_{varmax}$ . One of the variables had to be eliminated. In order to meet the requirement that the translation rate equal the component of the apparent forcing wind to be eliminated, in turn required that the 2 RAD value equal twice the radius of the original, unmodulated orbit plus the translation value for the half orbit over which the integral was performed. It was assumed that the half orbit translation values were equal for both sides of the drift vector. The assumption that the half orbit translation values were equal on both sides of the drift vector was possible because the change in the time required to complete the half orbits on either side of the drift vector, from the constant bank angle orbit, was less than four percent per degree. Thus, for small bank angle modulations, on the order of one or two degrees, the assumption was valid. The resulting formulation is provided in equation (5.9) where  $\theta$  was used due to the assumption of small bank angles made above. Substituting equation (5.9) into equation (5.8) resulted in equation (5.10), which was the desired formulation with a single equation in terms of the single unknown  $\phi_{varmax}$ .

$$2 \text{ RAD} = 2 R_1 + \frac{VWYO}{2} \frac{\pi}{\dot{\theta}} \quad (5.9)$$

$$2 R_1 + \frac{VWYO}{2} \frac{\pi}{\dot{\theta}} = \int_0^\pi \frac{V_T^2 \sin \eta}{g \sqrt{\left( \frac{1}{\cos(\phi_{nom} - \phi_{varmax} \sin \eta)} \right)^2 - 1}} d\eta \quad (5.10)$$

As was apparent in equation (5.10), the desired value,  $\phi_{varmax}$ , was not easily solved explicitly, and so the integral equation was best solved numerically. The integral was solved with the Newton-Cotes method using a polynomial of order two. A 20 point grid was employed over the 0 to  $\pi$  integration interval. An estimate of the error was as given in (5.12) where  $h$  was one half of the integration step interval and  $f^{iv}(\eta)$  was the fourth derivative of the integrand over each interval. For the smoothly varying sinusoidal function within the integral, the method was quite accurate. [Ref. 11:pp. 286-287] for a typical scenario, the maximum error was less than  $10^{-6}\%$ .

$$\begin{aligned}
& \text{residue} = -2 R_1 - \frac{VWYO \pi}{2\theta} \\
& + \sum_{n=1}^{20} \left[ \frac{V_T^2 \sin\left(\frac{(n-1)\pi}{20}\right)}{g \sqrt{\left( \frac{1}{\cos\left(\phi_{nom} - \phi_{varmax} \sin\left(\frac{(n-1)\pi}{20}\right)}\right)}^2 - 1}} \right. \\
& \quad + \frac{4V_T^2 \sin\left(\frac{(2n-1)\pi}{40}\right)}{g \sqrt{\left( \frac{1}{\cos\left(\phi_{nom} - \phi_{varmax} \sin\left(\frac{(2n-1)\pi}{40}\right)}\right)}^2 - 1}} \\
& \quad \left. + \frac{V_T^2 \sin\left(\frac{n\pi}{20}\right)}{g \sqrt{\left( \frac{1}{\cos\left(\phi_{nom} - \phi_{varmax} \sin\left(\frac{n\pi}{20}\right)}\right)}^2 - 1}} \right] \frac{\pi}{120}
\end{aligned} \tag{5.11}$$

$$\text{Error} = -\frac{1}{90} h^5 f^{iv}(\eta) \tag{5.12}$$

The code used in the  $\phi_{varmax}$  calculation was checked for programming errors by comparing the program output with a solution to the same integral equation calculated off-line from the simulation using the resident program in the HP-48SX hand held computer.

The effect of the anti-yoyo maneuver upon the model was included into the simulation by adding the negative of the canceled component of the apparent forcing wind to all the forcing wind vectors. The rest of the simulation was thus unaffected. The required  $\phi_{varmax}$  and phasing requirements were then calculated off-line. This was very efficient computationally. This technique ignored the variation in

orbit radius and orbit rate caused by the bank angle modulation. As was mentioned earlier, it was shown in Appendix F that the effects of the radius and orbit rate changes at the towplane caused by the bank angle modulations, could be neglected.

The simulation began with the towplane on a heading of 000 and so for a left hand orbit the required anti-yoyo angle of bank variation was as in equation (5.13) where DWYO was the direction from which the component of the apparent forcing wind to be canceled pointed and  $\phi_{var m}$  was the time dependent angle of bank variation at time step m. Note that the technique of adding the negative of the drift vector to be canceled highlighted the fact that the anti-yoyo maneuver was only effective at canceling a single vector. This vector could have been the apparent forcing wind at one of the gridpoints or some other selected vector.

$$\phi_{var m} = \phi_{var max} \cos(\dot{\theta} \Delta T m - (2\pi - DWYO)) \quad (5.13)$$

The phasing of the angle of bank variation was checked using a simple wind and anti-yoyo drift vector combination for which the correct phasing was easily determined. The tested wind profile was a constant 30 knot wind from 270 degrees at all altitudes of 15,000 feet and above and a zero velocity wind for all altitudes below. The apparent forcing wind was thus zero for all altitudes above 15,000 feet since this section of the wire and the aircraft were drifting

along this vector and the rest of the wire, below 15,000 feet was subjected to an apparent forcing wind which was the reciprocal of the wind vector. This apparent forcing wind vector was chosen for elimination and was the anti-yoyo drift vector. As mentioned earlier, the towplane heading was 000 at time zero and thus at  $\frac{1}{4}$  of the orbit period the towplane flight path vector and the desired anti-yoyo drift vector were collinear and thus the angle of bank variation should have been a minimum. This was exactly as developed by the model and thus the anti-yoyo phasing was validated by this test case. One note on semantics is in order. As defined here, the angle of bank variation was positive for an increasing angle of bank and negative for a decreasing angle of bank. This convention was irrespective of the direction of turn and thus for a left turn with a negative angle of bank, a positive angle of bank variation required increasing the angle of bank to a more negative value.

There now existed a numerical method for defining and describing the effects of an anti-yoyo maneuver optimized around a single chosen drift vector. The second and final task was to determine the appropriate scheme for finding the drift vector around which to implement the resulting maneuver. One logical choice was to select the total apparent forcing wind vector at one of the gridpoints along the length of the wire. Again, since only a single vector could be canceled, this in general resulted in the complete

elimination of the apparent forcing wind at a single gridpoint and of some portion of the apparent forcing wind at other gridpoints. Additionally, for extreme wind shear situations, it was entirely possible that the forcing function would be increased at some gridpoints. For this reason, the choice of the correct gridpoint and thus the drift vector, was crucial. Results varied widely based upon this choice.

The choice of a drift vector was analyzed using several wind profiles typical of the normal TACAMO operating areas. The first profile was a linearly increasing wind starting at 15 knots at the surface and increasing at 2.5 knots per thousand feet of altitude and coming from a 270 degree bearing. The second profile was also a linearly increasing wind with the same magnitude at each altitude but rotating from a heading of 225 degrees at the surface at 5 degrees per thousand feet. [Ref. 17] The third profile consisted of the winds present during the flight test cited in Chapter III and were similar to profile two with some irregularities expected of real wind profiles. Two other, less likely wind profiles were examined. The fourth profile consisted of a 30 knot wind from a heading of 270 degrees at altitudes above 15,000 feet and zero elsewhere. The fifth and final profile included a 40 knot wind layer from 270 degrees at altitudes of 11,000 to 14,000 feet and zero at all other altitudes.

The winds were defined at 1000 foot intervals and the steady-state model was used to determine which gridpoints were affected by which wind vector. As a typical flight scenario, a towplane airspeed of 156 KEAS, an altitude of 18,325 feet and a bank angle of 34 degrees were chosen. A wire length of 20,290 feet and the textbook derived aerodynamic coefficients were used. The sideforce coefficient was set to zero. Figure 5.4 is a plot of the wind direction for all five profiles and Figure 5.5 is a plot of the windspeed at each gridpoint for profiles one through three.

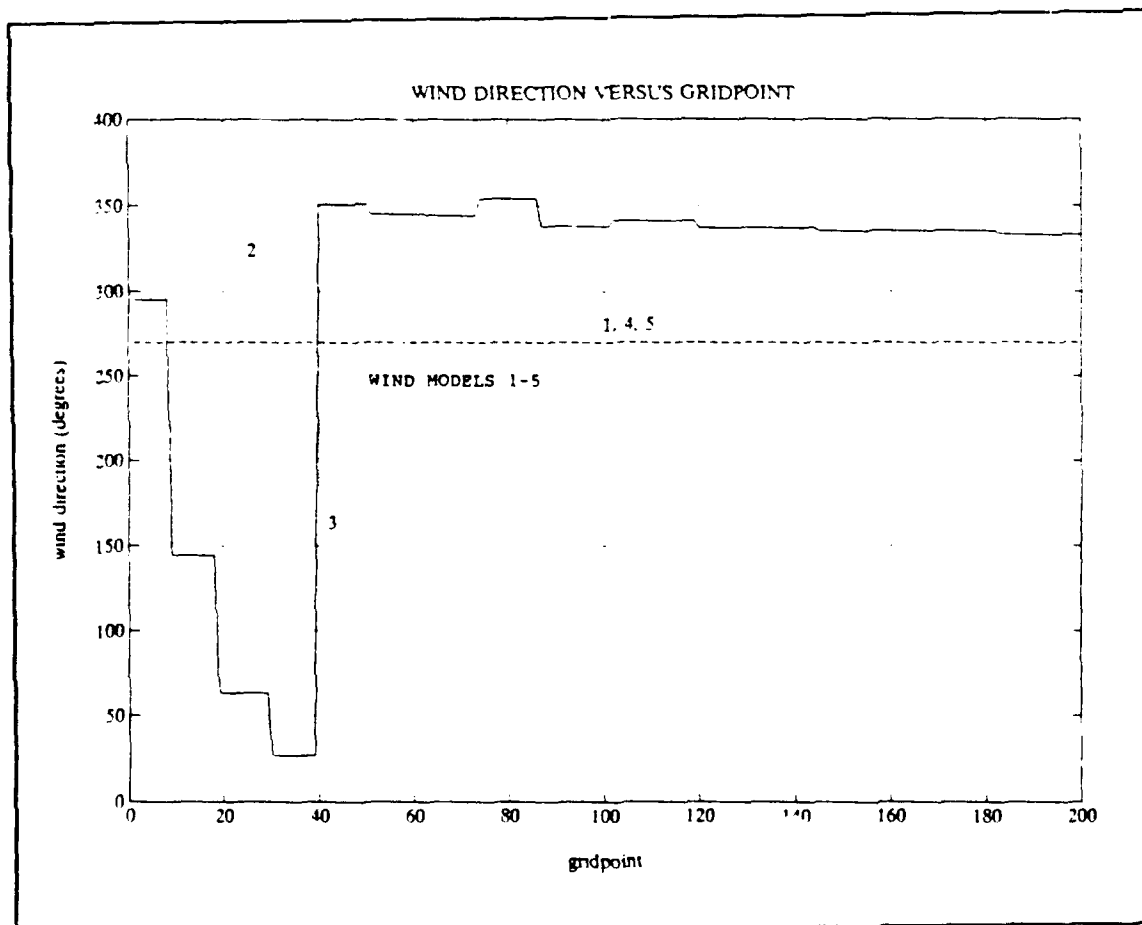
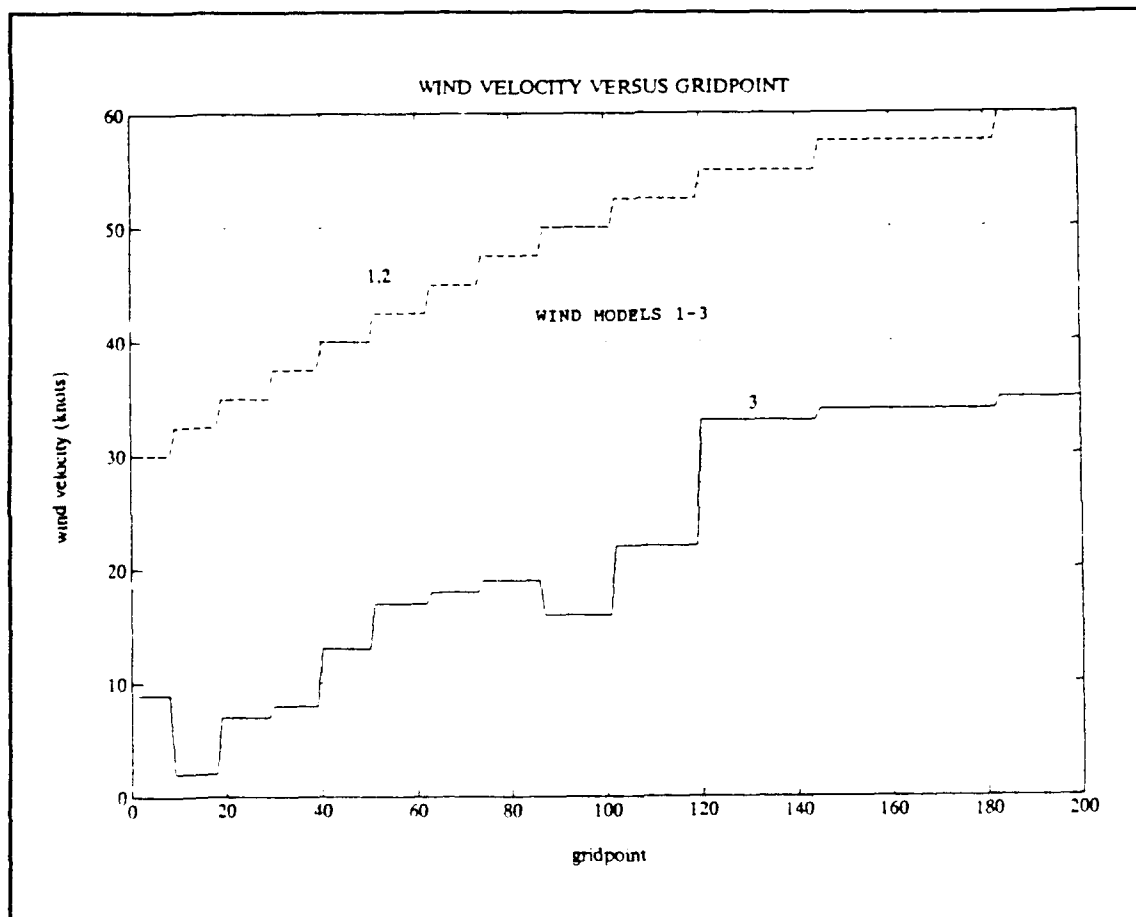


Figure 5.4: Wind Direction Versus Gridpoint



**Figure 5.5:** Wind Velocity Versus Gridpoint



Figure 5.6 is a plot of the verticality oscillation magnitude that resulted when each of the apparent forcing wind vectors that correspond to one or more gridpoints on the wire were selected for wind profiles one through three. Each wind vector, which applied to a thousand feet layer of altitude, affected a number of gridpoints and so thirteen steps are shown, corresponding to the 12,030 feet between the drogue and the towplane.

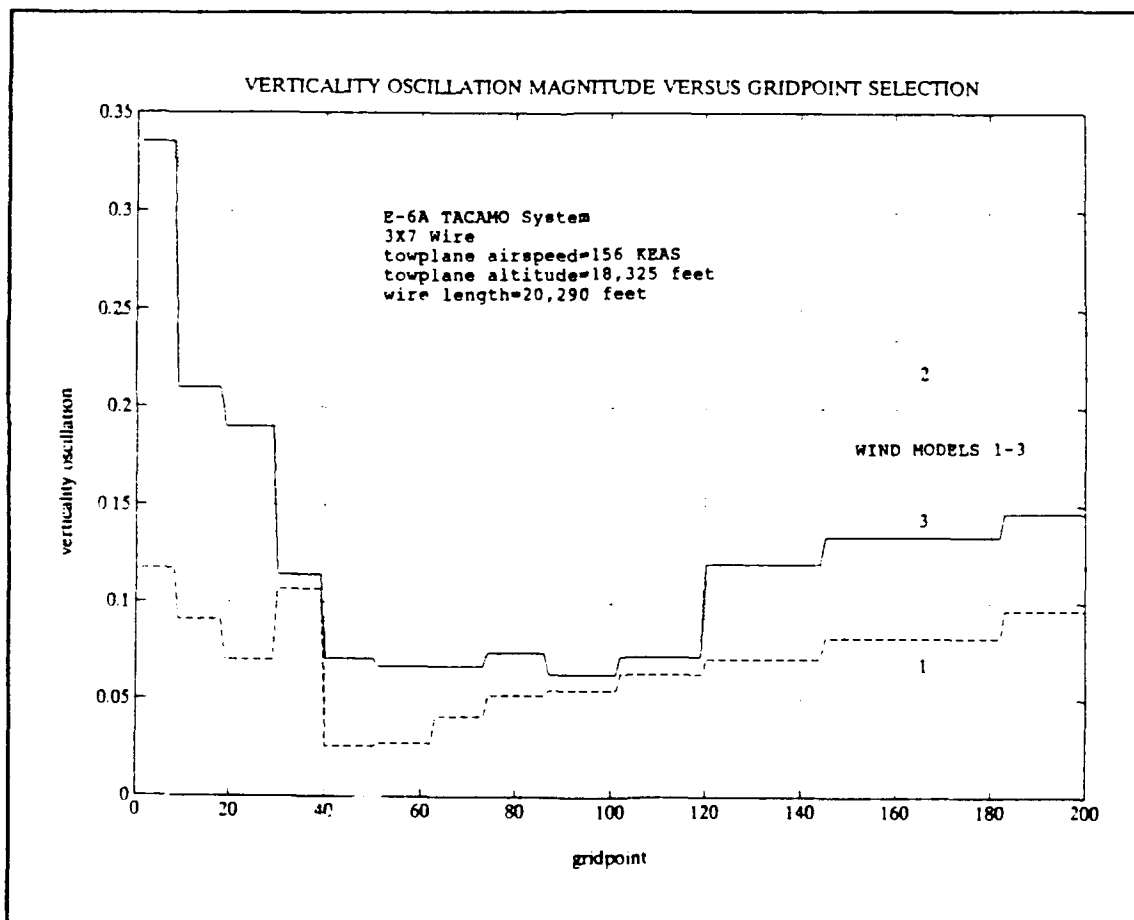


**Figure 5.6:** Verticality Oscillation Magnitude Versus Gridpoint Selection

A second technique for choosing the component of the apparent forcing wind to be canceled was proposed and was

proven to be quite successful. In this technique, the apparent forcing winds at all of the gridpoints were averaged and this average value was used as the anti-yoyo drift vector. This rule was proven to provide approximately a 50% or better reduction of the oscillations in all but one of the tested scenarios.

Table 5.1 contains the uncontrolled verticality oscillation magnitude for each of the wind profiles described above, the smallest oscillation value obtained by checking all of the apparent forcing winds as anti-yoyo drift vectors and finally, the verticality oscillation magnitude that resulted during the use of the average apparent forcing wind as the anti-yoyo drift vector. Note the consistent results of the averaging rule for all but profile four.

TABLE 5.1: VERTICALITY OSCILLATIONS FOR VARIOUS ANTI-YOYO LAWS

Wind Profile	Uncontrolled (%)	Gridpoint Selection (%)	Averaged Apparent Forcing Wind (%)
I	10.6	2.6	5.3
II	31.5	7.2	7.2
III	18.0	6.3	6.7
IV	18.0	10.9	9.2
V	13.5	13.4	10.8

Wind profiles four and five were chosen as remote but possible examples of extreme shearing conditions. Profile

four might be encountered if the pilot of the towplane opted to fly in a jet stream while the wire was trailed into still air. The averaging scheme worked quite well in this scenario. Profile five is highly improbable, requiring an extremely large shear over a small altitude band. This scenario was included as the one wind profile tested during which the averaging scheme and in fact the anti-yoyo process in general had limited effect. The averaging scheme and the anti-yoyo maneuver still helped but not to the extremes of the other wind profiles. The reason for this phenomenon was that the large shear and subsequent shear reversal caused significant forces to be applied over a small part of the wire. Attempting to reverse the effect by using part of the apparent forcing wind vector in this layer resulted in a new apparent forcing wind being induced over the remainder of the wire. The balance of the wire, which previously had no apparent forcing wind, was much longer than the part within the layer and so even small anti-yoyo inputs eliminated any gain in the reduction of the apparent forcing wind within the shear altitude band. The averaging scheme reduced the oscillation by around 25% in the case of wind scenario five but this was not as dramatic as the 50% or better reductions when considering wind profiles one through four; however, this scenario was presented as an extreme case and will be a rarity in flight.

Implementation of the averaging anti-yoyo scheme requires use of the static model to determine the static altitude of each gridpoint and the measurement of the wind vector at each altitude. The apparent forcing winds are then averaged and the  $\phi_{varmax}$  and phasing calculations performed. The result is a schedule of angle of bank variations versus heading which may be implemented using an autopilot.

The utility of the anti-yoyo scheme for verticality oscillation reductions was validated by flight test data. Flight test experiments were made using various combinations of anti-yoyo maneuver angle of bank magnitudes and phasing. During these tests, one was performed which correlated closely to the anti-yoyo maneuver called for by the averaging scheme. In both cases the angle of bank variation led the verticality oscillation by around 10 seconds. That is, when the verticality was around a maximum, the angle of bank became more negative, reaching its peak about 10 seconds before the verticality oscillation. The averaging scheme called for an angle of bank variation maximum of 1.5 degrees. The flight test was flown by hand and the maximum bank angle changes exceeded this amount at times by 1 degree or 2 degrees, however, the excursions were in both directions around the perfect sinusoid inputs and so the effect over an entire orbit period was to make the drift vector close to the vector called for by the anti-yoyo

program. Examination of the beacon derived space positioning data showed that the drift vector of the towplane remained about in the same direction of approximately 150 degrees but was reduced in magnitude to around 15 feet/second. This corresponded to a drift vector of 150 degrees at 15 feet/second. The averaging scheme called for a drift vector of 141 degrees at 22 feet/second and so the two schemes were approximately the same. Furthermore, despite the rough approximation of the sinusoidal angle of bank inputs, the space positioning data showed a smooth track over the ground which indicated that the angle of bank excursions averaged out to generate the desired ground track. The ground track, after all, was the desired quantity since it was the motion over the ground which generated the desired drift vector. Figure 5.7 is a comparison of the modeled verticality oscillation and the flight test experimental measurements. The test was performed for the TACAMO system with the 3X7 wire and the standard drogue with the towplane at an altitude of 18,325 feet, an airspeed of 156 KEAS and with an average bank angle of 34 degrees. The anti-yoyo maneuver was begun at time 450 seconds. The textbook derived wire aerodynamic coefficients listed in equation (3.75) were used. The modeled verticality oscillations compared to within approximately 5% with the experimental data.

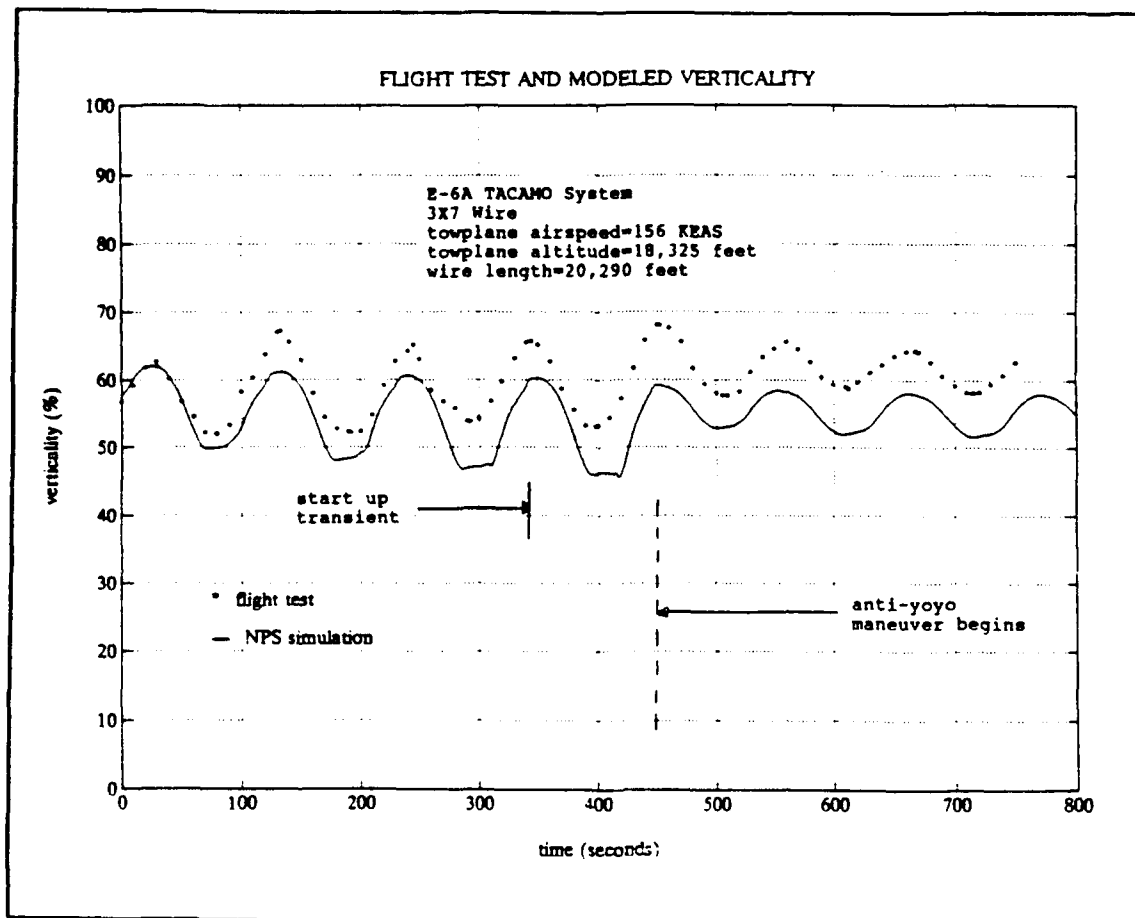


**Figure 5.7:** Flight Test and NPS Modeled Verticality Oscillations With and Without Anti-yoyo

The TACAMO NATOPS manual [Ref. 18:p. III-7-59] describes a version of the anti-yoyo maneuver. This maneuver has had limited success in verticality oscillation reduction and in fact has often increased the oscillation magnitude. Since this version of the maneuver is flown by hand, it is not flown as a sinusoidal bank variation but in four sections where the maximum variation is used in the 90 degree quadrant centered on the tension oscillation peak, the minimum, 180 degrees later and the nominal, steady-state bank angle, in the other two quadrants. The magnitude is

determined by using 1 degree for each 100 pounds of tension oscillation up to a maximum of 6 degrees. Lawton documented significant errors in the tension measurement system ranging from 3% to 40% as well as "flat spots" in the oscillation measurement which call into question the phase of the measured tension oscillations [Ref. 9:pp. 23-24, E1-E7]. Comparison of the dynamic model tension oscillations with the experimental flight test data exhibits differences in magnitude and phase on the order of the measurement errors documented by Lawton. The previous discussion highlighted that the magnitude as well as the phase of the anti-yoyo maneuver are critical to success. With too small of a magnitude of the bank angle variation, the full benefit of the maneuver is not achieved, but more importantly, as the magnitude is increased beyond the optimum value, a forcing function is induced by the resulting motion of the airplane that is in the opposite direction to the forcing function that the anti-yoyo maneuver was meant to cancel. Typical anti-yoyo maneuvers require from a fraction to several degrees of bank angle variation and so an error in the tension value of as little as 100 pounds can have a significant impact upon the success of the anti-yoyo maneuver. The published procedure has been limited by this dependence upon the unreliable tension measurement.

Application of the averaging anti-yoyo maneuver to wind profiles one through five indicated that the phase

relationship between the tension and the anti-yoyo bank change is often inconsistent with the NATOPS rule. No consistent correlation was noted in the phasing between the tension and the required bank angle modulation. This inconsistent phase requirement explains the concurrently inconsistent results of the anti-yoyo rule locked in phase to the tension oscillation. As an example, Figure 5.8 is the time history of the tension for wind profile two. Figure 5.9 is the time history of the angle of bank variation. Note that they are approximately 90 degrees out of phase.



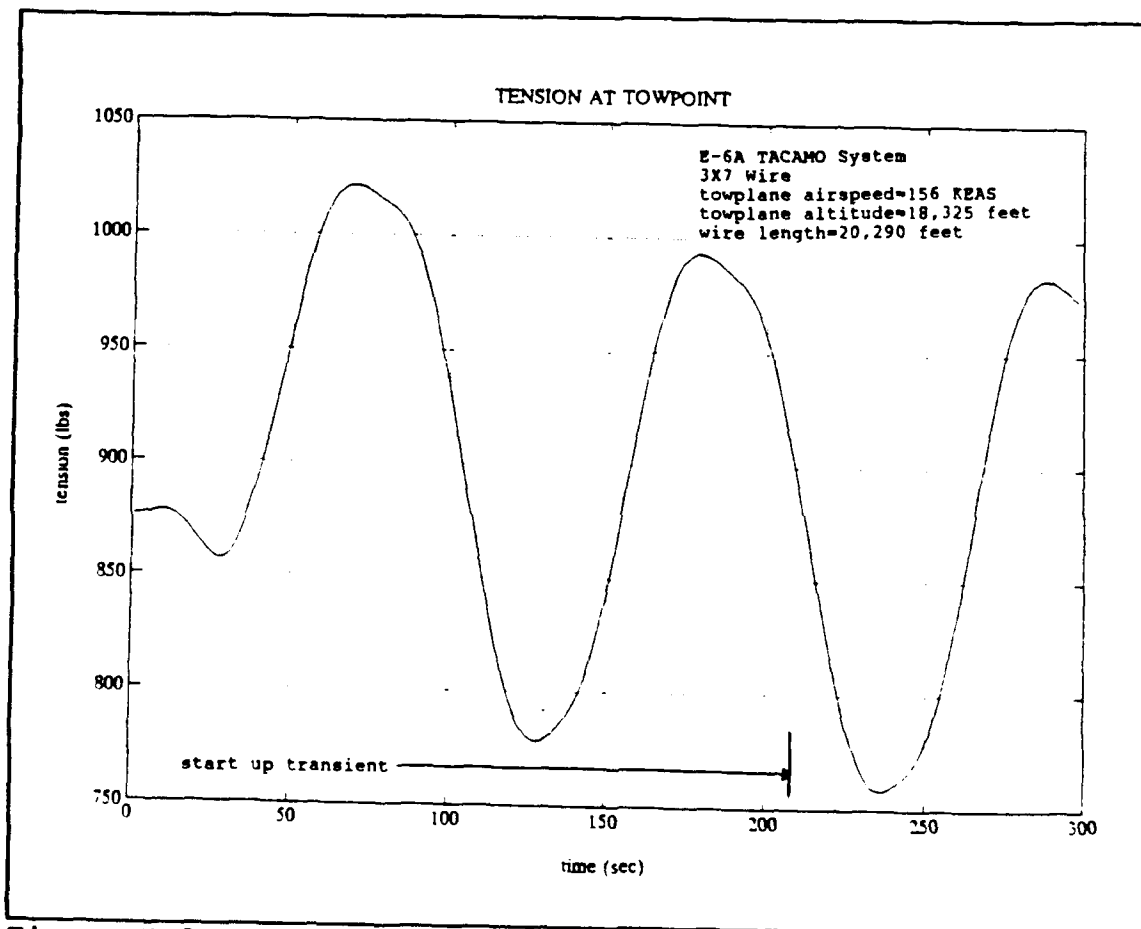
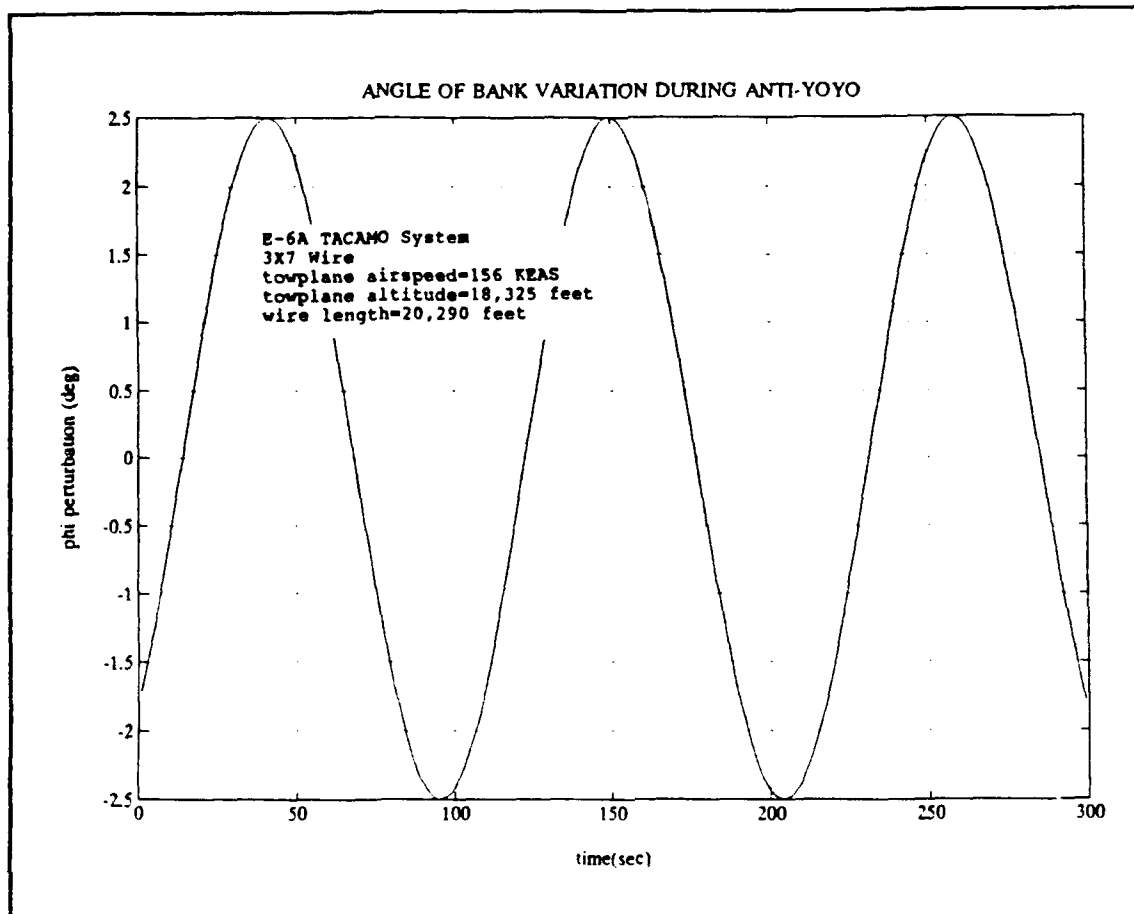


Figure 5.8: Time History of Tension at Towpoint



**Figure 5.9:** Time History of Angle of Bank Variation During Anti-yoyo

## **B. FLYING DROGUE**

The anti-yoyo scheme used the towplane at the top of the wire to control much of the wire oscillations. An alternate approach for controlling the verticality oscillations that was considered involved the use of a flying drogue at the lower end of the towed cable. The development of the flying drogue closely paralleled the previous model development in that a separate steady-state and dynamic model was

constructed. Two static and three dynamic control schemes were implemented and evaluated.

The static model had to be developed first. The first static model of the flying drogue was the most general. This model allowed the operator to select a steady-state bank angle and angle of attack within the aerodynamic limits of the flying drogue. The second model took a more narrow approach, implementing a possible candidate for the "best" choice of drogue bank angle and angle of attack. The development of both approaches shared many common calculations and so the two models were derived in parallel.

To start, it was assumed that the flying drogue was attached such that there was no moment at the wire attachment point. That is, the drogue was stable with or without the tow. It was desired to develop the equations to get  $T_1$ ,  $R_2$ ,  $\theta_2$ ,  $Z_2$  and  $T_2$  given the position at gridpoint 1. As was done in the static and dynamic modeling, it was assumed that the aerodynamic and inertial forces upon the first segment of the wire were small relative to the drogue forces. Applying this assumption, it was immediately written that  $T_1 = T_2$ . The angle of bank of the drogue was defined as  $\phi_D$  and use was made of the definitions of the drogue related variables provided during the steady-state drogue model development in Chapter III. Next, in accordance with the definition of the steady-state condition, the drogue drag vector was always aligned along

the  $\bar{e}_\theta$  coordinate direction, the lift vector and weight vector were always aligned along the  $\bar{e}_R$  coordinate direction and the drogue inertial vector was always aligned along the  $\bar{e}_R$  coordinate direction. The drag vector and the drag magnitude are presented in equations (5.14) and (5.15), the lift vector in equation (5.16), the lift vector magnitude in equation (5.17), the inertial vector in (5.18) and the weight vector in (5.19). Finally, a total resultant force vector upon the drogue is presented in equation (5.20). Note that the only unknowns in these equations were  $C_{DD}$ ,  $C_{LD}$  and  $\phi_D$ .  $C_{LD}$  and  $\phi_D$  remained as operator inputs in the most general static flying drogue case and  $C_{DD}$  will be derived from  $C_{LD}$ .

$$\bar{D}_D = C_{DD} \rho S_D \bar{e}_\theta \quad (5.14)$$

$$D_D = C_{DD} \rho S_D \quad (5.15)$$

$$\bar{L}_D = -L_D \sin \phi_D \bar{e}_R - L_D \cos \phi_D \bar{e}_K \quad (5.16)$$

$$L_D = C_{LD} \rho S_D \quad (5.17)$$

$$\bar{F}_{ID} = \frac{W_D}{g} \dot{\theta} R_1 \bar{e}_K \quad (5.18)$$

$$\overline{W}_D = -W_D \overline{e}_R \quad (5.19)$$

$$\overline{F}_{resultant} = \left( -L_D \sin \phi_D + \frac{W_D}{g} \dot{\theta}^2 R_1 \right) \overline{e}_R - D_D \overline{e}_\theta - (W_D + L_D \cos \phi_D) \overline{e}_K \quad (5.20)$$

It was apparent upon examining Figure 5.10 that the tension at gridpoint one was equal and opposite to the resultant force vector upon the drogue. Equation (5.21) was thus written.

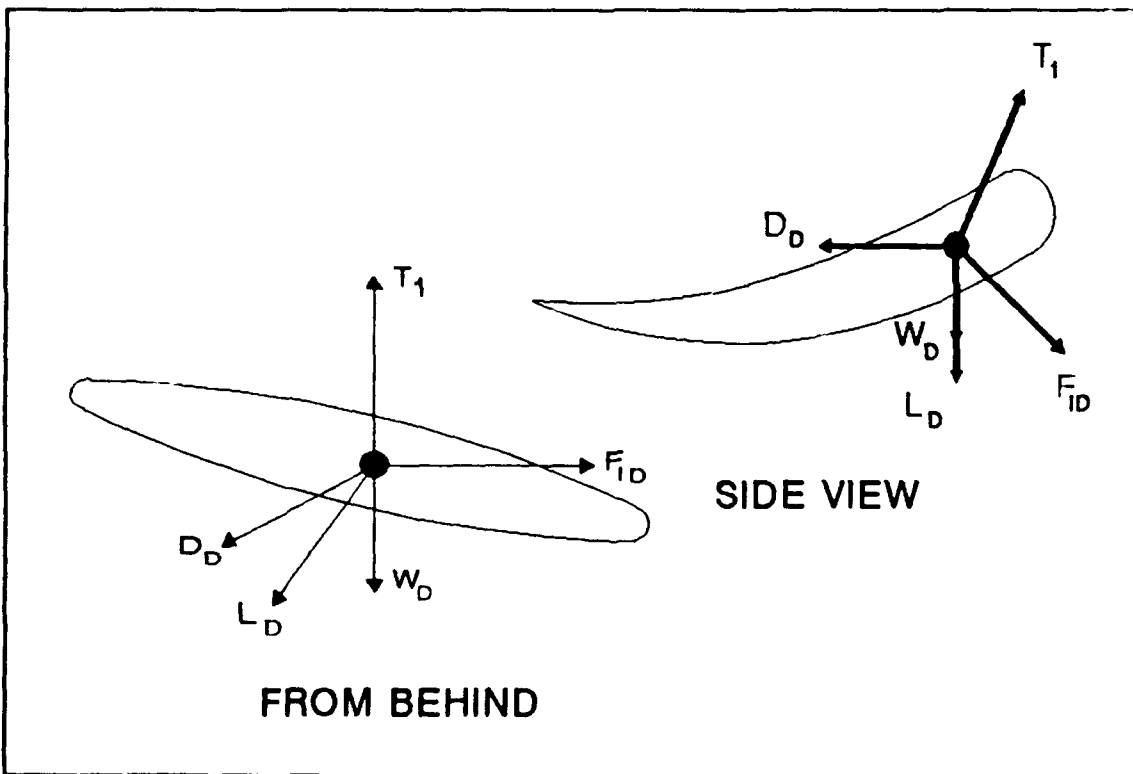


**Figure 5.10:** Steady State Forces Upon the Flying Drogue

$$F_{resultant} = T_1 = \sqrt{\left(-L_D \sin \phi_D + \frac{W_D}{g} \dot{\theta}^2 R_1\right)^2 + D_D^2 + (W_D + L_D \cos \phi_D)^2} \quad (5.21)$$

Remembering that  $T_1 = T_2$  and that the forces upon the first segment of wire were negligible compared to the drogue, the two gridpoint  $\Delta S$  requirement led to the calculation of  $R_2$ ,  $\theta_2$  and  $Z_2$ . The relations are presented as equations (5.22) through (5.24).

$$\theta_2 = \theta_1 + \frac{D_D \Delta S}{T_1 R_1} \quad (5.22)$$

$$R_2 = R_1 - \frac{\left(-L_D \sin \phi_D + \frac{W_D}{g} \dot{\theta}^2 R_1\right) \Delta S}{T_1} \quad (5.23)$$

$$Z_2 = Z_1 \pm \sqrt{\Delta S^2 - R_2^2 - R_1^2 + 2R_1 R_2 \cos(\theta_2 - \theta_1)} \quad (5.24)$$

Equations (5.14) through (5.24) provided the basis from which the most general version of the steady-state flying drogue model was developed. This model left an infinite number of bank angles and coefficients of lift from which to choose. A simple approach was needed for eliminating some of these possibilities. First, it was reasonable to assume that the maximum downward force and the least drag would

provide the best verticality. A version of the steady-state model was thus derived that made use of the special case where  $C_{LD}/C_{DD}$  was a maximum for the flying drogue. Next, it was reasonable to assume that verticality would benefit from a minimum of side forces upon the wire, so the bank angle was adjusted to just balance the inertial forces upon the drogue. Applying the assumptions above, equations (5.25) through (5.27) were written. Under the same assumptions as the more general case, equations (5.28) through (5.33) were also written.

$$\left(\frac{L_D}{D_D}\right)_{\max} = \left(\frac{C_{LD}}{C_{DD}}\right)_{\max} \quad (5.25)$$

$$F_{ID} = \frac{W_D}{g} \dot{\theta}^2 R_1 = L_D \sin \phi_D \quad (5.26)$$

$$\phi_D = a \sin \left( \frac{W_D \dot{\theta}^2 R_1}{g L_D} \right) \quad (5.27)$$

$$\overline{F_{resultant}} = \left( -L_D \sin \phi_D + \frac{W_D}{g} \dot{\theta}^2 R_1 \right) \overline{e_R} - D_D \overline{e_\theta} - (W_D + L_D \cos \phi_D) \overline{e_K} \quad (5.28)$$

$$T_1 = \sqrt{D_D^2 + (W_D + L_D \cos \phi_D)^2} \quad (5.29)$$

$$T_1 = T_2 \quad (5.30)$$

$$\theta_2 = \theta_1 + \frac{D_D \Delta S}{T_1 R_1} \quad (5.31)$$

$$R_2 = R_1 \quad (5.32)$$

$$Z_2 = Z_1 \pm \sqrt{\Delta S^2 - R_2^2 - R_1^2 + 2R_2 R_1 \cos(\theta_2 - \theta_1)} \quad (5.33)$$

It was desirable to implement both the general case, to allow the operator the maximum degree of freedom for experimentation, as well as the maximum  $L_D/D_D$  special case. The missing ingredients were the flying drogue aerodynamic coefficients and physical measurements. The requirements of a flying autonomous drone towed behind an airplane were similar in concept to those of a Remotely Piloted Vehicle (RPV). An RPV was selected that approximately fit the requirements of weight, size and configuration. The flying drogue was thus based upon the general design of the EXDRONE or SYMDEC 4 RPV with the engine removed. The details of the design were outlined in Appendix G.

Three versions of the flying drogue dynamic model were written to investigate three different control schemes. In the first scheme, the drogue was maneuvered to provide an



input to the wire perpendicular, or lateral, to the unit tangent vector of the wire at the final grid segment. In the second scheme, the drogue provided the input tangential to the wire. This was thus an input of pure tension. In the third case, the two inputs were combined and were tried together.

Appendix G outlines the design of the flying drogue and the development of the relations for the maximum force that the flying drogue could generate in the orthogonal  $X_{n,m}$  and  $Y_{n,m}$  directions. For the purpose of investigating the utility of the lateral input scheme described above, it was assumed that any force up to these maximum values could be applied.

The goal of the lateral control scheme was to eliminate displacements from the equilibrium position. Knowing this, the best control laws were based upon displacement, rate of displacement and acceleration of displacement from the steady-state position. Unfortunately, the implementation of such a control law was not practical due to the difficulty of measuring displacement from the steady-state position relative to the towplane position; however, control laws based upon these quantities provided the best possible control of the oscillations and as such provided an idea as to the feasibility of lateral force control.

The lateral force control schemes were tested using a towplane flight profile of 18,325 feet, 156 KEAS, an angle

of bank of 34 degrees and the textbook derived aerodynamic coefficients with the sideforce coefficient set equal to zero. The best reduction of verticality oscillation, tension oscillation and oscillations at the point 45 feet aft of the towplane resulted when using the displacement rule. Given the maximum force inputs defined in Appendix G, the control scheme was best described as linear displacement feedback with saturation. The simulations were repeated for the case of a steady-state drogue bank angle of -15 degrees and with both  $C_{LD}=0$  and 0.25, for a drogue bank angle of +15 degrees with  $C_{LD}=0.25$  and for the  $C_{LD}/C_{DD}=\text{max}$  case described earlier. The lift vector produced by the  $C_{LD}$  was pointed downward to enhance verticality. This will be the convention for the rest of this chapter. The anti-yoyo maneuver was selected for each simulation. Table 5.2 tabulates the steady-state verticality as well as the oscillation magnitudes in verticality, the radial coordinate 45 feet aft of the towplane and in tension. The results were somewhat disappointing.

Table 5.2: STEADY-STATE VERTICALITY AND VERTICALITY OSCILLATION MAGNITUDE FOR VARIOUS DROGUE FLIGHT CONDITIONS

Tow-plane angle of bank	-15°	-15°	+15°	$C_{LD}/C_{DD} = \text{max}$	anti-yoyo only
$C_{LD}$	0	0.25	0.25	N/A	N/A
Steady-State Vert.	59.002%	60.008%	60.067%	60.165%	55.005%
Vert. Osc.	6.7%	6.3%	6.55%	6.9%	8.7%
R(45 ft)	3.85 ft	3.85 ft	3.9 ft	4.05 ft	4.6 ft
Tension Osc.	215 lbs	220 lbs	222 lbs	226 lbs	247 lbs
X input	±40 lbs	±39 lbs	±36 lbs	±32 lbs	N/A
Y input	±35 lbs	±36 lbs	±33 lbs	±29 lbs	N/A

The best results were for the -15 degrees drogue angle of bank and the  $C_{LD}=0.25$ . Remember that the lift was a negative lift vector and so the bank angle of -15 degrees caused the vector to pull the drogue to the outside of the orbit and into a region where the dynamic pressure was higher. This meant that the drogue was able to produce more force at control saturation and thus the effect of the control was slightly better. The maximum force used as an input to the  $X_{n,m}$  and  $Y_{n,m}$  dangling chain calculations were also included in Table 5.2. All forces reached saturation for at least ¼ of the time. Also, note that the downward lift and greater dynamic pressure produced a better mean verticality. This increase in steady-state verticality will

be addressed at the end of this chapter as a separate topic. The result was a slight decrease in the verticality oscillations from 8.7% to 6.3% and an increase in steady-state verticality from 55% to 60%. This reduction in the verticality oscillation did not warrant the construction of such a sophisticated drogue. Additionally, since the -15 degrees and 0.25 control scheme pulled the drogue away from the center of the orbit, it tended to force the drogue closer to a situation where it could transition from the high to the low verticality distribution in flight regimes where these multiple solutions existed as discussed at the end of Chapter III. Table 5.2 was based upon a unit gain of input force versus displacement. A range of values were tried for this gain with no added success. The unit gain provided as good or better results than any other. The lateral control scheme was thus excluded as a valid control scheme.

Appendix G outlines the maximum force that the flying drogue could produce in the direction tangential to the wire. For the purpose of investigating the utility of the longitudinal input scheme, it was assumed that any force up to this maximum value could be produced in the direction of a tension increase and that the longitudinal force could be applied in the direction that resulted in a tension decrease up to the point where the tension equaled zero. In practice this limit was not reached since under the conditions

tested, the drogue was unable to produce enough force to cancel the steady-state tension at the drogue attachment point.

In the case of the tangential control scheme, the choice of which variable to base the control law upon was not as apparent as in the lateral control law case; however, Figure 3.14 shows that the wire is nearly vertical near the drogue location and so it was logical to choose the variation in altitude from the equilibrium case. Unlike the lateral control scheme test case, this choice could be approximately, but quite practically, implemented by observing the mean altitude of the drogue and applying the tension force proportional to the deviation from this observed value. The chosen law was thus best described as linear displacement feedback with saturation. Rate and acceleration control, also based upon drogue altitude, were tried with less successful results. A range of gains were attempted; however, the unit gain value provided as good or better results than any of the others.

Table 5.3 provides the steady-state verticality and the magnitude of the oscillations in verticality, the radial coordinate of the point 45 feet aft of the towplane and the tension and finally the maximum control forces applied in tension for the same cases previously discussed for the lateral control law. For the same reasons as the lateral control law, the best results were derived using the angle

of bank of -15 degrees,  $C_{LD}=0.25$  case. The results were very close to those discussed in the lateral control case with the best results being a reduction in the verticality oscillations from 8.7% to 6.3% and an increase in steady-state verticality from 55% to 60.8%. Again, the issue of the use of the drogue to increase steady-state verticality will be discussed at the end of this chapter. The tangential control law did not reduce the oscillations sufficiently to warrant the expense and complexity of the implementation of the tangential control law flying drogue.

Table 5.3: STEADY-STATE VERTICALITY AND VERTICALITY OSCILLATION MAGNITUDE FOR VARIOUS DROGUE FLIGHT CONDITIONS

Tow-plane angle of bank	-15°	-15°	+15°	$C_{LD}/C_{DD} = \text{max}$	anti-yoyo only
$C_{LD}$	0	0.25	0.25	N/A	N/A
Steady-State Vert.	58.80%	60.61%	60.44%	60.71%	55.01%
Vert. Osc.	6.6%	6.3%	6.6%	6.6%	8.7%
R(45 ft)	4.2 ft	4.25 ft	4.3 ft	4.25 ft	4.6 ft
Tension Osc.	158 lbs	172 lbs	158 lbs	142 lbs	247 lbs
$\Delta T$	$\pm 64$ lbs	$\pm 65$ lbs	$\pm 56$ lbs	$\pm 47$ lbs	N/A

The lateral and the longitudinal/tension control schemes were combined by noting that the lateral force input had two perpendicular components which were in turn orthogonal to the tension/tangential force. The two schemes were thus

combined without modification. Table 5.4 provided the results for the combined schemes under the same conditions as Table 5.2 and 5.3. Using both schemes, the minimum oscillation in verticality was actually a very slight amount better at an angle of bank of 15 degrees and  $C_{LD}=0.25$  and also during the  $C_{LD}/C_{DD}=\text{max}$  condition, however the tension oscillation was significantly less for the case of an angle of bank of -15 degrees and  $C_{LD}=0.25$ , leading to the same choice as in the two previous cases of the best control scheme. As before, the reduction in verticality oscillation magnitude was around 2% and the combined law was thus deemed of minimal value. Again, a range of control gains were attempted with no measurable improvement.

Table 5.4: STEADY-STATE VERTICALITY AND VERTICALITY OSCILLATION MAGNITUDE FOR VARIOUS DROGUE FLIGHT CONDITIONS

Tow-plane angle of bank	-15°	-15°	+15°	$C_{LD}/C_{DD}=\text{max}$	anti-yoyo only
$C_{LD}$	0	0.25	0.25	N/A	N/A
Steady-State Vert.	59.00%	60.08%	60.01%	60.16%	55.005%
Vert. Osc.	6.7%	6.6%	6.55%	6.7%	8.7%
R(45 ft)	3.85 ft	4.35 ft	3.9 ft	4.1 ft	4.6 ft
Tension Osc.	210 lbs	142 lbs	220 lbs	162 lbs	247 lbs
X input	±40 lbs	±32 lbs	±36 lbs	±32 lbs	N/A
Y input	±37 lbs	±29 lbs	±33 lbs	±29 lbs	N/A
ΔT	±47 lbs	±47 lbs	±35 lbs	±31 lbs	N/A

The combined law was written assuming the maximum forces for both the lateral and longitudinal schemes could be generated simultaneously. In general, this will not be possible and the actual results would be even less promising than those found in Table 5.4. Finally, as in the pure lateral and longitudinal control scheme cases, the chosen control law required moving the drogue outward radially. As before, this was an undesirable situation.

The attempt of using a controllable drogue at the bottom of the wire showed that the steady-state verticality of the wire could be significantly affected by the choice of a steady-state drogue lift coefficient and bank angle. As a final application of the new drogue, the bottom control force was used to enhance the steady-state verticality. This was then combined with the anti-yoyo law to determine the effect of this steady-state verticality enhancement scheme operating at the bottom and the towplane driven anti-yoyo law at the top. The previously developed steady-state controllable drogue program and the flying drogue dynamic program with the lateral and longitudinal control forces set to zero were used for the investigation and so no new software was required. To provide a fair comparison of the use of the steady-state forces with the normal TACAMO drogue, the weight of the flying drogue was changed to equal that of the normal TACAMO drogue. The differences in verticality were then due to the difference of configuration



between the cone and the flying drogue and the selection of the drogue bank angle and the drogue coefficient of lift. Table 5.5 shows the steady-state verticality and the oscillation magnitude for a range of bank angles and  $C_{LD}$ 's. The towplane conditions and wire parameters were the same used to develop Tables 5.2 through 5.4. Note that the best steady-state verticality was achieved using a maximum  $C_{LD}$  and a bank angle of -20 degrees. The steady-state verticality of the new drogue was 61.35% while the steady-state verticality of the cone was only 55.01%. This was an improvement of over 6%. Also note that the verticality oscillation was down to 6.35% from 8.2% for the cone. This was mostly a consequence of the higher flying drogue steady-state verticality and in a small part due to the added damping of the flying drogue.

Table 5.5: STEADY-STATE VERTICALITY AND VERTICALITY OSCILLATION FOR A NUMBER OF DROGUE CONFIGURATIONS

$\phi_D$	$C_{LD}=0.25$	$C_{LD}=0.5$	$C_{LD}=0.75$
-70°	57.55%, 7%	58.83%, 6.3%	59.68%, 6%
-50°	57.89%, 7%	60.17%, 6.2%	61.19%, 6.1%
-30°	57.94%, 7.1%	59.91%, 6.6%	61.34%, 6.2%
-20°	58.09%, 7.3%	59.98%, 6.8%	61.35%, 6.4%
-15°	58.12%, 7.3%	60.01%, 6.8%	61.23%, 6.6%
0°	58.18%, 7.4%	59.77%, 7%	60.85%, 6.8%
15°	58.00%, 7.3%	59.41%, 7%	60.23%, 7.1%
30°	57.72%, 7.4%	58.90%, 7.3%	59.67%, 7.1%
50°	57.26%, 7.7%	58.16%, 7.5%	58.74%, 7.5%
70°	56.62%, 7.8%	57.32%, 7.8%	57.6%, 7.6%

The new drogue simulation was applied to wire lengths of 15,000 feet and 25,000 which were near the maximum and minimum wire lengths for the TACAMO system. The towplane altitude and bank angles were adjusted to reflect typical TACAMO parameters for these wire lengths. For the 15,000 feet wire length, the altitude was 18,325 feet and the bank angle was 40 degrees. For the 25,000 feet wire length, the altitude was 20,000 feet and the bank angle was 34 degrees. The new drogue resulted in a 4% mean verticality increase and a 2% reduction in verticality oscillations for the 25,000 feet wire length and a 6% increase in mean verticality and a 2% reduction in verticality oscillation for the 20,000 feet wire length. For the scenarios tested, the new drogue produced a 4% to 6% increase in the steady-state verticality and a 2% reduction in the verticality oscillations.

## VI. CONCLUSIONS AND RECOMMENDATIONS

The technique of superimposing the dynamics of the classical dangling chain to the steady-state solution of the long wire towed behind an aircraft has been validated for a wide range of forcing functions and flight conditions. The code was checked against a number of analytical solutions and the final results show excellent correlation to flight test derived data for the special case of the E-6A TACAMO system. It is recommended that the models be considered for application to ongoing aircraft and ship trailing wire programs including the TACAMO program. It is further recommended that for the special case of the TACAMO program, the ongoing measurements of wind tunnel derived coefficients for both the wire and drogue be completed and added to the models to provide even closer correlation to the actual flight hardware dynamics.

The anti-yoyo maneuver formulated in this dissertation shows excellent potential for reducing oscillations of the trailing wire towed behind an orbiting aircraft by 50 percent. It is suggested that this anti-yoyo scheme be considered for addition during any future towplane autopilot upgrades including the E-6A airplane. The flying drogue shows promise for increasing the steady-state verticality of the wire on the order of four to six percent but is limited

in its ability to actively control wire oscillations. For systems using the cone shaped drogue, it is recommended that a new drogue be designed which increases the steady-state verticality.

## APPENDIX A

### STATIC MODEL CODE

```
PROGRAM TAC17
C THIS PROGRAM IS AN ITERATIVE SOLUTION TO THE STEADY
C STATE TACAMO WIRE PROBLEM.
C THE COEFFICIENTS AND DIMENSIONS REFLECT THE NEW 3X7 RATTAIL
C WIRE.
C*****
C DECLARE AND DIMENSION VARIABLES.
C
C SCALARS FIRST.
C
C A1, B1, C1, A2, B2, C2 ARE THE TENSION TIMES THE SLOPE AT
C THE HALF STEP POINTS USED IN THE ITERATIVE SOLUTION.
REAL A1,B1,C1
REAL A2,B2,C2
C A22, B22, C22 ARE PLACEHOLDERS USED DURING THE ITERATIONS.
REAL A22,B22,C22
C A2A2, B2B2, C2C2 ARE SUMMERS USED IN AVERAGING.
REAL A2A2,B2B2,C2C2
C AC IS THE AERODYNAMIC CENTER OF THE DROGUE MEASURED FROM THE LE.
REAL AC
C ALFAL IS THE DROGUE ANGLE OF ATTACK.
REAL ALFAD
C ALTTP IS THE TOWPLANE ALTITUDE IN FEET.
REAL ALTTP
C ASFD IS THE AERODYNAMIC SIDEFORCE OF THE DROGUE DUE TO THE
C SIDESLIP ANGLE BETA.
REAL ASFD
C BETA IS THE SIDESLIP ANGLE OF THE DROGUE.
REAL BETA
C CDD IS THE CD FOR THE DROGUE.
REAL CDD
C CD IS THE WIRE DRAG COEFFICIENT.
REAL CD
C CF IS THE WIRE SKIN FRICTION COEFFICIENT.
REAL CF
C CFSIDE IS THE SIDEFORCE COEFFICIENT FOR THE WIRE DUE TO THE
C "MAGNUS EFFECT" PHENOMENON.
REAL CFSIDE
C CG IS THE CENTER OF GRAVITY OF THE DROGUE, MEASURED AFT OF THE
C TIP.
REAL CG
C CLALD IS THE LIFT COEFFICIENT CURVE SLOPE FOR THE DROGUE.
REAL CLALD
C CLALDM IS THE MAXIMUM LIFT CURVE SLOPE FOR THE DROGUE.
REAL CLALDM
C CMACD IS THE COEFFICIENT OF MOMENT AROUND THE AERODYNAMIC
C CENTER FOR THE DROGUE.
REAL CMACD
C D IS THE WIRE DIAMETER.
REAL D
C DELTAS IS THE INCREMENT OF WIRE LENGTH AT THE N'TH GRIDPOINT.
```

```

C      REAL DELTAS
C      G IS THE ACCELERATION DUE TO GRAVITY.
C      REAL G
C      LEND IS THE LENGTH OF THE DROGUE.
C      REAL LEND
C      LD IS THE LIFT PRODUCED BY THE DROGUE.
C      REAL LD
C      MHU IS THE MASS OF THE WIRE PER UNIT LENGTH.
C      REAL MHU
C      PHI IS THE ANGLE OF BANK OF THE TOWPLANE.
C      REAL PHI
C      Q IS THE LOCAL DYNAMIC PRESSURE.
C      REAL Q
C      RADTP IS THE ORBIT RADIUS OF THE TOWPLANE.
C      REAL RADTP
C      RHO IS THE LOCAL AIR DENSITY.
C      REAL RHO
C      RNEW IS A PLACEHOLDER FOR R(1) WHILE AN UPDATE IS CALCULATED
C      ON THE OUTER LOOP.
C      REAL RNEW
C      STUFF1,2,3,4,5,6 ARE DUMMY VARIABLES FOR INTERIM CALCULATIONS.
C      REAL STUFF1, STUFF2, STUFF3, STUFF4, STUFF5, STUFF6
C      THEDOT IS THE ORBIT RATE IN RADIANS PER SECOND.
C      REAL THEDOT
C      RR IS A CONSTANT USED TO START THE RADIAL COORDINATE
C      CALCULATIONS AT THE DROGUE.
C      REAL RR
C      SD IS THE MAXIMUM CROSS SECTIONAL AREA OF THE DROGUE.
C      REAL SD
C      THTH IS A CONSTANT USED TO START THE THETA COORDINATE
C      CALCULATIONS AT THE DROGUE.
C      REAL THTH
C      VEAS IS THE TOWPLANE EQUIVALENT AIRSPEED.
C      REAL VEAS
C      VTRUE IS THE TOWPLANE TRUE AIRSPEED.
C      REAL VTRUE
C      WD IS THE WEIGHT OF THE DROGUE.
C      REAL WD
C      ZNEW IS A PLACEHOLDER FOR Z(1) WHILE AN UPDATE IS
C      CALCULATED ON THE OUTER LOOP.
C      REAL ZNEW
C
C      NOW INTEGERS.
C
C      N IS THE MAIN LOOP GRIDPOINT COUNTER.
C      INTEGER N
C      COUNT AND COUNT1 ARE COUNTERS USED DURING AN AVERAGING PROCESS.
C      INTEGER COUNT, COUNT1
C      INDEX CORRELATES THE GRIDPOINT ALTITUDE WITH THE INDEX OF THE
C      CORRECT DENSITY VALUE.
C      INTEGER INDEX
C      TICK COUNTS THE NUMBER OF OUTER LOOPS PERFORMED TO CONVERGENCE.
C      INTEGER TICK
C
C      FINALLY ARRAYS.
C
C      DENSITY(S) IS THE DENSITY MEASURED AT 1000 FEET INTERVALS.
C      REAL DENSITY(30)
C      R(N) IS THE GRIDPOINT RADIAL POSITION IN FEET.
C      REAL R(200)
C      T(N) IS THE GRIDPOINT TENSION. THE ACTUAL GRIDPOINT LOCATION
C      IS AT N-1/2.

```



```

G=32.174
PI=3.1415926535879
COUNT=1
TICK=1

C
C
C   WIRE CONSTANTS.

CD=1.03
CF=0.022
WRITE(6,*)'INPUT THE SIDEFORCE COEFF FOR WIRE='
READ(5,*)CFSIDE
D=0.1582/12
DELTAS=101.96
MHU=0.062107/G

C
C   RR AND THTH ARE CONSTANTS USED TO START THE CALCULATIONS
C   AT THE DROGUE.
C
RR=1.0
THTH=0.001

C
C   READ THE DENSITY DATA FILE.
C
OPEN (31,FILE='DENSITY.MAT',STATUS='OLD',FORM='FORMATTED',
: ACCESS='SEQUENTIAL',RECL=5)
5  READ (31,2,END=6)DENSITY
   GOTO 5
6  CLOSE(31)
C*****
C   CALCULATE THE RADIUS OF THE TOWPLANE FLIGHT PATH AND THE THEDOT.
C   THE PROGRAM WILL WORK AT ALL AIRSPEEDS AND ALTITUDES OF
C   INTEREST AND FOR BANK ANGLES OF BETWEEN 5 AND 50 DEGREES. FOR
C   BANK ANGLES ABOVE 45 DEGREES, AND AT TIMES AROUND THE LOCATION
C   OF THE JUMP PHENOMENON, A SMALL ADJUSTMENT TO THE PROGRAM
C   MAY BE REQUIRED. DOCUMENTATION WILL PRINT ON THE SCREEN IF
C   THIS SITUATION OCCURS THAT WILL EXPLAIN HOW TO MAKE THE
C   ADJUSTMENT.
C
WRITE(6,*)'INPUT AIRCRAFT KEAS, ALT IN FT, BANK ANGLE IN DEG'

C
READ(5,*) VEAS,ALTTP,PHI

C
C   CONVERT KNOTS TO FEET PER SECOND.
C
VEAS=VEAS*6076.1/3600.0

C
C   CONVERT TO RADIANS.
C
PHI=PHI*2.0*PI/360.0

C
C   LOCAL GRIDPOINT DENSITY. A FILE OF MEASURED DATA MAY BE USED
C   OR STANDARD ATMOSPHERE DATA MAY BE CALCULATED. COMMENT OUT THE
C   METHOD NOT CHOSEN.
C
INDEX=INT(ALTTP/1000.0)+1
RHO=DENSITY(INDEX)*0.0023769/1013.0

C
C   RHO=0.0023769*(((518.69-0.0035662*ALTTP)/518.69)**
C   : ((-1.0)*(1.0/(-0.0035662*53.3))+1.0))
C
C   RHO=0.002378*(1-0.006875*Z(N)/1000.0)**4.256
C

```



```

C      TRUE AIRSPEED FROM EQUIVALENT AIRSPEED.
C
C      VTRUE=VEAS/SQRT(RHO/0.0023769)
C
C      CALCULATE TOWPLANE ORBIT RADIUS.
C
C      RADTP=VTRUE**2/(G*SQRT(1/(COS(PHI))**2-1))
C
C      ORBIT RATE CALCULATION.
C
C      THEDOT=VTRUE/RADTP
C*****
C*****
C*****
C      THE INITIAL POSITION AT GRIDPOINT 1.
C      THIS IS AN INITIAL GUESS AT THE BOTTOM POSITION.  THIS VALUE IS
C      ITERATED TO MATCH THE BOUNDARY CONDITION POSITION AT THE
C      TOWPLANE.  THESE VALUES MAY ALSO BE ADJUSTED TO FORCE THE
C      MULTIPLE SOLUTIONS.  TO FORCE MULTIPLE SOLUTIONS THE INITIAL
C      POSITION MAY BE CHOSEN AT OR OUTSIDE THE TOWPLANE RADIUS OF
C      ORBIT.
C
C      THETA(1)=0.0
C      IF (PHI .GT. 32.0*2.0*PI/360.0) THEN
C      Z(1)=0.3*ALTTP
C      Z(1)=0.4*ALTTP
C      K(1)=0.2*RADTP
C      R(1)=1.6*RADTP
C      ELSE
C      Z(1)=0.6*ALTTP
C      Z(1)=0.2*ALTTP
C      R(1)=0.6*RADTP
C      R(1)=1.2*RADTP
C      ENDIF
C*****
20    CONTINUE
C
C      AT THE DROGUE.
C
C      GUESS AT THE POSITION USING THE FORCING FACTORS.
C
C      R(2)=R(1)+RR
C      THETA(2)=THETA(1)+THTH
C      Z(2)=Z(1)+SQRT(DELTAS**2-R(2)**2-R(1)**2+
: 2*R(2)*R(1)*COS(THETA(2)-THETA(1)))
C
C      DENSITY AT GRIDPOINT 1.  AGAIN, CHOOSE TABLE LOOKUP
C      OR STANDARD ATMOSPHERE.
C
C      INDEX=INT(Z(1)/1000.0)+1
C      RHO=DENSTY(INDEX)*0.0023769/1013.0
C
C      RHO=0.0023769*((518.69-0.0035662*Z(1))/518.69)**
: ((-1.0)*(1.0/(-0.0035662*53.3))+1.0))
C
C      RHO=0.002378*(1-0.006875*Z(N)/1000.0)**4.256
C
C      LOCAL DYNAMIC PRESSURE.
C
C      Q=0.5*RHO*(R(1)*THEDOT)**2
C
C      CALCULATE THE AOA AND SIDESLIP ANGLE OF THE DROGUE BY CALCU-

```

```

C      LATING THE MOMENT EQUATION RESIDUES AND CHOOSING THE AOA AND
C      SIDESLIP ANGLE AT WHICH THE RESIDUE COMES CLOSEST TO VANISHING.
C      ONE DEGREE INCREMENTS ARE CONSIDERED SUFFICIENT.
C
C      INITIALIZE THE RESIDUE HOLDERS SINCE THEY ARE REUSED AT EACH
C      NEW BOUNDARY SHOT.
C
C      STUFF2=1000.0
C      STUFF5=1000.0
C
C      LOOP THROUGH EACH ANGLE FROM 0 TO 90 DEGREES.
C      NEGLECT ALL OTHER ANGLES THROUGH PHYSICAL REASONING.
C
C      DO 50 N=1,90
C
C      USE INDEX TO GET ANGLE IN RADIAN.
C
C      ALFAD=N*2.0*PI/360.0
C      BETA=ALFAD
C
C      CALCULATE THE LIFT CURVE SLOPE AT THIS ANGLE.
C
C      CLALD=CLALDM*(PI-2.0*ALFAD)/PI
C      NOW THE RESIDUES AT THIS ANGLE.
C
C      FOR THE ANGLE OF ATTACK.
C
C      STUFF1=-CLALD*ALFAD*Q*SD*AC*COS(ALFAD)-CDD*Q*SD*AC*SIN(ALFAD)+
:      WD*CG*COS(ALFAD)+CMACD*Q*SD*LEND
C
C      FOR THE SIDESLIP ANGLE.
C
C      STUFF4=WD*THEDOT**2*R(1)*CG*COS(BETA)/G-CLALD*BETA*Q*SD*AC*
:      COS(BETA)+CMACD*Q*SD
C
C      SAVE RESIDUE AND ANGLE IF IT IS LESS THAN THE LAST.
C
C      FOR THE ANGLE OF ATTACK.
C
C      IF (ABS(STUFF1) .LT. ABS(STUFF2)) THEN
C      STUFF2=STUFF1
C      STUFF3=ALFAD
C      ENDIF
C
C      FOR THE SIDESLIP ANGLE.
C
C      ELIMINATE THE POSSIBILITY OF MULTIPLE SOLUTIONS BEYOND 45
C      DEGREES.
C
C      IF (BETA .GT. PI/4.0) THEN
C      GOTO 50
C      ENDIF
C      IF (ABS(STUFF4) .LT. ABS(STUFF5)) THEN
C      STUFF5=STUFF4
C      STUFF6=BETA
C      ENDIF
50  CONTINUE
C
C      SELECT THE MINIMUM RESIDUE ANGLE OF ATTACK AS THE DESIRED VALUE.
C
C      ALFAD=STUFF3
C      BETA=STUFF6

```

```

C
C      CALCULATE THE LIFT FORCE OF THE DROGUE DEFINED PERPENDICULAR TO
C      THE RELATIVE FLOW AND CALCULATE THE LIFT AND SIDEFORCE OF THE
C      DROGUE.
C
      CLALD=CLALDM*(PI-2.0*ALFAD)/PI
      LD=CLALD*ALFAD*Q*SD
      CLALD=CLALDM*(PI-2.0*BETA)/PI
      ASFD=CLALD*BETA*Q*SD
C
C      CALCULATE THE DRAG FORCE OF THE DROGUE DEFINED PARALLEL TO
C      THE RELATIVE FLOW.
C
      DD=CDD*Q*SD
C*****
C      NOW GET TENSION AT 1 AND POSITION AT 2 BY ASSUMING THE
C      AERODYNAMIC AND INERTIAL FORCES ON THE FIRST SEGMENT OF WIRE
C      ARE SMALL COMPARED TO THE DROGUE FORCES.
C
C      THE TENSION AT GRIDPOINT 1 MUST BALANCE THE VECTOR SUM OF THE
C      FORCES UPON THE DROGUE IN ORDER TO SATISFY STATIC EQUILIBRIUM.
C
      STUFF1=WD*THEDOT**2*R(1)/G
      T(1)=SQRT((STUFF1-ASFD)**2+DD**2+(LD-WD)**2)
C
C      ASSUME THAT THE FORCES ON THE FIRST SEGMENT OF THE WIRE ARE
C      SMALL COMPARED TO THE FORCES ON THE DROGUE.
C
      T(2)=T(1)
C
C      THE RESULTANT FORCE MUST ALSO BE IN THE RECIPROCAL DIRECTION
C      TO MAINTAIN STATIC EQUILIBRIUM.
C
      R(2)=R(1)-(STUFF1-ASFD)*DELTAS/T(1)
      THETA(2)=THETA(1)+DD*DELTAS/(T(1)*((R(1)+R(2))/2))
C
C      USE THE TWO POINT SEGMENT LENGTH CONSTRAINT TO GET THE Z AT
C      GRIDPOINT 2.
C
      Z(2)=Z(1)+SQRT(DELTAS**2-R(2)**2-R(1)**2+
: 2*R(2)*R(1)*COS(THETA(2)-THETA(1)))
C
C*****
C*****
C      ITERATE TO THE TOP.
C
C      MAKE INITIAL GUESSES AT THE ITERATION VALUES FOR GRIDPOINT TWO.
C
      A1=T(1)*(R(2)-R(1))/DELTAS
      B1=T(1)*(R(2)+R(1))*(THETA(2)-THETA(1))/(2*DELTAS)
      C1=T(1)*(Z(2)-Z(1))/DELTAS
C
C      DO 3500 N=3,200
C
C      GUESS AT NEXT POINT. USE THE THREE POINT UNIT TANGENT VECTOR
C      CONSTRAINT TO GET THE Z AT GRIDPOINT N.
C
      R(N)=R(N-1)+R(N-1)-R(N-2)
      THETA(N)=THETA(N-1)+THETA(N-1)-THETA(N-2)
      Z(N)=4*DELTAS**2-(R(N)-R(N-2))**2-R(N-1)**2*
: (THETA(N)-THETA(N-2))**2
C

```

```

C      PROTECT AGAINST A NEGATIVE RADICAND DURING THE ITERATIONS.
C
C      IF (Z(N) .LT. 0.0) THEN
C      Z(N)=0.000001
C      ELSE
C      ENDIF
C      Z(N)=Z(N-2)+SQRT(Z(N))
C
C      T(N)=T(N-1)+MHU*DELTAS*G/(R(N-1)*(THETA(N-1)-THETA(N-2))/DELTAS)
C*****
C      THE INNER LOOP FOR MOVING FROM ONE GRID POINT TO THE NEXT.
C
C      INITIALIZE COUNTERS FOR LATER USE.
C
C      COUNT=1
C      COUNT1=1
C
C      INITIALIZE SUMMERS FOR USE IN AVERAGING LATER.
C
C      A2A2=0.0
C      B2B2=0.0
C      C2C2=0.0
C
C 1000  CONTINUE
C
C      CALCULATE DENSITY.
C
C      INDEX=INT(Z(N)/1000.0)+1
C      RHO=DENSTY(INDEX)*0.0023769/1013.0
C
C      RHO=0.0023769*(((518.69-0.0035662*Z(N))/518.69)**
C : ((-1.0)*(1.0/(-0.0035662*53.3))+1.0))
C
C      RHO=0.002378*(1-0.006875*Z(N)/1000.0)**4.256
C
C      INCREMENT COUNTER.
C
C      COUNT=COUNT+1
C
C      NOW THE ITERATIONS.
C
C      STUFF1=SQRT(1-(R(N-1)**2*(THETA(N)-THETA(N-2))**2)/
C : (4*DELTAS**2))
C      STUFF2=0.5*RHO*D*CD*(R(N-1)*THEDOT)**2*STUFF1*
C : R(N-1)*(THETA(N)-THETA(N-2))*(R(N)-R(N-2))/(4*DELTAS**2)
C      STUFF3=((T(N)+T(N-1))/2)*R(N-1)*(THETA(N)-THETA(N-2))**2/
C : (4*DELTAS**2)
C      STUFF4=SIN((Z(N)-Z(N-2))/DELTAS)*CFSIDE*0.5*RHO*D*
C : (R(N-1)*THEDOT)**2
C      A2=A1+(STUFF3-STUFF2+STUFF4-MHU*THEDOT**2*R(N-1))*DELTAS
C
C      STUFF1=SQRT(1-(R(N-1)**2*(THETA(N)-THETA(N-2))**2)/
C : (4*DELTAS**2))
C      STUFF4=(T(N)+T(N-1))*(R(N)-R(N-2))*(THETA(N)-THETA(N-2))/
C : (8*DELTAS**2)
C      STUFF5=(R(N-1)**2*(THETA(N)-THETA(N-2))**2)/
C : (4*DELTAS**2)-1
C      B2=B1-(STUFF4+0.5*RHO*D*(R(N-1)*THEDOT)**2*
C : (-CF+CD*STUFF1*STUFF5))*DELTAS
C
C      STUFF1=SQRT(1-(R(N-1)**2*(THETA(N)-THETA(N-2))**2)/
C : (4*DELTAS**2))

```

```

      STUFF2=0.5*RHO*D*CD*(R(N-1)*THEDOT)**2*STUFF1*
: R(N-1)*(THETA(N)-THETA(N-2))*(Z(N)-Z(N-2))/(4*DELTAS**2)
      C2=C1+(-STUFF2+MHU*G)*DELTAS
C
      T(N)=SQRT(A2**2+B2**2+C2**2)
      R(N)=R(N-1)+A2*DELTAS/T(N)
      THETA(N)=THETA(N-1)+B2*2*DELTAS/(T(N)*(R(N)+R(N-1)))
      Z(N)=Z(N-1)+C2*DELTAS/T(N)
C
C      HERE, AGAIN APPLY A LITTLE TRICK.  FOR 8088 SYSTEMS AND
C      ON VERY RARE OCASSIONS FOR 16 BIT SYSTEMS, THE PROGRAM TENDS TO
C      ENTER A LIMIT CYCLE LIKE BEHAVIOR IN TENSION AFTER 100-200
C      ITERATIONS WHICH CYCLES EVERY 2-3 STEPS.
C      IT IS SOLVED BY SIMPLY AVERAGING THE VALUES OVER 20
C      STEPS ANY TIME 400 ITERATIONS ARE EXCEEDED.  THIS SIMPLE
C      SOLUTION HAS BEEN FOUND TO WORK FOR ALL CASES CHECKED.
C      AGAIN, USING THE 16 BIT 486 TYPE MACHINE TO RUN THE SOFTWARE
C      PRETTY MUCH PRECLUDES THE PROBLEM EXCEPT IN THE RAREST OF
C      CIRCUMSTANCES.
C
      IF (COUNT .LT. 400) THEN
      GOTO 1200
      ELSEIF (COUNT1 .LT. 21) THEN
      COUNT1=COUNT1+1
      A2A2=A2A2+A2
      B2B2=B2B2+B2
      C2C2=C2C2+C2
      GO TO 1200
      ELSE
      A2=A2A2/20.0
      B2=B2B2/20.0
      C2=C2C2/20.0
      GOTO 3000
      ENDIF
1200  CONTINUE
C
C      COMPARE TO THE CONVERGENCE CRITERIA.
C
      IF (ABS((A2-A22)/A2) .GT. 0.0001) THEN
      GOTO 2000
      ELSEIF (ABS((B2-B22)/B2) .GT. 0.0001) THEN
      GOTO 2000
      ELSEIF (ABS((C2-C22)/C2) .GT. 0.0001) THEN
      GOTO 2000
      ELSE
      GOTO 3000
      ENDIF
C
2000  CONTINUE
      A22=A2
      B22=B2
      C22=C2
      GOTO 1000
C
3000  CONTINUE
C
C      MOVE THE ITERATION VALUES FORWARD ONE TIME STEP.
C
      A1=A2
      B1=B2
      C1=C2
C

```

```

C      UPDATE THE POSITION VALUES AND THE TENSION USING ALL THE
C      LATEST INFORMATION.
C
      T(N)=SQRT(A2**2+B2**2+C2**2)
      R(N)=R(N-1)+A2*DELTAS/T(N)
      THETA(N)=THETA(N-1)+B2*2*DELTAS/(T(N)*(R(N)+R(N-1)))
      Z(N)=Z(N-1)+C2*DELTAS/T(N)
C
C      RESET THE SUMMERS FOR THE NEXT LOOP.
C
      A2A2=0.0
      B2B2=0.0
      C2C2=0.0
3500    CONTINUE
C
C*****
C      MATCH THE BOUNDARY CONDITION AT THE TOP. THAT IS, MATCH THE
C      TOP POSITION OF THE WIRE TO THAT OF THE TAIL OF THE TOWPLANE.
C      THE ERROR AT THE TOP IS INTERPOLATED AND USED AS A FACTOR TO
C      ADJUST THE BOTTOM POINT. ON OCCASSION, THE MULTIPLICATIVE
C      FACTORS BELOW MUST BE ADJUSTED TO ENSURE CONVERGENCE OF THE
C      BOUNDARY CONDITION SHOOTING ROUTINE. WHEN THIS IS REQUIRED,
C      THE PROGRAM PROVIDES GUIDANCE ON HOW TO PERFORM THE ADJUSTMENTS.
C
C      MATCH THE Z AT EACH CHOSEN RADIUS.
C
      IF (ABS(Z(200)-ALTTP) .GT. 50.0) THEN
C
      IF (R(1) .LT. 700.0) THEN
        ZNEW=Z(1)+0.1*(ALTTP-Z(200))
        GOTO 3550
      ELSEIF (R(1) .LT. 1000.0) THEN
        ZNEW=Z(1)+0.2*(ALTTP-Z(200))
        GOTO 3550
      ELSEIF (R(1) .LT. 1700.0) THEN
        ZNEW=Z(1)+0.25*(ALTTP-Z(200))
        GOTO 3550
      ELSE
        ZNEW=Z(1)+0.3*(ALTTP-Z(200))
      ENDIF
C
3550    CONTINUE
C
C      NOW ADJUST TO A NEW RADIUS.
C
      Z(1)=ZNEW
      RNEW=R(1)
      GOTO 3600
C
      ELSEIF (ABS(R(200)-RADTP) .GT. 10.0) THEN
C
      IF (R(1) .LT. 800.0) THEN
        RNEW=R(1)+0.07*(RADTP-R(200))
        GOTO 3560
      ELSEIF (R(1) .LT. 1000.0) THEN
        RNEW=R(1)+0.15*(RADTP-R(200))
        GOTO 3560
      ELSEIF (R(1) .LT. 2000.0) THEN
        RNEW=R(1)+0.15*(RADTP-R(200))
        GOTO 3560
      ELSE
        RNEW=R(1)+0.3*(RADTP-R(200))

```

```

        ENDIF
C
3560  CONTINUE
C
      R(1)=RNEW
      ZNEW=Z(1)
      GOTO 3600
      ELSE
      GOTO 3700
      ENDIF
C
3600  CONTINUE
C
      R(1)=RNEW
      Z(1)=ZNEW
C
3640  CONTINUE
C
      PRINT SOME OUTPUTS USEFUL IN KEEPING UP WITH HOW THE BOUNDARY
      CONDITION SHOOTING ITERATIONS ARE PROGRESSING.
C
      WRITE(6,*) 'R(1),Z(1)=',R(1),Z(1)
      WRITE(6,*) 'R(200),Z(200),T(200)=',R(200),Z(200),T(200)
      WRITE(6,*) 'RADTP,ALTTP=',RADTP,ALTTP
      WRITE(6,*) '*****'
C
      JUST BOOKKEEPING HERE FOR THE NEXT LOOP.
C
      DO 3650 N=2,200
      R(N)=0.0
      THETA(N)=0.0
      Z(N)=0.0
      T(N)=0.0
C
3650  CONTINUE
      TICK=TICK+1
C
      CHECK TO SEE IF THE UPDATE MULTIPLIERS ABOVE HAVE PLACED THE
      BOUNDARY SHOOTING PROCESS INTO AN "INFINITE LOOP" AND IF SO
      STOP THE PROCESS AND TELL THE OPERATOR HOW TO FIX THE PROBLEM.
C
      IF (TICK .GT. 400) THEN
      WRITE(6,*) 'YOU HAVE EXCEEDED 400 ATTEMPTS TO SHOOT THE BOUNDARY'
      WRITE(6,*) 'CONDITION AT THE TOP. TO MAKE THE PROGRAM RUN '
      WRITE(6,*) 'CORRECTLY YOU MUST ADJUST THE MULTIPLIER'
      WRITE(6,*) 'COEFFICIENTS IN THE PROGRAM BETWEEN LINES 3500 AND'
      WRITE(6,*) '3560. NOTE THE PRINTOUT OF R(1) AND Z(1) ABOVE AS'
      WRITE(6,*) 'THEY FLOP BACK AND FORTH ON EITHER SIDE OF THE '
      WRITE(6,*) 'CORRECT VALUE. FIRST TRY TO HALVE THE COEFFICIENT'
      WRITE(6,*) 'ASSOCIATED WITH THE P(1) VALUES YOU SEE (NOTE THE'
      WRITE(6,*) 'R(1) .LT. STATEMENT). IF YOU ARE STILL NOT '
      WRITE(6,*) 'CONVERGING, TRY THE Z(1) COEFFICIENT. YOU WILL HAVE'
      WRITE(6,*) 'TO RE-COMPILE AFTER EACH FIX. I RECOMMEND THAT'
      WRITE(6,*) 'YOU WRITE DOWN THE ORIGINAL VALUES AND RETURN THEM'
      WRITE(6,*) 'WHEN YOU ARE DONE. THESE MULTIPLIERS GIVE YOU THE'
      WRITE(6,*) 'QUICKEST CONVERGENCE FOR THE MAJORITY OF CASES OF'
      WRITE(6,*) 'INTEREST.'
C
      GOTO 6000
      ELSE
      ENDIF
C

```

```

      GOTO 20
C*****
C*****
C*****
3700  CONTINUE
      WRITE(6,*) 'NUMBER OF OUTER LOOPS=',TICK
C*****
C      WRITE OUTPUT TO THE THREE DATA FILES.
C      FIRST, CONVERT SOME BACK TO MORE RECOGNIZABLE FORMS.
C
      VEAS=VEAS*3600.0/6076.0
      PHI=PHI*360.0/(2.0*PI)
C
C      NOW, WRITE SOME OF THE CONSTANTS TO FILES.
C
      WRITE(11,*) 'TOWPLANE KEAS=',VEAS,'KTS'
      WRITE(11,*) 'TOWPLANE ALTITUDE=',ALTTP,'FEET'
      WRITE(11,*) 'TOWPLANE BANK ANGLE=',PHI,'DEGREES'
      WRITE(11,*) 'TOWPLANE ORBIT RADIUS=',RADTP,'FEET'
      WRITE(11,*) 'TOWPLANE ORBIT RATE=',THEDOT,'RAD/SEC'
      WRITE(11,*) 'DROGUE ANGLE OF ATTACK=',ALFAD,'RAD'
      WRITE(11,*) 'DROGUE SIDESLIP ANGLE=',BETA,'RAD'
      WRITE(11,*) 'DROGUE ORBIT RADIUS=',R(1),'FEET'
      WRITE(11,*) 'DROGUE AIRSPEED=',THEDOT*R(1),'FT/SEC'
      WRITE(11,*) 'VERTICALITY=',(ALTTP-Z(1))/(200.0*DELTAS)
      WRITE(11,*) 'DROGUE/TOWPLANE SEPARATION=',ALTTP-Z(1),'FEET'
      WRITE(16,1) THEDOT
      WRITE(17,1) CLALD*ALFAD
      WRITE(19,1) VTRUE
      WRITE(20,1) PHI*2.0*PI/360.0
C
C      WRITE THE POSITION AND TENSION TO DATA FILES.
C
      DO 4000 I=1,200
      WRITE(12,1) R(I)
      WRITE(13,1) THETA(I)
      WRITE(14,1) Z(I)
      WRITE(15,1) T(I)
4000  CONTINUE
C*****
C      BUILD A FILE THAT CONTAINS THE ANGLE OF ATTACK OF EACH WIRE
C      GRIDPOINT. NOTE THAT THIS DOES NOT INCLUDE THE FIRST OR LAST
C      POINTS.
C
      DO 5000 I=2,199
      STUFF1=ACOS(R(I)*(THETA(I+1)-THETA(I-1))/(2*DELTAS))
      STUFF1=STUFF1*360/(2*PI)
      WRITE(18,1)STUFF1
5000  CONTINUE
C*****
C      THESE FILES CONTAIN THE REYNOLDS NUMBER AND TRUE AIRSPEED AT
C      EACH GRIDPOINT.
C
      OPEN (UNIT=70,FILE='VTRUE.MAT')
      OPEN (UNIT=71,FILE='RE.MAT')
      DO 5100 I=1,200
      INDEX=INT(Z(I)/1000.0)+1
      RHO=DENSTY(INDEX)*0.0023769/1013.0
C      RHO=0.002378*(1-0.006875*Z(N)/1000.0)**4.256
C      RHO=0.0023769*((518.69-0.0035662*Z(N))/518.69)**
C      : ((-1.0)*(1.0/(-0.0035662*53.3))+1.0))
      VTRUE=R(I)*THEDOT

```



```

        STUFF1=RHO*VTRUE*D/.00000038
        WRITE(70,1)VTRUE
        WRITE(71,1)STUFF1
5100    CONTINUE
        CLOSE(70)
        CLOSE(71)
C*****
        WRITE(6,*)'
        WRITE(6,*)'RUN COMPLETE!!!'
        WRITE(6,*)'
        WRITE(6,*)'THE OUTPUT IS INCLUDED IN THE FOLLOWING:'
        WRITE(6,*)'DATA01.MAT CONTAINS MISCELLANOUS VALUES OF INTEREST.'
        WRITE(6,*)'DATA02.MAT CONTAINS EACH GRIDPOINT RADIAL COORD.'
        WRITE(6,*)'DATA03.MAT CONTAINS EACH GRIDPOINT THETA COORD.'
        WRITE(6,*)'DATA04.MAT CONTAINS EACH GRIDPOINT Z COORD.'
        WRITE(6,*)'DATA05.MAT CONTAINS EACH GRIDPOINT TENSION VALUE.'
        WRITE(6,*)'DATA06.MAT, DATA07.MAT AND DATA00.MAT CONTAIN VALUES'
        WRITE(6,*)'REQUIRED BY THE DYNAMIC SOLUTION PROGRAM.'
        WRITE(6,*)'DATA08.MAT CONTAINS THE TRUE ANGLE OF ATTACK OF'
        WRITE(6,*)'GRIDPOINTS 2 THROUGH 199. VTRUE .MAT CONTAINS THE'
        WRITE(6,*)'TRUE AIRSPEED AT EACH GRIDPOINT AND RE.MAT CONTAINS'
        WRITE(6,*)'THE REYNOLDS NUMBER AT EACH GRIDPOINT.'
C*****
6000    CONTINUE
        END

```

## APPENDIX B

### DANGLING CHAIN MODEL DEVELOPMENT

The derivation of the classical dangling chain problem was performed for the case of a vertically hanging chain. The classical dangling chain problem was later modified to include a mass at the end of the chain and then for use in the case of the wire towed behind an orbiting aircraft. In this initial, classical model, the influences of the circular orbit, including the aerodynamic effects and steady-state model tension distribution were ignored. The purpose of studying the classical model was to provide an insight into the physical properties and the equations required for the towed wire and to provide analytical solutions with which to validate the portion of computer code developed in Chapter IV.

Examining Figure B.1, the coordinate system origin was at the free end of the wire at  $x=0$  with the fixed upper end at  $x=L$ . The displacement from equilibrium was defined as  $v(x,t)$ . Note that the spatial distance along the classical dangling chain was defined as  $x$  vice the  $S$  used in Chapter IV. This was done to distinguish clearly between the classical dangling chain equations and the equations for the towed wire.

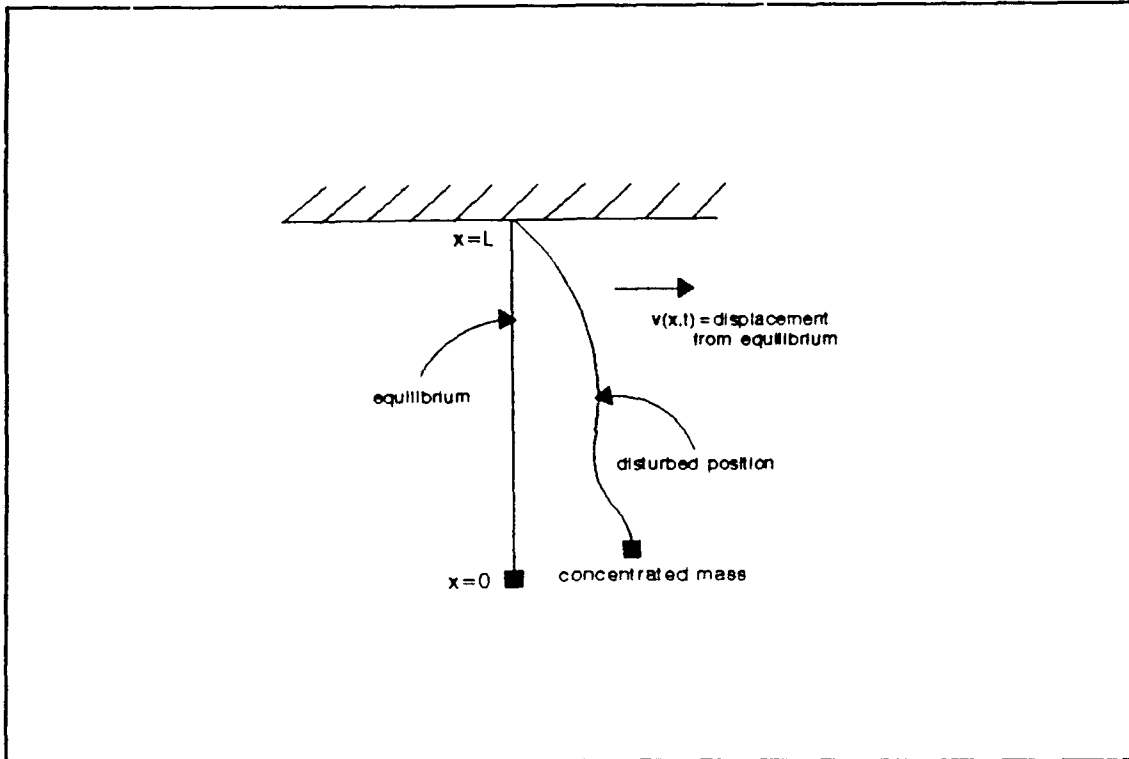


**Figure B.1:** Dangling Chain Model

A time independent tension distribution,  $T(x)$ , was defined for the dangling chain.  $T(x)$  could be any arbitrary distribution but was time independent in the classical problem. The validity of the use of the time independent  $T(x)$  vice the fully time dependent  $T(x,t)$  for the case of the towed cable was addressed in Chapter IV. Later in this appendix, a specific tension distribution will be defined for use in the solution of the classical equations.  $\mu$  was defined as the mass per unit length of chain and the displacements from equilibrium,  $v(x,t)$ , were assumed "small". The validity of this assumption was addressed in Chapter IV for the case of the towed cable. The net lateral force on an element of hanging chain is given by equation

(B.1). The net lateral force in (B.1) was equilibrated by the inertial reaction to provide the initial form of the hanging chain equation of motion in (B.2).

$$\left[ \pi(x) \frac{\partial v(x, t)}{\partial x} + \frac{\partial}{\partial x} \left( \pi(x) \frac{\partial v(x, t)}{\partial x} \right) dx \right] - \left[ \pi(x) \frac{\partial v(x, t)}{\partial x} \right] = \frac{\partial}{\partial x} \left( \pi(x) \frac{\partial v(x, t)}{\partial x} \right) dx \quad (\text{B.1})$$

$$\mu \frac{\partial^2 v(x, t)}{\partial t^2} dx = \frac{\partial}{\partial x} \left( \pi(x) \frac{\partial v(x, t)}{\partial x} \right) dx \quad (\text{B.2})$$

The arbitrary forcing function,  $Q(x, t)$ , was defined, which was perpendicular to the wire at any point and was in terms of force per unit length at time  $t$ . The origin of this forcing function for the towed wire case will be discussed in detail in Appendix C. In equation (B.3),  $Q(x, t)$  was added directly as a term to equation (B.2) above. Note that since  $dx$  was included in each term, it was eliminated from the expression.

$$\mu \frac{\partial^2 v(x, t)}{\partial t^2} = \frac{\partial}{\partial x} \left( \pi(x) \frac{\partial v(x, t)}{\partial x} \right) + Q(x, t) \quad (\text{B.3})$$

Volterra and Zachmanoglou outline the boundary conditions for the classical dangling chain or vibrating string problem with one fixed and one free boundary condition [Ref 19:pp.418-420].<sup>1</sup> Assuming that the chain begins at rest and for the equilibrium shape (vertically

---

<sup>1</sup> Volterra and Zachmanoglou also defined as a boundary condition that the partial derivative with respect to  $x$  had to vanish at the free end. This was incorrect as will be shown later in this appendix.

hanging), the formulation of the classical dangling chain problem was written as in equation (B.4)

$$\begin{aligned} \mu \frac{\partial^2 v(x, t)}{\partial t^2} &= \frac{\partial}{\partial x} \left( T(x) \frac{\partial v(x, t)}{\partial x} \right) + Q(x, t) \\ \text{B.C. } v(L, t) &= 0 \quad v(0, t) \rightarrow \text{Bounded} \\ \text{I.C. } v(x, 0) &= 0 \quad \frac{\partial v}{\partial t}(x, 0) = 0 \end{aligned} \quad (\text{B.4})$$

The classical dangling chain boundary conditions were then modified slightly to account for the presence of the drogue at the bottom of the wire. Remembering that the displacements for the dangling chain were defined lateral to the wire, the lateral component of the tension distribution when added to the forcing function at the drogue, had to balance the acceleration of the drogue. Thus a third boundary condition was immediately written. The modified governing equation with initial and boundary conditions is provided in equation (B.5) where  $W_D$  was the weight of the drogue.

$$\begin{aligned} \mu \frac{\partial^2 v(x, t)}{\partial t^2} &= \frac{\partial}{\partial x} \left( T(x) \frac{\partial v(x, t)}{\partial x} \right) + Q(x, t) \\ \text{B.C. } v(L, t) &= 0 \quad v(0, t) \rightarrow \text{Bounded} \\ \pi(0) \frac{\partial}{\partial x} v(0, t) &= \frac{W_D}{g} \frac{\partial^2 v(0, t)}{\partial t^2} \\ \text{I.C. } v(x, 0) &= 0 \quad \frac{\partial v}{\partial t}(x, 0) = 0 \end{aligned} \quad (\text{B.5})$$

Next, the classical problem was modified for use in the towed wire problem. The coordinate system was reversed with the upper gridpoint at  $S=0$  and the lower gridpoint at  $S=L$ . Note that both the classical problem and the towed wire problem used a wire length of  $L$ . As mentioned above, the

spatial distance along the wire was re-defined as  $S$  vice  $x$  and the initial condition was defined as the steady-state wire position,  $f(S)$  vice a zero displacement. The tension,  $T(S)$ , was the steady-state model tension distribution. The reformulated problem statement is presented in equation (B.6).

$$\begin{aligned} \mu \frac{\partial^2 v(S, t)}{\partial t^2} &= \frac{\partial}{\partial S} \left( T(S) \frac{\partial v(S, t)}{\partial S} \right) + Q(S, t) \\ \text{B.C. } v(0, t) &= 0 \quad v(L, t) = \text{Bounded} \\ T(L) \frac{\partial}{\partial S} v(L, t) &= \frac{W_D}{g} \frac{\partial^2 v(L, t)}{\partial t^2} \\ \text{I.C. } v(S, 0) &= f(S) \quad \frac{\partial v}{\partial t}(S, 0) = 0 \end{aligned} \tag{B.6}$$

In the towed wire problem, two separate, orthogonal solutions to equation (B.6) were required to model the two-dimensional displacement of each point around the equilibrium position. The  $\Delta S$  compatibility condition for the first internal gridpoint and the definition of the unit tangent vector for all subsequent gridpoints were then used to make the solution into a three-dimensional model. The procedure is fully discussed in Appendix D when the superposition formulas are developed.

The classical dangling chain problem both with and without a concentrated mass at the end was solved analytically to provide physical insight into the problem of the trailing wire antenna. The case where the concentrated mass was not present was solved by beginning with the definition of the dangling chain provided in (B.4). As

mentioned earlier, a specific tension distribution was chosen for solving the classical problem. A uniform tension distribution was assumed of the form  $T(x)=\mu gx$ . Limiting the analysis to the homogeneous solution allowed the forcing function,  $Q(x,t)$ , to equal zero. Substituting for  $T(x)$  in equation (B.4), eliminating  $Q(x,t)$  and canceling  $\mu$  from both sides resulted in equation (B.7). Equation (B.7) was solved using the technique of separation of variables.

$$\frac{\partial^2 v}{\partial t^2} = g \frac{\partial}{\partial x} \left( x \frac{\partial v}{\partial x} \right) \quad (\text{B.7})$$

Assuming a solution of the form of equation (B.8), and substituting into (B.7) resulted in (B.9), where the exponential terms were canceled from both sides. Applying the chain rule to the right hand side of (B.9) and simplifying, resulted in (B.10), which was beginning to take the form of Bessel's equation.

$$v(x, t) = V(x) e^{i\omega t} \quad (\text{B.8})$$

$$-V(x)\omega^2 e^{i\omega t} = g \frac{\partial}{\partial x} \left( x \frac{\partial}{\partial x} (V(x) e^{i\omega t}) \right) \quad (\text{B.9})$$

$$x \frac{d^2 V(x)}{dx^2} + \frac{dV(x)}{dx} + \frac{\omega^2}{g} V(x) = 0 \quad (\text{B.10})$$

Defining  $k^2 = \omega^2/g$ , a change of variable was performed in terms of  $z = 2kx^{1/2}$  by first, expanding each derivative in (B.10) in terms of  $z$ . For example, the term  $dV/dx$  was

expanded in (B.11) and the substitution for  $z$  was made to get the middle term in (B.10). The process was repeated for the second derivative term, substituted into (B.10) and the entire equation multiplied through by  $x/k^2$  to obtain (B.12) which was in the form of Bessel's equation. The solution of this form of Bessel's equation was in terms of Bessel functions of the first and second kind of order zero and the solution was written as in (B.13) where  $z$  was replaced by its definition and thus  $V$  was again in terms of  $x$ .

$$\frac{dV}{dx} = \frac{dV}{dz} \frac{dz}{dx} \quad (\text{B.11})$$

$$z^2 \frac{d^2 V}{dz^2} + z \frac{dV}{dz} + z^2 V = 0 \quad (\text{B.12})$$

$$V(x) = AJ_0\left(2\omega\sqrt{\frac{x}{g}}\right) + BY_0\left(2\omega\sqrt{\frac{x}{g}}\right) \quad (\text{B.13})$$

Now, it was a property of  $Y_m(z)$  that it approaches  $\infty$  as  $z$  approaches zero and thus by assuming that only bounded solutions were physically possible in this case, it could be seen that  $B$  had to equal zero. For the first boundary condition to be satisfied,  $\omega_n$  in (B.14) had to take on only those values such that the Bessel function had a zero crossing. The zero crossings may be derived via table look up or any number of standard software packages. There were an infinite set of these crossings corresponding to the



infinite set of eigenvalues. The three lowest eigenvalues are shown in (B.15) for a sample wire length of  $L=20,290$  feet. The eigenvector was derived by substituting the eigenvalue,  $\omega_n$ , into (B.14) and plotting  $V(x)$ . The homogeneous solution consisted of a mixture of this infinite set of eigenvectors.

$$V(x) = AJ_0 \left( 2\omega_n \sqrt{\frac{x}{g}} \right) \quad (\text{B.14})$$

$$\begin{aligned} \omega_1 &= \frac{2.40483}{2} \sqrt{\frac{32.2}{L}} = 0.0479006 \text{ sec}^{-1} \\ \omega_2 &= \frac{5.52008}{2} \sqrt{\frac{32.2}{L}} = 0.109952 \text{ sec}^{-1} \\ \omega_3 &= \frac{8.65373}{2} \sqrt{\frac{32.2}{L}} = 0.172369 \text{ sec}^{-1} \end{aligned} \quad (\text{B.15})$$

Next, the dangling chain problem was solved for the case where a concentrated mass was present at the end of the chain or wire as shown in equation (B.5). The concentrated mass corresponded to the drogue at the bottom and was of mass  $W_D/g$ . The concentrated mass was reexpressed as an equivalent length of chain with density  $\mu$  per unit length as in equation (B.16). The tension variation was adjusted for the influence of the concentrated mass as in equation (B.17).

$$L_{eq} = \frac{W_D}{\mu g} \quad (\text{B.16})$$

$$T(x) = \left( \mu x + \frac{W_b}{g} \right) g = \mu g(x + L_{eq}) \quad (B.17)$$

for  $0 \leq x \leq L$

Applying the same procedure outlined in the development of equations (B.7) through (B.10), the governing differential equation in (B.17) was re-expressed in terms of the modified tension equation in (B.18). Note that in this case, equation (B.18) did not apply to the portion of the chain beyond the original length,  $L$ . Applying the transformation  $y = x + L_{eq}$  and  $dx = dy$  resulted in (B.19). Stating the boundary conditions in terms of the variable  $y$  resulted in equation (B.20).

$$\frac{d}{dx} \left[ (x + L_{eq}) \frac{dV(x)}{dx} \right] + \frac{\omega^2}{g} V(x) = 0 \quad (B.18)$$

for  $0 < x \leq L$

$$\frac{d}{dy} \left[ y \frac{dV(y)}{dy} \right] + \frac{\omega^2}{g} V(y) = 0 \quad (B.19)$$

for  $L_{eq} < y \leq L + L_{eq}$

$$\begin{aligned} V(y) &= 0 \text{ at } y = L + L_{eq} \\ \frac{dV(y)}{dy} + \frac{\omega^2}{g} V(y) &= 0 \text{ at } y = L_{eq} \end{aligned} \quad (B.20)$$

The general solution of equation (B.19) is as shown in equation (B.21) with the requirement that the boundary conditions of (B.20) must be met. Unlike the previous problem without the concentrated mass, the boundary conditions do not allow the elimination of the  $Y_0$  term.

$$V(y) = AJ_0 \left( 2\omega \sqrt{\frac{y}{g}} \right) + BY_0 \left( 2\omega \sqrt{\frac{y}{g}} \right) \quad (\text{B.21})$$

The requirement of concurrent satisfaction of the boundary conditions in (B.20) and the general solution of (B.21) allowed the eigenvalue problem to be stated as shown in equation (B.22).

$$\begin{bmatrix} J_0\beta & Y_0\beta \\ J_1\alpha - \frac{1}{2}\alpha J_0(\alpha) & Y_1(\alpha) - \frac{1}{2}\alpha Y_0(\alpha) \end{bmatrix} \begin{bmatrix} A \\ B \end{bmatrix} = \begin{bmatrix} 0 \\ 0 \end{bmatrix}$$

where  $\beta = 2\omega \sqrt{\frac{L+L_{eq}}{g}}$   
and  $\alpha = 2\omega \sqrt{\frac{L_{eq}}{g}}$

(B.22)

The characteristic equation of the coupled transcendental functions presented in (B.22) was solved to obtain the first three eigenvalues as shown in equation (B.23) for a test case of 20,280 feet of wire, a drogue of 81.95 pounds and the 3X7 wire. The equivalent length,  $L_{eq}$ , of the drogue for this case was 1319 feet which changed the first few modal frequencies on the order of two percent.

$$\begin{aligned} \omega_1 &= 0.047 \text{ sec}^{-1} \\ \omega_2 &= 0.111 \text{ sec}^{-1} \\ \omega_3 &= 0.181 \text{ sec}^{-1} \end{aligned} \quad (\text{B.23})$$

As mentioned earlier, Volterra and Zachmanoglou defined a third boundary condition on the dangling chain problem as shown in equation (B.24). Careful examination of this

condition showed it to be incorrect. Equation (B.25) was the analytical solution for the dangling chain as derived earlier in this appendix.

$$V(L, t)=0, \quad v(0, t) \Rightarrow \text{Bounded}, \quad \frac{\partial v(0, t)}{\partial x}=0 \quad (\text{B.24})$$

$$V(x)=AJ_0\left(2\omega\sqrt{\frac{x}{g}}\right) \quad (\text{B.25})$$

For (B.24) to be true,  $dJ_0(0)/dx=0$  had to be true. Defining  $z$  as in equation (B.26) and applying the chain rule to find the derivative of (B.25) with respect to  $x$  resulted in (B.27). Performing the derivatives and substituting (B.26) into the result provided (B.28). In the limit, as  $x$  approached 0, (B.28) approached  $dJ_0(0)/dx=0/0$  requiring L'Hospital's rule.

$$z=2\omega\sqrt{\frac{x}{g}} \quad (\text{B.26})$$

$$\frac{dV(x)}{dx}=A\frac{dJ_0(x)}{dx}=A\frac{dJ_0(z)}{dz}\frac{dz}{dx} \quad (\text{B.27})$$

$$\frac{dV(x)}{dx} = -A \frac{J_1\left(2\omega\sqrt{\frac{x}{g}}\right)\omega}{\sqrt{g}\sqrt{x}} \quad (\text{B.28})$$

Multiplying (B.28) by  $z/z$  and applying L'Hospital's rule as well as the identity in equation (B.29) [Ref. 20:p. 3] resulted in equation (B.30). Equation (B.30) resulted in (B.31) and showed that the slope at the end of the wire was not zero but in fact finite. [Ref. 15]

$$\frac{d}{dz} zJ_1(z) = zJ_0(z) \quad (\text{B.29})$$

$$\frac{\frac{d}{dx} \left[ -2\omega\sqrt{\frac{x}{g}} J_1\left(2\omega\sqrt{\frac{x}{g}}\right)\omega \right]}{\frac{d}{dx} [2\omega x]} = - \frac{\omega^2 J_0\left(2\omega\sqrt{\frac{x}{g}}\right)}{g} = - \frac{\omega^2}{g} \quad (\text{B.30})$$

for  $z=x=0$

$$\frac{dJ_0(0)}{dx} = 0 \quad (\text{B.31})$$

The classical, analytical solution for the dangling chain did not account for a number of factors germane to the trailing wire antenna problem. The assumption of a linear tension distribution based upon the mass of the chain was in error as seen when compared to the static model tension distribution in Chapter III. Additionally, the classical dangling chain did not include a dissipation mechanism such as might be due to viscous damping or aerodynamic

influences. Finally, the real problem was three-dimensional in nature and could not be adequately modeled by the classical formulation. Despite these shortcomings, the classical problem was invaluable for providing insight into the physics of the problem and the form of the equations to use. These insights were applied several times in Chapter IV.

The dangling chain portion of the dynamic model was validated by modifying the code to simulate the case of the dangling chain without the concentrated mass on the end of the wire. Equation (B.14) indicated that for an arbitrary initial wire shape, solving the analytical, homogeneous solution would require the combination of some number of the infinite set of eigenvectors corresponding to the infinite set of eigenvalues,  $\omega_n$ . Comparison of the computer simulation homogeneous response to the analytical homogeneous solutions would then be a very tedious task. Due to the principle of orthogonality, a much simpler alternative existed whereby the initial gridpoint distribution was selected to be in the exact shape of an eigenvector [Ref. 15]. When then allowed to oscillate, a good numerical approximation was expected to repeat the same eigenvector shape at the frequency  $\omega_n$ , the eigenvalue or eigenfrequency. This was the technique chosen.

Equation (B.15) contains the first three eigenvalues for a wire length of 20,290 feet. The first two eigenfunctions

are plotted in Figure B.2. The solid line eigenvector shape in Figure B.2 was used as the initial wire distribution. Figure B.3 was the time history of the displacement of the free end gridpoint. Figure B.3 shows that the free end gridpoint oscillated with a period equal to 131 seconds which was the same as the period of  $\omega_1$ , the first eigenfrequency. The process was repeated for  $\omega_2$  and the dashed line eigenfunction of Figure B.2. Figure B.4 is the resulting time history of the free end gridpoint. The period of 57 seconds corresponded to the period of the eigenfrequency. Both Figures B.3 and B.4 show that the homogeneous oscillations continued to oscillate at the eigenfrequency without the intrusion of harmonics indicating that the model and the governing equation shared the same two eigenfrequencies and eigenvectors.

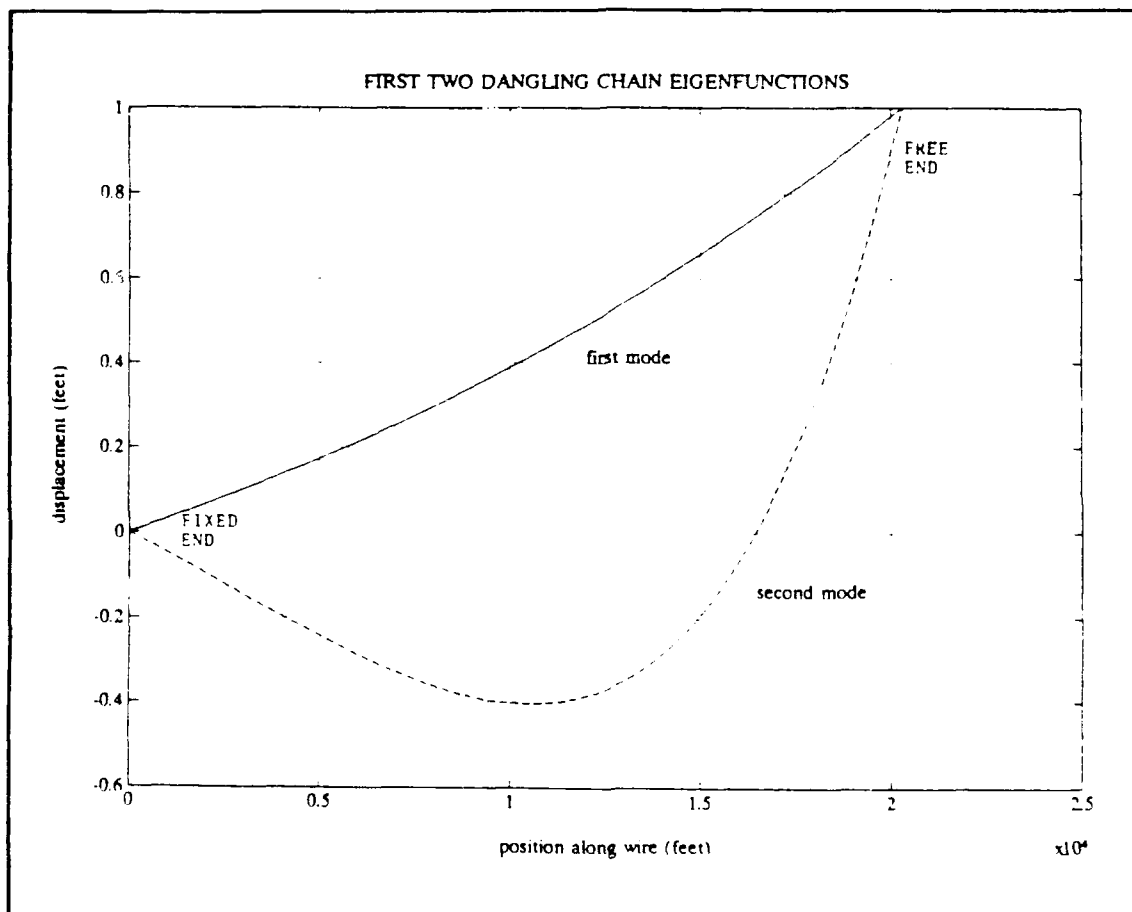


**Figure B.2:** First Two Dangling Chain Eigenfunctions



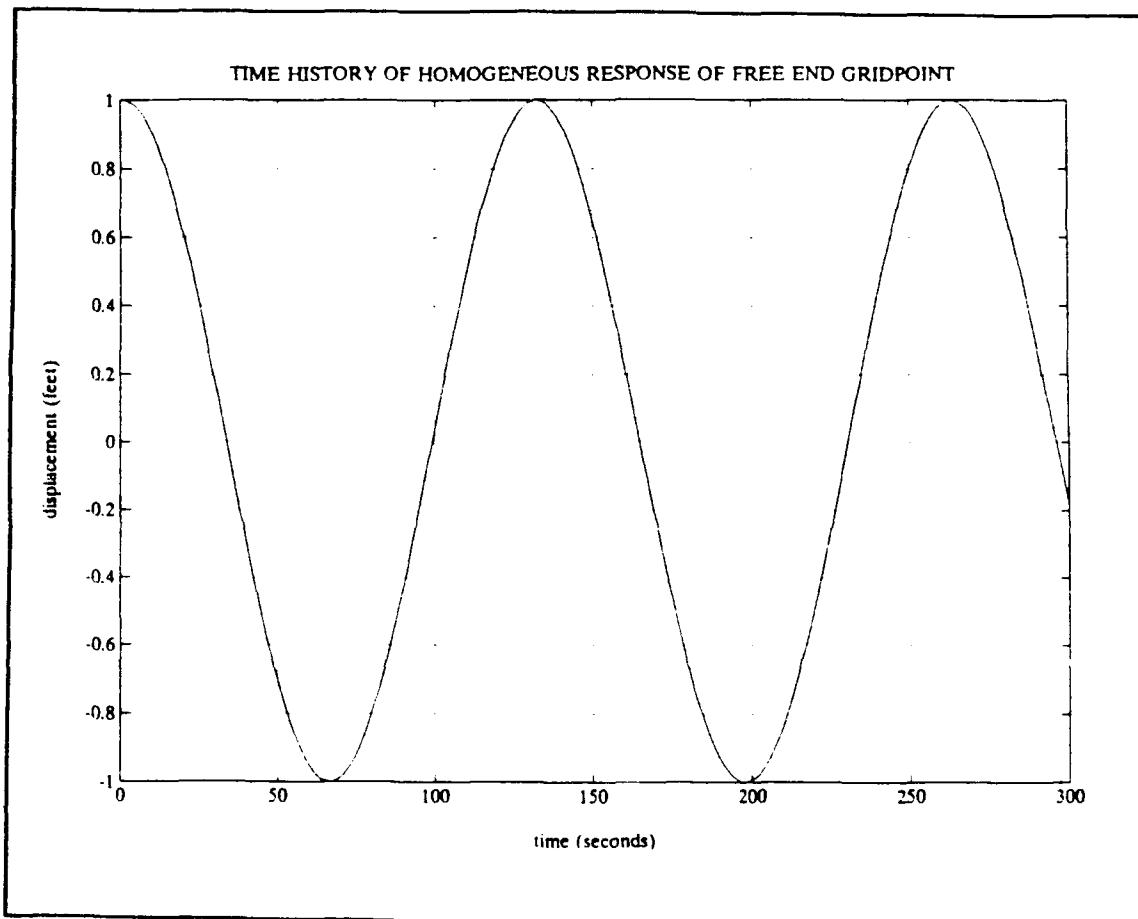


**Figure B.3:** Time History of Homogeneous Response of Free End Gridpoint as Modeled by Simulation

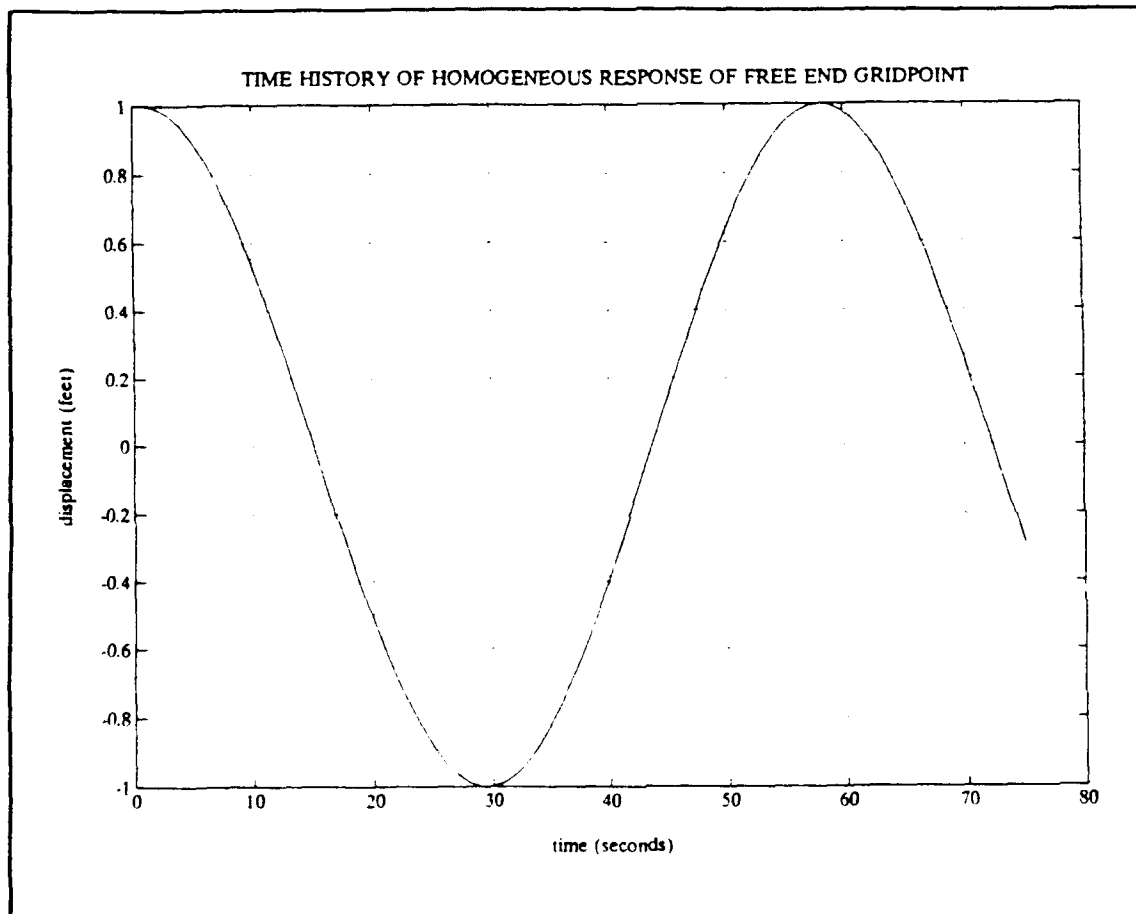


**Figure B.4:** Time History of Homogeneous Response of Free End Gridpoint as Modeled by Simulation

## APPENDIX C

### FORCING FUNCTION DEVELOPMENT

In applying the wind as a forcing function to the wire dynamics problem, it was important to first note that under the assumption of a steady-state angle of bank turn, the towplane moved with the airmass, and so the forcing function due to the wind was in fact zero at the towplane. The drifting towplane, in a constant angle of bank orbit, is depicted in Figure C.1. The required apparent forcing wind was then derived by adding the negative of the wind vector at altitude to the winds at each gridpoint including the towplane end gridpoint.

With the apparent forcing wind defined, an arbitrary reference system was set up such that the towplane was aligned with the heading of 000 at time zero. This was possible because the correlation between the defined cylindrical coordinate system and the compass direction was completely arbitrary. The convention chosen for the definition of the wind heading was that the wind direction was the heading from which the wind came from vice the actual direction that the wind vector pointed. This was the normal aeronautical definition used in the flight test data that will be discussed later. Equation (4.1), the governing equation of the dangling chain model, was derived assuming

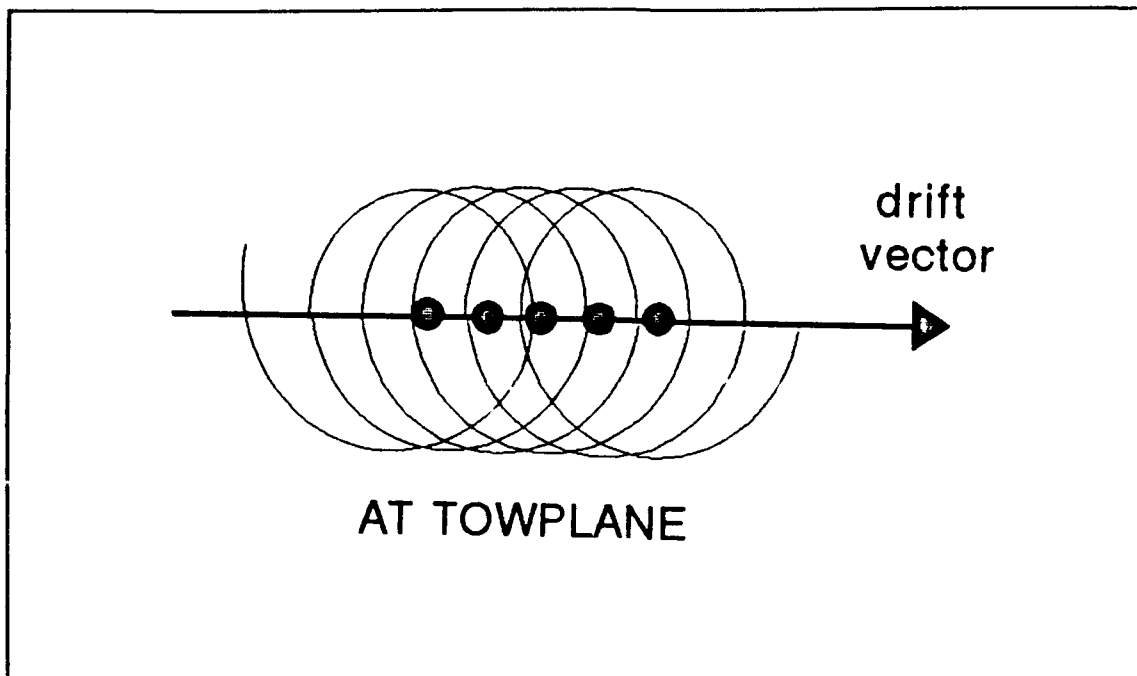


**Figure C.1:** Towplane Drift Due to Wind During Steady State Turn

that all displacements, as well as the forcing function,  $Q_{n,m}$ , were perpendicular to the chain.  $Q_{n,m}$  was thus defined as perpendicular to the wire tangent vector. The forcing function was defined from the apparent forcing wind. Since the forcing function was defined perpendicular to the wire, only that component of the apparent forcing wind perpendicular to the wire was used to calculate the forcing function. The orientation of the apparent forcing wind with the wire varied harmonically as the wire orbited within the airmass. The calculations were performed for each orthogonal component of the oscillation and so one harmonically varying wind induced forcing component was described using a sine function while the second was described using a cosine function. Two adjustments in

phasing were required to the harmonic functions. As mentioned above, the apparent forcing wind was resolved into components perpendicular to the wire. These calculations were performed for the case where the gridpoint  $\bar{e}_\theta$  vector was oriented along the 000 heading described earlier in this paragraph and assuming that the apparent forcing wind was coming from the 000 direction. The first phase correction was the  $\theta$  coordinate at each gridpoint to account for the fact that for every gridpoint except the towplane's, the wire shape had to rotate through the  $\theta$  angle for  $\bar{e}_\theta$  to be aligned with the 000 heading. The second phase correction accounted for the wind heading at each gridpoint being in general, different from 000. Finally, the aerodynamic coefficients of the wire were used to convert the forcing wind into a force vector, which was the true forcing function desired.

$\theta'$  was defined as the combined phase shift requirement at the current gridpoint,  $\theta$  as the current gridpoint angular coordinate and  $\theta_w$  as  $360^\circ$  wind direction. Next,  $A_n$  and  $B_n$  were defined as the orthogonal components of the maximum possible perpendicular component of the forcing function, in pounds force, at each gridpoint. Arbitrarily,  $A_n$  was assigned to correspond to the radial coordinate direction and  $B_n$  to the  $\theta$  coordinate direction. These were the forces that would exist upon a vertically oriented wire at a time when the orthogonal component of the apparent forcing

wind of interest was at a maximum. Since the wire was axisymmetric,  $A_n = B_n$ . Next,  $V_{\theta n}$  was defined as the magnitude of the component of  $B_n$  perpendicular to the unit tangent vector at each gridpoint  $n$  and  $V_{Rn}$  as the corresponding  $A_n$  component. Finally, note that in keeping with the small displacement assumptions, the entire forcing function development made use of the steady-state geometry whenever possible in order to simplify the final expressions. The process was begun by developing the  $\theta$  component of the forcing function. The central difference approximation of the definition of the unit tangent vector is repeated in (C.1) and used to determine the component of the maximum value of the forcing function resolved along the wire unit tangent vector in (C.2).

$$\overline{e_{sn}} = \left( \frac{R_{n+1} - R_{n-1}}{2\Delta S} \right) \overline{e_R} + R_n^2 \left( \frac{\theta_{n+1} - \theta_{n-1}}{2\Delta S} \right) \overline{e_\theta} + \left( \frac{Z_{n+1} - Z_{n-1}}{2\Delta S} \right) \overline{e_k} \quad (C.1)$$

$$B_n \overline{e_\theta} \cdot \overline{e_{sn}} = \frac{B_n R_n (\theta_{n+1} - \theta_{n-1})}{2\Delta S} \quad (C.2)$$

(C.3) was then the component of the maximum value of the forcing function perpendicular to the wire. (C.4) was the central difference approximation of (C.3). Equation (C.5) was a rearranged version of (C.4) in the form in which it is used.

$$\overline{V_{\theta n}} = B_n \overline{e_{\theta}} - (B_n \overline{e_{\theta}} \cdot \overline{e_{sn}}) \overline{e_{sn}} \quad (\text{C.3})$$

$$\overline{V_{\theta n}} = B_n \overline{e_{\theta}} - B_n R_n \left( \frac{\theta_{n+1} - \theta_{n-1}}{2\Delta S} \right) \left[ \left( \frac{R_{n+1} - R_{n-1}}{2\Delta S} \right) \overline{e_R} + R_n \left( \frac{\theta_{n+1} - \theta_{n-1}}{2\Delta S} \right) \overline{e_{\theta}} + \left( \frac{Z_{n+1} - Z_{n-1}}{2\Delta S} \right) \overline{e_K} \right] \quad (\text{C.4})$$

$$\overline{V_{\theta n}} = \frac{-B_n R_n (\theta_{n+1} - \theta_{n-1}) (R_{n+1} - R_{n-1})}{2\Delta S} \overline{e_R} + \left[ B_n - B_n \left( \frac{R_n (\theta_{n+1} - \theta_{n-1})}{2\Delta S} \right)^2 \right] \overline{e_{\theta}} - \frac{B_n R_n (\theta_{n+1} - \theta_{n-1}) (Z_{n+1} - Z_{n-1})}{2\Delta S} \overline{e_K} \quad (\text{C.5})$$

Equation (C.6) was needed because the dynamic model only required the magnitude of the vector derived in equation (C.5). The process was repeated for the second orthogonal component in (C.7) to (C.9). (C.10) was the maximum forcing function in terms of the apparent forcing wind velocity and aerodynamic coefficients and (C.11) and (C.12) are the final form of the forcing function equations.

$$V_{\theta n} = B_n \sqrt{\left( \frac{R_n (\theta_{n+1} - \theta_{n-1}) (R_{n+1} - R_{n-1})}{2\Delta S} \right)^2 + \left( 1 - \left( \frac{R_n (\theta_{n+1} - \theta_{n-1})}{2\Delta S} \right)^2 \right)^2 + \left( \frac{R_n (\theta_{n+1} - \theta_{n-1}) (Z_{n+1} - Z_{n-1})}{2\Delta S} \right)^2} \quad (\text{C.6})$$

$$A_n \overline{e_{sn}} \cdot \overline{e_R} = A_n \left( \frac{R_{n+1} - R_{n-1}}{2\Delta S} \right) \quad (\text{C.7})$$

$$\begin{aligned} \overline{V_{Rn}} = A_n \overline{e_R} - A_n \left( \frac{R_{n+1} - R_{n-1}}{2\Delta S} \right)^2 \overline{e_R} + A_n \left( \frac{R_{n+1} - R_{n-1}}{2\Delta S} \right) R_n \left( \frac{\theta_{n+1} - \theta_{n-1}}{2\Delta S} \right) \overline{e_\theta} \\ + A_n \left( \frac{R_{n+1} - R_{n-1}}{2\Delta S} \right) \left( \frac{Z_{n+1} - Z_{n-1}}{2\Delta S} \right) \overline{e_K} \end{aligned} \quad (C.8)$$

$$V_{Rn} = A_n \sqrt{\left( 1 - \left( \frac{R_{n+1} - R_{n-1}}{2\Delta S} \right)^2 \right)^2 + \left( \frac{(R_{n+1} - R_{n-1})}{2\Delta S} R_n \frac{(\theta_{n+1} - \theta_{n-1})}{2\Delta S} \right)^2 + \left( \frac{(R_{n+1} - R_{n-1})}{2\Delta S} \frac{(Z_{n+1} - Z_{n-1})}{2\Delta S} \right)^2} \quad (C.9)$$

$$A_n = B_n = \frac{1}{2} \rho_n V_{wn}^2 D (C_D + C_f) \quad (C.10)$$

$$\begin{aligned} \overline{Q_{eR}}(x) = V_{Rn} \sin(\dot{\theta} t - \theta') \\ \text{where} \\ \theta' = \theta - \theta_w \end{aligned} \quad (C.11)$$

$$\overline{Q_{\theta\theta}}(x) = V_{\theta n} \cos(\dot{\theta} t - \theta') \quad (C.12)$$

Equations (C.6), (C.9), (C.10), (C.11) and (C.12) provided a complete description of the forcing function caused by the apparent forcing wind at each gridpoint. Wind data may be contrived or radiosonde derived flight test data may be used. The simulation programs allow for winds to be defined internally to the program or imported as data files.



## APPENDIX D

### SUPERPOSITION EQUATIONS DEVELOPMENT

The development of the superposition equations was begun by restating the definition of the unit tangent vector in equation (D.1) and defining the  $X_{n,m}$  component as being contained in the  $\bar{e}_R, \bar{e}_\theta$  plane, that is, orthogonal to the Z axis. (D.2) was the normalized components of the unit tangent vector projected onto the  $\bar{e}_R, \bar{e}_\theta$  plane. The  $\bar{e}_R$  and  $\bar{e}_\theta$  components of  $X_{n,m}$  were then derived by crossing (D.2) with the  $\bar{e}_K$  vector and then multiplying the resulting vector, which was still a unit vector, by  $X_{n,m}$  in (D.3). The final result is in (D.4).

$$\bar{e}_{sn} = \left( \frac{R_{n+1} - R_{n-1}}{2\Delta S} \right) \bar{e}_R + \frac{R_n(\theta_{n+1} - \theta_{n-1})}{2\Delta S} \bar{e}_\theta + \left( \frac{Z_{n+1} - Z_{n-1}}{2\Delta S} \right) \bar{e}_K \quad (D.1)$$

$$projection = \frac{\left( \frac{R_{n+1} - R_{n-1}}{2\Delta S} \right) \bar{e}_R + \frac{R_n(\theta_{n+1} - \theta_{n-1})}{2\Delta S} \bar{e}_\theta}{\sqrt{\left( \frac{R_{n+1} - R_{n-1}}{2\Delta S} \right)^2 + \left( \frac{R_n(\theta_{n+1} - \theta_{n-1})}{2\Delta S} \right)^2}} \quad (D.2)$$

$$X'_{n,m} = X_{n,m} [projection \times \bar{e}_K] \quad (D.3)$$

$$X'_{n,m} = \frac{X_{n,m} \left[ \frac{R_n(\theta_{n+1} - \theta_{n-1})}{2\Delta S} \overline{e_R} + \left( \frac{R_{n+1} - R_{n-1}}{2\Delta S} \right) \overline{e_\theta} \right]}{\sqrt{\left( \frac{R_{n+1} - R_{n-1}}{2\Delta S} \right)^2 + \left( \frac{R_n(\theta_{n+1} - \theta_{n-1})}{2\Delta S} \right)^2}} \quad (D.4)$$

$Y_{n,m}'$  was derived by noting that  $X_{n,m}'$  and  $Y_{n,m}'$  are orthogonal. Equation (D.4) was changed into a unit vector by dividing by  $|X_{n,m}'|$  and crossed with the wire unit tangent vector to get the unit vector along the  $Y_{n,m}'$  direction, as in (D.5). Remember that the cross product of orthogonal unit vectors is already of unit magnitude and does not require subsequent normalization. Multiplying by  $Y_{n,m}$  and performing the cross product resulted in  $Y_{n,m}'$  as in (D.7) where *same* is defined in (D.6).

$$\overline{e_{y'n}} = \overline{e_{x'n}} \times \overline{e_{sn,m}} \quad (D.5)$$

$$same = \sqrt{\left( \frac{R_{n+1} - R_{n-1}}{2\Delta S} \right)^2 + \left( \frac{R_n(\theta_{n+1} - \theta_{n-1})}{2\Delta S} \right)^2} \quad (D.6)$$

$$\begin{aligned}
Y'_{n,m} = Y_{n,m} & \left[ \frac{\left( \frac{R_{n+1}-R_{n-1}}{2\Delta S} \right) \left( \frac{Z_{n+1}-Z_{n-1}}{2\Delta S} \right)}{\text{same}} \overline{e_R} \right. \\
& - \frac{R_n \left( \frac{\theta_{n+1}-\theta_{n-1}}{2\Delta S} \right) \left( \frac{Z_{n+1}-Z_{n-1}}{2\Delta S} \right)}{\text{same}} \overline{e_\theta} \\
& \left. + \frac{\left( \frac{R_n(\theta_{n+1}-\theta_{n-1})}{2\Delta S} \right)^2 - \left( \frac{R_{n+1}-R_{n-1}}{2\Delta S} \right)^2}{\text{same}} \overline{e_K} \right] \quad (D.7)
\end{aligned}$$

The next step was to add the  $\overline{e_R}$  and  $\overline{e_\theta}$  components of equations (D.4) and (D.7) to the steady-state  $R_n$  and  $\theta_n$  coordinates at each gridpoint to generate the superimposed  $RS_{n,m}$  and  $\theta S_{n,m}$  coordinates as in (D.8) and (D.9). Substitutions were made from (D.4), (D.6) and (D.7) to get (D.10) and (D.11), the final superposition equations in their implemented form.

$$RS_{n,m} = R_n + X'_{n,m} \overline{e_R} + Y'_{n,m} \overline{e_R} \quad (D.8)$$

$$\theta S_{n,m} = \theta_n + \frac{X'_{n,m}}{R_n} \overline{e_\theta} + \frac{Y'_{n,m}}{R_n} \overline{e_\theta} \quad (D.9)$$

$$RS_{n,m} = R_n + X_{n,m} \left[ \frac{R_n(\theta_{n+1}-\theta_{n-1})}{2\Delta S \text{ same}} \right] + Y_{n,m} \left[ \frac{(R_{n+1}-R_{n-1})(Z_{n+1}-Z_{n-1})}{(2\Delta S)^2 \text{ same}} \right] \quad (D.10)$$

$$\theta_{S_{n,m}} = \theta_n + X_{n,m} \left[ \frac{(R_{n+1} - R_{n-1})}{R_n 2\Delta S \text{ same}} \right] - Y_{n,m} \left[ \frac{(\theta_{n+1} - \theta_{n-1})(Z_{n+1} - Z_{n-1})}{(2\Delta S)^2 \text{ same}} \right] \quad (D.11)$$

The  $\Delta S$  constraint was then used to generate the superimposed  $Z$  coordinate for the first internal gridpoint as repeated in (D.12) and the central difference approximation of the unit tangent vector, repeated in (D.13), was solved for  $Z_{n,m}$  for all subsequent gridpoints.

$$Z_{n+1} = Z_{n-1} \pm \sqrt{4\Delta S^2 - (R_{n+1} - R_{n-1})^2 - R_n^2 (\theta_{n+1} - \theta_{n-1})^2} \quad (D.12)$$

$$\left( \frac{R_{n+1} - R_{n-1}}{2\Delta S} \right)^2 + R_n^2 \left( \frac{\theta_{n+1} - \theta_{n-1}}{2\Delta S} \right)^2 + \left( \frac{Z_{n+1} - Z_{n-1}}{2\Delta S} \right)^2 = 1 \quad (D.13)$$

## APPENDIX E

### DYNAMIC MODEL CODE

```
PROGRAM TAC29
C THIS PROGRAM SOLVES THE DANGLING CHAIN PROBLEM FOR A
C PROVIDED TENSION DISTRIBUTION, INITIAL POSITION AND FORCING
C FUNCTION AND THEN SUPERIMPOSES THE SOLUTION UPON THE WIRE
C STEADY STATE SOLUTION. A CENTRAL DIFFERENCE SCHEME IS USED.
C THIS MODEL DEPARTS FROM THE CLASSIC DANGLING CHAIN IN
C THAT PSEUDO-DAMPING IN THE SENSE OF LATERAL DRAG DUE TO THE
C OSCILLATION IS ACCOUNTED FOR AS WELL AS RESTORATIVE FORCES DUE
C TO THE CHANGE IN THE ANGLE OF ATTACK IN THE DISPLACED STATE.
C THE PROGRAM REQUIRES THE OUTPUT FILES FROM TAC17. ANTI-YOYO
C IS AVAILABLE FOR USE.
C*****
C DECLARE AND DIMENSION VARIABLES.
C
C SCALARS FIRST.
C
C ACCD IS THE ACCELERATION OF THE DROGUE AT EACH TIME STEP.
REAL ACCD
C ALFAS IS THE ANGLE OF ATTACK OF THE SUPERIMPOSED WIRE AT EACH
C GRIDPOINT.
REAL ALFAS
C CD IS THE PERPENDICULAR COEFFICIENT OF DRAG FOR THE WIRE.
REAL CD
C CDD IS THE COEFFICIENT OF DRAG FOR THE DROGUE.
REAL CDD
C CF IS THE COEFFICIENT OF SKIN FRICTION FOR THE WIRE.
REAL CF
C CLD IS THE COEFFICIENT OF LIFT OF THE DROGUE AT THE EQUILIBRIUM
C POSITION.
REAL CLD
C D IS THE DIAMETER OF THE WIRE.
REAL D
C DELM IS THE TIME DELAY IN TERMS OF THE NEAREST NUMBER OF DELTAT
C TIME STEPS FOR PROPAGATION OF TENSION DISTURBANCES FROM
C THE POINT APPLIED TO GRIDPOINT 1.
REAL DELM
C DELTAS IS THE INCREMENT OF WIRE LENGTH AT THE N'TH GRIDPOINT.
REAL DELTAS
C DELTAT IS THE TIME STEP INCREMENT.
REAL DELTAT
C DPRIM IS THE TOTAL MAGNITUDE OF THE RESTORATIVE FORCE DUE TO
C THE CHANGE IN THE ANGLE OF ATTACK DURING OSCILLATIONS.
REAL DPRIM
C DPRIME IS THE LATERAL "DRAG DAMPING" FORCE DUE TO THE
C OSCILLATORY MOTION.
REAL DPRIME
C DWYO IS THE DIRECTION OF THE AVERAGE APPARENT FORCING WIND.
REAL DWYO
C DWY01 IS USED TO HOLD DW(P) FOR LATER USE IN ANTI-YOYO PHASING.
C IT IS ONLY REQUIRED WHEN USING THE OPTION OF GRIDPOINT SELECTION
```

C FOR ANTI-YOYO.  
 C REAL DWY01  
 C E IS YOUNG'S MODULUS FOR THE WIRE.  
 C REAL E  
 C G IS THE ACCELERATION DUE TO GRAVITY.  
 C REAL G  
 C HOLD IS A SUMMER IN AN AVERAGING SCHEME USED TO PREVENT  
 C LIMIT CYCLE OSCILLATIONS IN THE ITERATIVE DISPLACEMENT  
 C CALCULATIONS.  
 C REAL HOLD  
 C MHU IS THE MASS OF THE WIRE PER UNIT LENGTH.  
 C REAL MHU  
 C PHI IS THE NOMINAL BANK ANGLE OF THE TOWPLANE.  
 C REAL PHI  
 C PHIVMX IS THE MAXIMUM VALUE OF THE BANK ANGLE VARIATION  
 C FROM STEADY STATE REQUIRED TO PERFORM THE ANTI-YOYO MANEUVER.  
 C REAL PHIVMX  
 C RADTP IS THE ORBIT RADIUS OF THE TOWPLANE.  
 C REAL RADTP  
 C THESE VARIABLES ARE USED AS PLACE KEEPERS FOR THE SUPERIMPOSED  
 C POSITION INFORMATION OF THE DROGUE OVER THE PREVIOUS TIME  
 C STEPS.  
 C REAL RS1,RS2,RS3,RS4  
 C REAL THETS1,THETS2,THETS3,THETS4  
 C REAL ZS1,ZS2,ZS3,ZS4  
 C SD IS THE MAXIMUM CROSS SECTIONAL AREA OF THE DROGUE.  
 C REAL SD  
 C STUFF1,2,3,4,5,6,7,8 ARE DUMMY VARIABLES USED TO BREAK UP LARGE  
 C EQUATIONS.  
 C REAL STUFF1, STUFF2, STUFF3, STUFF4  
 C REAL STUFF5, STUFF6, STUFF7, STUFF8  
 C THEDOT IS THE ORBIT RATE OF THE TOWPLANE.  
 C REAL THEDOT  
 C VTRUE IS THE TOWPLANE TRUE AIRSPEED.  
 C REAL VTRUE  
 C VWYO IS THE MAGNITUDE OF THE AVERAGE APPARENT FORCING WIND.  
 C REAL VWYO  
 C WD IS THE WEIGHT OF THE DROGUE.  
 C REAL WD  
 C XN AND YN ARE DUMMY VARIABLES USED IN ITERATING FOR THE  
 C OSCILLATORY DISPLACEMENT.  
 C REAL XN,YN  
 C YO IS A TOGGLE TO SWITCH BETWEEN THE SELECTION AND DESELECTION  
 C OF THE ANTI YOYO MANEUVER MODEL.  
 C REAL YO  
 C  
 C NOW INTEGERS.  
 C  
 C K IS THE NUMBER OF TIME STEPS DESIRED.  
 C INTEGER K  
 C N IS THE GRIDPOINT INDEX FROM THE TOP TO THE BOTTOM ALONG THE  
 C WIRE AND IS ALSO USED AS AN INDEX IN SOME CALCULATIONS OUTSIDE  
 C OF THE MAIN LOOP.  
 C INTEGER N  
 C M IS THE TIME STEP INDEX.  
 C INTEGER M  
 C I IS AN INDEX USED FOR VARIOUS PURPOSES THROUGHOUT THE PROGRAM.  
 C INTEGER I  
 C INDEX IS USED TO MATCH GRIDPOINT POSITIONS WITH THE CORRECT  
 C WIND MEASUREMENTS.  
 C INTEGER INDEX  
 C COUNT IS A COUNTER USED TO PREVENT INFINITE LOOPS IN THE MAIN

C INNER LOOP AS IT TRIES TO MATCH DISPLACEMENT AND PSEUDO-DRAG  
 C FORCES.  
 C INTEGER COUNT  
 C P IS AN INDEX USED TO IDENTIFY THE GRIDPOINT THAT YOU WISH TO  
 C OPTIMIZE THE ANTI-YOYO MANEUVER AROUND.  
 C INTEGER P  
 C  
 C FINALLY ARRAYS.  
 C  
 C A(N) AND B(N) ARE GEOMETRIC CONSTANTS WHICH ARE USED TO DEFINE  
 C HOW MUCH FORCING FUNCTION IS APPLIED AT EACH GRIDPOINT GIVEN  
 C THE WIND VELOCITY AND STEADY STATE WIRE ORIENTATION.  
 C REAL A(200), B(200)  
 C ALFA(N) IS THE ANGLE OF ATTACK OF THE STEADY STATE WIRE.  
 C REAL ALFA(200)  
 C DELT(M) IS THE TENSION OSCILLATION AT GRIDPOINT 1.  
 C REAL DELT(10000)  
 C DENSITY(S) IS A VECTOR OF THE MEASURED DENSITY VALUES AT 1000  
 C FEET INCREMENTS.  
 C REAL DENSITY(30)  
 C PHIV(M) IS THE PERTURBATION IN ANGLE OF BANK REQUIRED TO FLY  
 C THE ANTI-YOYO MANEUVER.  
 C REAL PHIV(10000)  
 C QX(N,M) IS AN ARBITRARY FORCING FUNCTION APPLIED IN THE X  
 C DIRECTION. IT MAY VARY ALONG THE WIRE AND IN TIME.  
 C REAL QX(200,3)  
 C QY(N,M) IS AN ARBITRARY FORCING FUNCTION APPLIED IN THE Y  
 C DIRECTION. IT MAY VARY ALONG THE WIRE AND IN TIME.  
 C REAL QY(200,3)  
 C R(N) IS THE RADIAL STEADY STATE POSITION OF THE WIRE BEHIND  
 C THE AIRPLANE. IT HAS BEEN CONVERTED TO THE TOP DOWN  
 C COORDINATE SYSTEM.  
 C REAL R(200)  
 C R1(N) IS USED TO READ IN AND INVERT THE INDICES OF R(N).  
 C REAL R1(200)  
 C R2(M) IS THE R POSITION OF THE SECOND GRID POINT.  
 C REAL R2(10000)  
 C R200(M) IS THE R POSITION OF THE DROGUE.  
 C REAL R200(10000)  
 C RS(N) IS THE SUPERIMPOSED TIME SOLUTION TO THE RADIAL POSITION.  
 C REAL RS(200)  
 C RHO(N) IS THE ATMOSPHERIC DENSITY AT EACH EQUILIBRIUM GRIDPOINT.  
 C REAL RHO(200)  
 C T(N) IS AN ARBITRARY TENSION DISTRIBUTION APPLIED TO THE WIRE.  
 C IT IS ASSUMED CONSTANT OVER TIME. THE TENSION DISTRIBUTION  
 C IS CALCULATED BY THE STEADY STATE MODEL AND THEN INVERTED  
 C TO ACCOUNT FOR THE COORDINATE SCHEME USED HERE.  
 C REAL T(200)  
 C T1(N) IS USED TO READ IN AND INVERT THE INDICES OF T(N).  
 C REAL T1(200)  
 C THETA(N) IS THE ANGULAR STEADY STATE POSITION OF THE WIRE  
 C BEHIND THE AIRPLANE. IT HAS BEEN CONVERTED TO THE TOP  
 C DOWN COORDINATE SYSTEM.  
 C REAL THETA(200)  
 C THETA1(N) IS USED TO READ IN AND INVERT THE INDICES OF THETA(N).  
 C REAL THETA1(200)  
 C THETA2(M) IS THE THETA POSITION OF THE SECOND GRIDPOINT.  
 C REAL THETA2(10000)  
 C THETAS(N) IS THE SUPERIMPOSED TIME SOLUTION TO THE THETA  
 C COORDINATE.  
 C REAL THETAS(200)  
 C VREL(P(N)) IS THE RELATIVE VELOCITY COMPONENT PERPENDICULAR





```

C      OPEN (1,FILE='DATA02.MAT',STATUS='OLD',FORM='FORMATTED',
: ACCESS='SEQUENTIAL',RECL=12)
      OPEN (2,FILE='DATA03.MAT',STATUS='OLD',FORM='FORMATTED',
: ACCESS='SEQUENTIAL',RECL=12)
      OPEN (3,FILE='DATA04.MAT',STATUS='OLD',FORM='FORMATTED',
: ACCESS='SEQUENTIAL',RECL=12)
      OPEN (4,FILE='DATA05.MAT',STATUS='OLD',FORM='FORMATTED',
: ACCESS='SEQUENTIAL',RECL=12)
      OPEN (8,FILE='DATA06.MAT',STATUS='OLD',FORM='FORMATTED',
: ACCESS='SEQUENTIAL',RECL=12)
      OPEN (9,FILE='DATA07.MAT',STATUS='OLD',FORM='FORMATTED',
: ACCESS='SEQUENTIAL',RECL=12)
      OPEN (40,FILE='WINDIR.MAT',STATUS='OLD',FORM='FORMATTED',
: ACCESS='SEQUENTIAL',RECL=5)
      OPEN (41,FILE='WINSPD.MAT',STATUS='OLD',FORM='FORMATTED',
: ACCESS='SEQUENTIAL',RECL=5)
      OPEN (42,FILE='DENSTY.MAT',STATUS='OLD',FORM='FORMATTED',
: ACCESS='SEQUENTIAL',RECL=5)

C
C      DEFINE THE INPUT FILE FORMATS.
C
C      FORMAT(F12.6)
10     FORMAT(F5.1)
11
C*****
C      INITIALIZE CONSTANTS.
C
C      GENERAL CONSTANTS.
C
      DELTAT=0.1
      G=32.174
      PI=3.1415926535879

C
C      WIRE CONSTANTS.
C
      CD=1.03
      CF=0.022
      D=0.1582/12
      MHU=0.062107/G
      DELTAS=101.96
      E=12000000.0*144.0

C
C      DROGUE CONSTANTS.
C
      CDD=0.41
      SD=PI
C      INPUT THIS FROM TAC16.
      READ(9,10) CLD
      CLOSE(9)
      WD=81.95

C
C      INPUT THE NUMBER OF TIME STEPS DESIRED.
C
      WRITE(6,*)'INPUT THE NUMBER OF DESIRED TIME STEPS='
      WRITE(6,*)'MUST USE AT LEAST 1000 AND LESS THAN 10,000'
      READ(5,*)K

C
C      DECIDE WHETHER TO ACTIVATE THE ANTI-YOYO MANEUVER MODEL.
C      THE MANEUVER MAY BE OPTIMIZED AROUND A CHOSEN GRIDPOINT OR
C      USED TO ELIMINATE THE AVERAGE OF THE APPARENT FORCING WIND.
C      STATEMENT OUT THE TECHNIQUE NOT USED AS REQUIRED
C      THROUGHOUT THE PROGRAM.

```

```

C      WRITE(6,*) 'DO YOU WANT TO USE ANTI-YOYO?  1=YES  0=NO'
C      READ(5,*) YO
C
C      THIS PART IS ONLY REQUIRED WHEN IT IS DESIRED TO SELECT THE
C      GRIDPOINT TO OPTIMIZE ANTI-YOYO AROUND.
C
C      IF (YO .EQ. 1.0) THEN
C      WRITE(6,*) 'WHICH GRIDPOINT DO YOU WANT TO OPTIMIZE THE'
C      WRITE(6,*) 'ANTI-YOYO MANEUVERS AROUND? 1-200'
C      READ(5,*) P
C      ELSE
C      ENDIF
C
C      ALERT THE OPERATOR TO THE REQUIRED RUN TIME.
C
C      WRITE(6,*) '
C      WRITE(6,*) '
C      WRITE(6,*) 'APPROXIMATE RUN TIME ON A 486 33 MHZ DX WILL BE:'
C      WRITE(6,*) 6.25*K/3000.0, ' MINUTES'
C      WRITE(6,*) 'YOU WILL SEE A COUNTER INCREMENT EVERY 100 TIME'
C      WRITE(6,*) 'STEPS.'
C      WRITE(6,*) '
C      WRITE(6,*) '*****'
C      WRITE(6,*) '*TO STOP THE RUN PRESS CTRL AND PAUSE AT THE SAME*'
C      WRITE(6,*) '* TIME! *'
C      WRITE(6,*) '*****'
C      WRITE(6,*) '
C*****
C      DEFINE THE INITIAL POSITION OF THE WIRE. ASSUME IT IS HELD
C      AT THIS POSITION FOR AT LEAST TWO TIME STEPS. ALSO,
C      INITIALIZE THE INITIAL TWO TIME
C      STEPS OF THE FORCING FUNCTION AS 0.0 TO ACT AS PLACE HOLDERS
C      FOR THE FORCING FUNCTION MATRIX.
C
C      DO 100 N=1,200
C      X(N,1)=0.0
C      Y(N,1)=0.0
C      X(N,2)=0.0
C      Y(N,2)=0.0
C      QX(N,1)=0.0
C      QY(N,2)=0.0
100  CONTINUE
C
C      INITIALIZE THE IMAGINARY GRIDPOINTS AT THE END.
C
C      X201=0.0
C      X202=0.0
C      Y201=0.0
C      Y202=0.0
C
C      INITIALIZE PLACEHOLDERS FOR POSITION VALUES USED IN THE
C      CALCULATIONS OF THE DROGUE'S ACCELERATION. A FIVE TIME STEP
C      SCHEME IS USED.
C
C      RS1=R(200)
C      RS2=R(200)
C      RS3=R(200)
C      RS4=R(200)
C      THETS1=THETA(200)
C      THETS2=THETA(200)
C      THETS3=THETA(200)

```

```

      THETS4=THETA(200)
      ZS1=Z(200)
      ZS2=Z(200)
      ZS3=Z(200)
      ZS4=Z(200)
      ZS(200)=Z(200)
C*****
C      READ THE TENSION DISTRIBUTION FROM THE INPUT FILE.
C
110     READ(4,10,END=115)T1
        GOTO 110
115     CLOSE(4)
C
C      READ THE WIRE POSITION FROM THE INPUT FILES.
C
120     READ(1,10,END=125)R1
        GOTO 120
125     CLOSE(1)
C
130     READ(2,10,END=135)THETA1
        GOTO 130
135     CLOSE(2)
C
140     READ(3,10,END=145)Z1
        GOTO 140
145     CLOSE(3)
C
C      READ THE ORBIT RATE FROM THE INPUT FILE.
C
        READ(8,10)THEDOT
        CLOSE(8)
C
C      NOTE THAT THE INPUT FILES ARE DEFINED WITH THE BOTTOM OF THE
C      WIRE AT GRIDPOINT 1.  HERE, THE OPPOSITE APPLIES, AND THE
C      GRIDPOINTS MUST BE INVERTED.  ALSO, IT IS DESIRABLE TO REDEFINE
C      THE TOWPLANE ATTACHMENT POINT AS THETA=0.0.
C
        DO 146 N=1,200
          R(N)=R1(201-N)
          THETA(N)=THETA1(201-N)-THETA1(200)
          Z(N)=Z1(201-N)
          T(N)=T1(201-N)
146     CONTINUE
C
C      THE USER MAY CHOOSE MEASURED DENSITY DATA DEFINED IN AN OUTSIDE
C      FILE OR CALCULATE DENSITY BASED UPON THE STANDARD ATMOSPHERE.
C      STATEMENT OUT THE TECHNIQUE NOT USED.
C
147     READ(42,11,END=148)DENSTY
        GOTO 147
148     CLOSE(42)
C
        DO 149 N=1,200
          INDEX=INT(Z(N)/1000.0)+1
          RHO(N)=DENSTY(INDEX)*0.0023769/1013.0
149     CONTINUE
C
        RHO(N)=0.0023769*((518.69-0.0035662*Z(N))/518.69)**
C      : ((-1.0)*(1.0/(-0.0035662*53.3))+1.0))
C
C      READ THE WIND DATA FROM THE INPUT FILES.
C

```

```

150  READ(40,11,END=152)WINDIR
      GOTO 150
152  CLOSE(10)
C
154  READ(41,11,END=155)WINSPP
      GOTO 154
155  CLOSE(11)
C
C      CONVERT THE 1000 FEET INTERVAL WIND DATA TO GRIDPOINT
C      DATA USING THE STEADY STATE Z(N).
C
      DO 156 N=1,200
        INDEX=INT(Z(N)/1000)+1
        VW(N)=WINSPP(INDEX)
        DW(N)=WINDIR(INDEX)
156  CONTINUE
C
C      THIS SECTION WAS ADDED TO ALLOW AN INVESTIGATION OF THE
C      LINEARITY OF THE FULL SUPERIMPOSED SOLUTION.
C
      WRITE(6,*)'INPUT WIND VELOCITY AT TOWPLANE IN KTS'
      READ(5,*)STUFF1
      STUFF1=STUFF1/200.0
      DO 157 N=1,200
        DW(N)=90.0
        VW(N)=STUFF1*(201.0-N)
C157 CONTINUE
C
C      CONVERT THE WIND DIRECTION TO RADIANs AND THE WINDSPEED TO
C      FEET/SECOND. ALSO, IT IS NECESSARY TO DO SOME
C      TRIGONOMETRIC CALCULATIONS WHICH REQUIRE DIVISION BY WIND
C      MAGNITUDES. THEREFORE, ELIMINATE ANY CHANCE OF DIVISION BY ZERO
C      BY SETTING A "MINIMUM" WINDSPEED OF 0.1 FT/SEC.
C
      DO 160 N=1,200
        DW(N)=DW(N)*2*PI/360.0
        VW(N)=VW(N)*6076.0/3600.0
        IF (VW(N) .EQ. 0.0) THEN
          VW(N)=0.1
        ELSE
          ENDIF
160 CONTINUE
C
C      NEXT, REMEMBER THAT THE AIRCRAFT IS DRIFTING AT THE GRIDPOINT
C      1 WINDSPEED AND DIRECTION AND SO THE FORCING FUNCTION IS
C      ZERO AT THE TOP AND ALL SUBSEQUENT GRIDPOINT FORCING FUNCTIONS
C      ARE DEFINED TAKING INTO ACCOUNT THE WIND VELOCITY
C      RELATIVE TO THE UPPER GRIDPOINT! FIRST, FIND THE RECIPROCAL
C      OF THE UPPER GRIDPOINT WIND VECTOR.
C
      STUFF1=DW(1)+PI
      IF (STUFF1 .GT. 2*PI) THEN
        STUFF1=STUFF1-2*PI
      ELSE
        ENDIF
C
C      NOW, VECTORALLY ADD THIS RECIPROCAL VECTOR TO ALL THE
C      GRIDPOINTS TO GET THE TRUE FORCING FUNCTION. FIRST CONVERT
C      THE RECIPROCAL VECTOR TO RECTANGULAR COORDINATES.
C
      STUFF2=VW(1)*COS(STUFF1)
      STUFF3=VW(1)*SIN(STUFF1)

```

```

C
C CONVERT EACH GRIDPOINT WIND TO RECTANGULAR COORDINATES,
C ADD THE RECIPROCAL VECTOR AND CONVERT BACK TO POLAR
C COORDINATES. BE CAREFUL ABOUT THE USE OF ACOS AND THE
C QUADRANT THE COMPONENT IS IN.
C
  STUFF7=0.0
  STUFF8=0.0
  DO 163 N=1,200
    STUFF4=VW(N)*COS(DW(N))+STUFF2
    STUFF7=STUFF7+STUFF4
    STUFF5=VW(N)*SIN(DW(N))+STUFF3
    STUFF8=STUFF8+STUFF5
    VW(N)=SQRT(STUFF4**2+STUFF5**2)
    IF (STUFF5 .GT. 0.0) THEN
      IF (STUFF4 .GT. 0.0) THEN
        DW(N)=ATAN(STUFF5/STUFF4)
      ELSE
        DW(N)=PI/2.0+ATAN(-STUFF4/STUFF5)
      ENDIF
    ELSE
      IF (STUFF4 .GE. 0.0) THEN
        DW(N)=3.0*PI/2.0+ATAN(STUFF4/(-STUFF5))
      ELSE
        DW(N)=PI+ATAN(STUFF5/STUFF4)
      ENDIF
    ENDIF
  163 CONTINUE
C
C HERE, THE SUMS OF STUFF4 AND STUFF5 ARE USED TO GET THE
C AVERAGE APPARENT FORCING WIND IN CYLINDRICAL COORDINATES.
C
  STUFF7=STUFF7/200.0
  STUFF8=STUFF8/200.0
  VWYO=SQRT(STUFF7**2+STUFF8**2)
  IF (STUFF8 .GT. 0.0) THEN
    IF (STUFF7 .GT. 0.0) THEN
      DWYO=ATAN(STUFF8/STUFF7)
    ELSE
      DWYO=PI/2.0+ATAN(-STUFF7/STUFF8)
    ENDIF
  ELSE
    IF (STUFF7 .GE. 0.0) THEN
      DWYO=3.0*PI/2.0+ATAN(STUFF7/(-STUFF8))
    ELSE
      DWYO=PI+ATAN(STUFF8/STUFF7)
    ENDIF
  ENDIF
C
C SAVE THE DIRECTION OF THE CHOSEN GRIDPOINT FOR USE IN ANTI-YOYO
C PHASE CALCULATIONS.
C
  IF (YO .EQ. 1.0) THEN
    DWY01=DW(P)
  ELSE
    ENDIF
C
C THE ANTI-YOYO MANEUVER IS MODELED BY ADDING THE RECIPROCAL
C OF THE GRIDPOINT APPARENT FORCING WIND FUNCTION TO BE CANCELED.
C THIS MODELS THE EFFECT OF SUPERIMPOSING THE MOVEMENT OF THE
C CENTER OF ROTATION OF THE WIRE IN THE SAME DIRECTION AND AT
C THE SAME SPEED AS THE APPARENT WIND FORCING FUNCTION.

```

```

C
C   FIRST CHECK TO SEE IF THE USE OF ANTI-YOYO HAS BEEN SELECTED.
C
C   IF (YO .EQ. 1.0) THEN
C
C       OPEN (43,FILE='DATA09.MAT',STATUS='OLD',FORM='FORMATTED',
:   ACCESS='SEQUENTIAL',RECL=12)
C       OPEN (44,FILE='DATA00.MAT',STATUS='OLD',FORM='FORMATTED',
:   ACCESS='SEQUENTIAL',RECL=12)
C
C       READ(43,10)VTRUE
C       CLOSE(43)
C       READ(44,10)PHI
C       CLOSE(44)
C
C       DETERMINE THE MAXIMUM AMOUNT THAT THE STEADY STATE BANK MUST BE
C       MODULATED TO PERFORM THE ANTI-YOYO MANEUVER.
C
C       DETERMINE THE TURN RADIUS OF THE TOWPLANE.
C
C       RADTP=VTRUE**2/(G*SQRT(1/(COS(PHI))**2-1.0))
C
C       USE A SEARCH OF VALUES OF PHIVMX FROM 0 TO 5 DEGREES.
C
C       INITIALIZE THE RESIDUE HOLDER.
C
C       STUFF2=1000000.0
C
C       LOOP THROUGH THE VARIOUS PHIVMX VALUES.
C
C       DO 168 I=1,51
C
C       INITIALIZE THE INTEGRATION SUMMER.
C
C       STUFF3=0.0
C
C       PHIVMX=((I-1)*0.1)*2*PI/360.0
C
C       PERFORM THE INTEGRAL OVER 20 SEGMENTS.
C
C       DO 167 N=1,20
C
C       INTEGRATE OVER 0 TO 2*PI USING A NEWTON-COTES SCHEME.
C
C       STUFF4=((N-1)*PI)/20
C       STUFF5=VTRUE**2*SIN(STUFF4)
C       STUFF6=(G*SQRT((1/(COS(PHI-PHIVMX*
:   SIN(STUFF4))))**2-1.0))
C       STUFF7=STUFF5/STUFF6
C       STUFF4=((2*N-1)*PI)/40
C       STUFF5=VTRUE**2*SIN(STUFF4)
C       STUFF6=(G*SQRT((1/(COS(PHI-PHIVMX*
:   SIN(STUFF4))))**2-1.0))
C       STUFF7=STUFF7+4*STUFF5/STUFF6
C       STUFF4=((N)*PI)/20
C       STUFF5=VTRUE**2*SIN(STUFF4)
C       STUFF6=(G*SQRT((1/(COS(PHI-PHIVMX*
:   SIN(STUFF4))))**2-1.0))
C       STUFF7=STUFF7+STUFF5/STUFF6
C       STUFF3=STUFF3+STUFF7*PI/120.0
C       STUFF7=0.0
167   CONTINUE

```

```

C
C   WITH THE INTEGRATION PERFORMED, CALCULATE THE RESIDUE.
C
C   STUFF1=-2.0*RADTP-ABS(VW(P))*PI/(2*THEDOT)+STUFF3
C
C   USE THIS PARTICULAR FORM OF STUFF1 WHEN USING THE AVERAGE
C   APPARENT FORCING WIND TECHNIQUE FOR ANTI-YOYO.
C
C   STUFF1=-2.0*RADTP-ABS(VWYO)*PI/(2*THEDOT)+STUFF3
C
C   SAVE THE PHIVMX WITH THE LOWEST RESIDUE VALUE.
C
C   IF (ABS(STUFF1) .LT. ABS(STUFF2)) THEN
C     STUFF2=STUFF1
C     STUFF8=PHIVMX
C   ELSE
C     ENDIF
168  CONTINUE
C     PHIVMX=STUFF8
C
C   APPLY ANTI-YOYO TO THE WIRE DYNAMICS BY CALCULATING ITS EFFECTS
C   UPON THE FORCING FUNCTION.
C
C     STUFF1=DW(P)+PI
C     IF (STUFF1 .GT. 2*PI) THEN
C       STUFF1=STUFF1-2*PI
C     ELSE
C       ENDIF
C
C     STUFF2=VW(P)*COS(STUFF1)
C     STUFF3=VW(P)*SIN(STUFF1)
C
C   THIS VERSION IS USED DURING THE AVERAGE APPARENT FORCING WIND
C   ANTI-YOYO TECHNIQUE.
C
C     STUFF1=DWYO+PI
C     IF (STUFF1 .GT. 2*PI) THEN
C       STUFF1=STUFF1-2*PI
C     ELSE
C       ENDIF
C
C     STUFF2=VWYO*COS(STUFF1)
C     STUFF3=VWYO*SIN(STUFF1)
C
C   DO 169 N=1,200
C     STUFF4=VW(N)*COS(DW(N))+STUFF2
C     STUFF5=VW(N)*SIN(DW(N))+STUFF3
C     VW(N)=SQRT(STUFF4**2+STUFF5**2)
C     IF (STUFF5 .GT. 0.0) THEN
C       IF (STUFF4 .GT. 0.0) THEN
C         DW(N)=ATAN(STUFF5/STUFF4)
C       ELSE
C         DW(N)=PI/2.0+ATAN(-STUFF4/STUFF5)
C       ENDIF
C     ELSE
C       IF (STUFF4 .GE. 0.0) THEN
C         DW(N)=3.0*PI/2.0+ATAN(STUFF4/(-STUFF5))
C       ELSE
C         DW(N)=PI+ATAN(STUFF5/STUFF4)
C       ENDIF
C     ENDIF
169  CONTINUE

```

```

C      ELSE
C      ENDDIF
C*****
C      NOW, CALCULATE THE GEOMETRIC CONSTANTS FOR EACH
C      GRIDPOINT THAT DEFINE THE AMOUNT OF THE FORCING FUNCTION THAT
C      IS PERPENDICULAR TO THE WIRE AT EACH POINT SINCE ONLY THIS
C      COMPONENT OF THE FORCING FUNCTION IS GERMANE TO THE DANGLING
C      CHAIN. NEXT, CALCULATE THE MAXIMUM FORCING FUNCTION VALUE
C      AT EACH GRIDPOINT, AND FINALLY, THE STEADY STATE COMPONENT
C      OF VELOCITY PERPENDICULAR TO THE WIRE AND THE
C      STEADY STATE ANGLE OF ATTACK ARE REQUIRED.
C
C      DO 170 N=2,199
C      STUFF1=1-((R(N+1)-R(N-1))/(2*DELTAS))**2
C      STUFF2=(R(N+1)-R(N-1))*R(N)*(THETA(N+1)-THETA(N-1))/
C      : (4*DELTAS**2)
C      STUFF3=(R(N+1)-R(N-1))*(Z(N+1)-Z(N-1))/(4*DELTAS**2)
C      VX(N)=SQRT(STUFF1**2+STUFF2**2+STUFF3**2)
C      STUFF1=1-(R(N)*(THETA(N+1)-THETA(N-1))/(2*DELTAS))**2
C      STUFF3=R(N)*(THETA(N+1)-THETA(N-1))*(Z(N+1)-Z(N-1))/
C      : (4*DELTAS**2)
C      VY(N)=SQRT(STUFF2**2+STUFF1**2+STUFF3**2)
C
C      A(N)=0.5*RHO(N)*VW(N)**2*D*(CD+CF)
C      B(N)=A(N)
C
C      VREL(N)=R(N)*THEDOT*SQRT(1-R(N)**2*(THETA(N+1)-THETA(N-1))**2
C      : /(4*DELTAS**2))
C
C      ALFA(N)=ACOS(R(N)*(-THETA(N+1)+THETA(N-1))/(2*DELTAS))
170 CONTINUE
C
C      ASSUME THAT THE SLOPES DO NOT CHANGE DRASTICALLY BETWEEN
C      THE FIRST AND SECOND AND LAST AND NEXT TO LAST GRIDPOINTS.
C      THIS IS BORNE OUT IN APPLICATION OF THIS PROGRAM AND MAKES THE
C      HANDLING OF THE TOP AND BOTTOM GRIDPOINTS MUCH EASIER. THE
C      ERRORS TURN OUT TO BE MINISCULE AND ONLY AFFECTS TWO OF THE
C      N GRIDPOINTS.
C
C      VX(1)=VX(2)
C      VY(1)=VY(2)
C      A(1)=0.5*RHO(1)*VW(1)**2*D*(CD+CF)
C      B(1)=A(1)
C      VX(200)=VX(199)
C      VY(200)=VY(199)
C      A(200)=0.5*RHO(200)*VW(200)**2*SD*CDD/DELTAS
C      B(200)=A(200)
C*****
C      OPEN SOME OF THE THE OUTPUT DATA FILES.
C
C      OPEN (UNIT=30,FILE='VERCLT.MAT')
C      OPEN (UNIT=31,FILE='R2.MAT')
C      OPEN (UNIT=32,FILE='THETA2.MAT')
C      OPEN (UNIT=33,FILE='Z2.MAT')
C      OPEN (UNIT=34,FILE='T1.MAT')
C      OPEN (UNIT=35,FILE='PHIV.MAT')
C      OPEN (UNIT=36,FILE='R200.MAT')
C
C*****
C*****
C*****

```



```

C
C THE OUTER TIME LOOP.
C
C DO 2000 M=3,K
C
C THE TOP GRIDPOINT POSITION.
C
C THIS JUST SAYS THAT THE TOP OF THE DANGLING CHAIN IS FIXED.
C
C X(1,3)=0.0
C Y(1,3)=0.0
C
C SINCE THE FIXED UPPER END OF THE DANGLING CHAIN IS DEFINED
C AT POINT 0.0, 0.0, IT IS KNOWN THAT THE SUPERIMPOSED
C POSITION IS MERELY THE STEADY STATE POSITION.
C
C RS(1)=R(1)
C THETAS(1)=THETA(1)
C ZS(1)=Z(1)
C
C CALCULATE THE FORCING FUNCTION AT THIS TIME STEP.
C
C DO 200 I=2,199
C QX(I,3)=A(I)*VX(I)*SIN(THEDOT*(M-2)*DELTAT-THETA(I)+2*PI-DW(I))
C QY(I,3)=B(I)*VY(I)*COS(THEDOT*(M-2)*DELTAT-THETA(I)+2*PI-DW(I))
200 CONTINUE
C I=200
C QX(I,3)=A(200)*VX(I)*SIN(THEDOT*(M-2)*DELTAT-THETA(I)+
C : 2*PI-DW(I))
C QY(I,3)=B(200)*VY(I)*COS(THEDOT*(M-2)*DELTAT-THETA(I)+
C : 2*PI-DW(I))
C *****
C MUST CALCULATE ALFAS FOR GRIDPOINT 200 NOW BEFORE THE PROGRAM
C UPDATES THETAS(198) SINCE THIS VALUE IS REQUIRED AT THE LAST
C TIME STEP.
C
C IF (M .GT. 3) THEN
C STUFF4=ABS(RS(199)*(THETAS(198)-THETAS(200))/(2*DELTAS))
C IF (STUFF4 .LT. 0.98) THEN
C ALFAS1=ACOS(RS(199)*(-THETAS(200)+THETAS(198))/(2*DELTAS))
C ELSE
C STUFF5=SQRT((RS(198)-RS(200))**2+(RS(199)*(THETAS(198)-
C : THETAS(200))**2+(ZS(198)-ZS(200))**2)
C ALFAS1=ASIN(SQRT((RS(198)-RS(200))**2+(ZS(198)-ZS(200))**2)/
C : STUFF5)
C ENDIF
C
C RESOLVE AMBIGUITIES IN NEGATIVE ANGLES OF ATTACK.
C
C IF (ZS(200)+RS(200) .GT. ZS(198)+RS(198)) THEN
C ALFAS1=-ALFAS1
C ELSE
C ENDIF
C ELSE
C ALFAS1=ALFA(199)
C ENDIF
C *****
C *****
C MARCH TO THE BOTTOM.
C
C ZERO OUT THESE FOR THE FIRST PASS THROUGH THE ITERATIVE

```

```

C      LOOP.
C
C      XN=0.0
C      YN=0.0
C
C      DO 1000 N=2,199
C
C      RESET THE ITERATION COUNTER AND THE DRAG DAMPING.
C
C      COUNT=0
C      DPRIME=0.0
C      HOLD=0.0
C*****
C      THESE CALCULATIONS ARE USED TO DETERMINE THE RESTORATIVE
C      FORCE DUE TO CHANGE IN ANGLE OF ATTACK AND ARE DEPENDENT
C      UPON VALUES CALCULATED IN THE PREVIOUS STEP AND SO THEY CAN BE
C      COMPUTED EXTERNAL TO THE LOOP.
C
C      STUFF4=ABS(RS(N)*(THETAS(N-1)-THETAS(N+1))/(2*DELTAS))
C      IF (STUFF4 .LT. 0.98) THEN
C      ALFAS=ACOS(RS(N)*(-THETAS(N+1)+THETAS(N-1))/(2*DELTAS))
C      ELSE
C      STUFF5=SQRT((RS(N-1)-RS(N+1))**2+(RS(N)*(THETAS(N-1)-
: THETAS(N+1))**2+(ZS(N-1)-ZS(N+1))**2)
C      ALFAS=ASIN(SQRT((RS(N-1)-RS(N+1))**2+(ZS(N-1)-ZS(N+1))**2)/
: STUFF5)
C      ENDIF
C
C      RESOLVE AMBIGUITIES FOR NEGATIVE ANGLES OF ATTACK.
C
C      IF (ZS(N+1)+RS(N+1) .GT. ZS(N-1)+RS(N-1)) THEN
C      ALFAS=-ALFAS
C      ELSE
C      ENDIF
C
C      DPRIM=CD*D*0.5*RHO(N)*VRELP(N)*SIN(ALFA(N)-ALFAS)*
: ABS(VRELP(N)*SIN(ALFA(N)-ALFAS))
C      DPRIM2=-ABS(X(N,2))*DPRIM/(SQRT(X(N,2)**2+Y(N,2)**2)+.0001)
C
C      THIS IS ADDED AS INSURANCE FOR THE RARE EVENTUALITY OF X AND
C      Y APPROACHING ZERO AND THE DPRIM2 BECOMING UNREALISTICALLY
C      LARGE. IT HAS NOT OCCURRED TO DATE BUT IT IS WORTH PROTECTING
C      AGAINST TO PREVENT FLOATING POINT ERRORS AND THE LOSS IN
C      ACCURACY WILL BE MINISCULE SINCE THE NUMBER OF EFFECTED
C      POINTS WILL BE SMALL.
C
C      IF (ABS(DPRIM2) .GT. 0.1) THEN
C      DPRIM2=0.1*DPRIM2/ABS(DPRIM2)
C      ELSE
C      ENDIF
C*****
C      HERE, CALCULATE THE INCREMENTAL CHANGE IN THE CF DRAG
C      COMPONENT TANGENTIAL TO THE WIRE TO ACCOUNT, IN PART, FOR
C      THE TENSION OSCILLATION. AS THE INCREMENTAL CHANGE IS
C      CALCULATED AT EACH POINT IT IS ADDED TO THE TOTAL AT THAT
C      TIME STEP. THE TIME FOR THE TENSION CHANGE TO PROPAGATE
C      TO THE TOP OF THE WIRE IS ACCOUNTED FOR.
C
C      DELM=NINT(((N*DELTAS*2.0)/D)*SQRT(MHU/(PI*E*G))/DELTAT)
C      DELT(M+DELM-1)=DELT(M+DELM-1)-0.5*RHO(N)*(R(N)*THEDOT)**2*
: D*DELTAS*CF*COS(ALFA(N))*(ALFA(N)-ABS(ALFAS))
C

```

```

C      SIMILARLY, ACCOUNT FOR THE COMPONENT OF CD DRAG
C      WHICH BECOMES TANGENTIAL ONCE THE STEADY STATE SLOPE OF THE
C      WIRE IS DISTURBED. REMEMBER THAT THE CD DRAG IS DEFINED
C      PERPENDICULAR TO THE STEADY STATE POSITIONS, THIS
C      RESULTS IN A COMPONENT OF THE CALCULATED DRAG ALONG THE
C      DISPLACED TANGENT VECTOR.
C
C      DELT(M+DELM-1)=DELT(M+DELM-1)-0.5*RHO(N)*VRELP(N)**2*
: D*DELTAS*CD*SIN(ALFA(N)-ALFAS)
C
C      NOW ACCOUNT FOR THE CONTRIBUTION OF THE FORCING FUNCTION TO THE
C      TENSION OSCILLATION.
C
C      DELT(M+DELM-1)=DELT(M+DELM-1)-0.5*RHO(N)*VW(N)**2*D*DELTAS*
: SIN(ALFA(N))*CF*SIN(THEDOT*(M-2)*DELTAT-THETA(N)+2*PI-DW(N))
C*****
C      THIS IS USED IN THE DAMPING DUE TO THE OSCILLATION RATE AND
C      NEED NOT BE CALCULATED INTERNAL TO THE ITERATIVE LOOP.
C
C      STUFF1=DELTAT**2/MHU
C*****
C      FINALLY, THE ITERATIVE SOLUTION FOR THE DANGLING CHAIN
C      DISPLACEMENT ACCOUNTING FOR THE HYPOTHEZIZED FORMS OF
C      DAMPING AND RESTORATIVE FORCES.
C
300  CONTINUE
C
C      THE DISPLACEMENT CALCULATION.
C
C      IF (N .EQ. 2) THEN
C      STUFF2=((T(N+1)+T(N))/2)*(X(N+1,2)-X(N,2))-
: ((T(N)+T(N-1))/2)*(X(N,2)-X(N-1,2))
C      STUFF3=2*X(N,2)-X(N,1)
C      XN=STUFF1*((STUFF2/DELTAS**2)+QX(N,2)-DPRIME-DPRIM2)+
: STUFF3
C      ELSEIF (N .EQ. 199) THEN
C      STUFF2=((T(N+1)+T(N))/2)*(X(N+1,2)-X(N,2))-
: ((T(N)+T(N-1))/2)*(X(N,2)-X(N-1,2))
C      STUFF3=2*X(N,2)-X(N,1)
C      XN=STUFF1*((STUFF2/DELTAS**2)+QX(N,2)-DPRIME-DPRIM2)+
: STUFF3
C      ELSE
C      STUFF2=((T(N+1)+T(N))/2)*(X(N+1,2)-X(N,2))-
: ((T(N)+T(N-1))/2)*(X(N,2)-X(N-1,2))
C      STUFF3=2*X(N,2)-X(N,1)
C      XN=STUFF1*((STUFF2/DELTAS**2)+QX(N,2)-DPRIME-DPRIM2)+
: STUFF3
C      ENDIF
C
C      THE OSCILLATORY MOTION DRAG DAMPING FORCE.
C
C      DPRIME=(CD+CF)*D*0.5*RHO(N)*((XN-X(N,1))/(2*DELTAT))*
: ABS((XN-X(N,1))/(2*DELTAT))
C
C      THE CONVERGENCE CRITERIA.
C
C      IF (ABS(XN-X(N,3)) .GT. 0.01) THEN
C      X(N,3)=XN
C
C      UPDATE THE ITERATION COUNTER.
C
C      COUNT=COUNT+1

```

```

C
C      THIS IS INCLUDED AS PROTECTION AGAINST AN INFINITE LOOP. THE
C      GRIDPOINT 200 CALCULATIONS ARE SUSCEPTABLE TO LIMIT CYCLE TYPE
C      BEHAVIOR DUE TO THE DISCONTINUITY IN THE EFFECTS OF LATERAL
C      VELOCITY OSCILLATIONS ON THE GREATER DROGUE SURFACE AREA
C      RELATIVE TO THE NEXT TO THE LAST GRIDPOINT. IT IS VERY RARELY
C      REQUIRED.
C
      IF (COUNT .GT. 50) THEN
      HOLD=HOLD+XN
      IF (COUNT .GT. 60) THEN
      X(N,3)=HOLD/11.0
      GOTO 305
      ENDIF
      ENDIF
C
      GOTO 300
      ELSE
      X(N,3)=XN
      ENDIF
305    CONTINUE
C*****
C      AGAIN, INITIALIZE THE DRAG DAMPING TERM FOR THE FIRST ITERATIVE
C      LOOP IN THE Y DIRECTION OF THE OSCILLATION AND THEN CALCULATE
C      THE RESTORATIVE FORCE DUE TO THE CHANGE IN THE ANGLE OF ATTACK.
C
      DPRIME=0.0
      COUNT=0
      HOLD=0.0
      DPRIM2=-ABS(Y(N,2))*DPRIM/(SQRT(X(N,2)**2+Y(N,2)**2)+.0001)
      IF (ABS(DPRIM2) .GT. 0.1) THEN
      DPRIM2=0.1*DPRIM2/ABS(DPRIM2)
      ELSE
      ENDIF
C*****
C      THE Y COMPONENT LOOP.
C
310    CONTINUE
      IF (: .EQ. 2) THEN
      STUFF2=((T(N+1)+T(N))/2)*(Y(N+1,2)-Y(N,2))-
: ((T(N)+T(N-1))/2)*(Y(N,2)-Y(N-1,2))
      STUFF3=2*Y(N,2)-Y(N,1)
      YN=STUFF1*((STUFF2/DELTAS**2)+QY(N,2)-DPRIME-DPRIM2)+
: STUFF3
      ELSEIF (N .EQ. 199) THEN
      STUFF2=((T(N+1)+T(N))/2)*(Y(N+1,2)-Y(N,2))-
: ((T(N)+T(N-1))/2)*(Y(N,2)-Y(N-1,2))
      STUFF3=2*Y(N,2)-Y(N,1)
      YN=STUFF1*((STUFF2/DELTAS**2)+QY(N,2)-DPRIME-DPRIM2)+
: STUFF3
      ELSE
      STUFF2=(T(N+1)*(Y(N+2,2)-Y(N,2))-T(N-1)*(Y(N,2)-Y(N-2,2)))
      STUFF3=2*Y(N,2)-Y(N,1)
      YN=STUFF1*((STUFF2/(4*DELTAS**2))+QY(N,2)-DPRIME-DPRIM2)+
: STUFF3
      ENDIF
      DPRIME=(CD+CF)*D*0.5*RHO(N)*((YN-Y(N,1))/(2*DELTAT))*
: ABS((YN-Y(N,1))/(2*DELTAT))
      IF (ABS(YN-Y(N,3)) .GT. 0.01) THEN
      Y(N,3)=YN
C
      COUNT=COUNT+1

```

```

C      IF (COUNT .GT. 50) THEN
        HOLD=HOLD+YN
        IF (COUNT .GT. 60) THEN
          Y(N,3)=HOLD/11.0
          GOTO 315
        ENDIF
      ENDIF

C      GOTO 310
      ELSE
        Y(N,3)=YN
      ENDIF
315    CONTINUE
C*****
C      CALCULATE THE SUPERIMPOSED SOLUTIONS.
C
      STUFF2=((R(N+1)-R(N-1))/(2*DELTAS))**2
      STUFF3=(R(N)*(THETA(N+1)-THETA(N-1))/(2*DELTAS))**2
      STUFF1=SQRT(STUFF2+STUFF3)

C
C      GIVE UP A LITTLE ACCURACY IN THE VERTICAL OR NEAR VERTICAL
C      CASE TO INSURE THAT THE PROGRAM DOES NOT CAUSE DIVISION BY
C      ZERO IN THE NEXT FEW CALCULATIONS.
C
      IF (STUFF1 .LT. 1.0) THEN
        STUFF1=1.0
      ELSE
      ENDIF

C
      RS(N)=R(N)+X(N,3)*R(N)*(THETA(N+1)-THETA(N-1))/(2*DELTAS*STUFF1)
      : +Y(N,3)*(R(N+1)-R(N-1))*(Z(N+1)-Z(N-1))/((2*DELTAS)**2*STUFF1)
      THETAS(N)=THETA(N)+X(N,3)*(R(N+1)-R(N-1))/(R(N)*2*DELTAS*STUFF1)
      : -Y(N,3)*(THETA(N+1)-THETA(N-1))*(Z(N+1)-Z(N-1))/
      : ((2*DELTAS)**2*STUFF1)

C
C      USE THE DELTAS CONSTRAINT FOR THE FIRST INTERNAL GRIDPOINT AND
C      THE CENTRAL DIFFERENCE APPROXIMATION OF THE DEFINITION OF THE
C      UNIT TANGENT FOR ALL OTHER GRIDPOINTS.
C
      IF (N .EQ. 2) THEN

C
        STUFF4=DELTAS**2-RS(N)**2-RS(N-1)**2+
        : 2*RS(N)*RS(N-1)*COS(THETAS(N)-THETAS(N-1))

C
C      THE NEXT BIT IS ADDED TO INSURE THAT IN THE NEAR VERTICAL CASE
C      THE PROGRAM DOES NOT ALLOW THE WIRE SECTION TO BECOME LONGER
C      THAN DELTAS.
C
      IF (STUFF4 .GT. DELTAS**2) THEN
        STUFF4=DELTAS**2
      ELSE
      ENDIF

C
C      WHEN THE DELTAS CONSTRAINT IS USED TO CALCULATE THE DISPLACED
C      Z(N), MUST CHECK FOR THE CASE WHERE THE INERTIALY REFERENCED
C      SLOPE OF THE WIRE BECOMES NEGATIVE.
C
      IF (STUFF4 .GE. 0.0) THEN
        ZS(N)=ZS(N-1)-SQRT(STUFF4)
      ELSE
        ZS(N)=ZS(N-1)+SQRT(-STUFF4)
      ENDIF

```

```

C      ENDIF
C
C      ELSE
C
C      STUFF4=4*DELTAS**2-(RS(N)-RS(N-2))**2-RS(N-1)**2*
: (THETAS(N)-THETAS(N-2))**2
C
C      IF (STUFF4 .GT. 4*DELTAS**2) THEN
C      STUFF4=4*DELTAS**2
C      ELSE
C      ENDIF
C
C      IF (STUFF4 .GE. 0.0) THEN
C      ZS(N)=ZS(N-2)-SQRT(STUFF4)
C      ELSE
C      ZS(N)=ZS(N-2)+SQRT(-STUFF4)
C      ENDIF
C
C      ENDIF
C
C      1000  CONTINUE
C*****
C*****
C      MATCH THE BOTTOM DANGLING CHAINBOUNDARY CONDITION.
C      FOR THE PURPOSES OF THE DRAG DAMPING AND THE RESTORATIVE FORCE
C      DUE TO CHANGES IN ANGLE OF ATTACK CALCULATIONS, ASSUME
C      THAT THE SLOPE CHANGES LITTLE FROM THE NEXT TO THE LAST TO
C      TO THE LAST GRIDPOINT. THEREFORE, CAN USE THE PREVIOUS STEP
C      GRIDPOINTS LESS ONE IN THE USUAL CALCULATIONS ABOVE. THE ERROR
C      DUE TO THIS APPROXIMATION IS SMALL SINCE IT INVOLVES CHANGES
C      IN SLOPE OVER A SINGLE GRIDPOINT AND GREATLY SIMPLIFIES THE
C      CALCULATIONS. THE MAJOR DIFFERENCE BETWEEN THE LAST TWO STEPS
C      IS ACCOUNTED FOR BY USING DROGUE VICE WIRE CONSTANTS.
C      IGNORE THE CHANGE IN ANGLE OF ATTACK DUE TO THE MOMENT
C      BOUNDARY CONDITION IN THE DISPLACED STATE. VARIOUS ANGLES
C      WERE TESTED AND IT WAS FOUND THAT THEY ONLY VERY SLIGHTLY
C      AFFECT THE GRID POSITION BEYOND ABOUT 5 FROM THE END. THE
C      COMPUTATIONS REQUIRED WOULD SLOW THE PROGRAM AND ARE NOT
C      CONSIDERED WORTH THE BULKY CODE THAT WOULD BE REQUIRED. THE
C      TEST CASES BRACKETED THE REASONABLE LIMITS OF ERROR TO
C      AROUND A TENTH OF A PERCENT OF TOTAL VERTICALITY CHANGE.
C
C      DPRIM=CLD*SD*0.5*RHO(N)*(VRELP(199)*SIN(ALFA(199)-ALFAS1))**2
: /DELTAS
C      DPRIM2=-X(199,2)*DPRIM/(SQRT(X(199,2)**2+Y(199,2)**2)+.0001)
C      IF (ABS(DPRIM2) .GT. 10.0) THEN
C      DPRIM2=10.0*DPRIM2/ABS(DPRIM2)
C      ELSE
C      ENDIF
C      N=200
C      DPRIME=0.0
C      COUNT=0
C      HOLD=0.0
C      STUFF1=DELTAT**2*G/WD
1100  CONTINUE
C      STUFF2=T(200)*(X(199,2)-X(200,2))
C      STUFF3=2*X(200,2)-X(200,1)
C      XN=STUFF1*((STUFF2/DELTAS)+QX(200,2)-DPRIME-DPRIM2)+
: STUFF3
C      DPRIME=CDD*SD*0.5*RHO(N)*((XN-X(200,1))/(2*DELTAT))*
: ABS((XN-X(200,1))/(2*DELTAT))/10.0
C

```

```

      IF (ABS(XN-X(200,3)) .GT. 0.1) THEN
      X(200,3)=XN
C
      COUNT=COUNT+1
C
      IF (COUNT .GT. 50) THEN
      HOLD=HOLD+XN
      IF (COUNT .GT. 70) THEN
      X(200,3)=HOLD/21.0
      GOTO 1105
      ENDIF
      ENDIF
C
      GOTO 1100
      ELSE
      X(200,3)=XN
      ENDIF
C
1105  CONTINUE
C*****
      DPRIME=0.0
      COUNT=0
      HOLD=0.0
      DPRIM2=-Y(199,2)*DPRIM/(SQRT(X(199,2)**2+Y(199,2)**2)+.0001)
C
      STUFF1=DELTAT**2*G/WD
1200  CONTINUE
      STUFF2=T(200)*(Y(199,2)-Y(200,2))
      STUFF3=2*Y(200,2)-Y(200,1)
      YN=STUFF1*((STUFF2/DELTAS)+QY(200,2)-DPRIME-DPRIM2)+
: STUFF3
      DPRIME=CDD*SD*0.5*RHO(N)*((YN-Y(200,1))/(2*DELTAT))*
: ABS((YN-Y(200,1))/(2*DELTAT))/DELTAS
      IF (ABS(YN-Y(200,3)) .GT. 0.1) THEN
      Y(200,3)=YN
C
      COUNT=COUNT+1
C
      IF (COUNT .GT. 50) THEN
      HOLD=HOLD+YN
      IF (COUNT .GT. 70) THEN
      Y(200,3)=HOLD/21.0
      GOTO 1205
      ENDIF
      ENDIF
C
      GOTO 1200
      ELSE
      Y(200,3)=YN
      ENDIF
1205  CONTINUE
C*****
C      CALCULATE THE GRIDPOINT 200 SUPERIMPOSED SOLUTIONS.
C      SINCE IT IS ASSUMED THAT THE LIFT IS CONSTANT ON THE DROGUE
C      IT MUST ALSO BE ASSUMED THAT THE SLOPE AT THE LAST GRIDPOINT
C      IS ALSO REASONABLY CONSTANT TO ALLOW THE MOMENT EQUILIBRIUM
C      BOUNDARY CONDITION TO BE APPROXIMATELY MET.
C
      RS(200)=RS(199)+(RS(199)-RS(198))
      THETAS(200)=THETAS(199)+(THETAS(199)-THETAS(198))
      ZS(200)=ZS(199)+(ZS(199)-ZS(198))
C

```

```

      STUFF4=DELTAS**2-RS(200)**2-RS(199)**2+
: 2*RS(200)*RS(199)*COS(THETAS(200)-THETAS(199))
C
C      AS IN THE CASE OF THE OTHER GRIDPOINTS, AGAIN MUST ENSURE
C      THAT THE WIRE IS NOT ALLOWED TO GROW BEYOND THE DELTAS LENGTH
C      IN THE VERTICAL AND NEAR VERTICAL CASES.
C
      IF (STUFF4 .GT. DELTAS**2) THEN
      STUFF4=DELTAS**2
      ELSE
      ENDIF
C
C      ACCOUNT FOR THE NEGATIVE SLOPE CASE.
C
      IF (STUFF4 .GE. 0.0) THEN
      ZS(200)=ZS(199)-SQRT(STUFF4)
      ELSE
      ZS(200)=ZS(199)+SQRT(-STUFF4)
      ENDIF
C*****
C      HERE, ACCOUNT FOR THE FORCE REQUIRED TO ACCELERATE THE
C      DROGUE THROUGH ITS SWINGS ACROSS THE SKY.  ACCOUNT
C      FOR THE VARIATION IN TENSION IN THE WIRE AT GRIDPOINT 1.
C      ALSO ALLOW FOR THE PROPAGATION TIME FOR THE
C      FORCE ALONG THE WIRE FROM BOTTOM TO TOP.
C
C      FIRST THE INERTIAL ACCELERATION OF THE DROGUE.
C
      STUFF1=(-RS(200)+16*RS4-30*RS3+16*RS2-RS1)/(12*DELTAT**2)
      STUFF2=(-RS(200)*THETAS(200)+16*RS4*THETS4-30*RS3*THETS3
: +16*RS2*THETS2-RS1*THETS1)/(12*DELTAT**2)
      STUFF3=(-ZS(200)+16*ZS4-30*ZS3+16*ZS2-ZS1)/(12*DELTAT**2)
      ACCD=SQRT(STUFF1**2+STUFF2**2+STUFF3**2)
      IF (ABS((Z(1)-Z(200))/(200.0*DELTAS)) .LT. 0.45) THEN
      ACCD=0.0
      ELSE
      ENDIF
C
C      NOW THE PROPAGATION TIME AND INCREMENT OF TENSION.
C
      DELM=NINT((200.0*DELTAS*2.0/D)*SQRT(MHU/(PI*E*G)))/DELTAT)
      DELT(M+DELM-2)=DELT(M+DELM-2)+(WD/G)*ACCD
C
C      THE WIND CAUSES AN INCREMENT IN TENSION JUST AS IT DOES FOR
C      ANY OF THE WIRE SEGMENTS.
C
      DELT(M+DELM-1)=DELT(M+DELM-1)+0.5*RHO(200)*VW(200)**2*SD*
: CDD*SIN(THEDOT*(M-2)*DELTAT-THETA(200)+2*PI-DW(200))
C*****
C      LASTLY, UPDATE THE DROGUE POSITION PLACE HOLDERS USED TO
C      CALCULATE THE VALUE OF ACCELERATION.
C
      RS1=RS2
      THETS1=THETS2
      ZS1=ZS2
      RS2=RS3
      THETS2=THETS3
      ZS2=ZS3
      RS3=RS4
      THETS3=THETS4
      ZS3=ZS4
      RS4=RS(200)

```



```

      THETS4=THETAS(200)
      ZS4=ZS(200)
C*****
C      SAVE THE CURRENT THREE STEPS FOR USE IN THE NEXT.
C
      DO 1800 I=1,200
      X(I,1)=X(I,2)
      Y(I,1)=Y(I,2)
      QX(I,1)=QX(I,2)
      QY(I,1)=QY(I,2)
      X(I,2)=X(I,3)
      Y(I,2)=Y(I,3)
      QX(I,2)=QX(I,3)
      QY(I,2)=QY(I,3)
1800  CONTINUE
C*****
C      CALCULATE THE VERTICALITY.
C
      VERCLT(M-2)=(ZS(1)-ZS(200))/(200*DELTAS)
C
C      SAVE SOME DATA OVER TIME.
C
      R2(M-2)=RS(2)
      THETA2(M-2)=THETAS(2)
      Z2(M-2)=ZS(2)
      R200(M-1)=RS(200)
C
C      IF USING ANTI-YOYO, SAVE THE REQUIRED BANK ANGLE VARIATION.
C
      IF (YO .EQ. 1.0) THEN
C
C          PHIV(M-2)=PHIVMX*COS(THEDOT*(M-2)*DELTAT-(2*PI-DWYO1))
C
C          THIS VERSION IS FOR THE ANTI-YOYO CASE USING THE AVERAGE
C          APPARENT FORCING WIND.
C
C          PHIV(M-2)=PHIVMX*COS(THEDOT*(M-2)*DELTAT-(2*PI-DWYO))
C
C      ELSE
C          ENDIF
C*****
C      OPTIONAL DATA FILES. IF THESE ARE USED, THEY PROVIDE SNAPSHOTS
C      OF THE DISPLACEMENTS AT VARIOUS TIMES.
C
      IF (M .EQ. K-1000) THEN
      OPEN (UNIT=11,FILE='DATA1.MAT')
      DO 1850 I=1,200
      WRITE(11,*) X(I,3)
1850  CONTINUE
      CLOSE(11)
      ENDIF

      IF (M .EQ. K-500) THEN
      OPEN (UNIT=12,FILE='DATA2.MAT')
      DO 1860 I=1,200
      WRITE(12,*) X(I,3)
1860  CONTINUE
      CLOSE(12)
      ENDIF

      IF (M .EQ. K-200) THEN
      OPEN (UNIT=13,FILE='DATA3.MAT')

```

```

DO 1870 I=1,200
WRITE(13,*) X(I,3)
1870 CONTINUE
CLOSE(13)
ENDIF

IF (M .EQ. K-100) THEN
OPEN (UNIT=14,FILE='DATA4.MAT')
DO 1880 I=1,200
WRITE(14,*) X(I,3)
1880 CONTINUE
CLOSE(14)
ENDIF

IF (M .EQ. K-50) THEN
OPEN (UNIT=15,FILE='DATA5.MAT')
DO 1890 I=1,200
WRITE(15,*) X(I,3)
1890 CONTINUE
CLOSE(15)
ENDIF

IF (M .EQ. K-40) THEN
OPEN (UNIT=16,FILE='DATA6.MAT')
DO 1900 I=1,200
WRITE(16,*) X(I,3)
1900 CONTINUE
CLOSE(16)
ENDIF

IF (M .EQ. K-30) THEN
OPEN (UNIT=17,FILE='DATA7.MAT')
DO 1910 I=1,200
WRITE(17,*) X(I,3)
1910 CONTINUE
CLOSE(17)
ENDIF

IF (M .EQ. K-20) THEN
OPEN (UNIT=18,FILE='DATA8.MAT')
DO 1920 I=1,200
WRITE(18,*) X(I,3)
1920 CONTINUE
CLOSE(18)
ENDIF

IF (M .EQ. K-10) THEN
OPEN (UNIT=19,FILE='DATA9.MAT')
DO 1930 I=1,200
WRITE(19,*) X(I,3)
1930 CONTINUE
CLOSE(19)
ENDIF

IF (M .EQ. K) THEN
OPEN (UNIT=20,FILE='DATA10.MAT')
DO 1940 I=1,200
WRITE(20,*) X(I,3)
19.0 CONTINUE
CLOSE(20)
ENDIF

```

C

```

C      END OF THE TIME LOOPS.
C
C      WRITE EACH 100TH M TO GIVE THE OPERATOR A PROGRESS REPORT.
C
      IF (NINT(M/100.0) .EQ. M/100.0) THEN
        WRITE(6,*)M
      ELSE
        ENDIF
2000    CONTINUE
C
C*****
C*****
C      WRITE VERTICALITY, POSITION VARIATION AT A POINT 45 FEET PAST
C      THE TOWPOINT, THE TENSION AT THE TOWPOINT AND THE VARIATION
C      IN PHI REQUIRED BY THE ANTI-YOYO MANEUVER TO FILES.
C
      DO 2050 I=1,K-2
        WRITE(30,10)VERCLT(I)
        WRITE(31,10)R(2)+(R2(I)-R(2))*45.0/DELTAS
        WRITE(32,10)THETA2(I)*45.0/DELTAS
        WRITE(33,10)Z(2)+(Z2(I)-Z(2))*45.0/DELTAS
        IF (DELT(I) .LT. 1000) THEN
          WRITE(34,10)(DELT(I)+T(1))
        ELSE
          ENDIF
        IF (YO .EQ. 1.0) THEN
          WRITE(35,10)PHIV(I)*360/(2.0*PI)
        ELSE
          ENDIF
        WRITE(36,10) R200(I)
2050    CONTINUE
C*****
C      IF DESIRED, MAY WRITE TO SCREEN FOR QUICK EVALUATION OF THE
C      RESULTS.
C
      DO 2100 I=1,200
        WRITE(6,*) I,RS(I),THETAS(I),ZS(I)
        IF (I .EQ. 20) THEN
          PAUSE
        ELSEIF (I .EQ. 40) THEN
          PAUSE
        ELSEIF (I .EQ. 60) THEN
          PAUSE
        ELSEIF (I .EQ. 80) THEN
          PAUSE
        ELSEIF (I .EQ. 100) THEN
          PAUSE
        ELSEIF (I .EQ. 120) THEN
          PAUSE
        ELSEIF (I .EQ. 140) THEN
          PAUSE
        ELSEIF (I .EQ. 160) THEN
          PAUSE
        ELSEIF (I .EQ. 180) THEN
          PAUSE
        ELSE
          ENDIF
C2100    CONTINUE
        WRITE(6,*)R,'    TIME STEPS COMPLETE!!!'
        WRITE(6,*)'
        WRITE(6,*)'THE OUTPUT IS INCLUDED IN THE FOLLOWING:'
        WRITE(6,*)'VERCLT.MAT IS A TIME HISTORY OF THE VERTICALITY.'

```

```
WRITE(6,*) 'R2.MAT IS A TIME HISTORY OF THE RADIAL COORDINATE'
WRITE(6,*) 'OF THE POINT 45 FEET BEHIND THE AIRCRAFT.'
WRITE(6,*) 'THETA2.MAT AND R2.MAT ARE THE CORRESPONDING THETA'
WRITE(6,*) 'AND R COORDINATES.'
WRITE(6,*) 'T1.MAT IS THE TOWPOINT TENSION TIME HISTORY.'
WRITE(6,*) 'PHIV.MAT IS THE VARIATION IN BANK ANGLE REQUIRED'
WRITE(6,*) 'TO FLY THE ANTI-YOYO MANEUVER IF IT IS SELECTED.'
WRITE(6,*) 'ALL FILES ARE INDEXED TO THE CORRESPONDING TIME'
WRITE(6,*) 'STEP AND NOT ACTUAL CLOCK TIME.'
WRITE(6,*) 'SELECTED SNAPSHOTS OF THE X DISPLACEMENTS ARE'
WRITE(6,*) 'AVAILABLE IN DATA1.MAT THROUGH DATA2.MAT.'
END
```

## APPENDIX F

### EFFECTS OF ANTI-YOYO MANEUVER INDUCED TOWPLANE RADIUS AND ORBIT RATE VARIATIONS

As mentioned in Chapter V, the angle of bank variations used by the anti-yoyo maneuver caused a change in both the towplane orbit radius and towplane orbit rate. Applying equation (5.4) to the mean and the maximum angles of bank for the test conditions described in Figure 5.7 showed that the turn radius varied 4% per degree of bank angle variation. Equation (5.3) demonstrated that  $\dot{\theta}$  also varied 4% per degree of angle of bank change. To analyze the effects of these harmonic variations, a two dimensional computer simulation of the dangling chain with the drogue attached to the lower end and a movable upper boundary condition was developed using the wire configuration used to generate Figure 5.7. The simulation is depicted in Figure F.1.

The upper end of the dangling chain was sinusoidally moved  $\Delta R = \pm 400$  feet over a range of frequencies. The limit of  $\Delta R = \pm 400$  feet corresponded to the maximum change in radius due to the angle of bank variation used in Figure 5.7. The simulation was performed for the completely undamped case and for the case where pseudo-damping due to the lateral oscillation rate was present as described in Chapter IV.

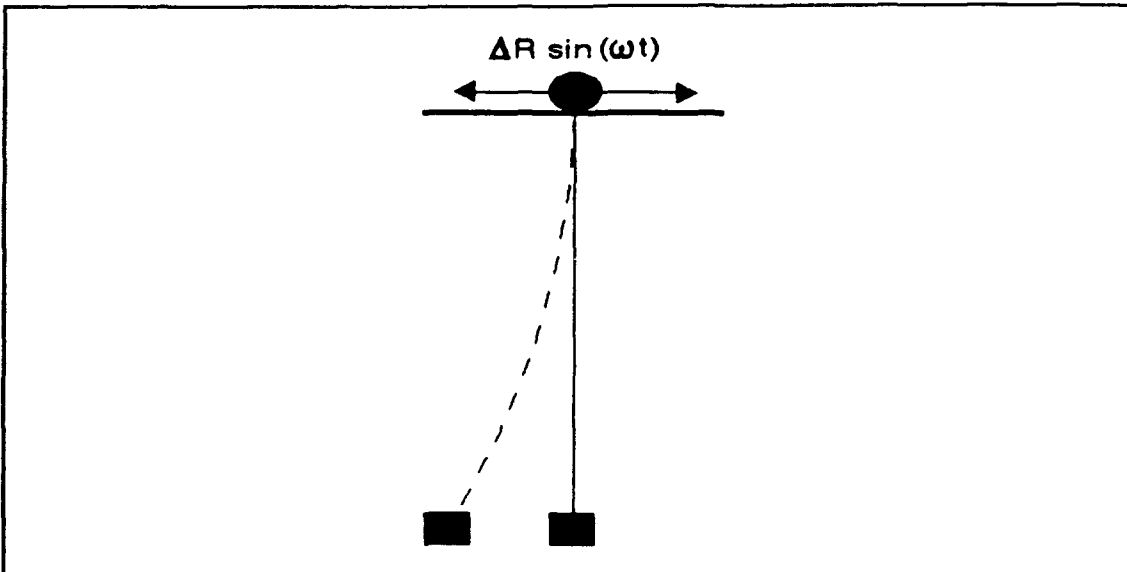


**Figure F.1:** Dangling Chain Model With Harmonically Moving Upper Boundary

The results are shown in Figure F.2 where the maximum drogue displacements, normalized by  $\Delta R$ , were plotted versus the frequency at which the upper end location was modulated. The resonant peaks for the undamped case corresponded to the theoretical singularities for the dangling chain with a weight attached to the free end calculated in Appendix B and listed in equation B.23. Note that with the application of the lateral rate drag, the resonant peaks were suppressed and the resulting magnitude of the oscillations were greatly reduced.

The simulation above applied only the pseudo-damping due to the lateral oscillation rate and was thus conservative. At the typical TACAMO orbit frequencies of between 0.04 rad/sec and 0.08 rad/sec, the gain between the input displacement magnitude at the upper end of the chain and the

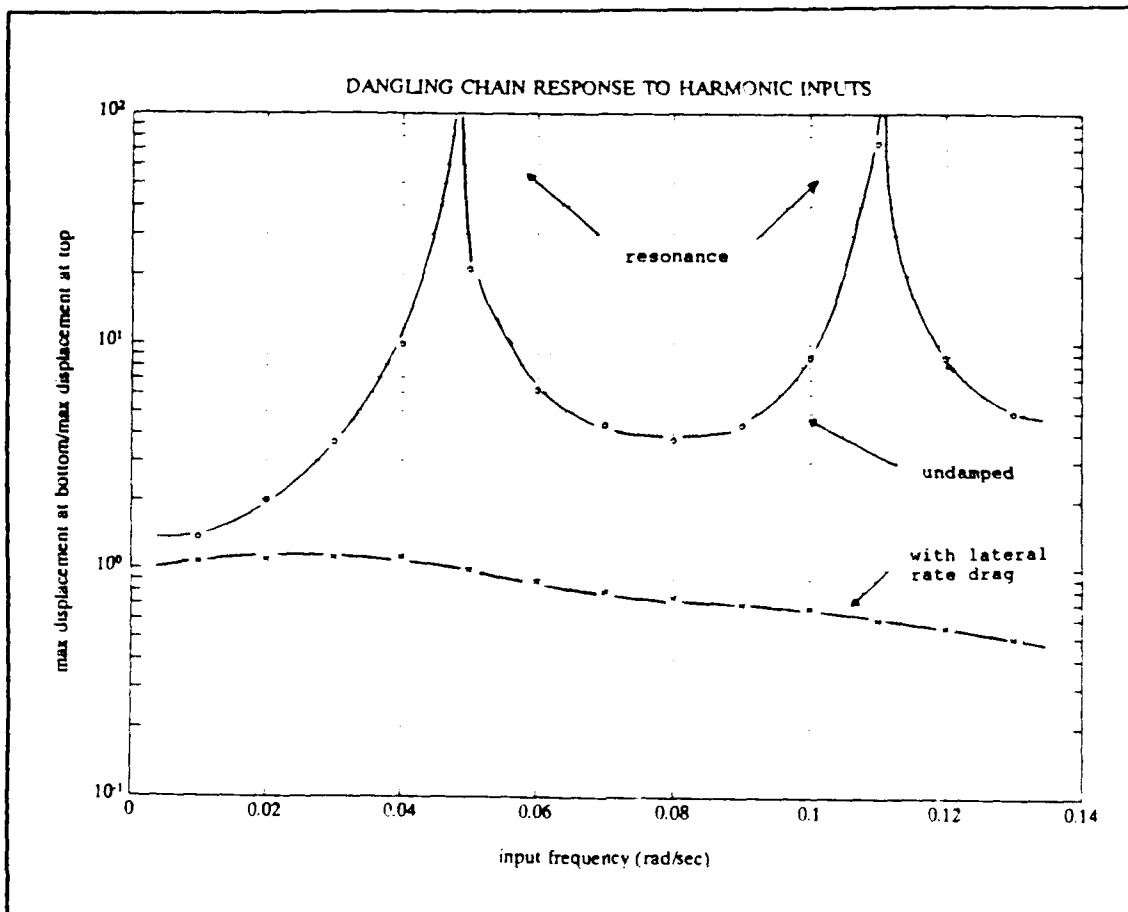


**Figure F.2:** Dangling Chain Response to Harmonic Displacements at the Top

displacement magnitude at the lower end near the drogue was approximately unity. The second form of pseudo-damping, which was due to the angle of bank variation, was applied for the test conditions of Figure 5.7. The input frequency was 0.057 rad/sec for these conditions. The effect of the restorative force due to angle of attack variations was to reduce the output to 50 feet/400 feet=0.125, an order of magnitude dissipation of the output from the input magnitude. The discussion in this appendix has shown that the effects of anti-yoyo maneuver induced towplane radius

and orbit rate variations were attenuated by pseudo-damping and thus they were neglected.

As a further analysis of the effects of pseudo-damping upon the dangling chain simulation, the static model was modified to allow the addition of a constant set of forcing function forces along the wire length. The forcing function forces were chosen equal to the forces calculated by the dynamic model at a single point in time. Figure F.3 is a comparison of the Z coordinate of the wire position for the dynamic model, the static model and for the static model with the addition of the forcing function forces (quasi-static solution). Note that the dynamic model position calculation was distinct from both the static model position as well as the quasi-static model position, highlighting the effects of the dangling chain governing equation. If the dynamic and quasi-static position calculations had been the same, it would have indicated that pseudo-damping had completely eliminated the effects of the dangling chain dynamics. Figures F.2 and F.3 demonstrate that the effects of pseudo-damping eliminate much, but not all, of the dangling chain dynamics.



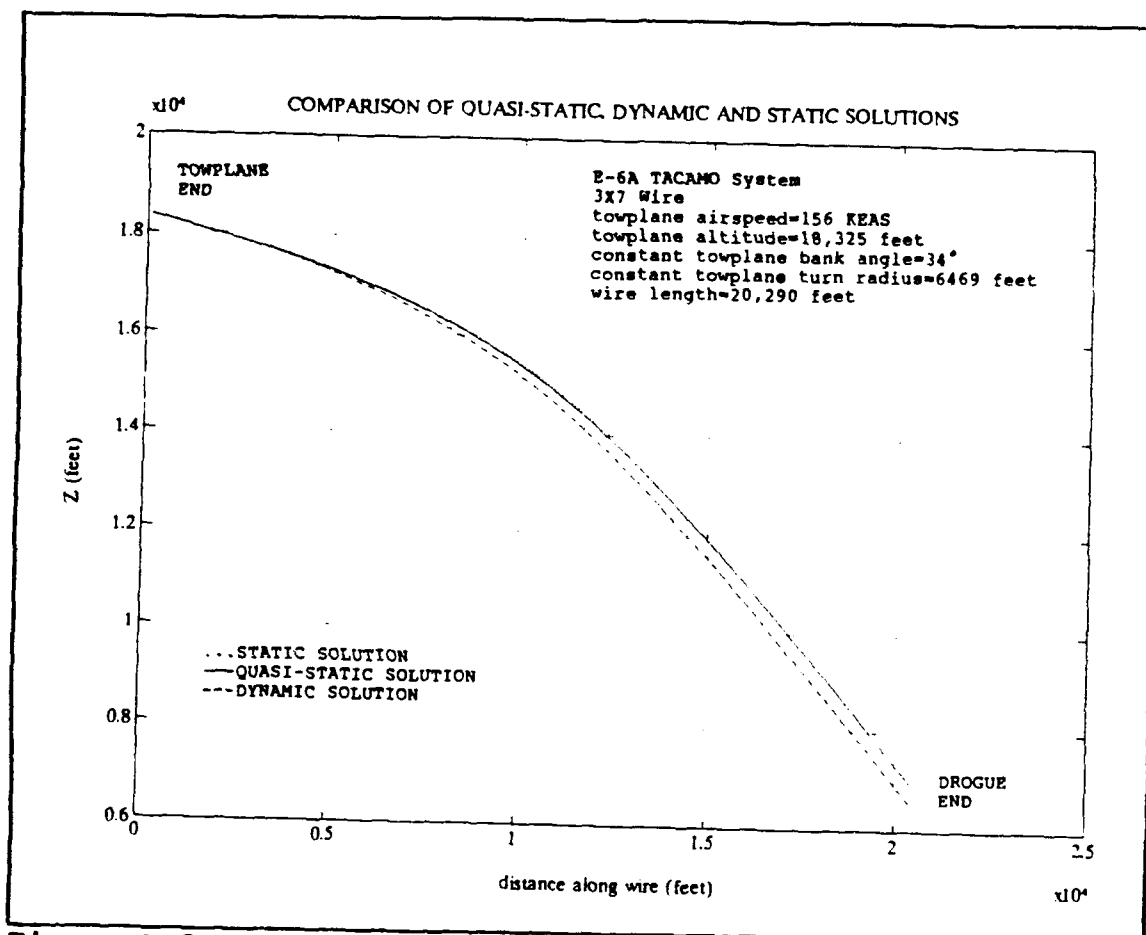


**Figure F.3: Comparison of Quasi-static, Dynamic and Static Vertical Coordinate Position Solutions**

## APPENDIX G

### FLYING DROGUE DESIGN

The requirements of a flying autonomous drone towed behind an airplane were similar in concept to those of a Remotely Piloted Vehicle (RPV). An RPV was selected that approximately fit the requirements of weight, size and configuration. The flying drogue was thus based upon the general design of the EXDRONE or SYMDEC 4 RPV with the engine removed. Hill provided a number of the desired parameters as outlined in (G.1) [Ref. 21:pp. 23-46] and Yip made available others in (G.2) [Ref. 22:pp. 34-46] where AR was the aspect ratio,  $b_D$  was the drogue span and  $l_D$  was the theoretical root chord.

$$\begin{aligned} &AR=3.14 \\ C_{L\alpha D}=2.53 & \text{ until } C_{LD}=0.8, \alpha=24^\circ \\ \left(\frac{L}{D}\right)_{\max} & \text{ at } C_{LD}=0.33, C_{DD}=0.031 \end{aligned} \quad (G.1)$$

$$\begin{aligned} S_D &= 21.24 \text{ ft}^2 \\ b_D &= 8.167 \text{ ft}^2 \\ l_D &= 4.458 \text{ ft} \end{aligned} \quad (G.2)$$

In addition, Hill provided a plot of  $C_{DD}$  versus  $C_{LD}$  at Reynolds numbers applicable to the sea level 45 to 100 knot regime of interest to the flying drogue. An analytical expression, vice a table look up, was much preferred for

programming purposes and so a number of points were extracted from this plot and used to perform a third order polynomial curve fit. The resulting polynomial is presented in equation (G.3). Since the EXDRONE data was being used as a rough approximation of the final drogue parameters, the inaccuracies introduced by curve fitting the experimental data were deemed acceptable. A maximum  $C_{LD}$  of 0.75 was used whenever appropriate since the stall  $C_{LD}$  for the EXDRONE was approximately 0.8. It should be emphasized that the flying drogue probably will not use the exact EXDRONE configuration. The EXDRONE data and configuration were used to approximate the maximum coefficients and forces which can be physically developed in flying hardware.

$$C_{DD} = 0.3129C_{LD}^3 + 0.084C_{LD}^2 - 0.153C_{LD} + 0.0205 \quad (G.3)$$

The pure lateral control scheme required both controlled drag as well as lift. This mix of forces allowed control of the vector perpendicular to the local tangent vector. Tailoring the lift of the drogue merely required controlling the angle of attack. The  $C_{L\alpha D}$  and other needed parameters were described as part of the steady-state flying drogue model. A split speedbrake configuration was chosen to develop the tailored drag. This required that the EXDRONE be modified such that the aft part of the wing inboard of the ailerons as well as the vertical tail split open on command to produce the required drag. The ailerons were moved as far out on the tips of the EXDRONE wing as possible

to maximize the area available to split. By splitting the last twenty inches of the wing as well as the vertical tail, approximately eleven square feet of area was available.

The effect of the split speedbrake was approximated using the 1958 Hoerner approximation for drag on a wedge of given half internal angle [Ref. 10:p. 3-18]. The speedbrakes were split to the approximate shape of a wedge with a half internal angle of  $\epsilon$ . Holes were added to the speedbrakes to enhance stability of the bluff body when the speedbrakes were split to a large angle. The combined effects of the holes and the effect of the EXDRONE fuselage was to reduce the drag generating capability and so only  $0.75 C_{D0}$  as provided by Hoerner was used. Since the Hoerner derived numbers were used only as a rough, early cut of the  $C_{D0}$  generated by the speedbrakes, a number of points were taken from the plot and used to develop a third order least squares polynomial curve fit of the  $C_{D0}$  versus  $\epsilon$  data. The resulting polynomial is included in equation (G.4).

$$\begin{aligned} C_{D0} &= 0.2322\epsilon^3 - 0.7816\epsilon^2 + 1.5665\epsilon + 0.6479 \\ C_{D0} &= 0.75 C_{D0} \quad \epsilon \text{ in radians} \\ C_{D0} \text{ reference area} &= \text{projected frontal area} \end{aligned} \quad (G.4)$$

Figure G.1 is a side on view of the split flap configuration.  $w$  was defined as shown in Figure G.1 and it was remembered that the flaps had a chordwise length of 20 inches. Next, it was assumed that the maximum deflection of the split speedbrakes was  $\epsilon_{\max} = 60^\circ$ . These assumptions

resulted in  $w_{\max}=1.44$  feet. The vertical tail was approximately triangular and 12 inches tall. For the purpose of simplifying the following calculations, all of the split surface, including the surface on the EXDRONE wing as well as the vertical tail was treated as a single surface. Knowing that the total split speedbrake area was  $11 \text{ ft}^2$  and that the chordwise length of the speedbrake was 1.667 ft, the equivalent spanwise length of the speedbrakes including both the wing and vertical tail area was found to be 6.6 ft. Using  $w_{\max}=1.44$  ft and remembering that this value was only half of the projected frontal height of the speedbrake wedge as seen in Figure G.1, provided a value of the maximum projected frontal area of the fully deployed speedbrakes,  $S_{\text{pf}}=19 \text{ ft}^2$ .

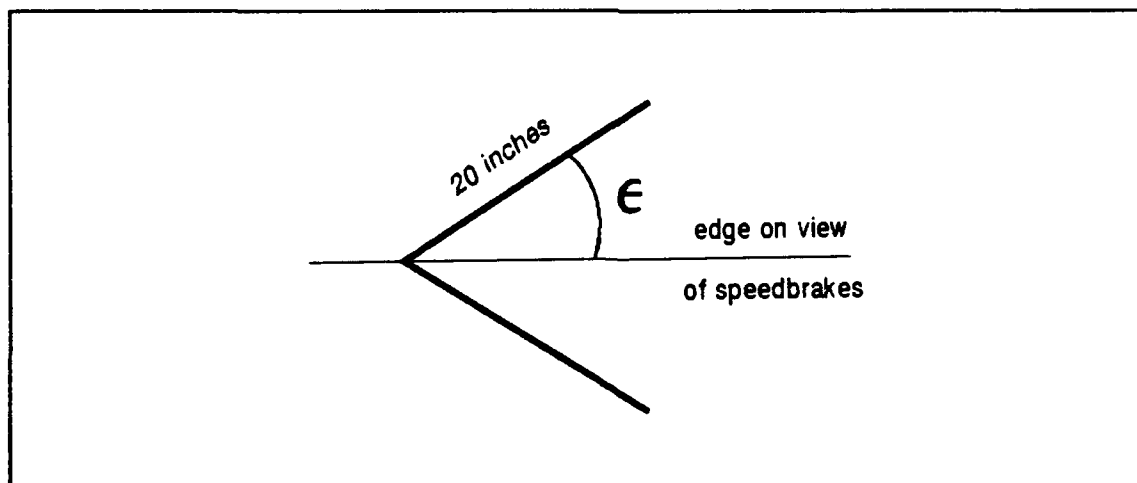


**Figure G.1:** Edge View of Split Speedbrakes

Using 0.75 of Hoerner's  $C_{D0}$  resulted in  $C_{D0\max}=1.275$  and applying this to the definition of the drag coefficient using the projected frontal area of the wedge as the

characteristic area resulted in equation (G.5). It was assumed that the commanded drag may range from the maximum value provided in (G.5) down to the zero lift drag of the EXDRONE which was dependent upon the EXDRONE  $C_{D0}$  provided in equation (G.4). The minimum drag value was included in equation (G.6) where the characteristic area was now the EXDRONE wing area. The minimum and maximum available lift were derived using a maximum lift coefficient under stall of  $C_{Lmax}=\pm 0.75$  and is provided in equation (G.7), where again the characteristic area was the total wing area.

$$D_{Dmax}=12.1\rho_M(R_N\dot{\theta})^2 \quad (G.5)$$

$$D_{Dmin}=0.2124\rho_M(R_N\dot{\theta})^2 \quad (G.6)$$

$$L_{Dmax/min}=\pm 7.965\rho_M(R_N\dot{\theta})^2 \quad (G.7)$$

When the wire was located at the high verticality multiple solution, the angle between the wire and the horizontal plane at the end of the wire near the drogue was approximately 90 degrees. Equation (G.8) was the angle between the wire segment connecting the drogue and the first internal gridpoint and the horizontal plane. As an example, for the flight profile and wind/drogue configuration used to develop Figures 3.10 through 3.14,  $\eta=89.9^\circ$ . Applying the

steady-state assumptions outlined in Chapter III, the drogue drag was approximately perpendicular to the wire at the lower grid segments and the lift was approximately tangential to the wire

$$\eta = a \cos \left[ \frac{(R_{N-1} + R_N)(\theta_{N-1} - \theta_N)}{\Delta S} \right] \quad (G.8)$$

Since the wire was approximately vertical, the  $X_{n,m}$  displacement was approximately entirely in the  $\bar{e}_R$  coordinate direction and the  $Y_{n,m}$  displacement was approximately entirely in the  $\bar{e}_\theta$  coordinate direction. Since the relative wind vector was in the  $\bar{e}_\theta$  direction in steady-state conditions and the drogue drag was collinear with the relative wind, the drag of the drogue was approximately in the  $Y_{n,m}$  dangling chain displacement direction at the drogue. By the same reasoning, as the drogue banked, the lift vector, which was perpendicular to the relative wind vector, developed a horizontal component which was approximately in the  $X_{n,m}$  dangling chain displacement direction. Finally, for the nearly vertical wire, the vertical component of lift was approximately in the wire tangential direction.

Under the conditions outlined above, the maximum control forces which could be applied as inputs to the  $X_{n,m}$  and  $Y_{n,m}$  dangling chain displacement equations were determined. Control forces were required in both the positive and negative directions and so for the case of the lateral  $Y_{n,m}$

control force direction, which was approximately all drag, the maximum force available was equal to half of the difference between the maximum and minimum drag forces available as shown in equation (G.5). Substituting from equations (G.5) and (G.6) resulted in (G.10).

$$F_{DYmax} = \frac{(D_{Dmax} - D_{Dmin})}{\cos\left(\frac{\pi}{2} - \eta\right)} \quad (G.9)$$

$$F_{DYmax/min} = \pm \left( \frac{\frac{(12.1 - 0.2124)}{2} \rho_M (R_N \dot{\theta})^2}{\cos\left(\frac{\pi}{2} - \eta\right)} \right) \quad (G.10)$$

As discussed in Chapter V, the drogue was, in general, flown at some non-zero steady-state bank angle and angle of attack.  $L_{Dss}$  was thus defined as the steady-state component of the drogue lift. Assuming the drogue could be banked to approximately  $\phi_D = \pm 90^\circ$  and could produce the maximum lift given in equation (G.7), the maximum force in the  $X_{n,m}$  displacement direction was shown in equation (G.11).

$$F_{DXmax/min} = \pm \sqrt{(7.965 \rho_M (R_N \dot{\theta})^2)^2 - L_{Dss}^2} \quad (G.11)$$

Since the wire was nearly vertical near the drogue, the maximum force available in the tangential direction was approximately determined by the maximum lift force which the drogue could develop. The maximum tangential control force was thus as shown in equation (G.7).



## LIST OF REFERENCES

1. Payne, C. M., *Paramaterization of a Linear Array During Ship Maneuvers*, Master's Thesis, Naval Postgraduate School, Monterey, California, March 1992.
2. Skop, R. A., and Choo, Y., "The Configuration of a Cable Towed in a Circular Path", *Journal of Aircraft*, Vol. 8, No. 11, November 1971.
3. Irvine, H. M., and Caughey, T. K., "The Linear Theory of a Suspended Cable", *Proceedings of the Royal Society of London*, Vol. 341 A, 1974.
4. Anderson, W. J., "Dynamic Instability of a Cable in Incompressible Flow", AIAA Paper No. 73-395, 1973.
5. Russell, J. J., *Equilibrium and Stability of a Whirling Cable*, Dissertation, University of Michigan, 1974.
6. Matteis, G., "Dynamics of a Towed Sailplane", AIAA Paper 91-2862, 1991.
7. U. S. Naval Air Development Center, *Mathematical Model for Long Cable Towed by Orbiting Aircraft*, NADC-AM-6849, by Huang, S. L., pp. 6-10, 12 June 1969.
8. Crist, S. A., "Analysis of the Motion of a Long Wire Towed from an Orbiting Aircraft", *The Shock and Vibration Bulletin*, Bulletin 41, Part 6, December 1970.
9. Cornell Aeronautical Laboratory Inc., Report JC5039-B-2, *TACAMO Flight Investigations*, by John G. Lawton, 30 June 1972.
10. Hoerner, S. F., *Fluid Dynamic Drag*, published by the author, 1958.
11. Gerald, C. F., and Wheatly, P. O., *Applied Numerical Analysis*, 4th ed., Addison-Wesley Publishing Company, 1990.
12. Stuart, T. D., *Experimental Study of the Effect of Helical Grooves on Infinite Cylinders*, Engineer's Thesis (draft), Naval Postgraduate School, Monterey, California, September 1992.
13. Beer, F. P., and Johnston, R. E., *Mechanics of Materials*, McGraw-Hill Book Company, 1981.

14. Scandrett, C., unpublished notes, 1992.
15. Schmidt, L. V., unpublished notes, 1992.
16. Anderson, D. A., and others, *Computational Fluid Mechanics and Heat Transfer*, Hemisphere Publishing Corporation, 1984.
17. Telephone conversation between LT Pat Leard, Naval Air Warfare Center, Aircraft Division, Force Warfare Aircraft Test Directorate and author, 26 March 1992.
18. Naval Air Systems Command, *Preliminary NATOPS Flight Manual Navy Model E-6A Aircraft*, A1-E6AAA-NFM-000, 15 April 1988.
19. Volterra, E., and Zachmanoglou, E. C., *Dynamics of Vibration*, Charles E. Merrill Books, Inc., 1965.
20. Bowman, F., *Introduction to Bessel Functions*, Dover Publications Inc., 1958.
21. Hill, M. L., "Delta Wing Mini-UAV's", *Unmanned Systems*, Spring 1989.
22. Yip, L. P., and others, "Wind-Tunnel and Flight-Test Investigation of the EXDRONE Remotely Piloted Vehicle Configuration", AIAA Paper No. 90-1261-CP, 1990.

### INITIAL DISTRIBUTION LIST

- |     |   |   |
|-----|---|---|
| 1.  | Defense Technical Information Center<br>Cameron Station<br>Alexandria, VA 22304-6145  | 2 |
| 2.  | Library, Code 0142<br>Naval Postgraduate School<br>Monterey, CA 93943-5002  | 2 |
| 3.  | Professor L. V. Schmidt, AA/Sc<br>Naval Postgraduate School<br>Monterey, CA 93940-5000  | 2 |
| 4.  | Professor D. J. Collins, AA/Co<br>Naval Postgraduate School<br>Monterey, CA 93940-5000  | 1 |
| 5.  | Professor R. M. Howard, AA/Ho<br>Naval Postgraduate School<br>Monterey, CA 93940-5000   | 1 |
| 6.  | Professor D. Danielson, MA/Dd<br>Naval Postgraduate School<br>Monterey, CA 93940-5000   | 1 |
| 7.  | Professor H. A. Titus, EC/Ts<br>Naval Postgraduate School<br>Monterey, CA 93940-5000  | 1 |
| 8.  | Naval Air Systems Command (PMA-271)<br>Naval Air Systems Command Headquarters<br>Washington, DC 20361-1271                          | 1 |
| 9.  | Director, Force Warfare Aircraft Test Directorate<br>Attn. CDR Hill (FW-03)<br>Naval Air Warfare Center<br>Patuxent River, MD 20670 | 1 |
| 10. | Director, Force Warfare Aircraft Test Directorate<br>Attn. FW-20<br>Naval Air Warfare Center<br>Patuxent River, MD 20670            | 1 |
| 11. | Director, Force Warfare Aircraft Test Directorate<br>Attn. FW-70<br>Naval Air Warfare Center<br>Patuxent River, MD 20670            | 1 |

12. Attn. Bob Allen  
Rockwell International  
Command and Control Systems Division  
3200 E Renner RD  
Richardson, TX 75082

1